Atomistic Simulations of Proton Transport in the Gas and Condensed Phases: Spectroscopy, Reaction Kinetics and Grotthuss Mechanism

Inauguraldissertation

zur
Erlangung der Würde eines Doktors der Philosophie
vorgelegt der
Philosophisch-Naturwissenschaftlichen Fakultät
der Universität Basel

von
Zhen-Hao Xu
von China

Basel, 2018

Genehmigt von der Philosophisch-Naturwissenschaftlichen Fakultät auf Antrag von:

Prof. Dr. Markus Meuwly
Prof. Dr. Anatole von Lilienfeld

Basel, den 22. Mai 2018

Prof. Dr. Martin Spiess
Dekan

Preface

A very great deal more truth can become
known than can be proven.

- *Richard Feynman* -

Man proposes but God disposes.

"Romance of the Three Kingdoms" – *G. Luo* (14th century)

Acknowledgments

I would like to express my special appreciation and thanks to my advisor Prof. Dr. Markus Meuwly for providing me an opportunity for a splendid doctoral study at the University of Basel with an outstanding and attractive research project and being a tremendous and informative mentor for me. I appreciated your guidance and shared experiences in all scientific fields with fruitful and inspiring discussions which allow me to grow as a research scientist. Another thanks is bid to Prof. Dr. Anatole von Lilienfeld for examining my thesis and Prof. Dr. Wolfgang Meier for kindly being the chairman of the defense.

I acknowledge Prof. Dr. Henrik G. Kjaergaard and Dr. Kasper Mackeprang from University of Copenhagen and Prof. Dr. Mark Johnson from Yale University for the research collaboration and providing the experimental data which marvelously improved the quality of my research work and brought useful and insightful information for a better understanding to the science behind this thesis.

A special thanks goes to the current and former group members for all kinds of support, knowledge exchanges and for the joyful moments during all years I spent in the city of Basel. The group was like a family which provided a superb atmosphere both during and after work hours. Many thanks for the great time.

Special thanks also goes to my friends and parents for the consistent support and encouragement. I would also like to thank the support from Swiss National Science Foundation (SNF), NCCR MUST and the department of Chemistry at the University of Basel.

Contents

Abstract

The empirical force field method of Molecular Mechanics with Proton Transfer (MMPT) follows concepts from a QM/MM scheme which treats the proton transfer (PT) process in its full dimensionality while improving on three important aspects of the problem: speed, accuracy, and versatility. Recent applications focused on the computation of infrared signatures for the shared proton between a donor and an acceptor atom. This was complemented and supported by recent experiments. Both conventional molecular dynamics and more advanced ring polymer molecular dynamics (RPMD) simulations were carried out to characterize the energetics, dynamics and spectroscopy of transferring protons in systems including formic acid dimer and protonated oxalate. The simulations were found reproducing infrared spectra in good agreement with experimental results.

Moreover, the primary kinetic isotope effects (KIEs) of intramolecular hydrogen transfer are determined in both classical molecular dynamics (MD) and quantum simulations with the MMPT force fields. For classical simulations, the parametric potential energy surfaces (PESs) were refined with zero point vibrational effects (ZPVEs) considered, which effectively leads to the reduction of reaction barrier heights for the corresponding systems such as malondialdehyde and acetylacetone. With ZPVE introduced, the effective barrier heights are different between the isotope unsubstituted and substituted systems. That led to the chemical contributions into the primary kinetic isotope effects. In addition to classical simulations, the nuclear quantum effects (NQEs) are explicitly included in the path integral simulations based on the same empirical potential surfaces. With the inclusion of NQEs, simulation results lead to the increase of KIE values at 250 K by a factor of $2.5 \sim 3.0$ compared to those from classical MD simulations.

Rather than performing proton transfer within a priori defined reaction motif, in this thesis work, MMPT was extensively developed to be capable of delocalizing and treating diffusive proton transport in both gas and condensed phases. This became possible by combining the MMPT force field with multi-surface adiabatic reactive molecular dynamics (MS-ARMD), which leads to the new multi-state MMPT (MS-MMPT) method. In this method, a global potential energy for proton transports is built by mixing multiple potential energy surfaces, each of which corresponds to an oscillatory PT reaction. That enables, for instance, all hydrogen atoms in a water bulk with excess protons to equally participate into the transfer reactions within the force field framework. The integrated MS-MMPT method was applied to performing proton diffusion simulations for $[H_2O]_nH^+$ clusters at the gas phase and bulk systems with the periodic boundary condition. Results were compared with both experiments and simulations using other established methods.

Part I.

Introduction

1. Overview

On the azure planet, the earth, water dominates and is the most abundant compound on its surface[1]. Water is not only a fundamental substance to constitute a life but also provides suitable living conditions for organism of all kinds in many aspects, including but not limited to maintenance of temperature, substance exchanges and participation of biochemical processes. Pure water is considered to be neutral in terms of acid-base neutrality, with a pH of 7, namely both concentration of hydrogen (H^+) and hydroxide (OH^-) ions are 10^{-1} mol/L. Acids have pH values less than 7 while bases have values greater than 7. In acidic solution, the excess hydrogen ion is usually accepted by a water molecule and present in forms of a hydronium ion (H_3O^+). However, the hydronium ion is not a long-stable ion but continuously pass its excess H^+ to other water molecules or a hydroxide ion, which forms a neutral water molecule. Such a process is called proton transfer.

More generally, a proton transfer process involves with simultaneous bond breaking and formation of a cationic hydrogen atom from its donor and acceptor atoms, such as O, N, S, Cl etc. The proton transfer (PT) reactions involve with a variety of important chemical and biological processes:[2–4], enzymatic catalysis[5] and protein-aided proton transport in membranes[6,7] etc. The importance of this reaction is of great interests in the scientific fields such as spectroscopy[8–14], reaction kinetics[15–18] and charge conduction regarding selective permeability and fuel cells.[19] In computational studies, the proton transfer reaction can be classified as oscillatory proton transfer and so-called Grotthuss mechanism.[3] An oscillatory PT process stands for forth-and-back proton hops between two acceptive atoms. In Grotthuss mechanism, on the other hand, a continuous procedure of stepwise PT moves is considered, which leads to a conduction process of cations. In aqueous systems, the network of hydrogen bonds is a more predominant factor to the diffusivity of the excess protons, compared to Brownian motions of proton carriers.[20] And the Grotthuss proton transport usually takes place in a picosecond timescale and *ab initio* molecular dynamics (AIMD) methods are one of the most realistic solutions for simulating such processes. However, these approaches are limited in high computational costs dealing with large biomolecular systems.[2] Despite of this fact, AIMD provide direct and descriptive insight upon the mechanism and energetics, which can be useful for approximate methods through parametrization. The hybrid QM-MM approaches, on the other hand, have a limitation that the QM subsystems are pre-defined in which proton diffusion is only allowed during the simulations. Moreover, there have been considerable interests in developing classical MD simulation methods which are capable of simulating Grotthuss proton transport.[21–24]

In recent years, Molecular Mechanics with Proton Transfer (MMPT) has been extensively developed which provides explicit treatment to atomistic systems involved with proton transfer reactions.[25,26] This method has been proven a promising technique to perform various types of proton transfer/hops in both gas and condensed phases. In this approach, multi-dimensional potential energy surfaces (PES) are modeled with overlapped Morse potential functions to perform sustainable dissociation and formation of $X - H$ bonds and parametrized to reproduce results from *ab initio* calculations. In this thesis, new features are added into MMPT, including a new model for double proton transfer (DPT) and feasibilities of using resonance structures and charge fluctuation. And more importantly, a novel method, so called multi-state MMPT (MS-MMPT), is introduced in the current work for simulation delocalized PT reaction processes, such as Grotthuss proton transport, especially in the condensed phase. This method focuses on solving technical challenges in several aspects: 1) Proton transport should be spontaneous and undirected in MD simulations; 2) Grotthuss proton transport leads to diffusion of the excess charge in the system, which requires a model featuring in charge delocalization other than using fixed point charges (FPC); 3) The diffusivity of the excess proton (or charge) in an aqueous system should be comparable between molecular dynamics and experiments; 4) The energy conservation should be obtained in MD simulations.

This thesis is organized as follows: Chapter 2 introduces the background methods for studying proton transport processes. Chapter 3 presents the formulation of the MMPT force field, which includes a new model for DPT reactions. A fast method of MMPT parametrization is also introduced in this chapter. Chapter 4 introduces the methodology and implementation of the new MS-MMPT method. The resonance structure and the charge transfer models are described as a part of the new development. Applications of MMPT and MS-MMPT methods are given in three chapters. Chapter 5 presents simulated infrared (IR) spectroscopies for formic acid dimer (FAD) and protonated oxalate ($p-$Oxa) which are compared to the experimental results. Chapter 6 investigates the kinetic isotope effects (KIE) of malondialdehyde (Mal) and acetylacetone (AcAc) from classical and quantum simulations using the MMPT force field. Chapter 7 presents simulations of proton diffusion using the new MS-MMPT method. And Chapter 8 is the conclusion and outlook.

2. Background

2.1. Quantum Mechanical Methods

2.1.1. Quantum Mechanics

The basic concept of *ab initio* or quantum mechanical (QM) molecular dynamics[27–29] is to propagate particles in the systems according to Newtonian forces applied on the nucleus. In classical molecular mechanics, the driving force is given by a empirical force field which moves corresponding degrees of freedom.[30,31] For *ab initio* MD simulation, it is due to solving the approximated Schrödinger's equation[32]

$$\hat{H}\psi = E\psi \tag{2.1}$$

for a many-particle system. ψ is the wave function which describes the probability distributions ($|\psi|^2$) of particles corresponding to the energy states. The Hamiltonian, $\hat{H}$, is the sum of the kinetic and potential energy of the system. Considering an isolated system of n particles with masses m_i, $\hat{H}$ can be given in forms of an operator

$$\hat{H} = \sum_{i=1}^{n} -\frac{\hbar^2}{2m_i}\nabla_i^2 + U(\boldsymbol{r}), \tag{2.2}$$

where ∇_i is the gradient operator and $U(\boldsymbol{r})$ is the potential energy of the system. The wave functions can be generalized to a three-dimensional situation which also creates the difficulties for solving the equations without simplifications or approximations.

Solving the Schrödinger equation for molecular systems is difficult mainly in the potential energy which is dependent of the geometric positions of all the electrons and nuclei. And in theory they are correlated to each other. In the regime of *ab initio* molecular dynamics (AIMD), the Born-Oppenheimer approximation[33,34] is a necessary and the most commonly used approximation to separate the treatment to electrons and nuclei. The theory is based on the observation that an electron is much lighter and moves much faster than those of a proton/neutron (ca. 1/1800).[35] That leads to the assumption that the kinetic energies of electrons are negligible and they respond instantaneously to any changes in the positions of the nuclei. Therefore, one electron is considered to be described by a Schrödinger equation under fixed configurations of nuclei, and on the other hand, the effective potential acted on the nuclei is partially contributed from electrons with their equilibrium electronic configurations. For a next MD step, the potential energy surface (PES) for the nuclei with changed positions can be re-mapped by recalculating electronic energies. That leads to Born-Oppenheimer molecular dynamics (BOMD).[36–39] The Car-Parrinello molecular dynamics (CPMD) is another extensively studied and developed method for simulating reactive process.[27,28] In the CPMD method, electrons are explicitly described using fictitious dynamics[40] and the wave function parameters are propagated as classical degrees of freedom (DOFs).[41]

2.1.2. Semi-empirical and Hybrid Quantum Mechanic/Molecular Mechanics Methods

The semi-empirical method are a simplified versions of Hartree-Fock[32,42] theory using empirical corrections (from experimental results) so as to reduce the computing costs for systems for which AIMD methods are too expensive to perform MD simulations.[43] Typical methods are AM1,[44] PM3[45] (PM6[46]) and MNDO.[47] To perform reactive simulations such as proton transfer, however, these semi-empirical methods fail to provide the energetic accuracy compared to *ab initio* data. To improve this requires specific reaction parameters[48,49] and for proton transfer such efforts were carried out by Wang *et al.*[50] from which the semi-empirical models were parametrized to reproduce key properties from QM calculations based on density-functional theory. The density functional tight-binding (DFTB)[51–53] method is another approximate method which have been employed for studying proton transfer processes in biological systems. For proton transfer reactions, such simulations were carried out for studying double proton transfer[54] and protonated water systems.[55–57] And the methods have been continuously developed for performing proton diffusions in good agreement with the experiments.[57,58]

Computational simulations can be further accelerated by using the hybrid QM-MM approaches, the quantum and classical regions are defined initially and remain unchanged during the simulations.[59–61] That leads to a shortcoming for these approaches which is the difficulty in performing diffusive processes because e.g. a proton is only allowed in the QM region. That requires the MM part to be capable of simulating proton diffusion. Jiang *et al.* used a continuous adaptive QM/MM approach (DAS[62]) to simulate a hydroxide migration process toward a methanol molecule in the alkaline solution.[63] For this, a hybrid PM6-DH+[46,64] and ReaxFF[23] scheme was employed. For this approach, it also requires the QM and the reactive MM methods to be comparable energetic descriptions for proton diffusion (e.g. the barrier height of PT) and diffusion constants in both subsystems.[65]

2.2. Force Field Methods

2.2.1. Empirical Molecular Mechanics

Molecular mechanics is to describe the motion of a molecular system based on classical Newtonian mechanics. In the classical mechanics, all atoms in the system are treated as particles with masses and their dynamics are driven by force field[66], which is also called empirical force field and does not perform reactive processes such as bond breaking or formations. The empirical force field are parametrized to reproduce the quantum mechanical calculations[67,68] or experimental observations (i.e. infrared and Raman spectroscopy).[12,69,70] Due to the limitation (or pursuit) to the computational performance, force field is usually approximated into simple and thus comprehensive forms[71]. The inter-atomic bonds are treated as springs with harmonic forces for describing bond stretches and bends. And the torsions are treated as trigonometric functions and the periodicities are determined from the characterization of specific bonds. For non-bonded interaction, van der Waals and coulomb forces are usually used. Thereafter, the total potential energy is given by the sum of all the energy terms from bonded and non-bonded interactions. The expression for a typical empirical force field can be given as[30,31,71]

$$
\begin{aligned}
V_{\mathrm{FF}} = & \sum_{\text{bonds}} \frac{1}{2} k_b (l_i - l_{eq})^2 + \sum_{\text{angles}} \frac{1}{2} k_a (\theta_i - \theta_{eq})^2 \\
+ & \sum_{\text{torsion}} k_d (1 + \cos(n\phi_i - \delta_0)) + \sum_{\text{improper}} \frac{1}{2} k_\psi (\psi_i - \psi_{eq})^2 \\
+ & \sum_{\text{vdW}} \epsilon_{i,j} \big[(\frac{r_{\min,i,j}}{r_{i,j}})^{12} - (\frac{r_{\min,i,j}}{r_{i,j}})^6 \big] + \sum_{\text{coulomb}} \frac{q_i q_j}{4\pi\epsilon_0 r_{i,j}}
\end{aligned}
\tag{2.3}
$$

In Eq. 2.3, all k values are the force constants to the respective types of bonded interactions. l_{eq} and θ_{eq} are the equilibriums of bond length and bending angles. For the energy term of a torsion, n is the periodicity of the dihedral and δ_0 stands for an offset at which the energy reaches its maximum. The improper terms control the planarity of star-shaped bond topologies (i.e. $\alpha-$carbon in amide compound).

The non-bonded energy is given in a form of the sum of all van der Waals (vdW) and electrostatic terms for all non-bonded atom-atom pairs with $r_{i,j}$ as inter-atomic distances. For the van der Waals term, a Lenard-Jones (LJ) potential is used. $\epsilon_{i,j} = \sqrt{\epsilon_i \cdot \epsilon_j}$ refers to the well depth and $r_{\mathrm{min},i,j} = \dfrac{r_{\mathrm{min},i} + r_{\mathrm{min},j}}{2}$ is the LJ energy minimum distance between atom i and atom j. For the coulomb force, q_i and q_j are the atomic partial charges and $1/(4\pi\epsilon_0)$ is the coulomb constant.

2.2.2. Multi-state Empirical Valence Bond

Based on the empirical valence bond (EVB) theory, originally proposed by A. Warshel and R. Weiss ,[72,73] multi-state EVB (MS-EVB)[22,74–78] is a force field based approach which has been extensively developed and applied in bulk and water cluster systems.[79,80] The EVB method considers a bond breaking/forming process as a transition from one conformational state to the other. And these states, within the MS-EVB formalism, stand for delocalized solvation structures and are alleged as *basis states* with their respective wave function $|\psi_i>$. The net state function with a given conformation is then represented by a linear combination of empirical valence bond states.

$$|\Psi> = \sum_{i=1}^{N} c_i \cdot |\psi_i> \tag{2.4}$$

where N is the number of states and c_i is the coefficient. The total potential energy of the system can be given under a similar fashion to Eq. 2.4. By solving the eigenvalue-eigenfunction problem[76], $\{c_i\}$ can be obtained. That gives

$$\hat{\boldsymbol{H}}\mathbf{c} = E_0\mathbf{c}, \tag{2.5}$$

where $\hat{\boldsymbol{H}}$ is the Hamiltonian matrix which is described by empirical force field, $\mathbf{c}$ is the eigen vector of c_i and E_0 is the ground-state energy of the system[22]. For a water bulk system with one excess proton, each state refers to a unique hydrogen bonding topology with one H_3O^+ ion structure. The coefficient c_i determines how much the i-th state contribute into the total empirical potential energy and the largest amplitude among $\{c_i\}$ is called a *pivot state* in which the modeled H_3O^+ structure is the most likely hydronium ion in the system[76,78]. Once the largest c_i changes, a proton transfer move is complete by forming another realistic H_3O^+ ion from the current one.

For Hamiltonian matrix – $\hat{\boldsymbol{H}}$, elements of this matrix are divided in two parts: the diagonal $\{h_{ii}\}$ elements and the off-diagonal $\{h_{ij}\}$. The diagonal element h_{ii} represents for the classical potential energy of each basis state, given by

$$h_{ii} = V^{\text{intra}}_{\text{H}_3\text{O}^+} + \sum_{k=1}^{N_{\text{H}_2\text{O}}} V^{\text{intra}}_{\text{H}_2\text{O}} + \sum_{k=1}^{N_{\text{H}_2\text{O}}} V^{\text{inter}}_{\text{H}_3\text{O}^+\cdots\text{H}_2\text{O}} + \sum_{k\neq l}^{N_{\text{H}_2\text{O}}} V^{\text{inter},k,l}_{\text{H}_2\text{O}\cdots\text{H}_2\text{O}}, \tag{2.6}$$

where $V^{\text{intra}}_{\text{H}_3\text{O}^+}$ and $V^{\text{intra}}_{\text{H}_2\text{O}}$ are respectively the internal potential energies of H_3O^+ and water molecule with the given bonding topology in the i-th state, and $V^{\text{inter}}_{\text{H}_3\text{O}^+\cdots\text{H}_2\text{O}}$ and $V^{\text{inter},k,l}_{\text{H}_2\text{O}\cdots\text{H}_2\text{O}}$ are correspondingly nonbonded interactions. With different MS-EVB models, systems can be treated with various types of force field (e.g. water molecules were treated with either harmonic[76] or anharmonic[77] water models). The off-diagonal elements h_{ij}, on the other hand, introduce coupling effects for performing proton transport. Rather than physically meaningful energy terms, h_{ij} are partially given by empirical functions with geometry dependence. In details, if state $|i>$ and state $|j>$ share a common hydrogen atom (and this one acts as a transferring proton if state $|i>$ changes to state $|j>$, and otherwise $h_{ij} \equiv 0$), h_{ij} is given by

$$h_{ij} = (V^{i,j}_{\text{coulomb}} + V^{i,j}_{\text{const}}) \cdot F(\mathbf{x}), \tag{2.7}$$

where $V^{i,j}_{\text{coulomb}}$ refers to the sum of electrostatic potentials between the H_5O_2^+ ion (formed by H_3O^+ ions from state $|i>$ and $|j>$ and the remaining $N_{\text{H}_2\text{O}}$ water molecules). $F(\mathbf{x})$ is a scaling factor and more details can be found in Ref. 76.

For the MS-EVB method, the dilemma between energy drift and the capability of numerous EVB states is a longstanding problem (though it has been quite improved in recent developments) and applies such a reactive simulation under a restricted level. If multiple excess protons are considered, the scaling effects create computational complexities which evolve exponentially. Regardless of these drawbacks, MS-EVB is a great and successful method which has been applied in investigating proton transfer/transport processes not only in water bulks[76,78] but also in various chemical[79–81] and biomolecular systems.[82–84]

2.2.3. Two-state EVB

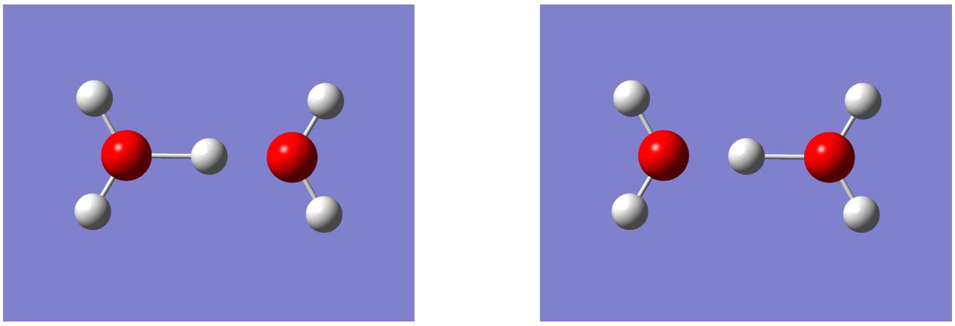

state I state II

Figure 2.1.: A two-state empirical valence bond model for an $H_5O_2^+$ ion

Alternative to MS-EVB, the two-state EVB method has been developed to provide a simplified PT algorithm, compared to multi-state approaches which require ca. 40∼50 states (per proton) to participate into calculations for each multi-state cycle. This method has been applied with larger spatial- and time-scales for several biochemical systems[85–87]. One of the most representative TS-EVB method is the WK model, proposed by Walbran and Kornyshev[24].

A TS-EVB formulation is similar to a conventional emperical valence bond model.[72,73] Focusing on the current model, an $H_5O_2^+$ ion is defined in two valence bond states: I) $H_3O^+ \cdots H_2O$ and II) $H_2O \cdots H_3O^+$. Thereafter, the global EVB model can be described in a form of Hamiltonian matrix, shown as the following[24]:

$$\begin{bmatrix} V_{\mathrm{I}}(\boldsymbol{x}) & \Lambda(Q) \\ \Lambda(Q) & V_{\mathrm{II}}(\boldsymbol{x}) \end{bmatrix}$$

Here $V_{\mathrm{I}}(\boldsymbol{x})$ and $V_{\mathrm{II}}(\boldsymbol{x})$ are the classical potential energies at a given set of coordinates $\boldsymbol{x}$ as a "water" molecule interacts with a "hydronium" ion in their corresponding state representations. $\Lambda(Q)$ is a parametric component, taken to be a function of reaction coordinate $Q = r_{\mathrm{O^*H}} - r_{\mathrm{OH}}$ (O^* stands for a

H_3O^+ oxygen). In details, we have

$$\Lambda(Q) = \begin{cases} 0 & : Q \leq -Q_1 \\ \Lambda_0\Big[\Big(\dfrac{Q}{Q_1}\Big)^4 - 2\Big(\dfrac{Q}{Q_1}\Big)^2 + 1\Big] & : -Q_1 < Q < Q_1 \\ 1 & : Q \geq Q_1 \end{cases} \tag{2.8}$$

where Λ_0 and Q_1 are the parameters.

From the standpoint of molecular dynamics, one important issue (or challenge) for describing proton transfer in a force field regime is the conservation of charges of the system with the presence of excess protons, considering the fact of charge diffusion. One possible solution is to equivalently distribute the net (or excess) charges into all possible particles (e.g. which play roles as proton carriers). By doing that, however, the excess charges can not be localized during the simulation which is relatively unrealistic. Rather than fixed partial charge model, individual formal charges should be defined within the ion carrier (i.e. an H_3O^+ or Zundel ion) for every MD step[88,89]. Then, the partial charges must vary in some fashions with either coordinates[90] or exchangeable states[22,74–76] which may also resemble a charge transfer (usually at the ground state) in quantum dynamics.

In WK model, the point partial charges for atoms within the Zundel ion can be given by[24]

$$\begin{aligned} \boldsymbol{q}_{O^*}(Q) &= (1 - f(Q)) \cdot q_{O^*} + f(Q) \cdot q_O \\ \boldsymbol{q}_O(Q) &= f(Q) \cdot q_{O^*} + (1 - f(Q)) \cdot q_O \end{aligned} \tag{2.9}$$

where $\boldsymbol{q}_{O^*}(Q)$ and $\boldsymbol{q}_O(Q)$ stand for the point partial charges of H_3O^+ (O^*) and H_2O (O) oxygen atoms in state I and respectively. q_{O^*} and q_O are parametric and represent for fixed point charges models for classical H_3O^+ and H_2O molecules. $f(Q)$ plays a role as a switch function, given as

$$f(Q) = \frac{1}{2} + \frac{\alpha}{5}\Big(\frac{Q}{Q_0}\Big)^5 - \frac{2\alpha}{3}\Big(\frac{Q}{Q_0}\Big)^3 + \alpha\Big(\frac{Q}{Q_0}\Big) \tag{2.10}$$

where $\alpha = 15/16$ and Q_0 is the parameter.

The TS-EVB method does, however, have some deficiencies. To perform a Grotthuss PT process, the two-state modeling should diffuse and act on different $H_5O_2^+$ ions in bulk systems. For a given hydronium ion (which can be easily determined by geometric evaluations), only one water molecule, which is the closest to the hydronium ion, is chosen as a partner H_2O molecule to form a Zundel ion within a TS-EVB framework. Once a proton transfer move is complete (from hydronium ion to its partner water molecule), this partnering procedure is reactivated again and a new $H_5O_2^+$ ion is selected and modeled with TS-EVB method. During the proton transfer reaction (when $0 < \Lambda(Q) < 1$), however, the partner selection stays unactivated no matter whether a solvent H_2O approaches closer to the H_3O^+ ion or not. That leads to two problems: First, besides the closest H_2O there can be two additional neighboring water molecules, which gives a possibility of forming an Eigen cation. Sometimes, an Eigen cation may become more energetically favorable during the transferring process. Second, a forcible switch of $H_5O_2^+$ models will lead to a discontinuity of the total potential of the system. Furthermore, this shortcoming restricts a charge delocalization effect beyond the partner cluster of the Zundel cation. That may lead to inaccurate description of dipole moment surface, which is particularly important for calculating vibrational spectra.[22]

2.2.4. Other Methods using Empirical Force Field

Obviously, using approaches with empirical force field methods show great advantages in computational efficiencies compared to *ab initio* approaches such as BOMD, CPMD and ADMP[91–93] etc. Therefore, interests were captured, over the decades, for fast simulations of proton transfer or transport, especially with explicit treatment on atoms which are directly involved with the transferring processes.

As one of the most famous force field solution to perform reactions, ReaxFF has been extensively developed over the year.[23,94–96] Introducing the bond-order, which generalizes inter-atomic interactions from short to long distance, is essential to this implementation. Using the ReaxFF force field, Doren *et al.* studied the proton transfer in glycine with its tautomerization of between the neutral and zwitterionic forms.[23] Later on, von Duin *et al.* parametrized ReaxFF for investigating proton/hydroxide migrations in the bulk phase[97] but the fitting qualities remained mediocre to the reference QM energies.

Quantum hopping (Q-HOP) molecular dynamics is another approximate method, which was originally formulated by M. Lill and V. Helms[98,99] and has been continuously developed for simulating proton transfer in various fields of condensed phases. Based on data from *ab initio* calculations, this parametric method calculates the probability of proton hopping events, also determined by coordinate-based functions (i.e. depending on the donor-acceptor distances)[98] or energetic information (i.e. reaction barriers).[98,100] If a proton transfer occurs, determined by a random number, the bonding topology of the system is thereby modified to adapt to a new location to which the proton hops. Q-HOP has been proven a very efficient method and its molecular dynamics has been successfully applied to study proton transfer in various systems at the condensed phase, such as air-water interface,[101] green fluorescent protein (GFP),[102] gated proton channels,[103] proton pumping proteins[104] and fuel cell membranes.[105]

Other methods were also implemented and employed in various applications related to proton transfer/transport, such as reactive molecular dynamics (RMD, which activates instantaneous proton hops),[21] hydrogen dynamics (HYDYN, which uses $\lambda-$dynamics to enable the continuous (dis-)appearance of active protons)[106] and many-body representation[107,108] (which gives a total potential as a sum of 1-, 2- and 3-body interactions and is accurate in predicting infrared spectra of water clusters with one excess proton) methods.

2.3. Experimental Measurement for Proton Diffusion in Water

One of the major interests in this thesis is the simulations of proton transport (or diffusion) in aqueous systems. Beside AIMD, semi-empirical and QM/MM methods, force field methods such as MS-EVB and TS-EVB are also capable of simulating such continuous processes. Then, it becomes necessary to the experimental background of how a proton diffusion is measured.

In aqueous solutions the acidic proton exists as hydronium ion, and is further hydrated which forms $H_5O_2^+$ (Zundel)[109] or $H_9O_4^+$ (Eigen)[110] ion structures. Regarding the mobility of excess proton in acidic solutions, it was found that the diffusion constant of H^+ (0.93 Å^2/ps)[111,112] is four-fold faster than that of water (0.23 Å^2/ps)[113] at the room temperature. This high speed mobility (compared with other ions with similar sizes) is considered attributed to contributions from two kinds of mechanisms: vehicular mechanism (also called *en masse* mechanism[114]) and Grotthuss mechanism (or "relay" mechanism). The vehicular mechanism refers to that the H_3O^+ ion migrate as a non-reactive entity. The Grotthuss mechanism, proposed more than 200 years ago,[115] leads to a contribution of faster transferring processes, in which different hydrogen atoms participate and the transfer usually occur through hydrogen bond network. In Agmon's explanation to Grotthuss mechanism, proton hops under a concerted fashion were also considered.[116]

One typical and comprehensive measurement for self-diffusion coefficient (or diffusion constant) is to measure the resistance of electrolyte solution.[112,117] Then, the conductivity can be easily obtained by calculating

$$\Lambda = \frac{1}{\rho C}, \tag{2.11}$$

where Λ is the conductance of solution, r is the resistivity and C is the molar concentration of electrolyte (which approximately scales with the density of water at different temperature[112]). Moreover, Λ is also the sum of individual ionic conductances. For an HCl solution, the conductance of H^+ is given by

$$\lambda_{\mathrm{H}^+} = \Lambda_{\mathrm{HCl}} - \lambda_{\mathrm{Cl}^-}. \tag{2.12}$$

To obtain the conductance of Cl^- ion, two approximations were proposed. First, λ_{Cl^-} is that of Cl^- ion (for example) in KCl solution (with the same concentration); Second, in KCl solution the conductance of Cl^- is approximately equal to that of K^+ cation. At the final, the diffusion constant of H^+ ion can be finally computed by using Nernst-Einstein equation:

$$D_{\mathrm{H}^+} = \frac{RT}{z_{\mathrm{H}^+}^2 F^2} \lambda_{\mathrm{H}^+} \tag{2.13}$$

where D_{H^+} is the self-diffusion coefficient, R is the gas constant, T is the temperature, z_{H^+} is the charge number of H^+ ion (which is +1) and F is Faraday's constant.

The conductance experiment were carried out by Speedy *et al.*[112] more than 30 years ago. Figure 2.2 shows the inverse temperature dependence of diffusion constant of H^+ in HCl solution at a concentration of 0.01 mol/L. At the room temperature (298.15 K), the diffusion constant for H^+ was found 0.919 $\mathrm{\AA}^2$/ps at this concentration. Using Arrhenius plot, the energy of activation for the proton diffusion is approximated 3.6 kcal/mol (Figure 2.2), compared to a lower $E_a = 2.1$ kcal/mol for water diffusion[113]. In 1970s, Roberts *et al.*[111,118] measured and analyzed the diffusion constants of both H^+ and D^+ in various

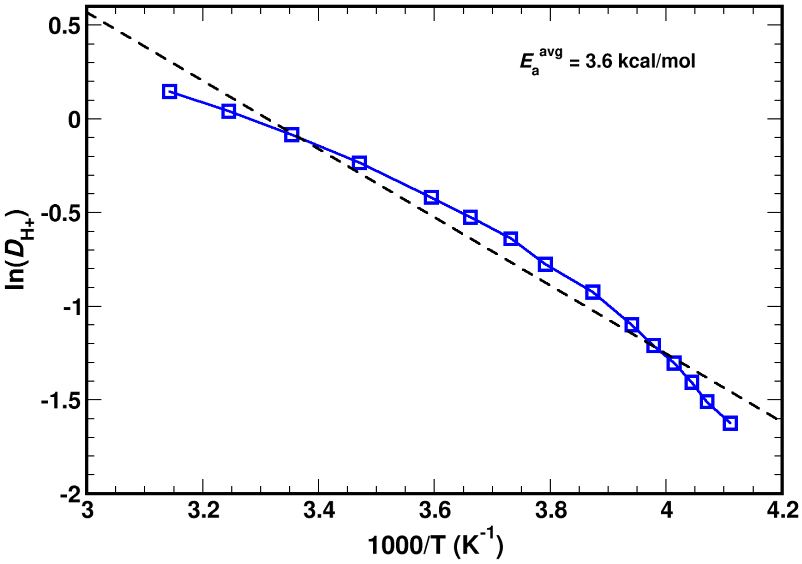

Figure 2.2.: logarithmic self-diffusion coefficient of H^+ in HCl solution with a concentration of 0.01 mol/L (measured at 20°C). Data are from Ref. 112.

electrolyte solutions, using polarography techniques. For each of supporting electrolyte (KCl, NaCl etc.), the diffusion constant of H^+ (or D^+) was measured at different molar concentrations and extrapolated to near-zero in concentration. Results for D_{H^+} and D_{D^+} were 0.931 Å^2/ps and 0.650 Å^2/ps, respectively.

More recently, Licht *et al.* measured the conductivity of ultra-pure water at a temperature range of 0°C $\sim$ 100°C[119]. However, there was no new data of λ_{H^+} derived from this experiment but instead they used literature data[117] (of λ_{H^+}) to calculate the conductivity of hydroxide ion ($\lambda_{OH^-} = \Lambda_0 - \lambda_{H^+}$). Choi *et al.* investigated proton diffusion in Nafion[114] and found that surface proton hopping (aided by SO_3^- groups) is considerable slower than H^+ diffusion in water bulk. Hence, proton transport more likely occurs in bulk water rather than at the surface, which leads to formation of water clusters away from the water-proof surface.

Regarding the conductance experiment, it is worth to note that the experimental condition is somewhat away from ideal infinite dilution of a bulk even if extrapolation of concentrations is considered. First, a high voltage must be applied to obtain sensitivity at the high resistance of electrolyte solutions[112].

Therefore, it is unclear how much the electric field affects the results and directionality of H^+ diffusion. Second, solutions were placed under certain confinement in space (i.e. a U-shape tube), for which the system lacks some isotropy in $y-$ and $z-$dimensions. Nevertheless, these experimental efforts had already successfully provided a meaningful and insightful picture of Grotthuss mechanism.

Part II.

Method and Development

3. Molecular Mechanics with Proton Transfer

In this chapter, the MMPT (Molecular Mechanics with Proton Transfer) force field method is summarized. MMPT has been extensively developed and studied[25,120] and contributes into the CHARMM program[30,31]. The chapter is organized as follows: First, the basic concept of MMPT force field is given and the difference between MMPT force field and a classical empirical force field is discussed. Next, prototype proton transfer (PT) potentials, obtained from high-level *ab initio* calculations are introduced and mathematical details are discussed. In addition to PT potentials which had been previously developed[25,26,120], in the current work a specialized model for double proton transfer (DPT) is proposed by introducing coupling effects upon multiple proton transfer systems. At the final, the approach for quickly generating MMPT potentials is discussed.

3.1. Molecular Mechanics with Proton Transfer

3.1.1. Ab-initio Based PT Potentials in MMPT Force Field

The basics of a proton transfer process is in fact a reactive process which involves with bond breaking and formation, like from $\mathrm{A-B\cdots C}$ to $\mathrm{A\cdots B-C}$. To perform such a process in MD simulation, additional energy terms, other than classical terms, are required. Thus, based on Eq. 2.3 the energy function, containing a PT reaction, can be written into

$$V_{\mathrm{total}} = V_{\mathrm{FF}} + V_{\mathrm{MMPT}} \tag{3.1}$$

where V_{MMPT} is given as[25,120]

$$V_{\mathrm{MMPT}} = V_{\mathrm{PT}}(\mathrm{A-B\cdots C}) + \sum_{\mathrm{bonded}} V_{\mathrm{CM}}. \tag{3.2}$$

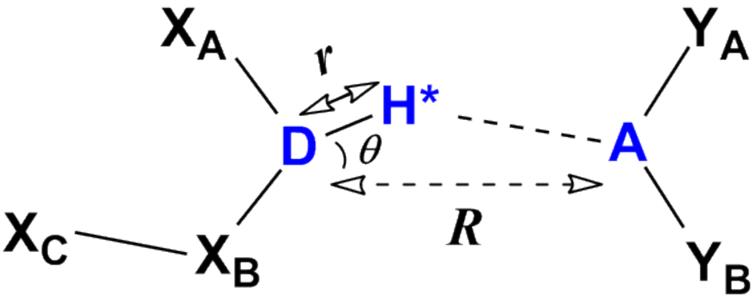

Figure 3.1.: An example of MMPT proton transfer motif.

In Eq. 3.2, $V_{\mathrm{PT}}(\mathrm{A}-\mathrm{B}\cdots\mathrm{C})$ is a specialized energy function (discussed in Section 3.1.1) for describing the DOFs and (more importantly) reactive process of A, B and C atoms and $\sum\limits_{\mathrm{bonded}} V_{\mathrm{CM}}$ include all classical bonded terms (bond, angles and dihedral and improper angles) which are switched on and off along the PT path. Such a switch is controlled by a switch factor (discussed in Section 3.1.2), depending on the bond formation between atom B and A or atom B and C.

Rather than $\mathrm{A}-\mathrm{B}\cdots\mathrm{C}$, the triatomic moiety for a complete PT process is defined as $\mathrm{D}-\mathrm{H}^*\cdots\mathrm{A}$ (Figure 3.1), in which H^* stands for the transferring hydrogen (or D^* if it is a deuterium) and D and A are the electronegative donor and acceptor of the transferring hydrogen (or proton). Therefore, in MMPT force field the PT involved degrees of freedoms (DOF) are chosen to represent for reaction coordinates and their energy terms are replaced from classical terms. The reaction coordinates are R – the distance between D and A, ρ – a unitless coordinate given as $\rho = (r - r_{\mathrm{min}})/(R - r_{\mathrm{min}})$, $r_{\mathrm{min}} = 0.8$ Åand θ – $\angle\ \mathrm{D}-\mathrm{H}^*-\mathrm{A}$.

Currently, MMPT force field supports a total of five types of PT potential for a single PT motif for which different potential energy surfaces (PESs) are considered (i.e. if the PT reaction contains a barrier or is barrier-less, etc.). And all the potential functions are explained in the followings:

1) **Symmetric Single Minimum (SSM)**

The MMPT potential with SSM model describes a barrier-less PT reaction and the prototype system for this model is $H_2O - H \cdots OH_2$ (namely, a Zundel ion). The potential function is given as

$$V(R,\rho,\theta) = V_0(R,\rho) + k \cdot \theta^2 \tag{3.3}$$

where $V_0(R,\rho)$ is the double Morse function (which are superposed to each other) and detailed as

$$\begin{aligned} V_0(R,\rho) = D_{eq}(R)[1 - e^{-\beta(R)(\rho-\rho_{eq}(R))}]^2 \\ + D_{eq}(R)[1 - e^{-\beta(R)(1-\rho-\rho_{eq}(R))}]^2 - D_{eq}(R) + c \end{aligned} \tag{3.4}$$

and $k \cdot \theta^2$ is the harmonic approximation for describing the bending DOF of the $D - H^* \cdots A$ motif. Alternatively, it can be $k \cdot d^2$ where $d = r \cdot \sin\theta$ (discussed in Sec. 4.1). The parameters for all components of Eq. 3.4 are given as

$$D_{eq}(R) = p_1(1 - e^{-p_2(R-p_3)})^2 + p_4 \tag{3.5}$$

$$\beta(R) = p_5 + p_6 R \tag{3.6}$$

$$\rho_{eq}(R) = p_7 \cdot e^{-p_8 R} + p_9 \tag{3.7}$$

$$k = p_{10} \tag{3.8}$$

$$c = p_{11} \tag{3.9}$$

2) **Symmetric Double Minimum (SDM)**

The SDM model describes a symmetric PES with two minimums which are equally the global minimums. The prototype system is the ammonia dimer, ${NH_4}^{+} \cdots H_3N$. The mathematical expression for the SDM model and its parametrization is the same to that of a SSM model albeit they are separately implemented in CHARMM due to the historical reason. It is also noteworthy that the barrier height is also dependent of the separation of D and A (namely R), as shown in Figure 3.2. When D and A set apart from each other, the barrier increases. On the other hand, the barrier will disappear when the two heavy atoms are close enough. In fact, whether a PES is of SSM or SDM mode only depends on where the global minimum is located in barrier-less or barrier-contained surface in the PES.

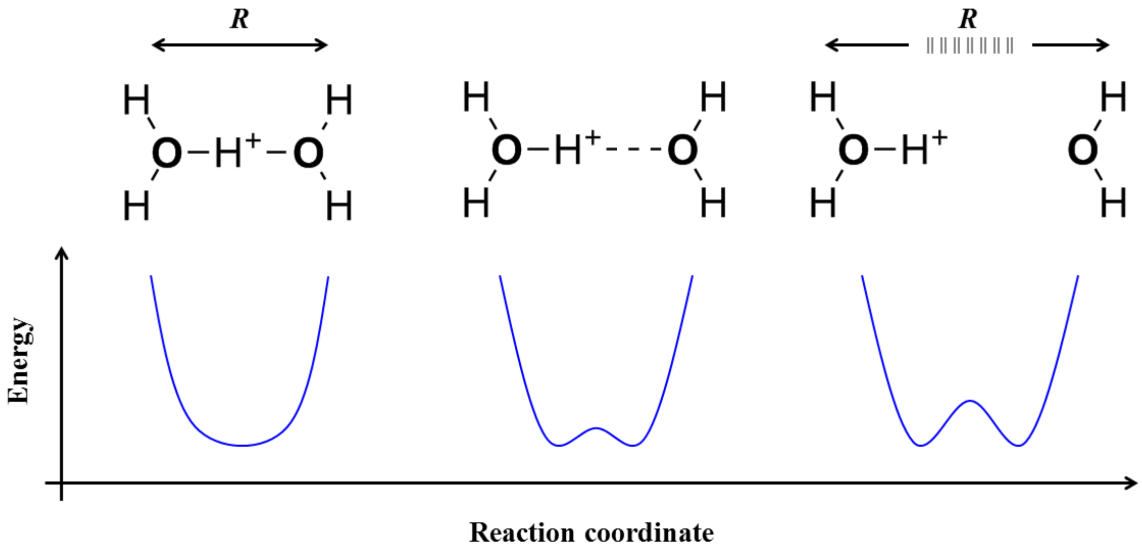

Figure 3.2.: One-dimensioned PES at different separations of H*-donor and acceptor.

3) **Asymmetric Single/double Minimum (ASM)**

The ASM model describes an asymmetric PES. The prototype system is $NH_4^+ \cdots H_2O$.

$$\begin{aligned} V_0(R,\rho) = D_{eq,1}(R)[1 - e^{-\beta_1(R)(\rho-\rho_{eq,1}(R))}]^2 \\ + D_{eq,2}(R)[1 - e^{-\beta_2(R)(\rho_{eq,1}(R)-\rho)}]^2 - c(R) \end{aligned} \tag{3.10}$$

And the parameters are given as

$$D_{eq,1}(R) = p_1(1 - e^{-p_2(R-p_3)})^2 + p_4 \tag{3.11}$$

$$\beta_1(R) = \frac{p_5}{1 - e^{-p_6(R-p_7)}} \tag{3.12}$$

$$\rho_{eq,1}(R) = p_8(1 - e^{-p_9(R-p_{10})})^2 + p_{11} \tag{3.13}$$

$$D_{eq,2}(R) = p_{12}(1 - e^{-p_{13}(R-p_{14})})^2 + p_{15} \tag{3.14}$$

$$\beta_2(R) = \frac{p_{16}}{1 - e^{-p_{17}(R-p_{18})}} \tag{3.15}$$

$$\rho_{eq,2}(R) = p_{19}(1 - e^{-p_{20}(R-p_{21})})^2 + p_{22} \tag{3.16}$$

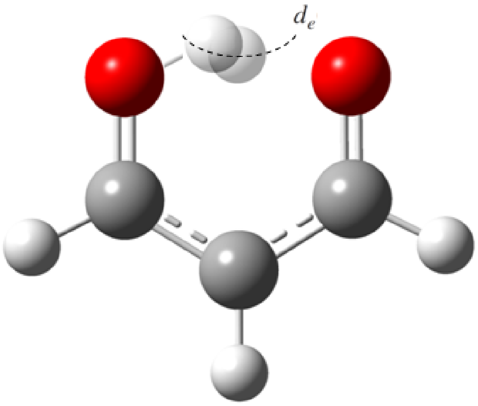

Figure 3.3.: The non-linear PT path in malondialdehyde with equilibrium d_e

4) **Non-linear Model (NLM)**

The NLM model describes proton transfer with a minimum energy path which is non-linear, as shown in Figure 3.3 and the total potential energy can be given as

$$V(R, \rho, d) = V_0(R, \rho) + V_d(R, \rho, d) \tag{3.17}$$

where ρ is modified into

$$\rho = (r \cdot \cos\theta - r_{\min})/(R - r_{\min}) \tag{3.18}$$

and $d = r \cdot sin\theta$. In Eq. 3.17, V_0 is given as the same to Eq. 3.4. For the harmonic approximation on the bending DOF (which now corresponds to d), V_d is formulated with a non-zero equilibrium $d_e(\rho)$ and the dependence of R and ρ.

$$V_d(R, \rho, d) = \frac{1}{2}\big[p_{10}V_0(R, \rho) + p_{12}\big] \cdot \big[d - d_e(\rho)\big]^2 \tag{3.19}$$

and

$$d_e(\rho) = p_{14} + p_{13}(\rho - 0.5)^2 \tag{3.20}$$

5) **Legendre Polynomial Expansion (LPE)**

The MMPT force field also provides a more sophisticated PES that explicitly couples all three coordinates (R, ρ and θ) for an accurate description to the PT energy landscape.[120] A function of the total potential energy can be expressed as

$$V(R,\rho,\theta)=\sum_{\lambda=0}^{n}V_\lambda(R,\rho)P_\lambda(\cos\theta) \tag{3.21}$$

where $P_\lambda(\cos\theta)$ is the λth-order Legendre polynomial that can be given in a recursive form

$$(\lambda+1)P_{\lambda+1}(x)=(2\lambda+1)xP_\lambda(x)-\lambda P_{\lambda-1}(x) \tag{3.22}$$

with $P_0(x)=1$ and $P_1(x)=x$. For the zeroth order $V_0(R,\rho)$ is given as

$$\begin{aligned} V_0(R,\rho) &= a_0(R)[1-e^{-a_1(R)(\rho-a_2(R))}]^2 \\ &\quad + a_0(R)[1-e^{-a_1(R)(1-\rho-a_2(R))}]^2 \\ &\quad + a_3(R)e^{-a_4(R)(\rho-0.5)^2}-a_5(R) \end{aligned} \tag{3.23}$$

which include the first 24 parameters in $a_i(R)$ and $i\in\{0,1,\cdots,5\}$.

$$a_i(R)=p_{i,1}\cdot\big\{\tanh\big[p_{i,2}(R-p_{i,3})\big]+p_{i,4}\big\} \tag{3.24}$$

For higher orders ($\lambda\neq 0$), $V_\lambda(R,\rho)$ is given as

$$V_\lambda(R,\rho)=b_{0,\lambda}+\frac{b_{1,\lambda}(R)}{b_{1,\lambda}\big[(\rho-0.5)^2+b_{1,\lambda}^2(R)\big]} \tag{3.25}$$

and each order includes 9 parameters which gives

$$b_{0,\lambda}(R)=f_0(\lambda) \tag{3.26}$$

$$b_{1,\lambda}(R)=f_1(\lambda)\big\{\tanh[f_2(\lambda)(R-f_3(\lambda))]+f_4(\lambda)\big\} \tag{3.27}$$

$$b_{2,\lambda}(R) = f_5(\lambda) + f_6(\lambda)[R - f_7(\lambda)]^2 + f_8(\lambda)[R - f_7(\lambda)]^2 \tag{3.28}$$

For the current implementation the expansion has been cut at $n = 10$, for which the total energy function contains 114 parameters. And for V_λ at higher orders, it is not necessary to activate all the terms and in fact only $\lambda = 0, 1, 3$ were tuned on for illustrating the PT PES for a $OH_3{}^+ \cdots H_2O$ system.[120]

Currently, MMPT force field has been implemented in the CHARMM package.[30,31,71] First, *ab initio* calculations were carried out by scanning the reactive PES using Gaussian-09 program.[121] The parametrization of MMPT potential was continued by using non-linear least squares fitting. A classical least squares fitting is, mathematically, to solve a minimization problem.[122,123]

$$\chi^2 = \sum_{i=1}^{n} [\frac{y_i^{obs} - y_i^{calc}(p_1, \cdots, p_m)}{\sigma_i}]^2, \tag{3.29}$$

where m is the number of the parameters and y^{obs} is the n-dimensioned vector of observed values and refers to the *ab initio* data in the current work. y^{calc} is the result of using potential function with given parameter set, $\vec{p}$. And σ_i represents for the uncertainty which can be assigned additionally. The estimation of the quality of minimization can be expressed as

$$\sigma^2 = \frac{\chi^2}{n - m}, \tag{3.30}$$

where n is the number of data and m is the number of parameters but usually ignorable when $n \gg m$.

3.1.2. A Complete Description of MMPT Force Field

Unlike classical MD simulations with empirical force field, using MMPT force field PT reactions are performed, in which bond breaking and formation are involved (i.e. from $D - H$ to $H - A$). Consequently, that also contradicts with the conventional definition of related covalent bonds and their energy terms. To solve this problem, in MMPT force field it takes account into both bonding topologies as the transferring hydrogen (H^*) is bonded to D and A atoms. Regarding Figure 3.1 as one example MMPT picture, H^* associated angular and dihedral terms such as $X_A - D - H^*$, $X_B - D - H^*$ and $X_C - X_B - D - H^*$ are included as classical energy terms if a $D - H$ bond is formed. When a $H - A$

bond is formed, these bonding topologies are not valid anymore but instead terms of $\mathrm{Y_A - A - H^*}$ and $\mathrm{Y_B - A - H^*}$ are taken into account. Thus, a PT reaction should also associate with a process that these energy terms can be smoothly switched on and off under the dependence of $\mathrm{D - H}$ and $\mathrm{H - A}$ formations. This process can be approached by introducing a hyperbolic switch function, which is geometry-dependent:

$$\gamma(R, r, \theta) = \frac{1}{2}\big[\tanh[2R \cdot r \cdot \cos\theta - R^2] + 1\big] \tag{3.31}$$

In Eq. 3.31, $\gamma = 1$ or 0 if $\mathrm{H^*}$ is bonded to donor or acceptor, respectively and $\gamma = 0.5$ at the transition state. Here, 'switch on' refers to adding a term (e.g. $\gamma \cdot E_{\text{angle}}(\mathrm{Y_A - A - H^*})$ in Figure 3.1) in force field calculation and 'switch off' amounts to partial removal of a bonded term which is already existent in standard force field (e.g. $(1-\gamma) \cdot E_{\text{angle}}(\mathrm{X_A - D - H^*})$ for example).

The MMPT module has been implemented in a form of a subroutine which provides and additive energy in the CHARMM energy calculation. For a standard CHARMM simulation, the classical bonding network, including $\mathrm{D - H^*}$ bond and relevant angles, is built at the beginning of MD simulations. Hence, MMPT is due to correct the classical energy terms and add all necessary terms which are missing in the initial session. Eventually, a complete MMPT force field is obtained by re-writing Eq. 3.2 into

$$\begin{aligned} V_{\text{MMPT}} = {} & V_{\text{PT}}(\rho, R, \theta) - E_{\text{bond}}(\mathrm{D - H^*}) \\ & + \gamma \cdot \sum_i \big[E_{\text{angle}}(\mathrm{Y}_i - \mathrm{A} - \mathrm{H^*}) - E_{\text{angle}}(\mathrm{X}_i - \mathrm{D} - \mathrm{H^*})\big] \\ & + \gamma \cdot \sum_{i,j} \big[E_{\text{dihedral}}(\mathrm{Y}_j - \mathrm{Y}_i - \mathrm{A} - \mathrm{H^*}) - E_{\text{dihedral}}(\mathrm{X}_j - \mathrm{X}_i - \mathrm{D} - \mathrm{H^*})\big] \\ & + \gamma \cdot \sum_{i,j} \big[E_{\text{improper}}(\mathrm{Y}_j - \mathrm{Y}_i - \mathrm{A} - \mathrm{H^*}) - E_{\text{improper}}(\mathrm{X}_j - \mathrm{X}_i - \mathrm{D} - \mathrm{H^*})\big] \end{aligned} \tag{3.32}$$

where $E_{\text{bond}}(\mathrm{D - H^*})$ is the bonded terms of $\mathrm{D - H^*}$ bond and to be removed and replaced by $V_{\text{PT}}(\rho, R, \theta)$.

3.2. MMPT Potential with Double Proton Transfer

The MMPT force field provides a variety of mathematical functions to describe proton transfer reactions within a selected molecular moiety. However, proton transfer in some multi-proton systems, e.g.

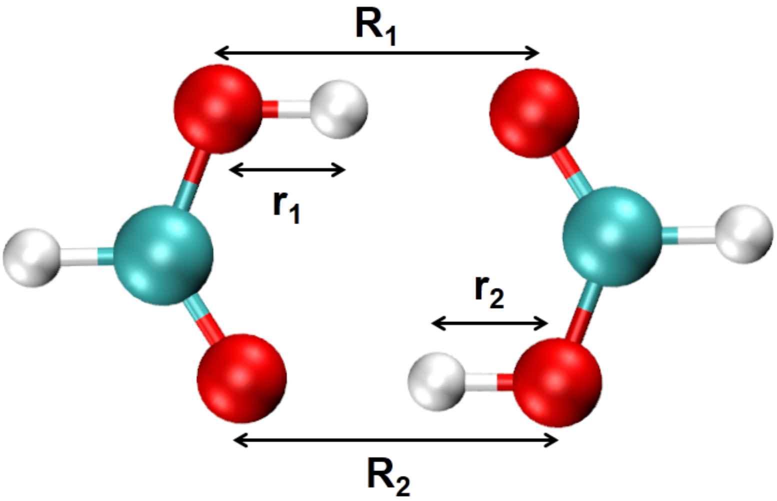

Figure 3.4.: The formic acid dimer (FAD) molecule.

dimerized formic-acid at the gas phase, contain coupling effects. That requires a PT potential which is able to associates higher dimensions (than three) of reaction coordinate but multiple proton transfer can only be independently treated in conventional MMPT package.[25,120,124] In this section, a modified MMPT force field has been developed to perform double-proton transfer (DPT) in a concerted reaction pathway. For this, the reactions of formic acid dimer (FAD) were used as an example system for the development.

In MMPT model, potential energies of barrier-contained proton transfer can be expressed by SDM model (See Eq. 3.4) if the reaction system contains a symmetric potential. For FAD, using SDM potential for both PT motifs will lead to a total of four global energy minimums in the entire potential surface. That contradicts to QM calculations in which only two minimums are found in FAD. This suggests a fact that the global energy minimum only appears when the transferring hydrogens are bonded to oxygen receptors from their respective formic acid groups (Figure 3.4). A complete transfer move requires the two hydrogens shuttling to the each other side at the meantime.

For a double proton transfer in FAD, the total potential is now given as

$$V_{\mathrm{DPT}} = V(r_1, r_2, R_1, R_2) \tag{3.33}$$

where r_i and R_i $(i = 1, 2)$ represent for $\mathrm{O-H}$ and $\mathrm{O-O}$ distances.

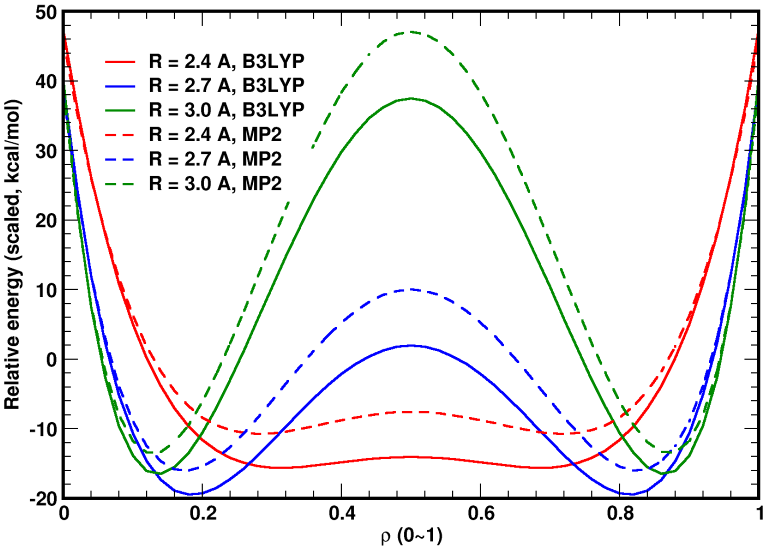

Figure 3.5.: The one dimensioned cross-section of PES by *ab initio* scans at the levels of B3LYP/6-31G(d,p) and MP2/6-311++G(2d,2p), at $R = 2.4$ Å, 2.7 Å and 3.0 Å.

In a minimum energy path (MEP) from *ab initio* calculations, these coordinates are actually associated to each other, in forms of $R = R_1 = R_2$ and $r_1 = r_2$. Figure 3.5 gives the QM energies with selected values of R. The barrier height is dependent on the $\mathrm{O} - \mathrm{O}$ separation (R) and results show that the reaction barriers are in general higher using the MP2/6-311++G(2d,2p)[125–128] level of theory than using that B3LYP/6-31G(d,p).[129–132] In order to simplify the DPT model, we first focus on dimension-reduced PESs of Eq. 3.33. That gives

$$V_{\mathrm{I}}(\mathbf{x}) = V(r_1, r_2 = r_1, R_1 = R, R_2 = R) \tag{3.34}$$

and

$$V_{\mathrm{II}}(\mathbf{x}) = V(r_1, r_2 = R - r_1, R_1 = R, R_2 = R), \tag{3.35}$$

, respectively. To clarify, they are defined as surface I (simplified as $V(r_1, R)$) and surface II ($V(r_1 = R - r2, R)$). These two potential surfaces should correspond to two diagonal parts of QM potential surfaces, which are shown in Figure 3.7. Both surface I and II can be completely represented by SDM (or SSM) model with accurate parametrization but surface I determines the minimum energy path and the reaction barrier while the *anti*-diagonal surface II provides additional constrains upon shuttling protons. For FAD, surface II is a barrier-less PES, which can be parametrized with SSM model in

MMPT framework. The total potential of double proton transfer is obtained as a sum of the potential surface for each PT motif. For each motif, the potential is determined by both surface I and II but also controlled by a two-dimensional switch factor $\eta(r_1, r_2, R_1, R_2) \in (0, 1)$ (inspired from γ discussed in Sec. 3.1.2). The total potential of a DPT reaction is given as

$$\begin{aligned} V_{\text{total}} = & \big[\eta \cdot V_{\text{I}}(r_1, R_1) + (1-\eta) \cdot V_{\text{II}}(r_1, R_1)\big] \\ & + \big[\eta \cdot V_{\text{I}}(r_2, R_2) + (1-\eta) \cdot V_{\text{II}}(r_2, R_2)\big] \end{aligned} \tag{3.36}$$

and the switch factor is given as

$$\begin{aligned} \eta(r_1, r_2, R_1, R_2) = \frac{1}{2}\Big\{ & 1 + \tanh[\sigma \cdot (r_1 \cdot R_1 - R_1^2/2)] \cdot \\ & \tanh[\sigma \cdot (r_2 \cdot R_2 - R_2^2/2)]\Big\} \end{aligned} \tag{3.37}$$

where σ is the parameter given with 2.639. Compared to the conventional MMPT force field, mixed surfaces in Eq. 3.36 abandons the axial symmetries of the PES in 2D-panels (See Fig. 3.7), but giving a diagonal symmetry instead.

All MMPT parameters from the current work for FAD are reported in Table 3.1 and the fitting qualities are shown in Figure 3.6. Table 3.2 reports *ab initio* calculations in which the reaction barriers of DPT in FAD were recorded. As a result, all reported QM methods agree with that the transition state of FAD features in symmetric reaction coordinate which is shown as $r_1 = R_1/2 = r_2 = R_2/2$.

Table 3.1.: Parameters for MMPT-MP2 and MMPT-B3LYP PESs.

parameters	MMPT-B3LYP		MMPT-MP2	
	V_{I}	V_{II}	V_{I}	V_{II}
p_1, kcal/mol	1338938	1338863	1339070	1338978
p_2, Å^{-1}	0.707	1.331	0.920	1.292
p_3, Å	-10.603	-5.251	-7.061	-4.872
p_4, kcal/mol	-1338591	-1338667	-1338459	-1338551
p_5, Å^{-1}	0.537	-0.792	0.685	-0.645
p_6, Å^{-2}	0.808	1.134	0.753	1.076
p_7, Å	76.535	54.564	73.937	42.080
p_8, Å^{-1}	2.777	2.602	2.817	2.516
p_9, Å	0.079	0.104	0.076	0.090
p_{10}, kcal/(mol· deg^2)	0.002	0.002	0.002	0.002
p_{11}, kcal/mol	32.85	62.78	51.03	113.38

Table 3.2.: Reaction barriers of double proton transfer in FAD and barriers with the energy correction of zero-point vibrational effect (ZPVE).

Method	barrier kcal/mol	barrier (ZPVE) kcal/mol	barrier reduction
MP2/6-311++G(2d,2p)	+8.2	+4.1	-39%
B3LYP/6-31G(d,p)	+5.4	+1.5	-72%
DFTB [51,133]	+5.4	+3.6	-33%
CBS-QB3 [134,135]	+7.3	+4.8	-34%
G4 [136,137]	+15.2	+5.0	-67%
CCSD(T)/aug-cc-pVTZ [138–141]	+9.4	(n.a)	(n.a)

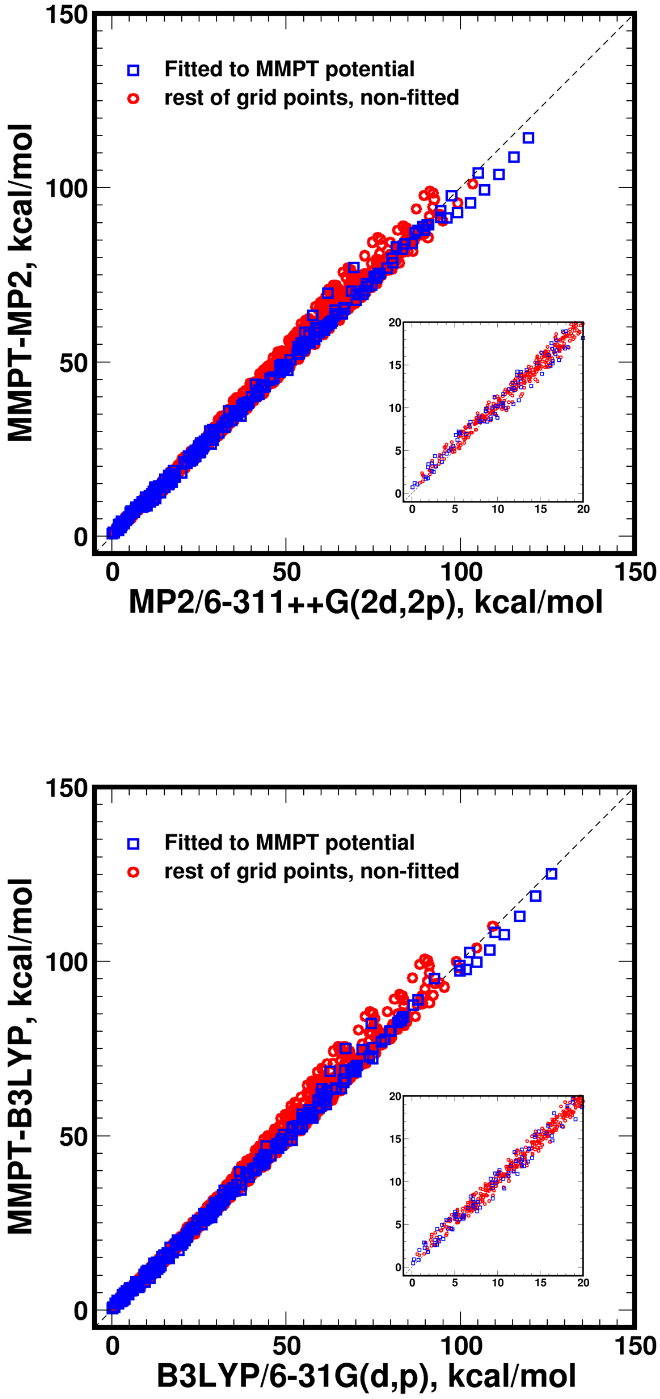

Figure 3.6.: Correlation between MMPT and MP2 and B3LYP potential energies.

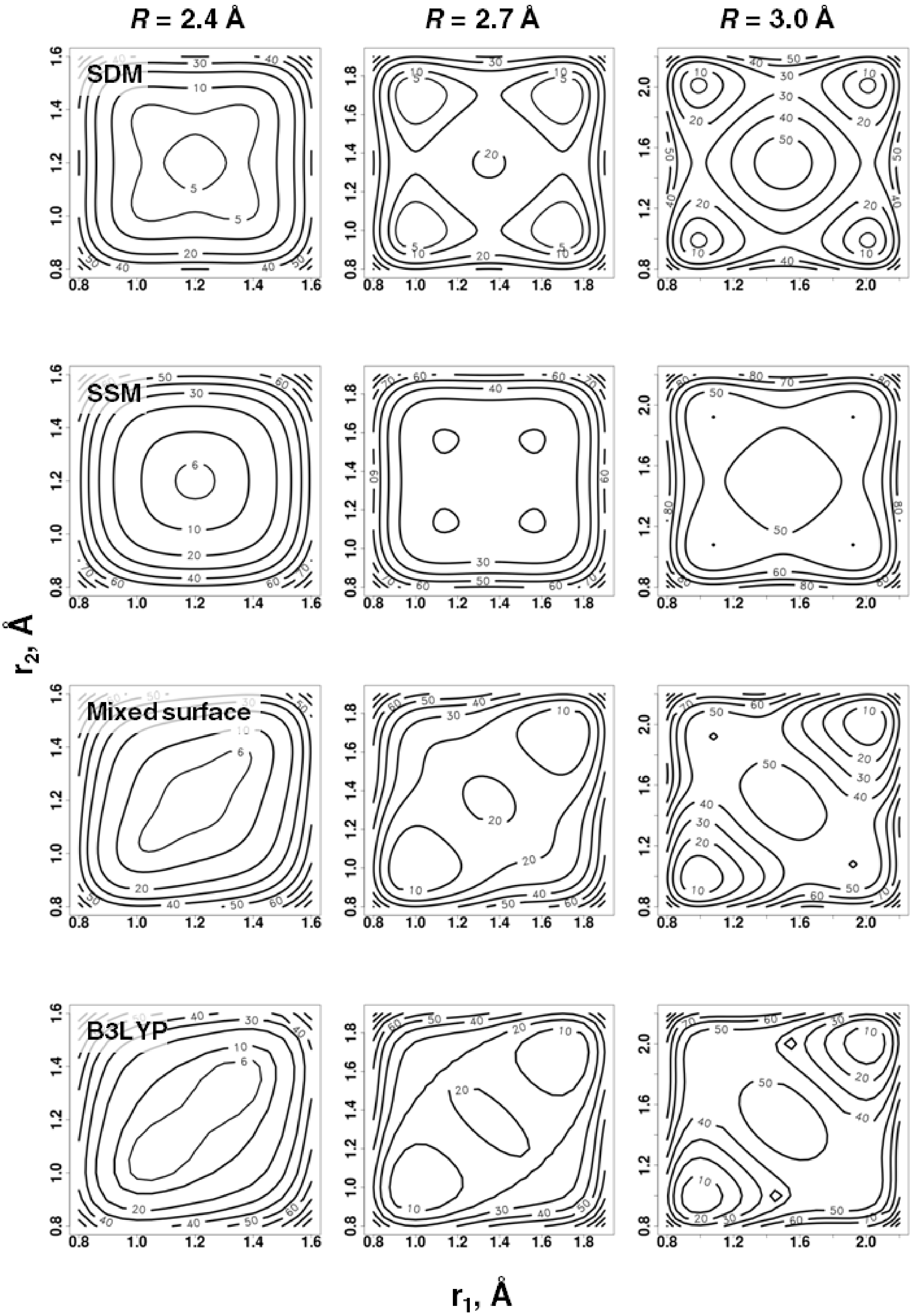

Figure 3.7.: Two-dimensioned potential surface of Surface I (V_I), Surface 2 (V_{II}) and MMPT potentials, compared to B3LYP/6-31G(d,p) data at $R = 2.4$ Å, 2.7 Å and 3.0 Å.

3.3. Generalization of MMPT Potential Surface

Previous sections provides an empirical solution to simulate PT reaction in force field regime. For the sake of accuracy, to obtain *ab initio* based PT potential of one reactive system usually requires *ab initio* calculations in which the configurational space is thoroughly explored to the reactively essential degrees of freedom. Data processing is then followed with mathematical parametrization or fits. Considering of a situation with high-throughput computing, i.e. to build a library of PT potentials for database amount of systems. Following the given protocol (*ab initio* calculations and fitting) to exploring all PESs could be extremely exhaustive in computing costs. Therefore, it is necessary to find a way to reduce the computing costs but with acceptable (or ideally negligible) loss of accuracy in energetics for PT reactions.

3.3.1. Morphing PES for PT Systems

Focusing on the MMPT potential with asymmetric PES (ASM, $H_3N - H^+ \cdots OH_2$), the empirical PES of a target system can be constructed by simply adding a multiplier to morph the given PES of a PT reaction.[142,143] In this section, PESs of derivative molecules of $H_3N - H^+ \cdots OH_2$ (NHO) were explored and parametrized, including dimers of methylammonium-water ($CH_3NH_2 - H^+ \cdots H_2O$, MAM), dimethylammonium-water ($(CH_3)_2NH - H^+ \cdots H_2O$, DMA) and chloroammonium-water ($ClH_2N - H^+ \cdots H_2O$, CLA).

The energy function of asymmetric MMPT potential surface has been given in Eq. 3.10. The new PES can be obtained by a linear transformation of its original PES, which is written as

$$V_{\text{target}}(R, \rho, \theta) = k_V \cdot V_{\text{MMPT}}(R', \rho', \theta) + c_V, \tag{3.38}$$

where k_V and c_V are the parameters for linear transformation. If $(R, \rho) \equiv (R', \rho')$, Eq. 3.38 shows a simplest form of morphing as only the potential surface is scaled linearly from the original one. In a more realistic case, the group substitution also changes the equilibriums of energy minimum and transition states. That also requires linear transformation of those reaction coordinates of concerns, i.e.

$$R' = k_R \cdot R + c_R \tag{3.39}$$

and

$$\rho' = k_\rho \cdot \rho + c_\rho \tag{3.40}$$

It also needs to be mentioned that linear morphing has been only applied for the 2D potential $V_0(R, \rho)$ and the harmonic approximation to the third dimension (namely $k \cdot \theta^2$) was treated and parametrized externally. With a given topology of PES for PT reactions, in the current work this approach shows great advantages in reconstructing accurate potential energy surfaces for new systems with considerably reduced computing costs in *ab initio* calculations.

Table 3.3.: MMPT Parameters of asymmetric PESs for MAM, DMA and CLA using complete fitting to *ab initio* calculations at the level of MP2/6-311++G(2d,2p)

	NHO	MAM	DMA	CLA
p_1, kcal/mol	10.438	10.272	10.842	16.865
p_2, Å^{-1}	1.271	1.238	1.269	0.433
p_3, Å	3.427	3.437	3.386	3.944
p_4, kcal/mol	109.957	109.663	107.941	100.665
p_5, unitless	5.800	5.879	5.790	8.380
p_6, Å^{-1}	1.509	1.432	1.457	1.050
p_7, Å	2.960	2.987	2.963	3.521
p_8, unitless	-0.109	-0.113	-0.115	-0.192
p_9, Å^{-1}	1.397	1.366	1.407	1.026
p_{10}, Å	2.527	2.496	2.485	1.837
p_{11}, unitless	0.177	0.181	0.185	0.247
p_{12}, kcal/mol	8.077	8.455	9.173	9.856
p_{13}, Å^{-1}	1.374	1.297	1.305	3.784
p_{14}, Å	3.304	3.301	3.242	-0.562
p_{15}, kcal/mol	69.564	58.749	49.735	63.072
p_{16}, unitless	7.603	9.940	10.694	43.046
p_{17}, Å^{-1}	1.483	1.283	1.299	0.755
p_{18}, Å	3.044	3.362	3.391	6.147
p_{19}, unitless	0.095	0.109	0.117	0.930
p_{20}, Å^{-1}	1.414	1.385	1.449	0.360
p_{21}, Å	2.598	2.575	2.568	-2.679
p_{22}, unitless	0.855	0.847	0.839	0.169
p_{23}, unitless	63.560	63.568	63.568	21.892
p_{24}, Å^{-1}	0.043	-0.006	-0.004	4.130
p_{25}, Å	-6.637	-6.409	-6.411	2.375
p_{26}, unitless	52.780	51.671	44.269	41.102
p_{27}, kcal/(mol·deg^2)	0.026	0.026	0.026	0.026

Table 3.4.: Parameters of asymmetric PESs for MAM, DMA and CLA using linear morphing approach.

	MAM	MAM (CCSD(T))	DMA	CLA
k_V	1.3583	1.3861	1.6398	0.6987
c_V	-0.5882	-1.0234	-0.8117	0.7378
k_ρ	0.9584	0.9560	0.9312	1.0416
c_ρ	0.0214	0.0215	0.0350	-0.0238
k_R	0.7516	0.7448	0.6412	1.3988
c_R	0.6582	0.6892	0.9415	-1.0784

Table 3.5.: Root mean squares errors (RMSE) of MMPT parametrization using linear morphing approach and complete fitting. (kcal/mol)

PT motif	morphing	fitting
NHO	(n.a.)	0.12
MAM	0.43	0.08
MAM (CCSD(T))	0.52	(n.a.)
DMA	0.68	0.09
CLA	0.70	0.11

3.3.2. Results and Discussion

The asymmetric PES for $H_3N - H^+ \cdots OH_2$ model system was obtained by parametrizing *ab initio* calculations at the level of MP2/6-311++G(2d,2p). Fitted parameters were used as reference parameters for linear morphing. In the present work, rigid scans were performed and a total of 297 grid points were sampled in a two-dimensioned range of $R \in [2.4, 3.4]$ Å (with an increment of 0.1 Å)and $r \in [0.8, (R - 0.8)]$ Å (with an increment of 0.05 Å). Parametrization of MMPT potentials was performed by using the ALGLIB software. For each of target system of MAM, DMA and CLA, complete *ab initio* scans were carried out for validation. MMPT parameters from complete fitting can be found in Table 3.3.1 for all systems.

For using the morphing approach, 23 (out of 297) grid points, distributed at $R = 2.7$, 3.0 and 3.3 Å and r sparsely between 0.8 Å and $R - 0.8$ Å, were chosen as training data for and remaining grids were regarded as test data. Parameters of linear coefficients were presented in Table 3.3.2 for all target systems. The assessment of fitting quality for using linear morphing approach was given by calculating root mean square errors (RMSEs) between the *ab initio* data and data reproduced by morphed PES (in complete grid points) and results were shown in Table 3.3.2. For MAM, using complete fitting yields with empirical PES with an almost perfect agreement with *ab initio* calculations (RMSE= 0.08 kcal/mol). In spite of relatively increased deviation to 0.43 kcal/mol, the theoretical PES given by linear morphing is in general of good agreement with the *ab initio* results. Furthermore, it is also highly of interests in whether a given MMPT PES can be morphed into a new PES with reference energies based on QM calculations at the different level of theory. Hence, for MAM *ab initio* calculations were carried out at the level of CCSD(T)/aug-cc-pVTZ upon the same grid points. The result shows with RMSE= 0.52 kcal/mol. Similar to the results in MAM, in DMA and CLA systems the deviations of 0.68 and 0.70 kcal/mol were given, compared to RMSE= 0.09 and 0.11 kcal/mol from complete fitting, respectively.

The 'morph-ability' between two PESs is based on a theory that two systems with similar chemical environments (i.e. MAM only differs to $H_3N-H^+\cdots OH_2$ with one CH_3 substituent) must have the same reaction process and thus may result in similar topologies on the PESs. As such topologies are described with dimensions of energy and reaction coordinates, morphing can be achieved by some transformations (which are mathematically simple but not necessarily linear) upon these dimensions. From Table 3.3.2, it can be found that all k_V values are somewhat different to 1. That suggests various curvatures of the potential surfaces in PT reactions of target systems and more importantly, the barrier heights of PT process under certain separations of N and O atoms. For k_ρ and c_ρ, in all studied cases the key reaction coordinates were not significantly transformed. And to some extent, using $\rho' = \rho$ could be a decent approximation if further simplification is in demand. But the transforming parameters acted upon the geometric coordinates, e.g. $\{k_R, c_R\}$, significantly differ from {1,0}.

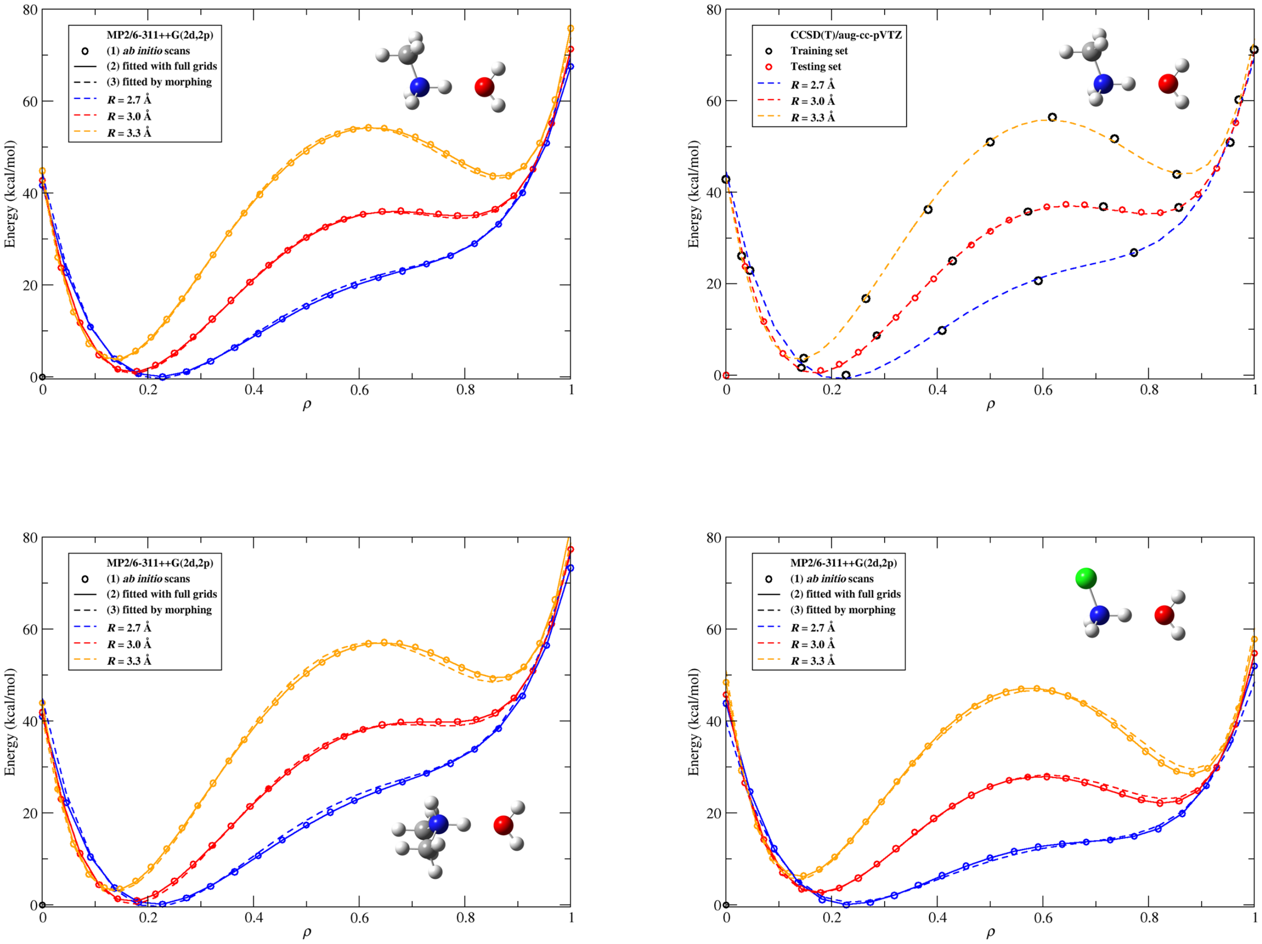

Figure 3.8.: One-dimensioned asymmetric PESs for MAM, DMA and CLA at $R = 2.7$ Å (blue), 3.0 Å (red) and 3.3 Å (orange) from *ab initio* calculations (dots) and MMPT potentials complete fitting (solid lines) and linear morphing (dashed lines).

4. Development of the Multi-state MMPT Method

The MMPT force field has been developed for describing proton transfer systems with energetics at the QM quality. For multiple PT reactions, efforts were attempted since this method was developed. A typical example of multiple PT reaction is double proton transfer, for which both sequential[124,144] and concerted[10] pathway have been investigated using MMPT force field. Nevertheless, there is obviously a limitation in the current method that a PT reaction only takes place within a predefined triatomic moiety which contains a transferring hydrogen (H^*) and its donor and acceptor atoms ($D - H^* \cdots A$). It is not possible for MMPT to delocalize the reaction site and perform a continuous PT reaction or a diffusion process of excess protons in MD simulations. Such reaction process is also called as Grotthuss mechanism. In order to implement Grotthuss mechanism in MMPT force field, the method of multi-state MMPT (MS-MMPT) is discussed in this chapter. The new development focuses on several technical challenges: 1) Continuous proton transports should be spontaneous and undirected in MD simulations; 2) Diffusion of excess protons in the condensed phase also leads to the diffusion of charge, hence modeling charge transfers is required; 3) The diffusivity of the excess proton (or charge) in an aqueous system should be comparable between molecular dynamics and experiments.

In this chapter, the context is organized as follows: 1) The improved MMPT force field for describing an $H_5O_2^+$ structure in the gas and the condensed phases; 2) The method of MS-MMPT for proton transports and 3) the implementation of MS-MMPT in CHARMM program.

4.1. A QM-like $H_5O_2^+$ ion with MMPT force field

Prior to simulations of Grotthuss proton transports, it is important to refine the current MMPT force field which describes an $H_5O_2^+$ ion in the gas phase. The aims is to build an overall potential energy of $H_5O_2^+$ in good agreement with *ab initio* calculations at the level of MP2/6-311++G(2d,2p). To distinguish between the previous and developmental version of MMPT force field, in the following text "current MMPT" refers to the published version of MMPT program from the previous works[25,120] and "MS-MMPT" stands for the developmental version in the current work.

4.1.1. Resonance Structures

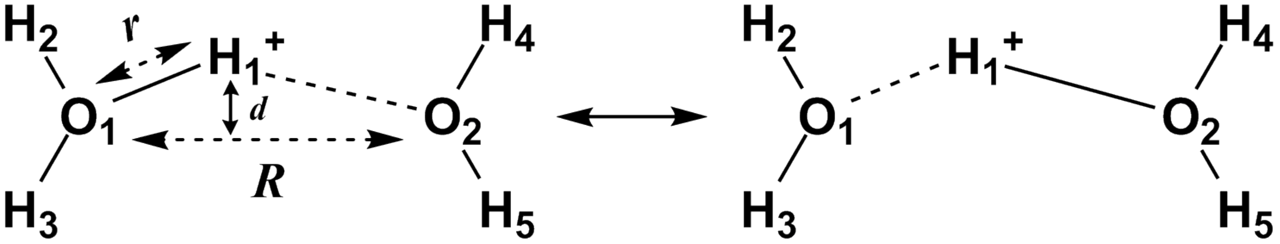

Figure 4.1.: Resonance representation for $[H_2O]_2H^+$.

For studying $H_5O_2^+$ with the current MMPT force field, the PT potential is slightly modified from Eq. 3.3 and given as

$$V(R, \rho, d) = V_0(R, \rho) + k \cdot d^2, \tag{4.1}$$

where $V_0(\rho, R)$ is the same to Eq. 3.4 but the angular term has been transformed to $k \cdot d^2 = k(r \cdot sin\theta)^2$ for the bending mode of H*. The parametrization of PT potential was carried out using ALGLIB fitting toolkit.[123] All parameters are recorded in Table 4.1 and the overall root mean square error (RMSE) was reported ±0.22 kcal/mol (Figure 4.2).

Table 4.1.: Parameters of MMPT potential for PT reactions in $H_5O_2^+$, fitted to *ab initio* calculations at the level of MP2/6-311++G(2d,2p). Parameters are in accordance from Eq. 3.5 to Eq. 3.9.

parameter	values
p_1	1.8337×10^6 kcal/mol
p_2	1.104 Å^{-1}
p_3	-6.952 Å
p_4	-1.8335×10^6 kcal/mol
p_5	-0.6763 Å^{-1}
p_6	1.232 Å^{-2}
p_7	41.77 Å
p_8	2.4648 Å^{-1}
p_9	0.0882 Å
p_{10}	49.28 kcal/(mol·Å^2)
p_{11}	0.917 kcal/mol

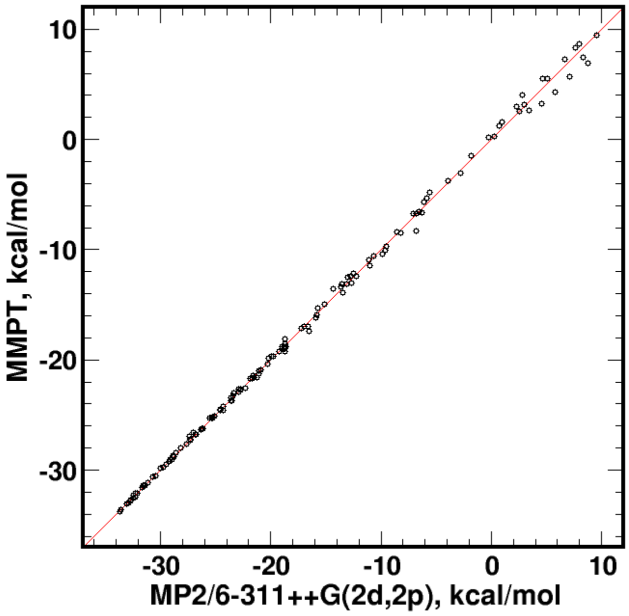

Figure 4.2.: The fitting quality of MMPT PT potential ($V_0(R,\rho)$, see Eq. 3.4), parametrized to *ab initio* scans at the level of MP2/6-311++G(2d,2p). The RMSE is 0.22 kcal/mol.

Figure 4.1 shows a typical structure of a $[H_2O]_2H^+$ complex, which is well known as a Zundel complex. From a classical standpoint, a Zundel complex can be modeled as a hydronium molecule interacts with a water molecule which shows as $H_3O^+ \cdots H_2O$. In MMPT force field, the potential energy for a Zundel complex can be written as

$$V_{H_5O_2^+} = V_{H_3O^+} + V_{H_2O} + V_{MMPT-H_5O_2^+}, \tag{4.2}$$

where $V_{H_3O^+}$ and V_{H_2O} include all classical energy terms (bond stretches and bends) for describing H_3O^+ ($H_2O_1H_3H_1^+$) and H_2O ($H_4O_2H_5$), respectively. $V_{MMPT-H_5O_2^+}$, on the other hand, introduces Eq. 4.1 as a replacement of the harmonic constrain on bond O_1–H_1^*

$$\begin{aligned} V_{MMPT-H_5O_2^+} &= V_{PT}(R,\rho,d) - E_{bond}(O_1 - H_1^*) \\ &- \gamma \cdot [E_{angle}(H_2 - O_1 - H_1^*) + E_{angle}(H_3 - O_1 - H_1^*)] \\ &+ \gamma \cdot [E_{angle}(H_4 - O_2 - H_1^*) + E_{angle}(H_5 - O_2 - H_1^*)]. \end{aligned} \tag{4.3}$$

In Eq. 4.3, $E_{\text{bond}}(\text{O}_1 - \text{H}_1^*)$ is the bond stretching terms with the classical force field representation. Along with the bond dissociation and formation between $\text{O}_1 - \text{H}_1^*$ and $\text{O}_2 - \text{H}_1^*$ during a PT process, Eq. 4.3 also takes account into the transformation of classical bending terms by introducing the switch factor – γ (mentioned in Eq. 3.31).

In the previous study, using a switch function has been found a simple but valid solution to simulate resonance forms of reactive systems.[69] In the case of a Zundel ion, the resonance representation is given as $[\text{H}_3\text{O}]^+ \cdots [\text{H}_2\text{O}] \longleftrightarrow [\text{H}_2\text{O}] \cdots [\text{OH}_3]^+$, including bond interactions for internal DOFs of H_5O_2^+ and non-bonded interactions between the Zundel ion and the environment. For the modified MMPT force field, the energies of the resonance representation can be given by

$$\begin{aligned} V_{\text{bonded}} = &\sum_{(i,j)\in\{(1,2),(1,3)\}} G_{\text{bond}}(\text{O}_i - \text{H}_j) - \sum_{(k,l)\in\{(2,4),(2,5)\}} G_{\text{bond}}(\text{O}_k - \text{H}_l) \\ &+ G_{\text{angle}}(\text{H}_2 - \text{O}_1 - \text{H}_3) - G_{\text{angle}}(\text{H}_4 - \text{O}_2 - \text{H}_5). \end{aligned} \tag{4.4}$$

In Eq. 4.4, G_{bond} refers to an energy term with mixed H_3O^+ and H_2O OH bonding terms, which is shown as

$$G_{\text{bond}}(\text{O}_i - \text{H}_j) = (1-\gamma) k_b^{\text{H}_3\text{O}^+}(l - l_{\text{eq}}^{\text{H}_3\text{O}^+})^2 + \gamma \cdot k_b^{\text{H}_2\text{O}}(l - l_{\text{eq}}^{\text{H}_2\text{O}})^2 - E_{\text{corr}}(\gamma) \tag{4.5}$$

where l is the bond length of $\text{O}_i - \text{H}_j$, $[k_b^{\text{H}_3\text{O}^+}, l_{\text{eq}}^{\text{H}_3\text{O}^+}]$ is the OH bond force field for a hydronium ion and $[k_b^{\text{H}_2\text{O}}, l_{\text{eq}}^{\text{H}_2\text{O}}]$ is that for a water molecule. $E_{\text{corr}}(\gamma)$ is a correction term for $G_{\text{bond}}(\text{O}_i - \text{H}_j)$ to obtain a zero minimum if the energy is minimized. Between any two pairs of parameters for harmonic potentials, i.e. $[k_1,\ l_{\text{eq},1}]$ and $[k_2,\ l_{\text{eq},2}]$, the correction term can be given by

$$E_{\text{cor}}(\gamma) = \frac{(l_{\text{eq},1} - l_{\text{eq},2})^2}{\dfrac{1}{(1-\gamma)\cdot k_1} + \dfrac{1}{\gamma \cdot k_2}}. \tag{4.6}$$

If $\left[k_1, l_{\text{eq},1}\right] = \left[k_2, l_{\text{eq},2}\right]$, $E_{cor}(\gamma) \equiv 0$ and $G_{\text{bond}}(\text{O}_i - \text{H}_j)$ is simply a classical harmonic bond term. For G_{angle} the same fashion is applied.

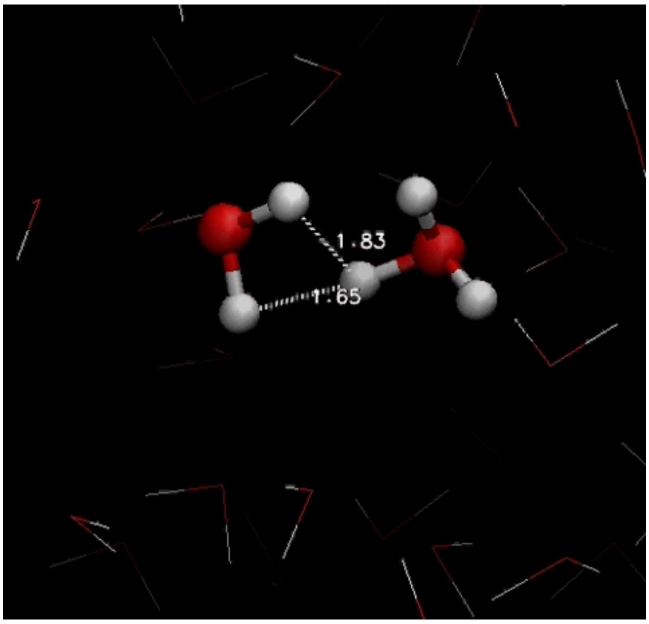

Figure 4.3.: The MD snapshot of an $H_5O_2^+$ ion from MD simulations using the current MMPT force field. Point charges were assigned to all atoms in $H_5O_2^+$ using SPC water model.[145,146]

In current MMPT force field, within $H_5O_2^+$ the non-bonded terms are deactivated for all inter-atomic interactions. However, non-bonded interactions are not negligible between solute and solvent molecules during MD simulations. From *ab initio* calculations, a Zundel molecule shows a symmetric configuration especially with $r_{\mathrm{O_1-H_1^+}} = r_{\mathrm{O_2-H_1^+}}$ when it is stabilized both in the gas phase and with a first solvation shell (i.e. $[H_2O]_6H^+$). However, in the condensed phase a Zundel molecule can be easily polarized by solvent molecules, for which the configuration can not retain as it is in the gas phase. That is because a gas-phase Zundel structure is neutral in dipole (if modeled with partial point charges in force field language) which is unstable with polarizable environment. A typical picture for this problem in current MMPT force field is shown in Figure 4.3, in which the partner H_2O molecule flips its hydrogen atoms towards the H_3O^+ ion. That requires additional constrains which is also considered to compensate the missing inter-molecular interactions within the $H_5O_2^+$ molecule. These extra terms can be also given in hybrid forms and by re-writing Eq. 4.3 into

$$\begin{aligned} V_{\mathrm{MS-MMPT-H_5O_2^+}} &= V_{\mathrm{PT}}(R,\rho,d) - E_{\mathrm{bond}}(\mathrm{O_1 - H_1^*}) \\ &+ (1-\gamma)\cdot[G_{\mathrm{angle-H^*}}(\mathrm{H_2 - O_1 - H_1^*}) + G_{\mathrm{angle-H^*}}(\mathrm{H_3 - O_1 - H_1^*})] \\ &+ \gamma\cdot[G_{\mathrm{angle-H^*}}(\mathrm{H_4 - O_2 - H_1^*}) + G_{\mathrm{angle-H^*}}(\mathrm{H_5 - O_2 - H_1^*})] \\ &+ \sum_{i,j} E_{\mathrm{torsion}}(\gamma,\Psi_{i,j}) \end{aligned} \tag{4.7}$$

where $G_{\mathrm{angle-H^*}}$ is given with

$$G_{\mathrm{angle-H^*}}(\mathrm{H}_i - \mathrm{O}_j - \mathrm{H_1^*}) = (1-\gamma)\cdot k_{\mathrm{a}}^{\mathrm{H_3O^+}}\cdot(\phi - \phi_{\mathrm{eq}}^{\mathrm{H_3O^+}})^2 + \gamma\cdot k_{\mathrm{a}}^{\mathrm{SP}}\cdot(\phi-\phi_{\mathrm{eq}}^{\mathrm{SP}})^2 - E_{\mathrm{corr}}(\gamma) \tag{4.8}$$

with ϕ as the angle of $\mathrm{H}_i - \mathrm{O}_j - \mathrm{H_1^*}$ and $(k_{\mathrm{a}}^{\mathrm{SP}}, \phi_{\mathrm{a}}^{\mathrm{SP}})$ as the force field of angular bends of $\mathrm{H^*\cdots O–H}$ for the transferring hydrogen $\mathrm{H^*}$ with its hydrogen bonded H_2O molecule. The isotropic potential – $V(R,\rho,d)$ also contains a constrain upon O_1–O_2 which implies O_1–O_2 has a bond-like character. Configurations of $H_5O_2^+$ structures were also improved by introducing a torsion constrain for each of [H_i–$\mathrm{O_1}$–$\mathrm{O_2}$–H_j] dihedral angles ($i = \{2,3\}$ and $j = \{4,5\}$), which gives

$$E_{\mathrm{torsion}}(\gamma,\Psi_{i,j}) = k_d\cdot(1+cos(\Psi_{i,j})) \tag{4.9}$$

where k_d is the force constant and $\Psi_{i,j}$ refers to the dihedral angles of [H_i–O_x–O_y–H_j]. For a brief conclusion, in MS-MMPT the total potential energy for a Zundel molecule in the gas phase is obtained by combining Eq. 4.4 and Eq. 4.7

$$V_{\mathrm{H_5O_2^+}}^{\mathrm{intra}} = V_{\mathrm{bonded}} + V_{\mathrm{MS\text{-}MMPT-H_5O_2^+}}, \tag{4.10}$$

Table 4.2.: Force field parameters of bonded interactions in H_3O^+ and H_2O representations in MS-MMPT force field.

	H_3O^+	H_2O
k_b, kcal/mol·Å^{-2}	552.9	592.2
l_{eq}, Å	0.973	0.966
k_a, kcal/mol·rad^{-2}	31.1	59.3
ϕ_{eq}	112.7°	106.6°
k_a^{SP}, kcal/mol·rad^{-2}	11.0	
ϕ_{eq}^{SP}	128.4°	
k_d, kcal/mol	0.22	

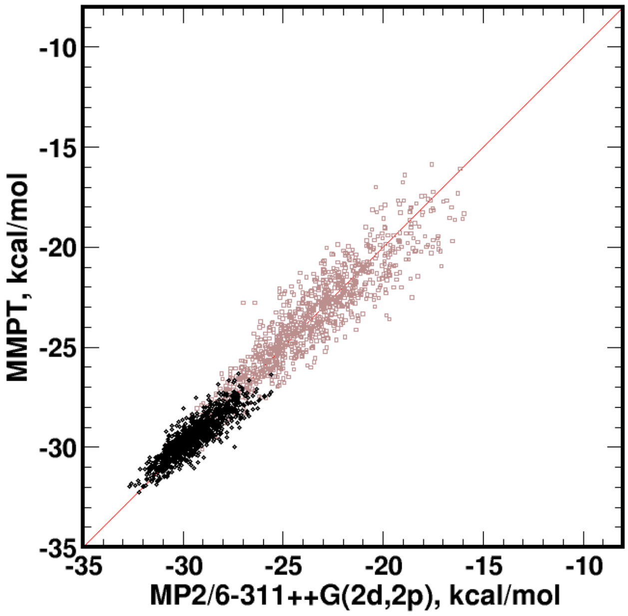

Figure 4.4.: The binding energies of arbitrary MD frames from MMPT simulations for $H_5O_2^+$, compared to *ab initio* calculations at the level of MP2/6-311++G(2d,2p). MD frames were collected from simulations at 300 K (black) and 750 K (brown).

The parameters for the internal potential energy surface within a Zundel ion (Eq. 4.10) were determined with respect *ab initio* calculations at the level of MP2/6-311++G(2d,2p). The parameters are given in Table 4.2 and the fitting quality shown in Figure 4.4. The RMSEs were given as ±0.57 kcal/mol and ±1.10 kcal/mol for MD frames from simulations at 300 K and 750 K, respectively. The fitting procedure consists of a total of nine fitting iterations when the convergences of parameters were seen (Figure 4.5).

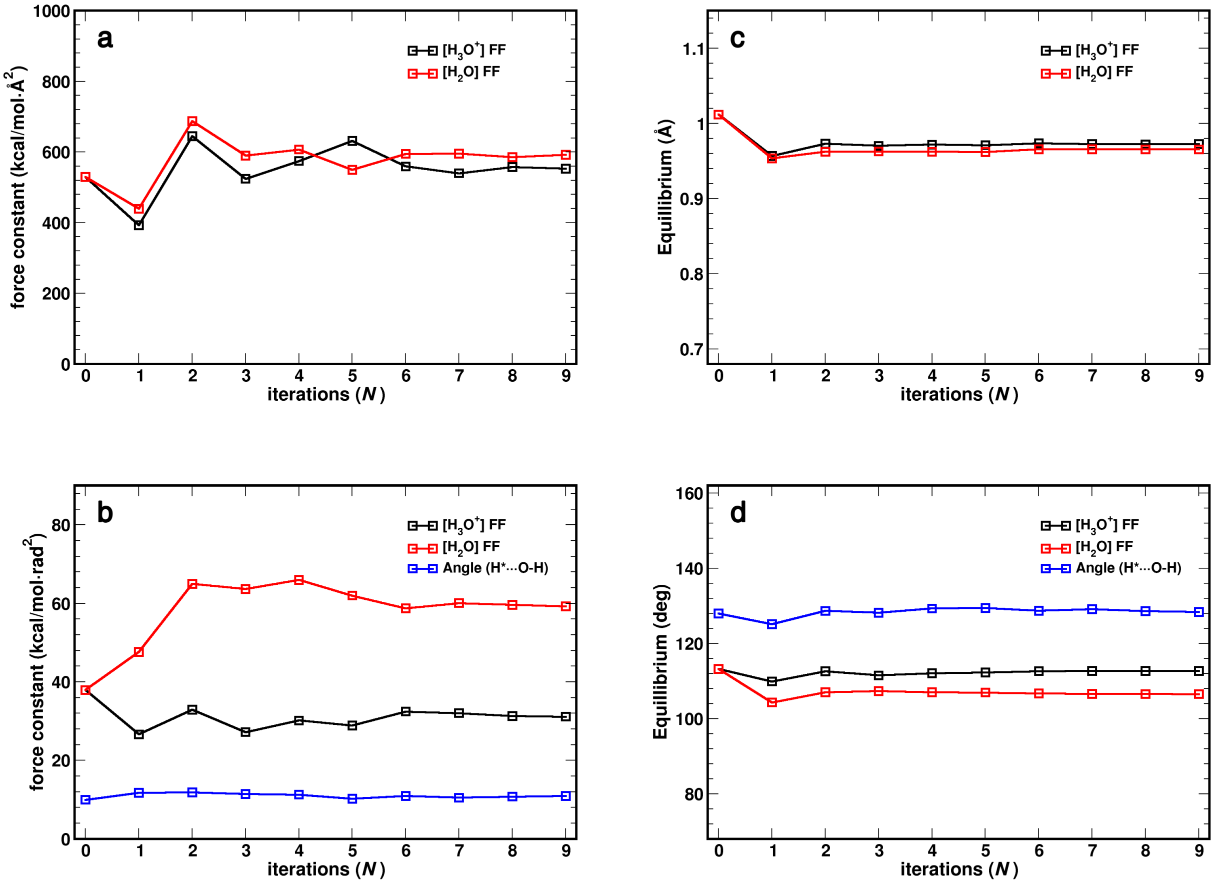

Figure 4.5.: Force field parameters for describing bonded terms in $[H_2O]_2H^+$ framework. At $N \leq 5$, for each iteration 1000 random configurations were generated from MD simulations at 300 K and the energies were calculated at the level of MP2/6-311++G(2d,2p); Starting from $N = 6$, 2000 random configurations were obtained by MD simulations at 300 K and 750K for each fitting iteration. Configurations for force field parametrization were 1) obtained from each iteration at $N \leq 5$ and 2) accumulatively collected at $N \geq 6$.

Figure 3.2 gives a proton transfer picture which undergoes a reaction barrier with the dependence of $O - O$ separation distance (R). In Figure 4.6, the similar potential surfaces were compared among *ab initio* scans (orange in Figure 4.6), PT potential (which is directly fitted to *ab initio* calculations and shown in red) and force field PES scans using MS-MMPT with given parameters for $H_5O_2^+$ which are mentioned above. This comparison validate the current work of force field refinement for $H_5O_2^+$ in the other aspect. Introducing force field does not affect the PT potential surface on the the transferring path.

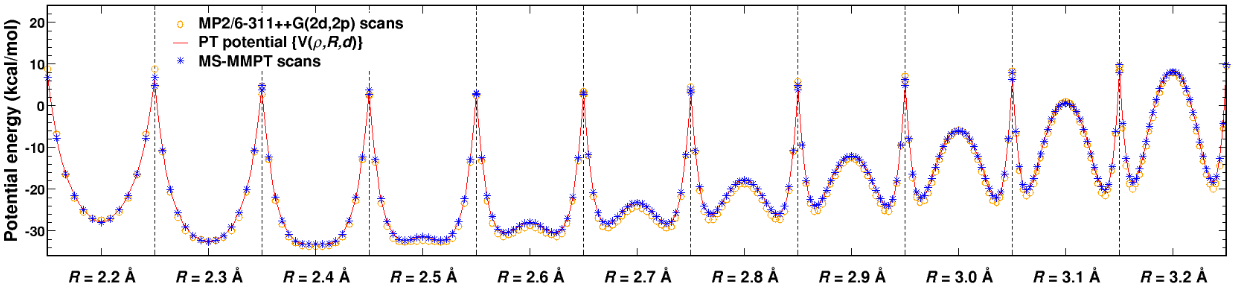

Figure 4.6.: One dimensioned cut of PT PES for $H_5O_2^+$, with R in a range of 2.2 ∼ 3.2 Å. For each panel, the $x-$axis stand for the transferring reaction coordinate ρ ($\in [0, 1]$).

4.1.2. Charge Transfer Model

In the last section, proton transfers within a $H_5O_2^+$ ion has been successfully modeled at gas phase. In this section, the point charge model is introduced. For simulations in the condensed phase with periodic boundary condition (PBC), non-bonded interactions (including electrostatic and van der Waals interactions) are not negligible. And the proton transport process requires the excess charge to drift throughout the whole system. That brings the difficulty in using fixed point charge model.

Following the concept of resonance structure of an $H_5O_2^+$ ion, a proton transfer move should also involve with a charge transfer process. Depending on the positioning of H^* along $O-O$, the partial charges of all atoms within $H_5O_2^+$ can be represented in a mixed form:

$$Q_{\mathrm{O}} = (1-\gamma)\cdot Q_{\mathrm{O}^*} + \gamma \cdot Q_{O_{\mathrm{w}}}, \tag{4.11}$$

where Q_{O^*} and $Q_{O_{\mathrm{w}}}$ stand for fix partial charges for O atoms in H_3O^+ and H_2O. Charges of non-transferring hydrogen atoms (or H atoms on the water side) in $H_5O_2^+$ are treated in the same fashion. For H^* atom, the charge is fixed during the transfer process. That is because the H^* atom is regarded as a hydrogen atom of a hydronium from the both side in the resonance picture, which leads to $Q_{\mathrm{H}} = (1-\gamma)\cdot Q_{\mathrm{H}^*} + \gamma \cdot Q_{\mathrm{H}^*} = Q_{\mathrm{H}^*}$. Using fixed charge model for H^* is also supported by its natural bond orbital (NBO) charge from *ab initio* calculations. Figure 4.7 shows the variance of NBO charges for the H_3O^+ ion within a $H_5O_2^+$ molecule from *ab initio* scans. Results show that the charge of H^* remains almost unchanged through most of the range of $\gamma \in (0,1)$.

In the current work, the charge of H^* was modeled the same the other two hydrogens in H_3O^+. The charge of water molecules were taken from SPC water model.[145,146] The Lennard-Jones parameters were treated in the same fashion and all parameters for non-bonded interactions are given in Table 4.3. For the interests of *ab initio*-based charge fitting, the H^* charges at the invariant region (e.g. $\gamma = 0.5$) were computed with variance of R. Figure 4.8 shows such results. With R increased, $Q_{\mathrm{H}^*}(R)$ trends to converge into $+1$, which is also the net excess charge of an $H_5O_2^+$ ion. That suggests a comprehensive fact that H^* appears as a single (and only) cation in a full dissociation picture of $H_2O\cdots H^+\cdots H_2O$.

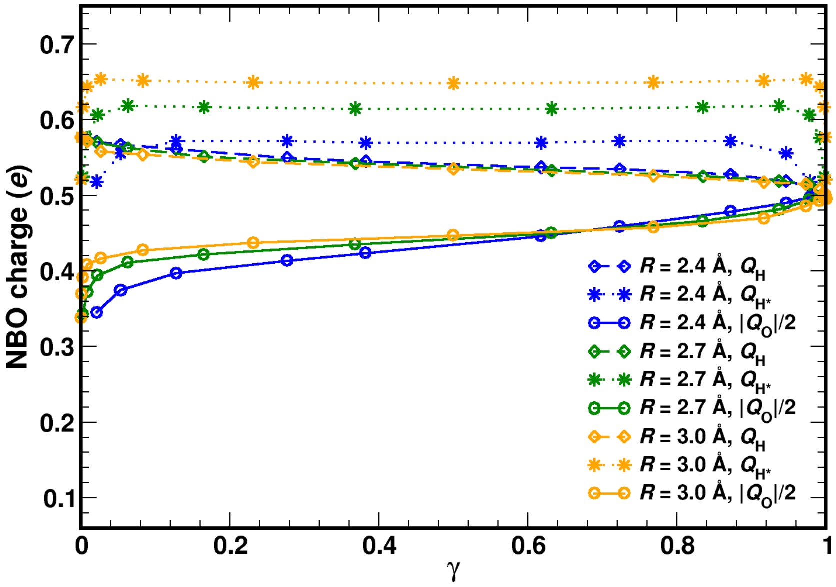

Figure 4.7.: Natural bond orbital charges for atoms of the H_3O^+ ion with H^* moving along the transferring path in a $H_5O_2^+$ framework. The switch factor, γ, is used as progression coordinate with $R = 2.4$,2.7 and 3.0 Å.

Therefore, $Q_{H^*}(R)$ can be expressed with an exponential function, which is written as

$$Q_{H^*} = 1 - e^{b-a\cdot R} \tag{4.12}$$

where $a = 0.44643$ Å^{-1} and $b = 0.20430$ are the parameters. And the remaining charge from excess charge is redistributed into other atoms. Both fixed charge and $R-$dependent charge models for H_3O^+ ion were implemented in the MS-MMPT development. In the current work, the simpler fixed charge model was used.

Table 4.3.: Force field parameters of non-bonded interactions of H_3O^+ and H_2O model in MS-MMPT force field.

	H_3O^+	H_2O
ϵ_O, kcal/mol	-0.1980	-0.1554
$r_{\mathrm{min,O}}$, Å	1.734	1.777
ϵ_H, kcal/mol	0.0	0.0
$r_{\mathrm{min,H}}$, Å	0.0	0.0
q_O, $\boldsymbol{e}$	-0.98	-0.82
q_{H^*}, $\boldsymbol{e}$	0.66	N.A.
q_H, $\boldsymbol{e}$	0.66	0.41

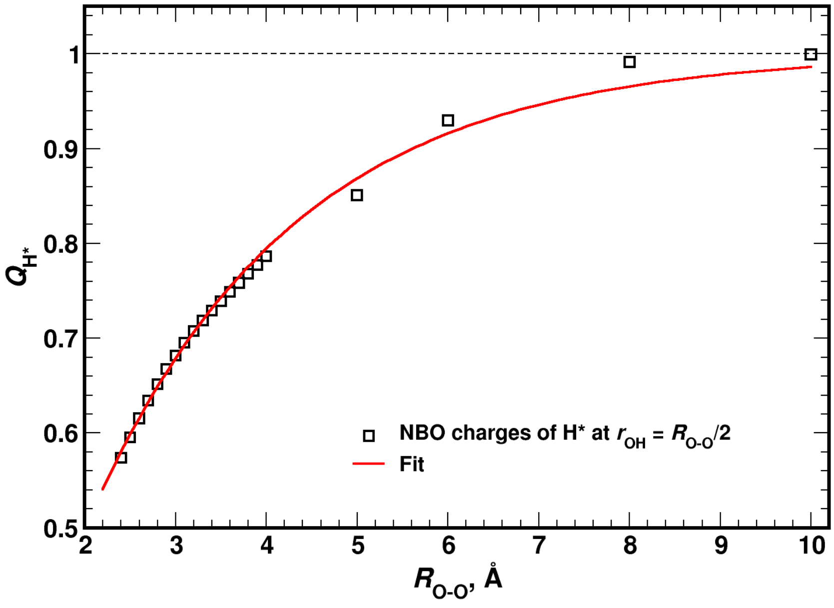

Figure 4.8.: NBO charges of H^* at $\gamma = 0.5$ with fits.

4.2. Multi-state MMPT Method for Performing Grotthuss Proton Transports

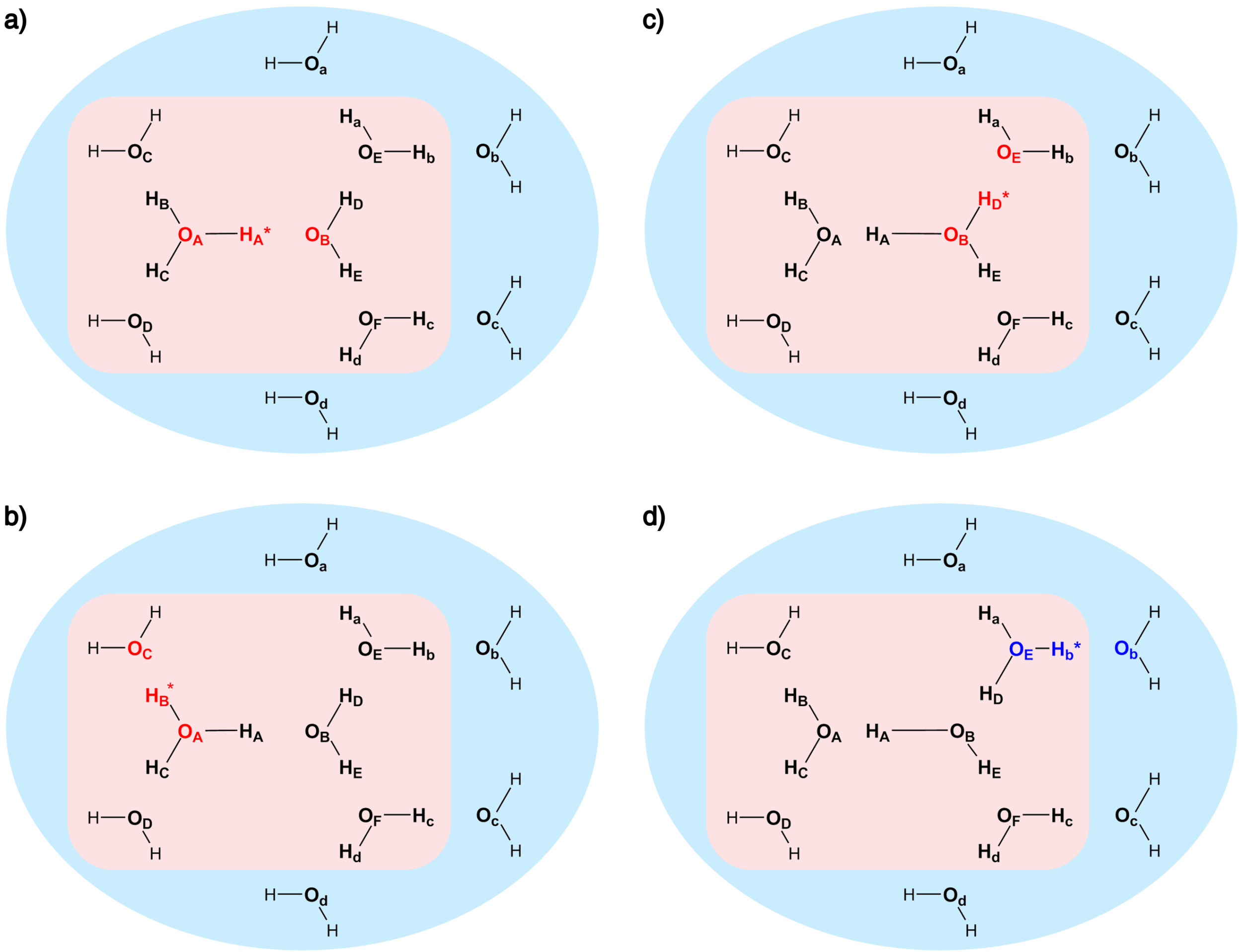

Figure 4.9.: OH bond network of exemplary PT states in MMPT-ARMD scheme. From top to bottom: a) the primary state with a 'seed' motif of $O_A - H_A^+ - O_B$ and the candidate states with b) $O_A - H_B^+ - O_C$, c) $O_B - H_D^+ - O_E$ and d) $O_E - H_b^+ - O_b$. The first and second solvation shells of the representative Zundel complex from the primary state are shown in red and blue as background colors.

Unlike simulations of oscillatory proton transfers between donor and acceptor atoms, MS-MMPT aims to determine where the PT reaction takes place (namely reactive sites) in aqueous systems. Such reactive sites should be delocalized with thermodynamics. For each selected reactive site, a state is defined and determined with a $H_5O_2^+$ ion which contains a PT motif and the bond topology assigns the rest of atoms as environmental molecules accordingly.

Figure 4.9 shows the representative states together with PT motifs handled in the MS-MMPT framework. For each state, the potential energy $V_j(\mathbf{x})$ is determined by the current geometry under individually defined bonding topology and PT motifs which are tracked by MS-MMPT. The total potential energy of one such state is written as

$$V_j(\mathbf{x}) = V^{\text{intra}}_{\text{H}_5\text{O}_2^+} + V^{\text{intra}}_{\text{solv}} + V^{\text{inter}}_{\text{H}_5\text{O}_2^+-\text{solv}} + V^{\text{inter}}_{\text{solv}-\text{solv}} \tag{4.13}$$

Here, $V^{\text{intra}}_{\text{H}_5\text{O}_2^+}$ is that given in Eq. 4.10, $V^{\text{intra}}_{\text{solv}}$ includes all intramolecular (bonded) energies of solvent molecules and $V^{\text{inter}}_{\text{H}_5\text{O}_2^+-\text{solv}}$ and $V^{\text{inter}}_{\text{solv}-\text{solv}}$ refer to the intermolecular interactions of $H_5O_2^+$–solvent and solvent–solvent pairs. In particular for $V^{\text{inter}}_{\text{H}_5\text{O}_2^+-\text{solv}}$, the charge transfer model was introduced for the $H_5O_2^+$ ion, which is discussed in Sec. 4.1.2.

The total potential energy for a given geometry is then a linear combination of energies of selected states. It can be given by

$$V_{\text{tot}}(\mathbf{x}) = \sum_{j=1}^{m} w_j(\mathbf{x}) \cdot V_j(\mathbf{x}), \tag{4.14}$$

where

$$\begin{aligned} w_j(\mathbf{x}) &= \frac{w_j^0(\mathbf{x})}{\sum\limits_{j=1}^{m} w_j^0(\mathbf{x})} \\ w_j^0(\mathbf{x}) &= \exp(-\frac{S_j(\mathbf{x}) - S_{\text{min}}(\mathbf{x})}{\Delta E}) \end{aligned} \tag{4.15}$$

In Eq. 4.14, $w_j(\mathbf{x})$ is the normalized weight.[147] $w_j^0(\mathbf{x})$ is determined by a geometry-based scoring function $S_j(\mathbf{x})$, which evaluate whether and how much a state is appropriate to describe a proton transfer reaction (lower the score is, more favorable the state is) and $S_{\text{min}}(\mathbf{x})$ is the minimum score of all states. In the current work, the internal potential of a $H_5O_2^+$ structure was chosen as the scoring function

$$S_j(\mathbf{x}) = V_{[\text{H}_5\text{O}_2^+]_j}(\mathbf{x}) \tag{4.16}$$

where $[H_5O_2^+]_j$ corresponds to the $H_5O_2^+$ structure for the j-th state. ΔE is the only parameter which controls how much those selected states contribute into $V_{\text{tot}}(\mathbf{x})$. The gradient of total potential energy is readily available from

$$
\begin{aligned}
\nabla V_{\text{tot}}(\mathbf{x}) &= \nabla\Big[\sum_{j=1}^{m} w_j(\mathbf{x}) \cdot V_j(\mathbf{x})\Big] \\
&= \frac{1}{\Delta E} \cdot \frac{1}{\sum\limits_{j=1}^{m} w_j^0(\mathbf{x})} \cdot \sum_{j=1}^{m} \Big\{ w_j^0(\mathbf{x}) \cdot \big[\Delta E \cdot \nabla V_j(\mathbf{x}) \\
&+ (V_{\text{tot}}(\mathbf{x}) - V_j(\mathbf{x})) \cdot \nabla V_{[\text{H}_5\text{O}_2^+]_j}(\mathbf{x})\big] \Big\}
\end{aligned}
\tag{4.17}
$$

which is needed for MD simulations. The detailed deduction to Eq. 4.17 can be found in the Appendix. For Eq. 4.15-4.16, it is understood that a state with a minimum potential energy among all candidate states is the primary state which contributes the most to the total potential energy. Because the force field is fully reactive, it is possible for other low energy states to become the minimum energy state during dynamical simulations. That eventually comes out with a surface cross between candidate states and then the location of oscillatory PT reactions is changed. From a chemical standpoint, that refers to Grotthuss proton transports.

In order to explain the construction of MS-MMPT states, there is an explicit example shown in Figure 4.9. In this example, the primary state is that with $\text{O}_\text{A} - \text{H}_\text{A}^+ - \text{O}_\text{B}$ PT motif (Figure 4.9a). And based on this motif (as a 'seed' motif) the first solvation shell is built and shown in the red and shaded area. The first solvation shell is defined by two spherical regions with radius of 4 Åaround O_A and O_B from the seed motif. Within the first solvation shell, in Figure 4.9 four additional water molecules are found (with oxygen labels from O_C to O_F). For this, new candidate motifs and the corresponding states are generated. Figure 4.9b and c show examples of new motifs within the first solvation shell: $\text{O}_\text{A} - \text{H}_\text{B}^+ - \text{O}_\text{C}$ and $\text{O}_\text{B} - \text{H}_\text{D}^+ - \text{O}_\text{E}$. For the later, in Figure 4.9c the H_A atom changes its bond connection from $\text{O}_\text{A} - \text{H}_\text{A}$ to $\text{O}_\text{B} - \text{H}_\text{A}$. For MS-MMPT, it is also optional to extend the search of states into the second solvation shell which is constructed (in this example) by searching 4 Å radius spheres based on atoms $\text{O}_\text{C} - \text{O}_\text{F}$. In Figure 4.9d, the bond network is further changed from $\text{O}_\text{B} - \text{H}_\text{D}$ to $\text{O}_\text{E} - \text{H}_\text{D}$ (compared to Figure 4.9c) and a PT motif with $\text{O}_\text{E} - \text{H}_\text{b}^+ - \text{O}_\text{b}$ has been identified. Moreover, all candidate motifs should suffice the geometric criteria that the angle of $\angle \text{DH}^*\text{A}$ in a $\text{D} - \text{H}^* - \text{A}$ motif should be no larger than 90°. In MS-MMPT simulations, the selection box of states with the corresponding PT motifs is updated on every MD time step and a detailed protocol for MS-MMPT method is given in Figure 4.10. In the present work, for all simulations the state search underwent within the second solvation shell unless other situations were specifically mentioned.

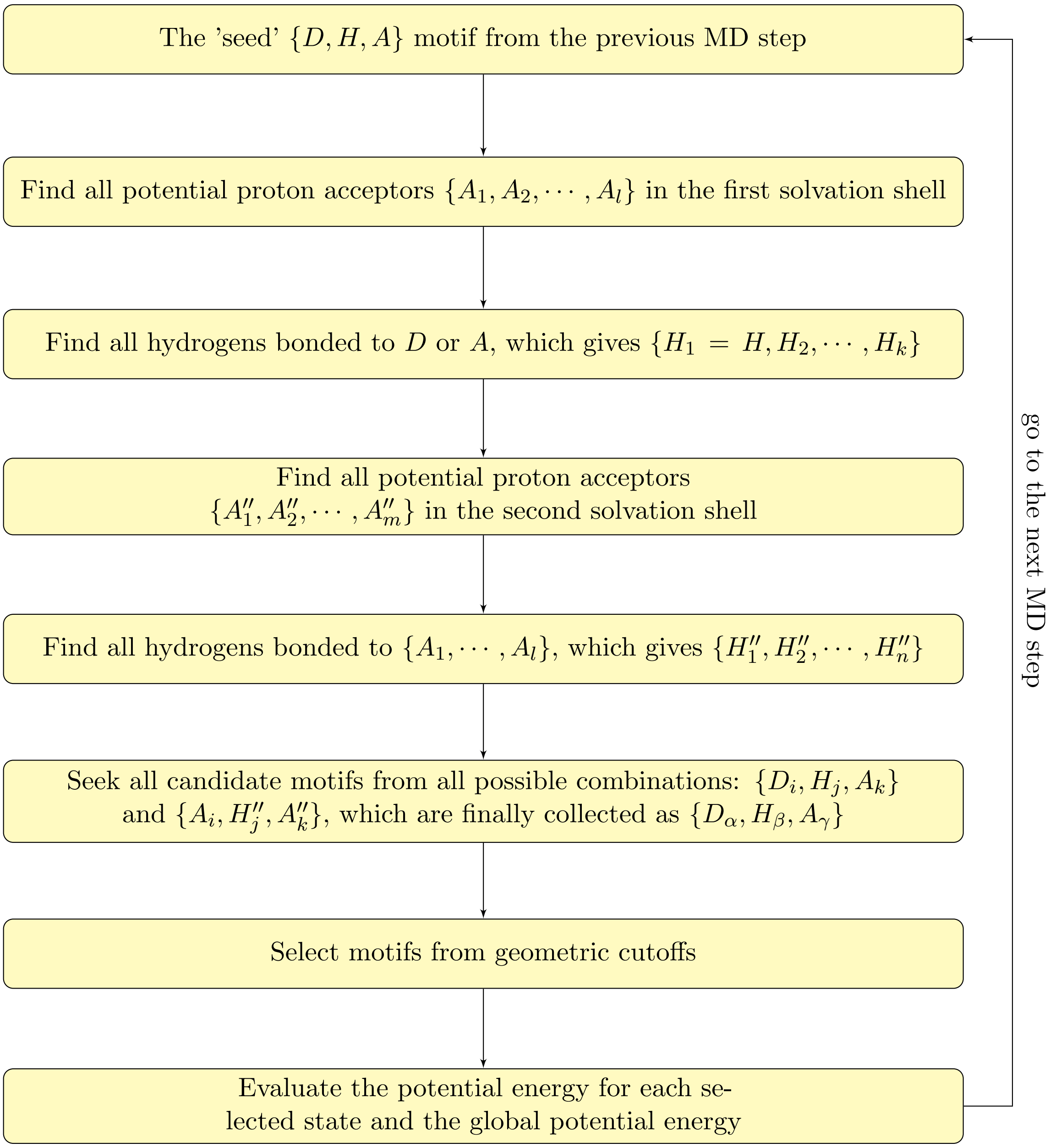

Figure 4.10.: The flowchart of motif search in MS-MMPT.

4.3. Implementation of MS-MMPT in CHARMM program

For the implementation of MS-MMPT in CHARMM,[31] similar to the current MMPT scheme, the MS-MMPT potential $V_{\rm tot}$ (Eq. 4.14) is given in a form of a correction term into the potential of a system using classical force field. That writes

$$V_{\rm MS-MMPT}(\mathbf{x}) = V_{\rm tot}(\mathbf{x}) - V_{\rm CM}(\mathbf{x}), \tag{4.18}$$

and Eq. 4.13 is a one-state situation under the MS-MMPT framework. For each MD step, the state generation (see Section 4.2) is based on the 'seed' motif (with a label of $[\rm D-H-A]$, standing for the state as well) which belongs to the minimum energy state (or the primary state) from the previous MD step. Assume that there is a candidate PT state with $[\rm D'-H'-A']$ which is other than the 'seed' $[\rm D-H-A]$. The potential energy of the primary state $[\rm D-H-A]$ can be easily given by the one-state MMPT framework. The state $[\rm D'-H'-A']$ may involve with a rearrangement of bonding topology from the one given by the previous MD step, according to MS-MMPT method. Nevertheless, its state energy can be given with a similar correction term in an MMPT language:

$$V_{\rm MS-MMPT}^{\rm D'-H'-A'}(\mathbf{x}) = V_{\rm PT}^{\rm D'-H'-A'}(\mathbf{x}) - V_{\rm CM}^{\rm D-H-A}(\mathbf{x}). \tag{4.19}$$

Here, $V_{\rm PT}^{\rm D'-H'-A'}(\mathbf{x})$ is that given by Eq. 4.13. Then, Eq. 4.19 is re-written in a variant form which gives

$$\begin{aligned} V_{\rm MS-MMPT}^{\rm D'-H'-A'}(\mathbf{x}) = &\left[V_{\rm PT}^{\rm D'-H'-A'}(\mathbf{x}) - V_{\rm CM}^{\rm D'-H'-A'}(\mathbf{x})\right] \\ &+ \left[V_{\rm CM}^{\rm D'-H'-A'}(\mathbf{x}) - V_{\rm CM}^{\rm D-H-A}(\mathbf{x})\right], \end{aligned} \tag{4.20}$$

where $V_{\rm CM}^{\rm D'-H'-A'}$ is the classical potential for a bonding topology which includes a $\rm D'-H'$ bond and an $\rm H'-A'$ hydrogen bond. In Eq. 4.20, the term of $V_{\rm PT}^{\rm D'-H'-A'}(\mathbf{x}) - V_{\rm CM}^{\rm D'-H'-A'}(\mathbf{x})$ is the conventional MMPT interpretation as if $[\rm D'-H'-A']$ is computed as the one-state model. $V_{\rm CM}^{\rm D'-H'-A'}(\mathbf{x}) - V_{\rm CM}^{\rm D-H-A}(\mathbf{x})$ is the difference of classical energies between two bonding topologies. For more details, in the first-solvation shell mode a change of such topology only occurs when $\rm A = D'$ which requires a bond change from $\rm D-H$ to $\rm H-A$ (and multiple bond changes should be expected using the second- or possibly higher- solvation shell modes). If no bond change is applied (e.g. when $\rm D = D'$), $V_{\rm CM}^{\rm D'-H'-A'}(\mathbf{x}) - V_{\rm CM}^{\rm D-H-A}(\mathbf{x}) = 0$.

The MS-MMPT method can also be generalized to a system with multiple excess protons, which considers all possible combinations of PT states for each excess proton. A valid combination should suffice the following rules: 1) One donor or acceptor can not contribute or receive two protons at the same MD step; 2) One hydrogen atom can not represent for two different excess protons at the same MD step; 3) It is possible for oxygens atoms to play a role of both donor and acceptor atoms simultaneously but in different PT motifs. The validation and applications of the MS-MMPT method with multiple excess protons can be expected in the future works.

Part III.

Applications

5. Application I: Intramolecular PT reactions and IR Spectroscopy

5.1. Formic Acid Dimer

In hydrocarbons and in the vapor phase, formic acids appear with a dimerized for rather than individual molecules.[148,149] That is due to the strong double hydrogen-bond and the gaseous formic acid does not obey the ideal gas law.[149] The dimerized formic acid, or formic acid dimer (FAD), is a system highly of interests and has been extensively studied from both experiments (spectroscopy mainly)[150–153] and computational efforts.[154–156] In this paper (*Phys. Chem. Chem. Phys.*, 2016, **18**, 24654),[10] the molecular dynamics of formic acid dimer was studied using MMPT force field with the double proton transfer (DPT) model. The aim was to predict the reaction barrier height of the DPT reaction, using a combined approach of MD simulations and spectroscopy experiments. The morphing technique was employed obtain the effective PES, based on which the simulated infrared spectra from MMPT simulations were found in good agreement with experimental data, especially for the proton transferring region near 3000 cm^{-1}. This paper was written together with the group of Prof. H. G. Kjaergaard and Dr. K. Mackeprang contributed the experimental results.

PCCP

PAPER

View Article Online
View Journal | View Issue

Cite this: *Phys. Chem. Chem. Phys.*, 2016, **18**, 24654

Spectroscopy and dynamics of double proton transfer in formic acid dimer†

Kasper Mackeprang,[a] Zhen-Hao Xu,[b] Zeina Maroun,[a] Markus Meuwly*[b] and Henrik G. Kjaergaard*[a]

Received 20th May 2016,
Accepted 11th August 2016

DOI: 10.1039/c6cp03462d

www.rsc.org/pccp

We present the isolated gas phase infrared spectra of formic acid dimer, $(HCOOH)_2$, and its deuterated counterpart formic-d acid, $(DCOOH)_2$, at room temperature. The formic acid dimer spectrum was obtained by spectral subtraction of a spectrum of formic acid vapor recorded at low pressure from that recorded at a higher pressure. The spectra of formic acid vapor contain features from both formic acid monomer and formic acid dimer, but at low and high pressures of formic acid, the equilibrium is pushed towards the monomer and dimer, respectively. A similar approach was used for the formic-d acid dimer. Building on the previous development of the Molecular Mechanics with Proton Transfer (MMPT) force field for simulating proton transfer reactions, molecular dynamics (MD) simulations were carried out to interpret the experimental spectra in the OH-stretching region. Within the framework of MMPT, a combination of symmetric single and double minimum potential energy surfaces (PESs) provides a good description of the double proton transfer PES. In a next step, potential morphing together with electronic structure calculations at the B3LYP and MP2 level of theory was used to align the computed and experimentally observed spectral features in the OH-stretching region. From this analysis, a barrier for double proton transfer between 5 and 7 kcal mol^{-1} was derived, which compares with a CCSD(T)/aug-cc-pVTZ calculated barrier of 7.9 kcal mol^{-1}. Such a combination of experimental and computational techniques for estimating barriers for proton transfer in gas phase systems is generic and holds promise for further improved PESs and energetics of these important systems. Additional MD simulations at the semi-empirical DFTB level of theory agree quite well for the center band position but underestimate the width of the OH-stretching band.

1 Introduction

Aerosols play an important role in atmospheric and health sciences, and organic acids have been investigated as possible precursors to the formation of aerosols.[1–5] The simplest organic acid, formic acid, is among the most abundant trace gases in the atmosphere, with a concentration on the order of 10 parts per billion by volume detected in urban areas and slightly lower concentrations in rural areas.[6–11] Formic acid also serves as a useful model system for larger carboxylic acids, especially in theoretical studies, in which calculations on larger organic acids quickly become unfeasible. For this reason, numerous studies on formic acid exist in the literature.[12–18] In the gas phase, organic acids primarily exist in their dimeric form. These dimers are characterized by a cyclic form and are held together by two hydrogen bonds (see Fig. 1). The ability of the organic acids to form these strong dimers influences their atmospheric impact significantly, as it changes the amount of organic acid available to form precursor complexes with *e.g.* water.

Infrared spectroscopy is a powerful tool to detect, investigate and characterize hydrogen bonded systems, XH···Y, where the donor atom X is more electronegative than H, and Y is the acceptor atom or group of atoms.[19–37] The gas-phase infrared spectra of formic acid monomer and dimer have been studied extensively.[16,38–49] Upon hydrogen bond formation a redshift, intensity enhancement, and line broadening of the XH-stretching transition usually occur.[19,20] These hydrogen bond characteristics are often used to detect and identify hydrogen bonded systems. However, for formic acid these characteristics complicate the spectrum and its interpretation, as the OH-stretching transition

---

[a] *Department of Chemistry, University of Copenhagen, Universitetsparken 5, DK-2100 Copenhagen Ø, Denmark. E-mail: hgk@chem.ku.dk; Fax: +45 35320322; Tel: +45 35320334*

[b] *Department of Chemistry, University of Basel, Klingelbergstrasse 80, 4056 Basel, Switzerland. E-mail: m.meuwly@unibas.ch; Fax: +41 (0)612673855; Tel: +41 (0)612673821*

† Electronic supplementary information (ESI) available: Details of the spectral subtraction, parameters for the MMPT force field, point charges used to calculated the dipole moment. Figures of the simulated spectra of FAD and d-FAD with the modified MMPT force fields, a comparison of the potential energy surfaces obtained with the SDM model, SSM model, mixed surface model and at the B3LYP/6-31G(d,p) level of theory, correlation between the MMPT, MP2 and B3LYP energies, and power spectra in the CD-stretching region. See DOI: 10.1039/c6cp03462d

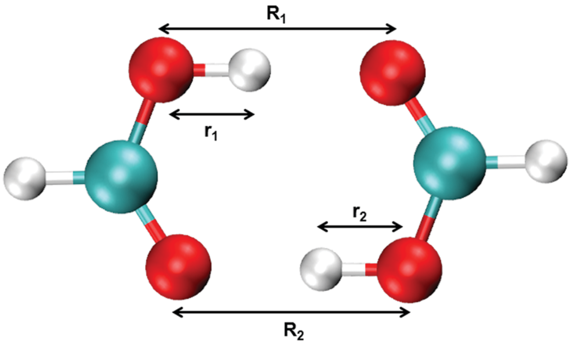

Fig. 1 Structure of formic acid dimer (FAD) with the definition of bond lengths.

shifts and broadens, such that it overlaps with bands in the CH-stretching region. Additionally, the monomer and dimer equilibrium is shifted towards the strongly bound dimer with an equilibrium constant for formic acid dimerization, *K*, of ~300 at room temperature (values in the range 135–405 have been reported in the literature).[13–16,39,50–55] As such, features from both the monomer and the dimer will be present at all sample pressures in the gas phase infrared (IR) spectrum, which further complicates band interpretation in the CH- and OH-stretching region.

Previously, the line shape and broadening of the fundamental OH-stretching band in formic acid dimer were simulated using first-principles anharmonic couplings.[45] In that study, a cubic force field was calculated along the internal coordinates of the dimer and projected onto a normal mode basis. Mixed vibrational states were generated and the line shape and broadening in the OH-stretching region were predicted, assuming Gaussian line shapes for the calculated vibrational transitions. The experimental broadening and line shape in the OH-stretching region was reproduced reasonably well. The line shape of vibrational transitions depends on several elements such as the transition dipole moment, but it is also related to the dynamics of the system, especially the proton transfer (PT) of formic acid dimer.[43] Previously, the line shape of the HCl-stretching transition in the HCl–acetonitrile complex and the OH-stretching transition in the deuterated and undeuterated single proton embedded oxalate anion have been modelled using a combination of ensemble averaging and normal mode harmonic oscillator calculations.[56,57] In the former, the ensemble averaging is based on an MD simulation, and in the latter, the averaging is based on a Monte Carlo simulation. MD is often used to study dynamic systems and has been used to determine that the two PT motifs in formic acid dimer are coupled.[58–60] With the advantages of low computing costs, the force field methods have been extensively developed to perform proton transfer reactions in simulations. An early example is the empirical valence bond (EVB) method[61] which treats a reactive system with resonance forms of ionic and covalent states. The multistate(MS)-EVB method is an extension of EVB which allows simulations with multiple excess protons.[62–65] More recently, proton transfer reactions have been studied using ReaxFF[66] and Hydrogen Dynamics,[67] a method in which a proton moves by morphing between a hydronium ion and a water molecule.

The MMPT force field is more akin to a mixed quantum mechanics/molecular mechanics (QM/MM) formulation. It has been shown to provide QM qualities at much reduced computational cost.[68–71] Recently, MMPT has been used to study the molecular dynamics and infrared spectrum of the enol form of acetylacetone (AcAc).[72] The spectral features of AcAc were satisfactorily reproduced and the MD simulations were compared with the measured OH-stretching region to estimate the proton transfer barrier height to be 2.4 kcal mol^{-1}. Furthermore, double proton transfer (DPT) was investigated in a Pt-containing organometallic complex by independent treatment of NH···N and OH···O as PT motifs, but not including the coupling between the individual PT motifs.[73]

In the present study, we have successfully obtained the isolated infrared spectrum of formic acid dimer (FAD) and the dimer of the deuterated species, DCOOH (d-FAD), in the fundamental OH- and CH-stretching region by spectral subtraction of a low pressure infrared spectrum of formic acid vapor from a spectrum recorded at a higher pressure. These spectra have been compared with those obtained from MD simulations using a modified MMPT force field generalized to DPT and on-the-fly MD simulations, where the potential energy surface (PES) is calculated using the semi-empirical DFTB method.[74–78] From the comparison of the experimental and simulated spectra, the barrier height for DPT is estimated.

2 Methods

2.1 Experimental

Formic acid (HCOOH, Aldrich, 98%) and formic-d acid (DCOOH, Aldrich, 98% D, 95% in H_2O) were purified with several freeze, pump and thaw cycles. The IR spectra were recorded with a VERTEX 70 (Bruker) Fourier transform infrared (FTIR) spectrometer with a 1 cm^{-1} resolution and 500 scans at room temperature (296 ± 1 K). The spectrometer was fitted with a mid-infrared (MIR) light source, KBr beamsplitter and a liquid nitrogen cooled MCT (Mercury Cadmium Telluride) detector. The spectra of formic acid and formic-d acid were recorded with a 10 cm and 19 cm cell, respectively. The samples were introduced in to the cell through a glass vacuum line (J. Young) equipped with valves to control the sample pressure, which was measured with a Varian PCG-750 pressure gauge. The sample was left to equilibrate until the pressure was stable before the spectrum was recorded. The spectral subtractions were performed with OPUS 6.5.

Spectral subtraction. The infrared spectra of FAD and d-FAD were measured in the region from 600 to 4200 cm^{-1}. The equilibrium constant for formic acid dimer formation is large (~300),[13–16,39,50–55,79] and is expected to be of the same order of magnitude for formic-d acid. This is confirmed by calculation of equilibrium constants of complex formation for FA and d-FA at the wB97X-D/aug-cc-pVTZ level of theory using Gaussian09,[80] as the calculated equilibrium constants for FA and d-FA differ by only ~5%. As a consequence, spectroscopic signatures from the dimer are observed even at low sample pressures. The formic acid monomer transitions have a clear rotational structure, and these sharp rotational lines, in combination with a vapor pressure of formic acid that is not sufficiently large to push the equilibrium entirely towards the dimer, mean that features from the monomer are observed even at the highest sample pressures. Consequently, it is difficult to obtain an isolated spectrum of FAD and d-FAD at room temperature, and it has to our knowledge not been reported previously. Careful considerations were necessary in the spectral subtraction in order to obtain the spectrum of the dimer. The spectral subtraction was performed using two spectra, one recorded at high pressure, where the equilibrium is pushed towards the dimer, and the other recorded at a lower pressure, where the equilibrium is pushed towards the monomer. To obtain the spectrum of the dimer, the low-pressure spectrum was scaled and subtracted from the high-pressure spectrum. The low-pressure spectrum was scaled appropriately so that a flat baseline was obtained in the OH-stretching region of the monomer and the rotational lines from the monomer transitions disappear, which indicates that we have obtained the isolated spectrum of pure dimer (see the ESI,† pages S2, S3 and Fig. S1 for details).

2.2 Molecular dynamics simulations

MMPT for double proton transfers. Molecular Mechanics with Proton Transfer is a parametrized method to simulate bond breaking and formation between a hydrogen atom (or a proton) and its donor (X) and acceptor (Y), respectively.[68–71] The total interaction energy for the system with coordinates $\mathbf{Q}$ is:

$$V(\mathbf{Q}) = V_{\mathrm{MM}}(\mathbf{q}) + V_{\mathrm{PT}}(R, r, \theta), \tag{1}$$

where the proton transfer motif XH–Y is described by $V_{\mathrm{PT}}(R, r, \theta)$. This contribution is determined from quantum chemical calculations. Here, the coordinates are R (the distance between the X and Y atoms), r (the distance between the X and H atoms), and θ (the angle between the unit vectors along R and r, see Fig. 1). The dependence of the total potential energy on the remaining degrees of freedom (DOF) of the system ($\mathbf{q}$) is given by a conventional force field V_{MM}. The implementation adds, modifies, and removes force-field terms that include bonded and non-bonded interactions, in a smooth and energy conserving fashion by using switching functions whenever the migrating H transfers from donor to acceptor.[69]

MMPT treats the proton transfer process in its full dimensionality while addressing three important aspects of the problem: speed, accuracy, and versatility. While speed and accuracy are rooted in the QM/MM formulation, the versatility of the approach is exploited by using the morphing potential method.[81] To this end, it is important to realize that a wide range of proton transfer processes can be described based on three prototype model systems: (a) symmetric single minimum (SSM, the optimized structure of the system has equal sharing of the proton between X and Y), (b) symmetric double-minimum (SDM, the optimized structure of the system has unequal sharing of the proton between X and Y but is symmetric with respect to the transition state), and (c) asymmetric single minimum (ASM, the optimized structure of the system has unequal sharing of the proton and is asymmetric with respect to the transition state).[69] The PES of these three model systems (SSM, SDM, or ASM), can be morphed into a suitable PES to reproduce important topological features of the target PES by a transformation of the type

$$V_{\mathrm{morph}}(R', r', \theta') = \lambda(R, r, \theta)V_{\mathrm{orig}}(R, r, \theta), \tag{2}$$

where λ can either be a constant or a more complicated function of one or more coordinates.[81] In the present work, λ was a scalar throughout. The morphing approach not only avoids recomputing a full PES for the PT motif but also reduces the rather laborious task of fitting an entirely new parametrized PES.

Standard MMPT, as described above, treats proton transfers independently and is not necessarily suitable to describe double proton transfer (DPT).[73] Therefore, a modified MMPT approach is required. Such an extension is afforded by working with a DPT potential, V_{DPT}, which explicitly couples both X–Y distances (R_1, R_2) and both donor-hydrogen distances (r_1, r_2) (see Fig. 1) in the following fashion:

$$\begin{aligned} V_{\mathrm{DPT}}(r_1, r_2, R_1, R_2, \theta_1, \theta_2) &= [V_{\mathrm{SDM}}(r_1, R_1, \theta_1)\cdot\gamma + V_{\mathrm{SSM}}(r_1, R_1, \theta_1)\cdot(1-\gamma)] \\ &\quad + [V_{\mathrm{SDM}}(r_2, R_2, \theta_2)\cdot\gamma + V_{\mathrm{SSM}}(r_2, R_2, \theta_2)\cdot(1-\gamma)] \end{aligned} \tag{3}$$

where

$$\begin{aligned} \gamma(r_1, r_2, R_1, R_2) &= \frac{1}{2}\Big\{1 + \tanh\left[\sigma\cdot\left(r_1\cdot R_1 - R_1{}^2/2\right)\right] \\ &\quad \cdot\tanh\left[\sigma\cdot\left(r_2\cdot R_2 - R_2{}^2/2\right)\right]\Big\} \end{aligned} \tag{4}$$

The explicit coupling between the DOFs is in the mixing coefficient, $\gamma(r_1, r_2, R_1, R_2) \in (0, 1)$, acting on V_{SDM} and V_{SSM}. For double proton transfer in FAD, the PES is centrally-symmetric as predicted by the modified MMPT formulation and its QM reference (see Fig. S2, ESI†). Using standard MMPT with two independent V_{SDM} potentials for each of the PT motifs yields an unrealistic PES with four global minima. Mixing V_{SDM} and V_{SSM} as in the V_{DPT} potential leads to two isoenergetic minima while eliminating the two other minima, see Fig. S2C (ESI†). The details of the mixing are determined by γ which depends on one free parameter σ that can be tuned to reproduce particular reference data.

Force field parametrization. Fitting of V_{DPT} was carried out with respect to reference calculations at the B3LYP/6-31G(d,p)[82,83] and MP2/6-311++G(2d,2p)[84–87] levels of theory. The minimum energy conformation of FAD and the transition state for DPT have been obtained for the two methods and are summarized in Table 1. The corresponding CCSD(T)/aug-cc-pVTZ values have been included for comparison. At the MP2 level, the minimum energy conformation of FAD has an O–H bond length of 0.9924 Å, slightly longer than that of the formic acid monomer (FAM) of 0.9675 Å due to the hydrogen bonds, and the O–O distance is 2.6868 Å. B3LYP gives a slightly longer O–H bond length and a shorter O–O distance. The CCSD(T) results generally lie in between those of B3LYP and MP2, but closer to the MP2 results.

Table 1 Selected internal coordinates (in Å) of the energy minimum (MIN) and transition state (TS) structure of FAD and its monomer (MON), calculated at the B3LYP/6-31G(d,p) and MP2/6-311++G(2d,2p) level of theory and from their parametrized MMPT force fields. Additionally, the CCSD(T)/aug-cc-pVTZ calculated internal coordinates are presented for comparison

	B3LYP			MMPT-B3LYP	
	MON	MIN	TS	MIN	TS
O–H	0.9738	1.0075	1.2093	1.0035	1.2089
O–O		2.6509	2.4183	2.6574	2.4178
	MP2			MMPT-MP2	
	MON	MIN	TS	MIN	TS
O–H	0.9675	0.9924	1.2042	0.9871	1.2031
O–O		2.6853	2.4074	2.6868	2.4062
	CCSD(T)				
	MON	MIN	TS		
O–H	0.9701	0.9957	1.2040		
O–O		2.6741	2.4070		

The transition state for DPT in FAD suggests a symmetric conformation with the transferring hydrogens between the two oxygens. Additionally, for the calculated minimum energy conformations of FAD at all the levels of theory, the OH–O PT motif is almost but not exactly collinear.

Starting from the minimized structures, PES scans along $R = R_1 = R_2$, ranging from 2.2 Å to 3.2 Å with an increment of 0.1 Å and $r = r_1 = r_2$ from 0.8 Å to $R - 0.8$ Å with an increment of 0.05 Å were carried out for both methods in order to parametrize V_{SDM}. For parametrizing V_{SSM} similar PES scans were carried out for $r_1 = R - r_2$. Next, the parameter σ in eqn (4) has been fitted to best reproduce the target data at the B3LYP level, which yields $\sigma = 2.639$ Å^{-2}. The quality of this fit is $r^2 = 0.999$ for B3LYP as the target energies, and $r^2 = 0.998$ for MP2. Given this good agreement, no further optimization of σ was considered for the MP2 reference data. The two PESs are labelled as MMPT-B3LYP and MMPT-MP2 in the following, respectively (see Fig. S3, ESI†).

The fitted MMPT-MP2 PES has an optimized O–H bond length of 0.9871 Å which differs by ~0.005 Å from the MP2 reference calculations, and the O–O distance differs even less. On the other hand, B3LYP gives a slightly longer O–H bond length and a shorter O–O distance. For the TS structures, both MMPT-MP2 and MMPT-B3LYP yield results close to their respective QM references. Moreover, the reaction barriers were well reproduced to within <0.1 kcal mol^{-1}, which further establishes the quality of the parametrized PESs.

Simulation details. All *NVE* MD simulations were performed with CHARMM[88–90] in the gas phase at 300 K, following heating and equilibration (1 ps for each trajectory with $\Delta t = 0.1$ fs). Since DPT involves an appreciable barrier (7.9 kcal mol^{-1} at the CCSD(T) level), 100 ns production runs have been carried out. For direct comparison, on-the-fly molecular dynamics at the semi-empirical DFTB[77,91,92] level (MD-DFTB) have been carried out for 10 ns with the same simulation conditions as for the force field simulations described above.

Infrared spectra. The infrared spectrum is computed from the total dipole moment, $\vec{M}(t)$, obtained from each step in the MD trajectory. The dipole–dipole correlation, $C(t)$, is given by

$$C(t) = \langle \vec{M}(0)\vec{M}(t) \rangle, \tag{5}$$

where $\vec{M}(t)$ is the total molecular dipole moment at time t along the MD trajectory determined from the charge model given in Table S3 (ESI†). The angular brackets denote an average over the time origins. If $C(\omega)$, the Fourier transform of $C(t)$, is weighted with the Boltzmann distribution, the classical infrared spectrum, $A(\omega)$, is obtained:[93,94]

$$A(\omega) = \omega\{1 - \exp[-\hbar\omega/(k_{\mathrm{B}}T)]\}C(\omega) \tag{6}$$

where ω is the transition frequency, k_{B} is the Boltzmann constant and T is the temperature. Such an approach does not satisfy detailed balance $I(\omega) = \exp(\hbar\omega/k_{\mathrm{B}}T)I(-\omega)$ because it is derived from a classical correlation function for which $I_{\mathrm{cl}}(\omega) = I_{\mathrm{cl}}(-\omega)$.[95] To remedy this, various quantum correction factors (qcf) have been proposed.[95,96] On the other hand, it has been found that different qcf yield results of different quality for formaldehyde.[97] Hence it is not *a priori* clear which of the qcf to choose for a particular problem. Furthermore, in the classical limit $\lim_{T\to\infty} \exp(\hbar\omega/k_{\mathrm{B}}T) = 1$. Therefore, the spectra reported here are all determined from eqn (6). It is also possible to determine power spectra corresponding to specific internal coordinates, q, from the MD trajectory. This is particularly useful to assign spectroscopic features to the motion along these coordinates and identify couplings between internal degrees of freedom. For this purpose, the correlation function $\langle q(0)q(t)\rangle$ is Fourier transformed and weighted with the Boltzmann distribution to yield the power spectrum.

3 Results and discussion

We have obtained isolated gas phase spectra of the pure FAD and pure d-FAD at room temperature as described in the Experimental section, and show these in Fig. 2. The spectral signatures for the two systems are very similar, especially the structure of the band associated with the OH-stretching transition. As expected upon deuteration, the fundamental CH/CD-stretching transition is shifted from 2939 cm^{-1} in the FAD spectrum to 2210 cm^{-1} in the spectrum of d-FAD. The OH-stretching transition in both spectra is very broad and the transition assigned to the OH-stretch is observed in the region from 2600–3400 cm^{-1} in agreement with previously recorded spectra that contain a mixture of formic acid monomer and dimer.[40,48] Broad OH-stretching transitions are very common in hydrogen bonded complexes[72,98,99] and have also been observed for overtone transitions of the intramolecular hydrogen bond in pyruvic acid.[100] It is the spectral features in the OH-stretching region that are of particular interest here as these features are ideally suited to relate experiment, proton transfer energetics and dynamics, and computed IR spectra. Typically, such spectral features are not readily explained by standard static vibrational

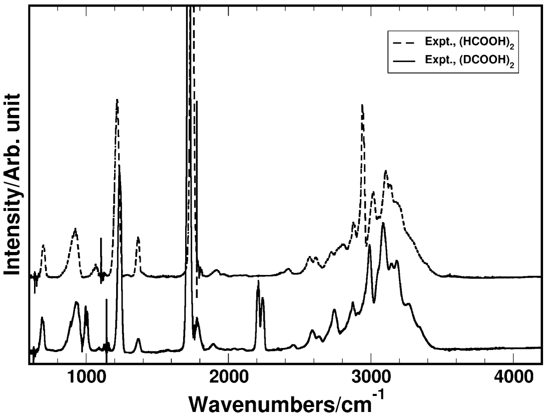

Fig. 2 Experimentally recorded IR spectra of FAD (upper dashed trace) and d-FAD (lower solid trace).

models such as the harmonic oscillator normal mode model, anharmonic local mode theory, or second-order vibrational perturbation theory (VPT2).[101–103]

The MD simulated IR-spectra of FAD with the different PESs are compared in Fig. 3. In the region near 3000 cm^{-1}, spectral features arise from a very broad OH-stretching band and a sharp CH-stretching peak near 2900 cm^{-1}. The OH- and CH-stretching power spectra are compared with the measured IR-spectrum in Fig. 3. The position of the CH-stretching peak predicted by the MD simulated spectra compares well with that of the experimental spectrum. However, the broad OH-stretching band is blue shifted compared to that of the experiment in all three simulations in Fig. 3. Recently, it was shown that the center frequency of the broad OH-stretching band in acetylacetone was affected significantly by the height of the proton transfer barrier.[72] This is not surprising, as a change in the barrier height inevitably affects the shape of the PES in the region near the two global minima. In order to investigate the correlation between the OH-stretching peak position and the DPT reaction barrier, the height of the reaction barrier was changed in the MMPT-MP2 force field by morphing with the parameter λ (see the Methods section). The MMPT-MP2 force field has a DPT barrier height of 8.2 kcal mol^{-1} and features from the OH-stretching transition were observed centered around 3300 cm^{-1}. If the barrier height is lowered to, for example, 5.2 or 2.2 kcal mol^{-1} the center of the OH-stretching transition red shifts significantly to $\sim$2700 or $\sim$1700 cm^{-1}, respectively, compared to the original spectrum (see Fig. 4). All remaining transitions are more or less unaffected.

The unmorphed barrier height of the MMPT-B3LYP force field is 5.4 kcal mol^{-1}, which is similar to the morphed MMPT-MP2 barrier height (5.2 kcal mol^{-1}). However, the centers of the OH-stretching bands in the two infrared spectra differ substantially (see Fig. 3 and 4), despite the fact that the barrier heights only differ by 0.2 kcal mol^{-1}. Hence, factors other than the barrier height alone, such as the local curvature of the PES, influence the position of the OH-stretching band position. We found that if the proton transfer reaction barriers are morphed to 5.1 kcal mol^{-1} and 7.2 kcal mol^{-1} for the MMPT-B3LYP and MMPT-MP2 force field, respectively, the position of the simulated OH-stretching band fits well with the experimental OH-stretching band position.

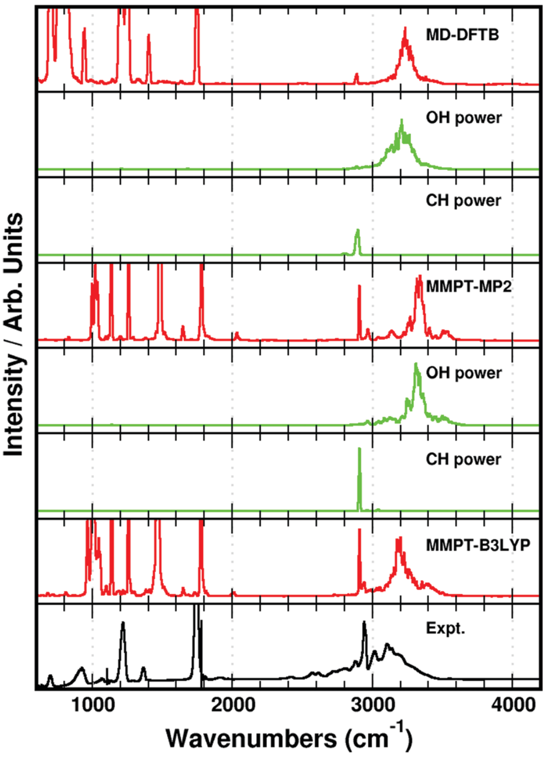

Fig. 3 Spectra obtained from MD simulations with different energy functions. From top to bottom: MD-DFTB (DPT barrier of 7.5 kcal mol^{-1}) and its OH and CH power spectra (green); MMPT-MP2 (DPT barrier of 8.2 kcal mol^{-1}) and the OH and CH power spectra (green), and MMPT-B3LYP (DPT barrier of 5.4 kcal mol^{-1}). The experimentally recorded spectrum of FAD has been included for comparison (bottom).

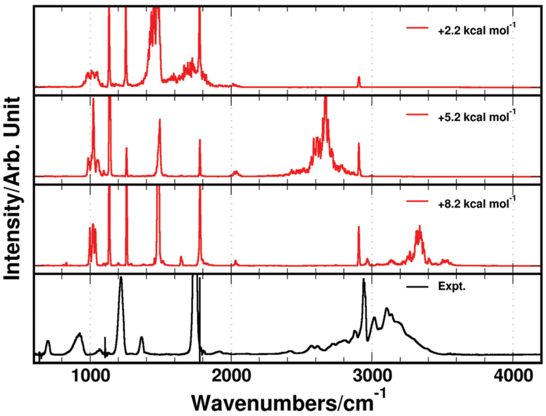

Fig. 4 MD simulated spectra with the MMPT-MP2 force field of FAD, with morphed barrier heights of 2.2 kcal mol^{-1} (top), 5.2 kcal mol^{-1} (middle) and 8.2 kcal mol^{-1} (unscaled, bottom). The experimental spectrum has been included for comparison.

In other words, the barrier to proton transfer can at best be determined to within ±1 kcal mol^{-1}. In comparison, the CCSD(T)/aug-cc-pVTZ calculated barrier is 7.9 kcal mol^{-1} using MOLPRO,[104] which is close to the barrier of 7.2 kcal mol^{-1} found with the morphed MMPT-MP2 force field, but is higher than the barrier obtained with the MMPT-B3LYP force field.

Up to this point the parameters in the conventional force field (see $V_{\mathrm{MM}}(\mathbf{q})$ in eqn (1)) were those of the C36 force field[105] and the only modifications of the MMPT-force field concerned the height of the barrier for DPT. Considering Fig. 3 and 4 slight adjustments in the force field may improve in particular the position of the CH-stretching band. Hence, in order to improve the simulated spectra the harmonic force constant for the CH/CD-stretch was rescaled from 330 to 340 kcal mol^{-1} Å^{-2}. Furthermore, *ab initio* calculations at the B3LYP/6-31G(d,p) level along the bending potential of the transferring hydrogen (HOO-bend) in FAD suggest that the bending force constant from the SSM and SDM model potentials (k = 33 kcal mol^{-1} rad^{-2}, see eqn (S3) in ESI†) should be decreased to k = 17.5 kcal mol^{-1} rad^{-2} to match the reference calculations. With these adjustments the IR spectra for FAD and d-FAD were recomputed and are reported in Fig. 5. For the simulated spectra with the modified DPT barriers and force constants the agreement in the fundamental OH-stretching region compared to that of the experimental spectrum has improved (see Fig. 5). For the B3LYP-MMPT force field, the CH-stretching frequency for FAD shifts from 2910 to 2950 cm^{-1} as the arrow around 2900 cm^{-1} in the left hand panel of Fig. 5 indicates. Also, the H-transfer band shifts its maximum from 3200 cm^{-1} to 3100 cm^{-1} upon morphing the barrier height from 5.4 to 5.1 kcal mol^{-1}. The signal at ~2700 cm^{-1} for d-FAD with k = 33 kcal mol^{-1} rad^{-2} shifts to 2900 cm^{-1} for k = 17.5 kcal mol^{-1} rad^{-2} and can be associated with the unbound H–O stretch frequency from analysis of the power spectra, however, the mode is heavily mixed. The width and position of the OH- and CH-stretching band depend only little on the bending force constant, k, (see dashed and solid lines in Fig. 5) and are satisfactorily reproduced compared to previous line shape studies on formic and acetic acid dimer.[45,106] Depending on the force constant k, the fundamental COH-bend is located at ~1400 cm^{-1} and ~1500 cm^{-1} for k = 17.5 and k = 33 kcal mol^{-1} rad^{-2} for FAD, respectively. Experimentally this transition is observed at 1220 cm^{-1}.

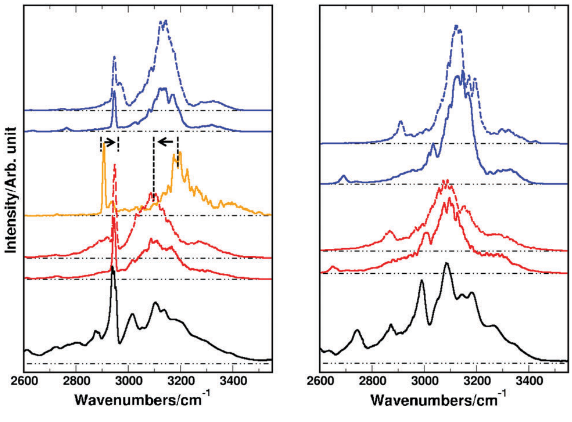

Fig. 5 Comparison of experimental spectra (black traces) with simulated spectra (average over 10 independent MD simulations of 100 ns each) for FAD (left panel) and d-FAD (right panel). Red and blue traces for the MMPT-B3LYP and MMPT-MP2 parametrizations, respectively, with morphed barriers of 5.1 kcal mol^{-1} and 7.2 kcal mol^{-1} and the CH-stretching force constant adjusted to reproduce the experimentally observed value. Solid traces for simulations with k = 33 kcal mol^{-1} rad^{-2} and dashed traces for k = 17.5 kcal mol^{-1} rad^{-2} (see text). The orange line in the left panel is for the unmorphed DPT barrier height (MMPT-B3LYP) and the original CH force constant (330 kcal mol^{-1} Å^{-2}) with the arrows indicating in which direction the bands shift upon changing the force field.

It is also of interest to comment on the clearly discernible and almost equally-spaced progressions (~125 cm^{-1}) in the experimental spectra. Most of the sub-structure in the OH-stretching region have previously been attributed the coupling between the OH-stretch and the symmetric and anti-symmetric COH-bend.[45] Giese *et al.* observed a similar progression in the OH-stretching region of the simulated stick spectrum of malonaldehyde.[107] They found that the progression was a result of strong mixing of the intramolecular hydrogen bound OH-stretching vibration with the in-plane OH-bending vibration. As such, we conclude that the progressions in the OH-stretching spectra of FAD and d-FAD is due to the coupling between the OH-stretching vibration and vibrations that partially break the hydrogen bond such as the COH-bending and in-plane OH-bending vibration.

During 250 ns of MD simulations with the MMPT-B3LYP (with the morphed barrier height of 5.1 kcal mol^{-1}) 25 proton transfers were observed, *i.e.* corresponding to a DPT rate of 0.1 ns^{-1}. Test calculations show that irrespective of the number of DPT events the IR spectra are all very similar. For this, IR spectra were determined over several separate 50 ns intervals and compared. In the 250 ns simulations with the MMPT-MP2 PES (with the unmorphed barrier of 8.2 kcal mol^{-1}) and in the 10 ns MD-DFTB simulation no DPT was observed. Previously, PT has been explicitly been linked to the spectra features of the OH-stretching band,[43] but we find here that the actual occurrence of DPT is not necessarily required for observing a broad OH-absorption in the IR spectrum.

One increasingly important aspect of current force field development is the issue of transferability, *i.e.* the question how easily a given parametrization can be adapted to a chemically related situation. For halogenated molecules this has recently been assessed and it was found that scaling van der Waals parameters can lead to largely transferable parametrizations.[108] For single- and double proton transfer the overall shape (symmetric single minimum, symmetric double minimum, asymmetric double minimum) of the potential energy surface is usually known *a priori*. Hence, starting from a correct topology, morphing transformations between the correct topology and the target PES, characterized by the barrier height and the relative stabilizations of the two minima (for asymmetric double minimum), morphing transformations will be an efficient means to develop appropriate force fields for a new system. As an example, for derivatives RCOOH–HOOCR of FAD (*e.g.* acetic acid dimer) it is reasonable to assume that the general topology of the PES is related to that of FAD.

Depending on the chemical identity of the R-group (*e.g.* CH_3, halogen) the height of the DPT barrier will change, though. This can be accounted for by suitable linear or nonlinear morphing transformations. Hence, with a limited number of electronic structure calculations the necessary information about the target PES can be obtained and the morphing parameters which describe DPT in RCOOH–HOOCR can be determined.

4 Conclusion

The vibrational spectroscopy of FAD has been investigated experimentally and by computer simulations. Spectra at low pressures of formic acid, HCOOH, and formic-d acid, DCOOH, vapor were recorded to push the equilibrium towards the monomer. These spectra were scaled and subtracted from the corresponding spectra recorded at higher pressures of formic acid and formic-d acid vapor, where the equilibrium is pushed towards the dimer. Successful subtractions of the monomer from the high pressure spectra were achieved, and the isolated gas phase spectra of formic acid and formic-d acid dimer (FAD and d-FAD) at room temperature were obtained. A modified version of the MMPT force field was developed and successfully applied to FAD and d-FAD to facilitate interpretation of the isolated dimer spectra in the OH-stretching region. After rescaling the proton transfer barrier of the MMPT force field and changing the CH/CD-stretching and HOO-bending force constants, the computed infrared spectra of FAD and d-FAD favorably agreed with those from experiment in the OH-stretching region. The scaled proton transfer barrier of 7.2 kcal mol^{-1} in the MMPT-MP2 force field was found to be comparable to the barrier height of 7.9 kcal mol^{-1} obtained at the CCSD(T)/aug-cc-pVTZ level of theory. However, the scaled barrier height includes entropic contributions as it involves dynamics on the full-dimensional PES from which the spectroscopy was determined. The $T = 0$ K calculation at the higher CCSD(T)/aug-cc-PVTZ level of theory does not include such entropic contributions. It is reassuring that the $T = 0$ K value is an upper bound to the barrier height from finite-temperature MD simulations, as it should be. The scaled barrier height in the MMPT-B3LYP force field that provided a good fit of the central OH-stretching frequency was lower by 2 kcal mol^{-1} compared to that of the MMPT-MP2 force field which is considered to be the more realistic value. The present work shows that MMPT can be extended to treat DPT in a meaningful fashion which is also applicable to larger carboxylic acids where more computationally demanding on-the-fly MD simulations are not feasible.

Acknowledgements

We thank the Danish Council for Independent Research—Natural Sciences, the Danish Center for Scientific Computing (DCSC), and the Department of Chemistry at the University of Copenhagen for funding. KM is grateful to the Ministry of Higher Education and Science for the "EliteForsk" travel scholarship. The work in Basel is supported by the Swiss National Science Foundation (Grant 200020-132406 and the NCCR MUST) and the University of Basel.

References

1 G. Myhre, D. Shindell, F.-W. Bréon, W. Collins, J. Fuglestvedt, J. Huang, D. Koch, J.-F. Lamarque, D. Lee, B. Mendoza, T. Nakajima, A. Robock, G. Stephens, T. Takamura and H. Zhang, *Climate Change 2013: The Physical Science Basis. Contribution of Working Group I to the Fifth Assessment Report of Intergovernmental Panel on Climate Change*, 2013.

2 A. Chebbi and P. Carlier, *Atmos. Environ.*, 1996, **30**, 4233–4249.

3 S. Yu, *Atmos. Res.*, 2000, **53**, 185–217.

4 M. Kanakidou, J. H. Seinfeld, S. N. Pandis, I. Barnes, F. J. Dentener, M. C. Facchini, R. Van Dingenen, B. Ervens, A. Nenes, C. J. Nielsen, E. Swietlicki, J. P. Putaud, Y. Balkanski, S. Fuzzi, J. Horth, G. K. Moortgat, R. Winterhalter, C. E. L. Myhre, K. Tsigaridis, E. Vignati, E. G. Stephanou and J. Wilson, *Atmos. Chem. Phys.*, 2005, **5**, 1053–1123.

5 M. Hallquist, J. C. Wenger, U. Baltensperger, Y. Rudich, D. Simpson, M. Claeys, J. Dommen, N. M. Donahue, C. George, A. H. Goldstein, J. F. Hamilton, H. Herrmann, T. Hoffmann, Y. Iinuma, M. Jang, M. E. Jenkin, J. L. Jimenez, A. Kiendler-Scharr, W. Maenhaut, G. McFiggans, T. F. Mentel, A. Monod, A. S. H. Prévôt, J. H. Seinfeld, J. D. Surratt, R. Szmigielski and J. Wildt, *Atmos. Chem. Phys.*, 2009, **9**, 5155–5236.

6 G. A. Dawson, J. C. Farmer and J. L. Moyers, *Geophys. Res. Lett.*, 1980, **7**, 725–728.

7 J. C. Farmer and G. A. Dawson, *J. Geophys. Res.: Oceans*, 1982, **87**, 8931–8942.

8 P. L. Hanst, N. W. Wong and J. Bragin, *Atmos. Environ.*, 1982, **16**, 969–981.

9 R. W. Talbot, K. M. Beecher, R. C. Harriss and W. R. Cofer, *J. Geophys. Res.: Atmos.*, 1988, **93**, 1638–1652.

10 M. O. Andreae, R. W. Talbot, T. W. Andreae and R. C. Harriss, *J. Geophys. Res.: Atmos.*, 1988, **93**, 1616–1624.

11 J. E. Lawrence and P. Koutrakis, *Environ. Sci. Technol.*, 1994, **28**, 957–964.

12 L. George and W. Sander, *Spectrochim. Acta, Part A*, 2004, **60**, 3225–3232.

13 M. D. Taylor and J. Bruton, *J. Am. Chem. Soc.*, 1952, **74**, 4151–4152.

14 J. R. Barton and C. C. Hsu, *J. Chem. Eng. Data*, 1969, **14**, 184–187.

15 R. Büttner and G. Maurer, *Ber. Bunsenges. Phys. Chem.*, 1983, **87**, 877–882.

16 J. Vander Auwera, K. Didriche, A. Perrin and F. Keller, *J. Chem. Phys.*, 2007, **126**, 124311.

17 J. E. Bertie and K. H. Michaelian, *J. Chem. Phys.*, 1982, **76**, 886–894.

18 J. E. Bertie, K. H. Michaelian, H. H. Eysel and D. Hager, *J. Chem. Phys.*, 1986, **85**, 4779–4789.

19 E. Arunan, G. R. Desiraju, R. A. Klein, J. Sadlej, S. Scheiner, I. Alkorta, D. C. Clary, R. H. Crabtree, J. J. Dannenberg,

P. Hobza, H. G. Kjaergaard, A. C. Legon, B. Mennucci and D. J. Nesbitt, *Pure Appl. Chem.*, 2011, **83**, 1619–1636.

20 E. Arunan, G. R. Desiraju, R. A. Klein, J. Sadlej, S. Scheiner, I. Alkorta, D. C. Clary, R. H. Crabtree, J. J. Dannenberg, P. Hobza, H. G. Kjaergaard, A. C. Legon, B. Mennucci and D. J. Nesbitt, *Pure Appl. Chem.*, 2011, **83**, 1637–1641.

21 S. Chung and M. Hippler, *J. Chem. Phys.*, 2006, **124**, 214316.

22 M. Hippler, *J. Chem. Phys.*, 2007, **127**, 084306.

23 M. Hippler, S. Hesse and M. A. Suhm, *Phys. Chem. Chem. Phys.*, 2010, **12**, 13555–13565.

24 B. Michielsen, J. J. J. Dom, B. J. v. d. Veken, S. Hesse, Z. Xue, M. A. Suhm and W. A. Herrebout, *Phys. Chem. Chem. Phys.*, 2010, **12**, 14034–14044.

25 L. Du and H. G. Kjaergaard, *J. Phys. Chem. A*, 2011, **115**, 12097–12104.

26 J. J. J. Dom, B. J. van der Veken, B. Michielsen, S. Jacobs, Z. Xue, S. Hesse, H.-M. Loritz, M. A. Suhm and W. A. Herrebout, *Phys. Chem. Chem. Phys.*, 2011, **13**, 14142–14152.

27 L. Du, J. R. Lane and H. G. Kjaergaard, *J. Chem. Phys.*, 2012, **136**, 184305.

28 B. Michielsen, C. Verlackt, B. van der Veken and W. Herrebout, *J. Mol. Struct.*, 2012, **1023**, 90–95.

29 L. Du, K. Mackeprang and H. G. Kjaergaard, *Phys. Chem. Chem. Phys.*, 2013, **15**, 10194–10206.

30 N. Bork, L. Du and H. G. Kjaergaard, *J. Phys. Chem. A*, 2014, **118**, 1384–1389.

31 N. Bork, L. Du, H. Reiman, T. Kurtèn and H. G. Kjaergaard, *J. Phys. Chem. A*, 2014, **118**, 5316–5322.

32 A. S. Hansen, L. Du and H. G. Kjaergaard, *Phys. Chem. Chem. Phys.*, 2014, **16**, 22882–22891.

33 A. S. Hansen, L. Du and H. G. Kjaergaard, *J. Phys. Chem. Lett.*, 2014, **5**, 4225–4231.

34 C. L. Andersen, C. S. Jensen, K. Mackeprang, L. Du, S. Jørgensen and H. G. Kjaergaard, *J. Phys. Chem. A*, 2014, **118**, 11074–11082.

35 K. H. Møller, A. S. Hansen and H. G. Kjaergaard, *J. Phys. Chem. A*, 2015, **119**, 10988–10998.

36 M. Heger, M. A. Suhm and R. A. Mata, *J. Chem. Phys.*, 2014, **141**, 101105.

37 M. Heger, R. A. Mata and M. A. Suhm, *Chem. Sci.*, 2015, **6**, 3738–3745.

38 L. G. Bonner and R. Hofstadter, *J. Chem. Phys.*, 1938, **6**, 531–534.

39 A. Clague and H. Bernstein, *Spectrochim. Acta, Part A*, 1969, **25**, 593–596.

40 P. Excoffon and Y. Maréchal, *Spectrochim. Acta, Part A*, 1972, **28**, 269–283.

41 Y. Maréchal, *J. Chem. Phys.*, 1987, **87**, 6344–6353.

42 D. Hurtmans, F. Herregodts, M. Herman, J. Liévin, A. Campargue, A. Garnache and A. A. Kachanov, *J. Chem. Phys.*, 2000, **113**, 1535–1545.

43 M. V. Vener, O. Kühn and J. M. Bowman, *Chem. Phys. Lett.*, 2001, **349**, 562–570.

44 M. Freytes, D. Hurtmans, S. Kassi, J. Liévin, J. V. Auwera, A. Campargue and M. Herman, *Chem. Phys.*, 2002, **283**, 47–61.

45 G. M. Florio, T. S. Zwier, E. M. Myshakin, K. D. Jordan and E. L. Sibert, *J. Chem. Phys.*, 2003, **118**, 1735–1746.

46 R. Georges, M. Freytes, D. Hurtmans, I. Kleiner, J. V. Auwera and M. Herman, *Chem. Phys.*, 2004, **305**, 187–196.

47 D. L. Howard and H. G. Kjaergaard, *J. Chem. Phys.*, 2004, **121**, 136–140.

48 F. Ito, *J. Chem. Phys.*, 2008, **128**, 114310.

49 A. Perrin, J. V. Auwera and Z. Zelinger, *J. Quant. Spectrosc. Radiat. Transfer*, 2009, **110**, 743–755.

50 H. C. Ramsperger and C. W. Porter, *J. Am. Chem. Soc.*, 1926, **48**, 1267–1273.

51 A. S. Coolidge, *J. Am. Chem. Soc.*, 1928, **50**, 2166–2178.

52 R. C. Herman, *J. Chem. Phys.*, 1940, **8**, 252–258.

53 A. Winkler and P. Hess, *J. Am. Chem. Soc.*, 1994, **116**, 9233–9240.

54 S. Miyamoto, S. Nakamura, Y. Iwai and Y. Arai, *J. Chem. Eng. Data*, 1999, **44**, 48–51.

55 F. Kollipost, R. W. Larsen, A. V. Domanskaya, M. Nörenberg and M. A. Suhm, *J. Chem. Phys.*, 2012, **136**, 151101.

56 N. Bork, V. Loukonen, H. G. Kjaergaard and H. Vehkamaki, *Phys. Chem. Chem. Phys.*, 2014, **16**, 24685–24690.

57 C. T. Wolke, A. F. DeBlase, C. M. Leavitt, A. B. McCoy and M. A. Johnson, *J. Phys. Chem. A*, 2015, **119**, 13018–13024.

58 H. Ushiyama and K. Takatsuka, *J. Chem. Phys.*, 2001, **115**, 5903–5912.

59 P. R. L. Markwick, N. L. Doltsinis and D. Marx, *J. Chem. Phys.*, 2005, **122**, 054112.

60 L. C. T. Pierce, P. R. L. Markwick, J. A. McCammon and N. L. Doltsinis, *J. Chem. Phys.*, 2011, **134**, 174107.

61 A. Warshel and R. M. Weiss, *J. Am. Chem. Soc.*, 1980, **102**, 6218–6226.

62 U. Schmitt and G. Voth, *J. Phys. Chem. B*, 1998, **102**, 5547–5551.

63 T. Day, A. Soudackov, M. Cuma, U. Schmitt and G. Voth, *J. Chem. Phys.*, 2002, **117**, 5839–5849.

64 Y. Wu, H. Chen, F. Wang, F. Paesani and G. A. Voth, *J. Phys. Chem. B*, 2008, **112**, 467–482.

65 J. M. J. Swanson, C. M. Maupin, H. Chen, M. K. Petersen, J. Xu, Y. Wu and G. A. Voth, *J. Phys. Chem. B*, 2007, **111**, 4300–4314.

66 O. Rahaman, A. C. T. van Duin, W. A. Goddard, III and D. J. Doren, *J. Phys. Chem. B*, 2011, **115**, 249–261.

67 M. G. Wolf and G. Groenhof, *J. Comput. Chem.*, 2014, **35**, 657–671.

68 S. Lammers and M. Meuwly, *J. Phys. Chem. A*, 2007, **111**, 1638–1647.

69 S. Lammers, S. Lutz and M. Meuwly, *J. Comput. Chem.*, 2008, **29**, 1048–1063.

70 Y. Yang and M. Meuwly, *J. Chem. Phys.*, 2010, **133**, 064503.

71 S. Lutz, I. Tubert-Brohman, Y. Yang and M. Meuwly, *J. Biol. Chem.*, 2011, **286**, 23679–23687.

72 D. L. Howard, H. G. Kjaergaard, J. Huang and M. Meuwly, *J. Phys. Chem. A*, 2015, **119**, 7980–7990.

73 J. Huang, D. Haeussinger, U. Gellrich, W. Seiche, B. Breit and M. Meuwly, *J. Phys. Chem. B*, 2012, **116**, 14406–14415.

74 M. Elstner, D. Porezag, G. Jungnickel, J. Elsner, M. Haugk, T. Frauenheim, S. Suhai and G. Seifert, *Phys. Rev. B: Condens. Matter Mater. Phys.*, 1998, **58**, 7260–7268.

75 M. Elstner, T. Frauenheim, E. Kaxiras, G. Seifert and S. Suhai, *Phys. Status Solidi B*, 2000, **217**, 357–376.

76 T. Frauenheim, G. Seifert, M. Elstner, T. Niehaus, C. Köhler, M. Amkreutz, M. Sternberg, Z. Hajnal, A. D. Carlo and S. Suhai, *J. Phys.: Condens. Matter*, 2002, **14**, 3015.

77 Q. Cui, M. Elstner, E. Kaxiras, T. Frauenheim and M. Karplus, *J. Phys. Chem. B*, 2001, **105**, 569–585.

78 J. Pu, J. Gao and D. G. Truhlar, *J. Phys. Chem. A*, 2004, **108**, 5454–5463.

79 Z. Maroun, K. Mackeprang and H. G. Kjaergaard, 2016, unpublished work.

80 M. J. Frisch, G. W. Trucks, H. B. Schlegel, G. E. Scuseria, M. A. Robb, J. R. Cheeseman, G. Scalmani, V. Barone, B. Mennucci, G. A. Petersson, H. Nakatsuji, M. Caricato, X. Li, H. P. Hratchian, A. F. Izmaylov, J. Bloino, G. Zheng, J. L. Sonnenberg, M. Hada, M. Ehara, K. Toyota, R. Fukuda, J. Hasegawa, M. Ishida, T. Nakajima, Y. Honda, O. Kitao, H. Nakai, T. Vreven, J. A. Montgomery, Jr., J. E. Peralta, F. Ogliaro, M. Bearpark, J. J. Heyd, E. Brothers, K. N. Kudin, V. N. Staroverov, R. Kobayashi, J. Normand, K. Raghavachari, A. Rendell, J. C. Burant, S. S. Iyengar, J. Tomasi, M. Cossi, N. Rega, J. M. Millam, M. Klene, J. E. Knox, J. B. Cross, V. Bakken, C. Adamo, J. Jaramillo, R. Gomperts, R. E. Stratmann, O. Yazyev, A. J. Austin, R. Cammi, C. Pomelli, J. W. Ochterski, R. L. Martin, K. Morokuma, V. G. Zakrzewski, G. A. Voth, P. Salvador, J. J. Dannenberg, S. Dapprich, A. D. Daniels, O. Farkas, J. B. Foresman, J. V. Ortiz, J. Cioslowski and D. J. Fox, *Gaussian09 Revision D.01*, Gaussian Inc., Wallingford CT, 2009.

81 M. Meuwly and J. M. Hutson, *J. Chem. Phys.*, 1999, **110**, 8338–8347.

82 P. M. Gill, B. G. Johnson, J. A. Pople and M. J. Frisch, *Chem. Phys. Lett.*, 1992, **197**, 499–505.

83 R. Parr and W. Yang, *Density-Functional Theory of Atoms and Molecules*, Oxford University Press, USA, 1989.

84 M. Head-Gordon, J. A. Pople and M. J. Frisch, *Chem. Phys. Lett.*, 1988, **153**, 503–506.

85 M. J. Frisch, M. Head-Gordon and J. A. Pople, *Chem. Phys. Lett.*, 1990, **166**, 281–289.

86 M. J. Frisch, M. Head-Gordon and J. A. Pople, *Chem. Phys. Lett.*, 1990, **166**, 275–280.

87 M. Head-Gordon and T. Head-Gordon, *Chem. Phys. Lett.*, 1994, **220**, 122–128.

88 B. R. Brooks, C. L. Brooks, III, A. D. Mackerell, Jr., L. Nilsson, R. J. Petrella, B. Roux, Y. Won, G. Archontis, C. Bartels, S. Boresch, A. Caflisch, L. Caves, Q. Cui, A. R. Dinner, M. Feig, S. Fischer, J. Gao, M. Hodoscek, W. Im, K. Kuczera, T. Lazaridis, J. Ma, V. Ovchinnikov, E. Paci, R. W. Pastor, C. B. Post, J. Z. Pu, M. Schaefer, B. Tidor, R. M. Venable, H. L. Woodcock, X. Wu, W. Yang, D. M. York and M. Karplus, *J. Comput. Chem.*, 2009, **30**, 1545–1614.

89 B. Brooks, R. Bruccoleri, D. Olafson, D. States, S. Swaminathan and M. Karplus, *J. Comput. Chem.*, 1983, **4**, 187–217.

90 A. MacKerel Jr., C. Brooks III, L. Nilsson, B. Roux, Y. Won and M. Karplus, *CHARMM: The Energy Function and Its Parameterization with an Overview of the Program*, John Wiley & Sons, Chichester, 1998, vol. 1, pp. 271–277.

91 Y. Yang, H. Yu, D. York, Q. Cui and M. Elstner, *J. Phys. Chem. A*, 2007, **111**, 10861–10873.

92 D. Riccardi, P. Schaefer, Y. Yang, H. Yu, N. Ghosh, X. Prat-Resina, P. Konig, G. Li, D. Xu, H. Guo, M. Elstner and Q. Cui, *J. Phys. Chem. B*, 2006, **110**, 6458–6469.

93 D. A. McQuarrie, *Statistical Mechanics*, University Science Books, 1st edn, 2000.

94 M. Schmitz and P. Tavan, *J. Chem. Phys.*, 2004, **121**, 12233–12246.

95 R. Ramirez, T. Lopez-Ciudad, P. Kumar and D. Marx, *J. Chem. Phys.*, 2004, **121**, 3973–3983.

96 S. A. Egorov, K. F. Everitt and J. L. Skinner, *J. Phys. Chem. A*, 1999, **103**, 9494–9499.

97 M. Schmitz and P. Tavan, *J. Chem. Phys.*, 2004, **121**, 12247–12258.

98 D. L. Howard and H. G. Kjaergaard, *J. Phys. Chem. A*, 2006, **110**, 10245–10250.

99 Y.-L. Cheng, H.-Y. Chen and K. Takahashi, *J. Phys. Chem. A*, 2011, **115**, 5641–5653.

100 K. L. Plath, K. Takahashi, R. T. Skodje and V. Vaida, *J. Phys. Chem. A*, 2009, **113**, 7294–7303.

101 E. B. Wilson, *Phys. Rev.*, 1934, **45**, 706–714.

102 M. L. Sage and J. Jortner, *Bond Modes*, John Wiley & Sons, Inc., 2007, pp. 293–322.

103 J. Vazquez and J. F. Stanton, *Mol. Phys.*, 2006, **104**, 377–388.

104 H.-J. Werner, P. J. Knowles, G. Knizia, F. R. Manby, M. Schütz, P. Celani, T. Korona, R. Lindh, A. Mitrushenkov, G. Rauhut, K. R. Shamasundar, T. B. Adler, R. D. Amos, A. Bernhardsson, A. Berning, D. L. Cooper, M. J. O. Deegan, A. J. Dobbyn, F. Eckert, E. Goll, C. Hampel, A. Hesselmann, G. Hetzer, T. Hrenar, G. Jansen, C. Köppl, Y. Liu, A. W. Lloyd, R. A. Mata, A. J. May, S. J. McNicholas, W. Meyer, M. E. Mura, A. Nicklass, D. P. O'Neill, P. Palmieri, D. Peng, K. Pflüger, R. Pitzer, M. Reiher, T. Shiozaki, H. Stoll, A. J. Stone, R. Tarroni, T. Thorsteinsson and M. Wang, *MOLPRO, version 2012.1, a package of ab initio programs*, 2012.

105 O. Guvench, S. S. Mallajosyula, E. P. Raman, E. Hatcher, K. Vanommeslaeghe, T. J. Foster, F. W. Jamison, II and A. D. MacKerell, Jr., *J. Chem. Theory Comput.*, 2011, **7**, 3162–3180.

106 P. Durlak and Z. Latajka, *Chem. Phys. Lett.*, 2009, **477**, 249–254.

107 K. Giese, M. Petković, H. Naundorf and O. Kühn, *Phys. Rep.*, 2006, **430**, 211–276.

108 F. Hedin, K. elHage and M. Meuwly, *J. Chem. Inf. Model.*, 2016, DOI: 10.1021/acs.jcim.6b00280.

5.2. Protonated Oxalate

The second case of spectroscopic prediction using MMPT simulations is the protonated oxalate. Oxalate is one of the smallest molecules which form intramolecular hydrogen bond and is important to biochemical cycles. Infrared and Raman spectroscopies were experimentally observed and studied for oxalate in various forms: anion[157,158] ($C_2O_4^{2-}$), deprotonated oxalic acid[11] ($HC_2O_4^-$, or protonated oxalate, $p-$Oxa) and natural oxalate[159]. For natural oxalates, interestingly, they were considered as a potential marker for the pre-existence of life[159] (on the surface of Mars[160]) because low-leveled organisms like lichen and fungi can control the intakes of metallic atoms through expulsion of metal salts like oxalate minerals.[161]

In this paper (*J. Phys. Chem. A*, 2017, **121**, 5389-5398),[69] The dynamics and infrared spectroscopy of intramolecular hydrogen bonding in $p-$Oxa was studied from classical and quantum molecular dynamics. For both simulations, the MMPT force field was used as the energy engine and the infrared spectra were computed. For the classical simulations, the quantum mechanical ground state probability distribution of the proton transfer within the $\mathrm{O}\cdots\mathrm{H}\cdots\mathrm{O}$ motif was obtained from MDs at 600 K. That best reproduced the experimentally observed proton transferring band and its half maximum full width (HMFW). Comparison with the experimental spectra successfully estimated the barrier height for the proton transfer reactions which can not be easily and directly observed. The barrier height of 4.2 kcal/mol was determined which agrees with the *ab initio* calculations at the level of CCSD(T)/aug-cc-pVTZ. In addition to the classical MDs, quantum simulations were carried out using ring polymer molecular dynamics (RPMD),[162–166] which has been implemented in Python-based i-PI software.[167] Quantum simulations lead to further broadened spectral patterns with respect to proton transferring bands.

THE JOURNAL OF
PHYSICAL CHEMISTRY A

Article

pubs.acs.org/JPCA

Vibrational Spectroscopy and Proton Transfer Dynamics in Protonated Oxalate

Zhen-Hao Xu and Markus Meuwly*

Department of Chemistry, University of Basel, Klingelbergstrasse 80, CH-4056 Basel, Switzerland

Supporting Information

ABSTRACT: The dynamics and infrared spectroscopic signatures of proton transfer in protonated oxalate (p−Oxa) are studied using classical and quantum dynamics. The intermolecular interactions are described by a force field suitable to follow proton transfer. This allows to carry out multiple extended classical molecular dynamics (MD) and ring polymer MD simulations from which the infrared spectrum is determined. Simulations at 600 K sample the quantum mechanical ground state probability distribution and best reproduce the experimentally observed maximum absorption wavelength and part of the line shape. Comparison with the experimentally measured spectrum provides an estimate for the barrier height for proton transfer which can not be determined directly from experiment. A barrier of 4.2 kcal/mol is found to best reproduce the position and width of the infrared absorption of the transferring proton in p−Oxa and also leads to an infrared (IR) spectrum in good agreement with experiment for the deuterated species d−Oxa. A novel means to capture the two resonance forms of oxalate depending on the localization of the excess proton on either CO moiety is found to yield improved results for the spectroscopy in the framework region between 1000 and 2000 cm^{-1}.

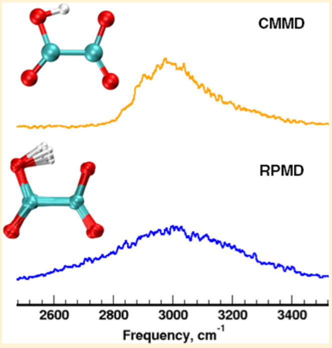

1. INTRODUCTION

The energetics and dynamics of proton and hydrogen transfer (PT/HT) is of fundamental importance in biology and chemistry.[1−3] Such processes are primarily governed by the height of the barrier for proton/hydrogen transfer which is, however, difficult to determine reliably through direct experimentation. Possibilities include high resolution spectroscopy where the splitting of spectral lines can provide information about the barrier height,[4] or nuclear magnetic resonance (NMR) experiments.[5,6] On the other hand, kinetic isotope effects or shift of vibrational bands in the infrared alone can not be used directly to determine the energetics for PT.

Proton transfer in systems containing X−H*···Y motifs—where X and Y are the donor and acceptor atoms, respectively, and H* is the transferring hydrogen—can lead to characteristically broadened features in vibrational spectra.[7] This broadening reflects strong coupling between the X−H stretch and other framework modes of the environment and structural heterogeneity.[8] The broadening even persists down to low temperatures and cooling the species does not lead to sharper bands.[9,10]

In experiments, the broadening of spectral lines in X−H*···Y species has been extensively observed and reported in the liquid and gas phase.[11] For example, in liquid water, the maximum in the OH-stretching spectrum shifts to the red as the temperature decreases from +47 °C to −6 °C, with concomitant increase of the intensity by 16%[12] even without hydrogen or proton transfer to take place. In the high-density liquid, the line shapes in the OH stretching spectra of supercritical methanol was found to be sensitive to the hydrogen bonding network which depends on temperature.[11]

Spectral shifts and their broadening are even more pronounced in systems where a transferring proton H* is shared by a donor and acceptor moiety and potentially provides information about the proton transfer energetics. An empirical relationship between the position of the infrared (IR) absorption and the height of the proton transfer barrier has been recently found in combined computational/experimental investigations of acetylacetone[13] and formic acid dimer.[14] Earlier studies of the infrared spectroscopy of protonated ammonia dimer have also established that the IR-signatures are broad and correlated with the barrier height for proton transfer.[15]

Protonated oxalate ([C_2O_4H]$^-$), which is an oxalate dianion to which an extra proton has been added, is an ideal system to investigate the dynamics and ensuing spectroscopic signatures of a transferring proton coupled to framework modes of the surrounding molecular scaffold.[8] Previous computational work concerned the kinetic isotope effects from electronic structure calculations[16] and the solution dynamics of hydrated p−Oxa.[17]

Studying the dynamics and spectroscopy of a transferring proton requires an energy function that allows to describe bond-formation and bond-breaking. One such way is afforded by molecular mechanics with proton transfer (MMPT) which was designed as a way to combine accuracy for a small

Received: March 9, 2017
Revised: June 7, 2017
Published: June 9, 2017

ACS Publications

5389

DOI: 10.1021/acs.jpca.7b02234
J. Phys. Chem. A 2017, 121, 5389−5398

subsystem (the transferring proton bound to a donor and an acceptor) and a lower-level empirical force field for the remaining degrees of freedom.[18] This is similar in spirit to a mixed quantum mechanical/molecular mechanics treatment (QM/MM) with, however, the added value that energy and force evaluations can be carried out at the speed of empirical force fields and in an analytical fashion which allows long MD simulations.[19,20]

The accuracy of the underlying potential energy surface is that of the parametrized fit to the reference energy from quantum chemical calculations which is Møller−Plesset second order perturbation theory (MP2) for MMPT. The 3-dimensional PES describing the proton motion can be represented with high accuracy (fractions of a kcal/mol)[18] and together with potential morphing[21] provides flexibility for adapting important characteristics, such as the barrier height and position of the minima, to the chemical nature of the donor and acceptor moieties. More recently, alternative ways to represent high-dimensional potential energy surfaces have been explored. One of them is based on neural networks and was applied to bulk silicon or the H+HBr reaction.[22−24] The evaluation of the neural network, once trained, is orders of magnitude faster than the underlying reference density functional theory calculations with a typical accuracy of 0.2 kcal/mol per atom[22] which can be, however, further improved.[24] Another method based on machine learning concepts are representations based on reproducing kernel Hilbert space (RKHS) interpolations.[25] They have demonstrated their utility for high-accuracy studies as they are capable of exactly reproducing the reference data.[26−29] Finally, exploiting the high symmetry of malonaldehyde and formic acid dimer, fully dimensional PESs have been constructed using Morse variables.[30,31]

The present work is concerned with the infrared spectroscopy of the oxalate ion. The spectral signature of the PT-band is particularly sensitive to the H-transfer energetics. Both classical and ring polymer MD simulations are used together with reactive proton transfer potentials from which the infrared spectra are computed and compared with available experiments. From this, inferences about the effective barrier height for proton transfer can be made. Because of the relatively small size of the system, the dynamics can also be studied using semiempirical and density functional theory-based techniques which provides a useful benchmark for simulations using refined empirical force fields in the present work.

2. METHODS

2.1. Intermolecular Interactions and Reactive Force Fields. Protonated oxalate (p−Oxa) consists of a characteristic five-membered ring consisting of the CA−OA−H*−OB−CB motif (see Figure 1). For parametrizing the necessary force field, bonded parameters for the nonreactive part were based on those from CGenFF for carboxylic acid.[32] These parameters were then further refined to better reproduce structural and spectroscopic data from experiment and reference calculations at the MP2/6-311++G(2d,2p) level of theory, as explained further below.

For the reactive part, the MMPT force field to describe the motion of a transferring H* between a donor (D) and an acceptor (A) was used. Contrary to model systems such as $[H_2O{-}H^+\cdots H_2O]$ or $[NH_3{-}H^+\cdots NH_3]$[18] where the H* moves on a linear path between D and A, the PT path in p−Oxa is curved. This is similar to the situation in malondialdehyde (MA)[20] and acetylacetone (AcAc).[13] Hence, this parametrized form is also used in the present case.

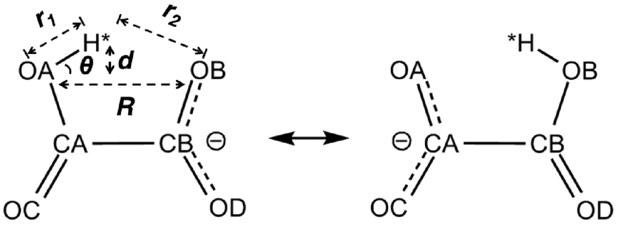

Figure 1. Resonance form of a proton transfer in a protonated oxalate. Oxygen atoms are labeled OA through OD and carbons are CA and CB. The transferring hydrogen is H*. Important coordinates are labeled.

A proton transfer motif consists of a donor and an acceptor atom which share a transferring hydrogen atom/proton (H*) and the corresponding potential energy surface (PES) can be expressed as

$$V_{\mathrm{NLM}}(R, \rho, d) = V_0(R, \rho) + V_d(R, \rho, d) \tag{1}$$

Here R is the distance between D and A, ρ is a transformed H*-coordinate, $\rho = (r \cos \theta - 0.8\ \text{Å})/(R - 1.6\ \text{Å})$ (see Figure 1) and d is the distance of H* from the linear path. The two-dimensional isotropic PES $V_0(R, \rho)$ is represented as a sum of two Morse functions for a PT potential surface with symmetric double minimum. In addition, the nonlinear proton transfer path is represented by $V_d(R, \rho, d)$, and its explicit form is described in the Supporting Information.

The force field parameters were determined by fitting the barrier height to quantum chemical calculations and the vibrational spectroscopy known from experiment.[8] The isotropic part V_0 in eq 1 was fitted to reference energies at the MP2/6-311++G(2d,2p) level of theory,[33−36] by using nonlinear least-squares fitting.[37,38] Reference energies were calculated on a grid along the minimum energy path at each value of $R \in [2.2, 3.0]$ Å in increments of 0.1 Å. The nonlinear part of the PES, V_d, was parametrized to reproduce the minimum energy (MIN) and transition state (TS) structures and the vibrational frequencies of OH* bending modes. All force field parameters are summarized in Table S1.

Upon proton transfer, the nature of the neighboring carbon−oxygen bonds changes from single to partial-double bond or partial-double bond to double bond character. Figure 1 illustrates the two possible resonance forms. Specifically, in Figure 1 the CA−OB bond changes from a single-bond to a partial double-bond character upon H*-transfer. If H* is bonded to a donor (OA, or an acceptor as OB), its neighboring C−O is formally a single bond; once H* transfer occurs, a carboxylated structure $[COO]^-$ is formed. This can be expected as the multiple bonds between two atoms with large difference in electronegativity are more strongly affected by their neighboring bonds.[39] Hence, a coupled representation is introduced to describe the change between two bond types as a superposition of two energy terms $E_{\mathrm{bond,a}}$ and $E_{\mathrm{bond,b}}$ for a same chemical bond, depending on whether H* is bound to OA or OB, respectively. (See Figure 1)

$$E_{\mathrm{bond,0}}(\gamma, l) = (1 - \gamma)E_{\mathrm{bond,a}}(l) + \gamma E_{\mathrm{bond,b}}(l) \tag{2}$$

Here, l is the bond length and $E_{\mathrm{bond},i}(l) = k_i(l - l_{\mathrm{eq},i})^2$ ($i = \{\mathrm{a, b}\}$) are the two different types of bonds (e.g., single and

DOI: 10.1021/acs.jpca.7b02234
J. Phys. Chem. A 2017, 121, 5389−5398

partial double bonds or partial double and double bonds). A switch function

$$\gamma(R, r_1, \theta) = \frac{1}{2}[\tanh[2R(r_1 \cos\theta - 0.5R)] + 1] \tag{3}$$

controls the mixing of $E_{\mathrm{bond,a}}$ and $E_{\mathrm{bond,b}}$ depending on the position of H* along the OA−OB coordinate. At the TS geometry, $\gamma = 0.5$, and at the minimum energy geometries, $\gamma \simeq 0$ or $\gamma \simeq 1$, when H* is bound to OA or OB, respectively.

Along the minimum energy path for an H* transfer, all bonding energies for the remaining degrees of freedom are minimized. However, unless $l_{\mathrm{eq,a}} = l_{\mathrm{eq,b}}$ eq 2 introduces an artificial contribution to the energetics along the PT path. This is accounted for by using a term $E_{\mathrm{cor}}(\gamma)$ such that the total contribution for describing the electronic effects upon proton transfers reads

$$E_{\mathrm{bond}}(\gamma, l) = E_{\mathrm{bond,0}}(\gamma, l) - E_{\mathrm{cor}}(\gamma) \tag{4}$$

and

$$E_{\mathrm{cor}}(\gamma) = \frac{(l_{\mathrm{eq,a}} - l_{\mathrm{eq,b}})^2}{\frac{1}{(1-\gamma)k_{\mathrm{a}}}} + \frac{1}{\gamma k_{\mathrm{b}}} \tag{5}$$

In the present work, the [CA−OA, CB−OB] pair (single and partial double bond) and the [CA−OC, CB−OD] pair (double and partial double bond) are treated in such a fashion. Moreover, the parameters $\{k_i, l_{\mathrm{eq},i}\}$ were parametrized (see Table S1) to give good agreement with experimental frequencies of corresponding modes and equilibrium bond-lengths at the MP2/6-311++G(2d,2p) level. The resulting structural parameters at the minimum energy and TS geometries are given in Table 1.

In the previous MMPT simulations,[14,18] no partial atomic charges were used in the parametrization due to the small size of the system. This is also the case here as nonbonded interactions are only evaluated between atoms more than three bonds away from each other. This only leaves the H*−OC and H*−OD pairs which, however, contribute less than 0.05 kcal/mol to the total interaction energy. As all simulations were performed in the gas phase, intermolecular interactions are of minor interest in the present work.

Table 1. Optimized Geometries of *p*−Oxa[a]

	MIN		TS	
	MP2	PES V_1	MP2	PES V_1
	atomic distance, Å			
$R_{\mathrm{OA-OB}}$	2.49	2.48	2.33	2.34
$r_{\mathrm{OA-H*}}$	1.00	1.01	1.22	1.23
$r_{\mathrm{OB-H*}}$	1.69	1.67	1.22	1.23
d	0.49	0.49	0.37	0.37
$r_{\mathrm{CA-OA}}$	1.35	1.36	1.31	1.30
$r_{\mathrm{CB-OB}}$	1.28	1.27	1.31	1.30
$r_{\mathrm{CA-OC}}$	1.21	1.21	1.22	1.22
$r_{\mathrm{CB-OD}}$	1.24	1.24	1.22	1.22
$r_{\mathrm{CA-CB}}$	1.58	1.57	1.58	1.57
	angle, deg			
∠OA−H*−OB	133.4	133.8	144.7	145.0
∠H*−OA−CA	98.2	96.6	90.9	90.3
∠H*−OB−CB	88.0	89.3	90.9	90.3
∠OA−CA−CB	109.4	111.0	106.7	107.3
∠OB−CB−CA	110.1	109.4	106.7	107.3
∠OC−CA−CB	127.7	122.5	124.9	124.9
∠OD−CB−CA	118.3	123.5	124.9	124.9

[a] The reference calculations are carried out at the MP2/6-311++G(2d,2p) level of theory (abbreviated as MP2) and compared with the MMPT PES V_1 which was fitted to the reference points at the same level of theory.

2.2. Classical MD Simulations. All classical[40] and DFTB[41−45] MD simulations were carried out in the gas phase using CHARMM.[46] Starting from the energy minimized structure, heating and equilibration was run for 20 ps with a time-step of $\Delta t = 0.1$ fs. Then, 10 ns production simulations were carried out for both, *p*−Oxa and deuterated *d*−Oxa. Snapshots for analysis were collected every 2 fs. During the analysis, the fixed point charge model (FPC, fitted to natural bond orbital[47−50] charges) was used for calculating the dipole moments for every frame (Table 1). The classical infrared spectrum is obtained from the Fourier transformed dipole−dipole autocorrelation function $C(t) = \langle \boldsymbol{u}(0)\cdot\boldsymbol{u}(t)\rangle$.[13,20,51] MD simulations were performed at temperatures ranging from 50 to 600 K. For each combination of input parameters—such as the MMPT potential used, temperature, transferring H* or D*—the results of 10 independent trajectories were averaged. For both molecules, respectively, one trajectory using semiempirical DFTB was run at 300 K for 10 ns. In addition to classical and semiempirical simulations, Atom-centered density matrix propagation (ADMP) molecular dynamics[52−54] was also employed to perform atomistic simulations at the B3LYP/6-31G level (abbreviated as B3LYP in the discussion below) with 10 ps equilibration and 100 ps production at 300 K. For each sampled frame, the dipole moments were calculated by using the CHelpG charge model[55] and the current FPC model for classical MDs, respectively.

2.3. Ring Polymer Molecular Dynamics Simulations. Ring polymer MD (RPMD) simulations allow to include quantum effects (zero point energy and tunneling) by representing each physical particle by a necklace consisting of a number n of fictitious particles.[56] The path integral representation of the partition function of an N−particle system is $Q_n = \frac{1}{(2\pi\hbar)^f}\int d^f\mathbf{p}\int d^f\mathbf{r}e^{-\beta_n H_n(\mathbf{P},\mathbf{R})}$ where $f = 3Nn$, n is the number of beads per particle and $\mathbf{r}$ and $\mathbf{p}$ are $\{r_1,\cdots,r_n\}$ and $\{p_1,\cdots,p_n\}$, respectively.

$H_n(\mathbf{p},\mathbf{r})$ is the classical Hamiltonian of beads connected by a harmonic spring

$$H_n(\mathbf{p}, \mathbf{r}) = \sum_{j=1}^{n}\left[\frac{p_j^2}{2m} + \frac{1}{2}m\omega_n^2(r_j - r_{j-1})^2 + V(r_j)\right] \tag{6}$$

with $r_0 = r_n$ ("ring polymer"), $\beta_n = \beta/n = 1/(nk_BT)$, $\omega_n = 1/(\beta_n\hbar)$, and $V(r_j)$ is the external potential acting on each bead.[56] The Hamiltonian in eq 6 is employed to generate the classical trajectories according to Hamilton's equations of motion

$$\dot{\mathbf{p}} = -\frac{\partial H_n(\mathbf{p}, \mathbf{r})}{\partial \mathbf{r}} \text{ and } \dot{\mathbf{r}} = +\frac{\partial H_n(\mathbf{p}, \mathbf{r})}{\partial \mathbf{p}} \tag{7}$$

from which $\mu_n(\mathbf{r}) = \frac{1}{n}\sum_{j=1}^{n}\mu(\mathbf{r}_1^{(j)}, ..., \mathbf{r}_N^{(j)})$ at every time step t is available and the correlation function

$$\tilde{C}(t) = \frac{1}{(2\pi\hbar)^f Q_n}\int d^f\mathbf{p}\int d^f\mathbf{r}e^{-\beta_n H_n(\mathbf{p},\mathbf{r})}\mu_n(\mathbf{r}_0)\mu_n(\mathbf{r}_{\mathrm{t}}) \tag{8}$$

DOI: 10.1021/acs.jpca.7b02234
J. Phys. Chem. A 2017, 121, 5389−5398

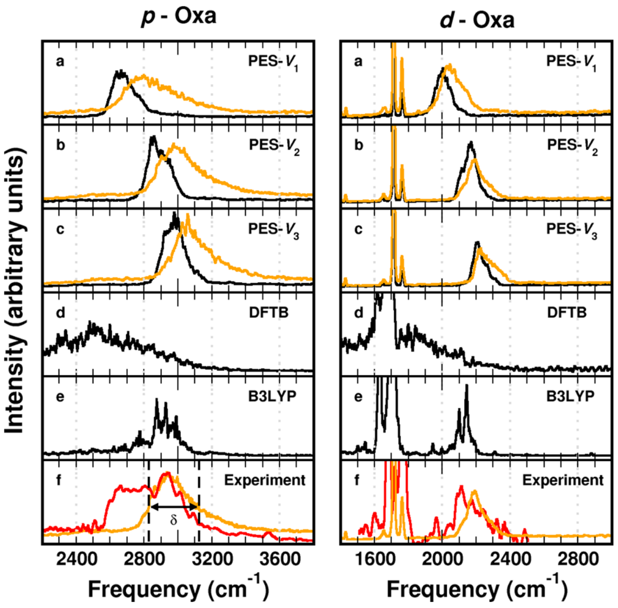

Figure 2. Simulated IR spectra of p−Oxa (the left panel) and d−Oxa (right) from classical MD simulations by using different PESs and methods: (a−c) simulations with V_1 to V_3 at 300 K (black) and 600 K (orange, p−Oxa) or 450 K (orange, d−Oxa), (d) DFTB simulations at 300 K, (e) B3LYP simulations at 300 K with dipole moments calculated by using CHelpG (black) and FPC (blue) charges, and (f) experimental spectrum[8] (red) compared with computed spectrum from panel b (orange). Panels a−c show averaged spectra over 10 runs with 10 ns simulation for each run whereas for the spectra in panels d and e one run of 10 ns and 100 ps was carried out, respectively. In panel f, δ is defined as full width at half-maximum.

can be computed. Then, the infrared spectrum is again computed from the Fourier transform of the correlation function in eq 8.[56−59]

In the present work, RPMD simulations were carried out with the Python-based i-PI software,[60] interfaced with an external routine that provides the MMPT energy and forces for given positions of all particles. For spectroscopic applications thermostated RPMD simulations are recommended.[59] In the production simulations, each atom was represented by 128 beads. To remove spurious contributions from the internal vibrations of the beads, the elements of the friction matrix were multiplied with a damping factor $\lambda = 0.5$.[59] For each run of the simulations, a 2 ps equilibration simulation was performed, followed by an 80 ps production run with a time step of $\Delta t = 0.2$ fs at 50 and 300 K, respectively. Snapshots were collected every 4 fs. All spectra from RPMD simulations were obtained by averaging the results from 40 independent trajectories.

3. RESULTS AND DISCUSSION

3.1. Optimized geometries and Potential Energy Surface. The PT reaction of p−Oxa involves a double well potential with a barrier between the two minimums of 3.3 kcal/mol at the MP2/6-311++G(2d,2p) level of theory. This compares with a 3.5 kcal/mol barrier for the parametrized MMPT force field. The fitting quality of V_0 in eq 1 is reported in Figure S1 and shows an average error of ±0.2 kcal/mol. The minimum energy structures from MP2 and MMPT optimizations show that all bond lengths and most bond angles are reproduced to within ±2%, see Table 1. Hence, the parametrization of the MMPT force field is of good quality and should provide a meaningful basis for dynamics simulations.

3.2. Classical MD Simulations. In the following classical MD simulations on three PESs are described. Surface V_1 is that fitted to the MP2/6-311++G(2d,2p) reference energies with a barrier height of 3.5 kcal/mol. For surface V_2 the barrier height is scaled (see below) to the value obtained from CCSD(T)/aug-cc-pVTZ calculations, which is 4.2 kcal/mol. Finally, V_3 has an even higher barrier of 4.5 kcal/mol, which will be motivated further below.

In the following, a spectroscopic band is characterized by the maximum absorption $\omega_{\max}$ and its full width at half-maximum δ (fwhm, see Figure 2f). Figure 2 (left column) reports the spectra from simulations for p−Oxa. In Figure 2a the simulated spectra for PES V_1 at 300 K (black) and 600 K (orange) is shown. At 300 K, the spectrum exhibits a prominent peak at $\omega_{\max} = 2675$ cm^{-1} with a fwhm of $\delta = 150$ cm^{-1}. This compares with a center position at 2945 cm^{-1} and an estimated fwhm of 455 cm^{-1} as found in experiments,[8] see Figure 2f (left and in black). Obviously, neither the position nor the width of the OH-band is well captured by classical MD simulations at 300 K using V_1.

Previous work[13,14] has found an empirical correlation between the position of the OH-absorption peak and the barrier height for proton transfer. Therefore, potential morphing of $V_0(R, \rho)$ was considered whereby the barrier for proton transfer was changed according to

$$V_0^{\mathrm{new}}(R, \rho) = \frac{\Delta E_b^{\mathrm{new}}}{\Delta E_b} V_0(R, \rho) \tag{9}$$

in order to better describe the experimentally observed center position of the spectroscopic band. The overall topology of the PES was not modified because this was considered to be captured correctly by the reference MP2 calculations. As mentioned above, V_2 is the PES with a barrier height of 4.2 kcal/mol which is the value found from higher-level CCSD(T)/aug-cc-pVTZ calculations. However, it must be emphasized that the physical meaning of these two barrier heights is different. The electronic barrier is that determined from electronic structure calculations (at $T = 0$) whereas the scaled barrier of the reference PES which correctly describes the finite-temperature dynamics is an effective barrier, strictly valid at the conditions of the simulations. Hence, these two values can not be compared directly.

After inspection of the results from MD simulations using V_2, a third PES (V_3) with a barrier of 4.5 kcal/mol was considered. The results from these simulations are reported in Figure 2, parts b and c. Compared to the results from simulations with PES V_1, with V_2 the OH band peaks at 2850 cm^{-1}, closer to the experimental position at $\omega_{\max} = 2945$ cm^{-1}, and gives a width of 155 cm^{-1} whereas with V_3 the simulated spectrum shifts the peak further to 2980 cm^{-1} but with the same width. Hence, the previous empirical relationship[13,14] between barrier height and its effect on the position of the PT band is confirmed. However, the width of the band is clearly underestimated. This point will be considered further below.

It is also of interest to consider the results from semiempirical (DFTB) and DFT MD simulations which are reported in Figure 2, parts d and e. DFTB simulations[15,44] are often a satisfactory and computationally efficient alternative to

DOI: 10.1021/acs.jpca.7b02234
J. Phys. Chem. A 2017, 121, 5389−5398

more expensive QM/MD simulations. However, for the present case, the main peak appears at 2500 cm^{-1} at the DFTB level which is considerably shifted to the red compared to the experiment. Using density functional theory at the B3LYP/6-31G level yields better agreement (2880 cm^{-1}) with experiment. In order to probe to what extent the charge model used to compute the IR spectrum from the configurations, (a) the dipole moment for the DFT MD snapshots was also computed using the FPC model and (b) the molecular dipole moment calculated at the B3LYP level of theory. These spectra are reported in Figure S2 and show that they are almost independent of the particular charge model used. Concerning the width, DFTB clearly yields a much broader spectrum whereas the one from B3LYP simulations is too narrow. The barrier for proton transfer is 3.4 kcal/mol at the B3LYP/6-31G level but only 0.4 kcal/mol using DFTB.

Additional simulations were carried out for *d*−Oxa (right-hand column in Figure 2) which can also be compared with the experiments. The OH-band is considerably red-shifted (Figure 2a−c) and narrower than for *p*-Oxa. The maximum absorption ω_{max} ranges from 2000 to 2205 cm^{-1} for simulations with PESs V_1 to V_3. Again, the widths are underestimated. Simulations were also carried out at the DFTB and B3LYP levels of theory (Figures 2d to e, the right column). As for *p*−Oxa the spectrum from DFTB simulations is shifted far too much to the red and the width is considerably overestimated whereas for the B3LYP simulations the band position agrees well with the experiment but the width is clearly underestimated.

In none of the classical MD simulations analyzed so far the width of the OH-transfer absorption band was close to that observed experimentally. Also, it should be remembered that the estimated temperature of the experiments[8] was approximately 30 K and all simulations reported so far were run at a considerably higher temperature. The concept of "temperature" in small molecular systems in the gas phase is, however, debatable. Hence, it is not a priori evident what temperature is most meaningful to be used in MD simulations to directly compare with experiment.

As an alternative to choosing a particular temperature a priori, the classical and quantum probability distribution functions along the proton transfer coordinates were considered. First, the 1-dimensional Schrödinger equation was solved and the ground state probability distribution $|\Psi(\Delta r)|^2$ was determined where $\Delta r = r_1 - r_2$ (see the definition in Figure 1). Figure 3 shows the quantum mechanical ground state probability distribution function (solid red line) for V_2 which is delocalized, as expected. Next, MD simulations at different temperatures were carried out and the classical distribution function $P(\Delta r)$ was computed. Simulations at 50 and 300 K show that the transferring H* remains either localized in one well or the width of $P(\Delta r)$ is smaller than that of $|\Psi(\Delta r)|^2$. Only when the MD simulation is run at 600 K the classical density approaches the quantum probability distribution (orange line in Figure 3).

Hence, in order to arrive at representative sampling, another set of MD simulations at 600 K was carried out for *p*−Oxa such that the $P(\Delta r)$ sampled is representative of $|\Psi(\Delta r)|^2$. The spectra from these simulations are shown as orange traces in Figure 2. For PES V_2 and compared to simulations at 300 K the OH band broadens to a width of 265 cm^{-1} and ω_{max} shifts to 2980 cm^{-1}. Hence, it is found that the widths of the infrared spectra corresponding to the transferring H atom are strongly affected by the simulation temperature which is attributed to the increased sampling along the PT coordinate. Similar to PES V_2, a temperature of 600 K was also found to be most representative for PES V_1 and V_3. Simulations with these two PESs yield widths of 325 and 215 cm^{-1} and shift the peaks to 2800 and 3060 cm^{-1} from those at 300 K. Among the three PESs, PES V_2 gives the closest ω_{max} to the experimental result whereas the OH band given by PES V_3 shifts to the blue as the temperature increases. Corresponding simulations were also carried out for *d*−Oxa (see Figure 2 right-hand column) at 300 and 450 K, respectively, which was again chosen to best reproduce the quantum density. The infrared spectrum computed with V_2 is an almost quantitative agreement with experiment without further adjustment of the PES.

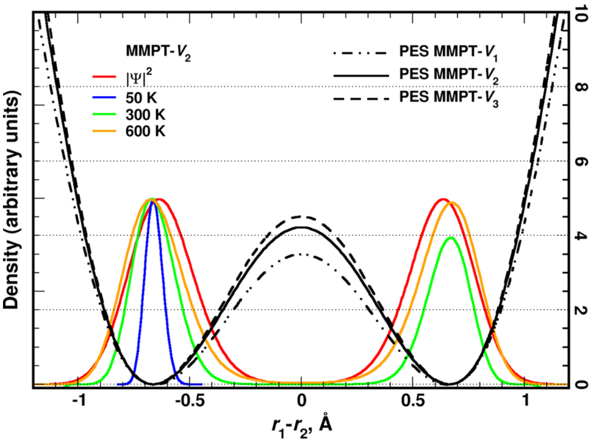

Figure 3. 1-Dimensional potential energy curves for V_1 to V_3 along the proton transfer coordinate. For V_2, the 1-dimensional Schrödinger equation was solved to obtain the ground state density $|\Psi(\Delta r)|^2$ (red). The classical densities from simulations at 50 K (blue), 300 K (green), and 600 K (orange) are shown for comparison. The progression coordinate is the difference $r_1 - r_2$; see Figure 1.

3.3. Results from RPMD Simulations.

In order to directly assess the influence of quantum effects, RPMD simulations were carried out. Convergence studies at $T = 50$ K established that with $n = 64$ beads convergence of the spectrum for the transferring hydrogen atom is obtained, see inset in Figure 4a. The simulated spectra at 50 K from RPMD simulations with $n = 128$ beads per particle are reported in Figure 4. Figure 4a shows the IR spectra from simulations using PESs V_1 to V_3. As for the classical MD simulations, ω_{max} the OH band shifts to the blue as a consequence of the increased barrier height for PT. For V_1 the simulations give the averaged spectrum with a maximum absorption at $\omega_{\text{max}} = 2845$ cm^{-1} which coincides with the results from classical MD simulations carried out at 600 K using V_1. The width of the band is 910 cm^{-1}, significantly increased from those found by classical MD simulations. Using V_2, the maximum absorption is at 3005 cm^{-1}, which is closest to the experimental data, and the width is 530 cm^{-1}. With PES V_3, $\omega_{\text{max}} = 3025$ cm^{-1} and $\delta = 535$ cm^{-1}. Overall, including quantum effects increases the width of the spectra compared to classical MD simulations. Figure 4b compares the computed spectra from RPMD simulations using V_2 at 50 and 300 K. For the simulations at 300 K, the spectrum is broadened to a width of 575 cm^{-1}, with ω_{max} shifted to 3055 cm^{-1}.

Parts b and c of Figure 4 also allow to compare the computed spectra from RPMD and classical MMPT/MD (CMMD) simulations using V_2 at 50 and 600 K, respectively. The positions of the absorption maxima ω_{max} for the two methods

DOI: 10.1021/acs.jpca.7b02234
J. Phys. Chem. A 2017, 121, 5389−5398

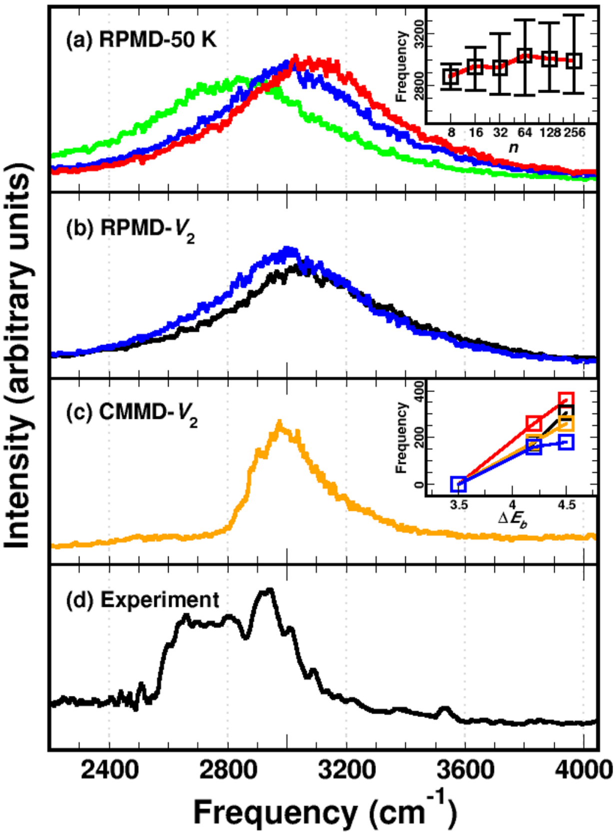

Figure 4. From top to bottom: (a) simulated IR spectra of *p*−Oxa from RPMD simulations with 128 beads per particle at 50 K with PES V_1 (green), V_2 (blue), and V_3 (red); (b) RPMD spectra at 50 K (blue, see panel a) and 300 K (black) with PES V_2; (c) spectrum from classical MD (CMMD) simulations at 600 K with PES V_2 (also see in Figure 2b); (d) experimental data.[8] The inset in panel a reports the convergence of the H-transfer peak position $\omega_{\max}$ and its width with increasing number of beads *n* in the RPMD simulations. With $n = 64$ the simulations appear to be sufficiently converged. The inset in panel c reports the shift of $\omega_{\max}$ depending on the PT barrier height for classical MD (black for 300 K, orange for 600 K) and RPMD simulations at 50 K (blue) and from normal modes (red).

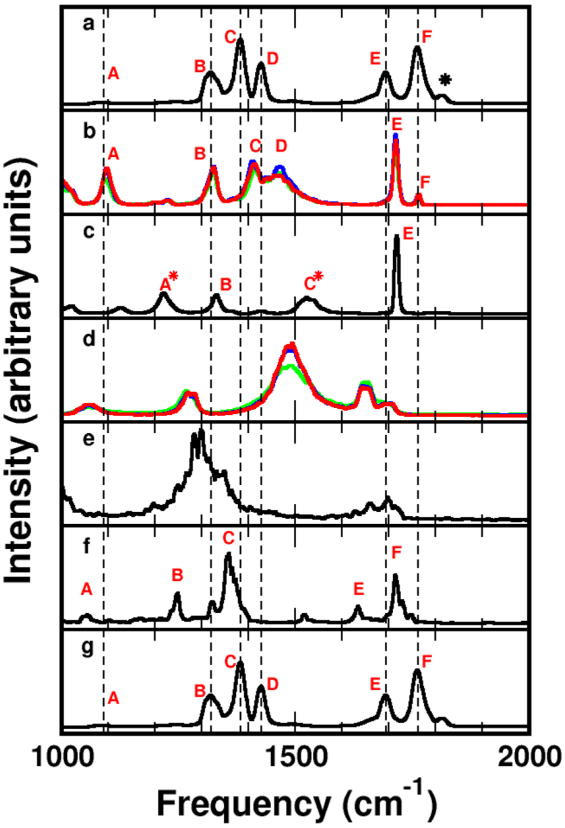

Figure 5. From top to bottom: (a and g) IR spectra in the 1000−2000 cm^{-1} range from experiment; (b) MMPT simulations with PESs V_1 to V_3 (green, blue and red); (c) MMPT simulations with PES V_2 and force field with independent representation for CO bonds; (d) RPMD simulations (128 beads per particle) with PES V_1 to V_3 (colors as in panel b); (e) DFTB; (f) B3LYP.

using the same PES agree well, but their widths and the lineshapes on the red edge differ appreciably. In particular, the RPMD-computed spectra lead to a largely symmetric line shape which is neither found for the classical MD simulations nor for the experimental data. With both, classical MD and RPMD simulations, the maximum peak frequency shifts to the blue as the barrier height increases, see inset in Figure 4c. This is a consequence of the increasing curvature when morphing the barrier height by a factor >1. Also, the influence of anharmonicity can be seen when considering harmonic frequencies from a normal-mode analysis using PESs V_1 to V_3. However, for formic acid dimer it was found that factors other than the barrier height, e.g., the equilibrium position and curvature along the proton transfer path, also affect the location of $\omega_{\max}$.[14]

3.4. Framework Modes.

Figure 5 compares the simulated spectra from classical, DFTB/MD and RPMD simulations for the frequency range from 1000 to 2000 cm^{-1}. Spectral features are labeled A to F and the experimental assignments are given in ref 8. Independent of the PES used (V_1 to V_3), the spectra from classical MD simulations closely agree, see Figure 5b (red, green, and blue traces). Also, the simulation temperature does not affect the spectroscopy in this region contrary to the OH stretch. Comparison of the computed spectra with the experimental line positions shows that lines A−F in Figure 5 are well reproduced. It should be emphasized that the overall force field was fitted to *ab initio* reference data and further improvements would, in principle, be possible through explicit fitting to the experiment. The small feature around 1810 cm^{-1} (indicated by a star in Figure 5a) has been assigned to a Fermi resonance[8] which we do not expect to be captured by classical MD simulations. Some of the relative intensities are not particularly well reproduced which can, however, be accomplished with an improved dipole moment surface going beyond the point charge representation used in the present work.[61,62]

The RPMD (Figure 5d), DFTB/MD (Figure 5e) and B3LYP/MD results (Figure 5f) do not capture the experimentally observed spectra particularly well in this wavelength region. The RPMD spectra for the framework modes are generally broad and the maximum absorption is shifted relative to the experimental line positions. This has already been found in earlier work.[59] Despite the 10 ns trajectory, DFTB/MD simulations with dipole moments computed from the fixed point charge model lead to broad absorption features. Such broad features are also found when considering the power spectra. Finally, B3LYP/MD simulations with CHelpG charges computed on every snapshot give a meaningful spectrum above 1600 cm^{-1} but the region around 1300 cm^{-1} is not particularly well described.

Upon proton transfer, the bonding characteristics of the CO bonds change; see Figure 1. Such changes in the electronic structure (single to partial double bond or double to partial single bond) affect the vibrational spectroscopy because the bond strength and hence also the force constants of these bonds change dynamically. Usual force field parametrizations do not capture such effects.[63] The coupled representation used for the CO bonds, see eq 2, can account for these changes. It is of interest to assess to what extent such a more detailed force field is capable of capturing specific effects for the CO-stretch vibrations. For this, exploratory simulations in which the CA−OA and CB−OB were treated as single bonds (stretching force constant k = 594 kcal/mol and equilibrium separation r_e = 1.32 Å) and CA = OC and CB = OD were double bonds (stretching force constant k = 660 kcal/mol and equilibrium separation r_e = 1.22 Å) were carried out. The corresponding infrared spectrum is reported in Figure 5c. Both, the spectral pattern between 1300 and 1500 cm^{-1} and between 1700 and 1800 cm^{-1} changes appreciably compared to the pattern in panel b. Instead of the experimentally found triplets (around 1400 cm^{-1}, label B−D) and doublets (1750 cm^{-1}, E and F), simulations without eq 2 are unable to correctly describe these splittings. This differs from simulations including this term and highlights that it is possible to incorporate such electronic effects into empirical force fields in a meaningful fashion.

In order to assign the CO stretching modes in the IR spectra, the power spectra of the CA−OA and CA−OC bond distances were determined (see Figure S3). The power spectrum of CA−OA from the present MMPT simulation (black trace in Figure S3c) gives a C−O band at 1100 cm^{-1} (label A) compared with 1091 cm^{-1} from experiment (low intensity[8]). From simulations with the independent (and conventional) representation for describing CO bonds, this feature appears at 1220 cm^{-1} in both the power spectrum and the IR spectrum (red traces in Figure S3, panels b and c). Concerning the absorption features between 1700 and 1800 cm^{-1} the simulations including and excluding the resonance term show both excitations in the power spectra (Figure S3, panels c and d). Despite using the same charge model, the IR spectra (Figure 5 panels b and c) differ in that the high-frequency peak is absent if a conventional force field is used. Close inspection reveals, however, that the high-frequency feature (label F) is present but with low intensity. Simulations with isotopically substituted oxygens at positions OC and OD allow assignment of label F to the C═O stretch whereas label E corresponds to the CO_2^- asymmetric stretch (Figure S4). It is worthwhile to point out that the double-peak structure between 1700 and 1800 cm^{-1} for the C═O stretch vibrations is also found in the simulations for d−Oxa, see Figure 2a−c.

The most significant difference between the two force field representations concerns the region between 1300 and 1500 cm^{-1} (labels B−D). All assignments are based on power spectra as reported in Figures S3, S4, and S5. For the MMPT simulations with coupled representations for the CO-bonds, the CO_2^- symmetric stretch occurs at 1330 cm^{-1} compared to 1320 cm^{-1} from experiment (Figure 5b). The spectral signatures (label C) to the blue of label B are associated with HOC bending vibrations. This is expected because the transition between the two structures in Figure 1 involves significant displacement along the HOC-coordinate. Such an assignment is also consistent with previous work in that this region of the spectrum is mixed due to mode coupling. The HOC bending vibration is coupled with spectral signatures at 1400 and 1470 cm^{-1} (label D), which is also verified from the power spectrum of HOC (Figure S3e) and test simulations with mass perturbation on H* (Figure S5). Earlier assignments[8] suggested that the 1470 cm^{-1} band is a combination band of C-out-of-plane and OH-out-of-plane motions.

Next, the simulation for the independent CO oscillators (without eq 2) are described, see Figure 5c. The CO_2^- symmetric stretch appears at 1330 cm^{-1} (label B, Figure 5c) which agrees with experiment (1320 cm^{-1}) and the simulations with coupled representation. The HOC bending vibration (label C*) occurs at 1525 cm^{-1} which is, however, blue-shifted by 120 cm^{-1} relative to that in the coupled representation. This is a consequence of the stretch−bend coupling between the CO stretch and the HOC bend which is shown in the red trace in Figure S3e. Contrary to the coupled representation, no band D is found when the independent representation for CO-bonds is applied in the simulations.

RPMD simulations with coupled CO-stretches (i.e., the equivalent to Figure 5b) do not lead to a particularly realistic spectrum in the 1300 and 1500 cm^{-1} range (see Figure 5d) and hence no detailed analysis was carried out. Similarly, DFTB/MD simulations (Figure 5e) are not able to describe the spectroscopy in this frequency range; the CO_2^- symmetric stretches and HOC bends overlap and appear as a broad feature around 1290 cm^{-1}. In B3LYP/MD simulations the CO_2^- symmetric stretching band is red-shifted by 70 cm^{-1} (label B, Figure 5f) from the experimental data but the HOC bend was found at 1360 cm^{-1} (label C) which is close to the experimental data.

Finally, the present results can also be compared with earlier simulations.[8] These calculations were carried out at the B3LYP/6-311++G(d,p) level of theory using second order vibrational perturbation theory (VPT2) and superpositions of bright and doorway states in the harmonic approximation. Such an approach allowed assignments of the framework modes in the region between 1000 and 2000 cm^{-1}. The computations also suggested that the structure of oxalate is asymmetric which is confirmed by the current simulations, see Figure 6. The transferring proton is localized for several vibrational periods on either of the two oxygen atoms OA and OB. For the spectroscopy in the OH-stretch region, an adiabatic separation between the OH vibration and the environmental modes similar in spirit to earlier adiabatic separation techniques[64] had been used.[8] The line shape from analyzing 2000 conformations sampled from the ground state quantum probability distribution function is qualitatively similar to the present spectrum reported in Figure 2c. In other words, the main peak at 3000 cm^{-1} is captured realistically whereas the plateau extending to the red of the main peak is not. It is worthwhile to mention that for d−Oxa the experimentally measured line shape does not exhibit such a plateau (see Figure 2f) and the computed lineshapes from the previous[8] and the present work are quite realistic. In contrast to the earlier work[8] the present simulations do not invoke additional approximations such as an adiabatic separation between the PT and the framework modes. On the other hand, a force field, as accurate as it may be, is always a compromise between speed and accuracy because it is only an approximate representation of the intermolecular interactions and only comparison with experiment establishes its validity.

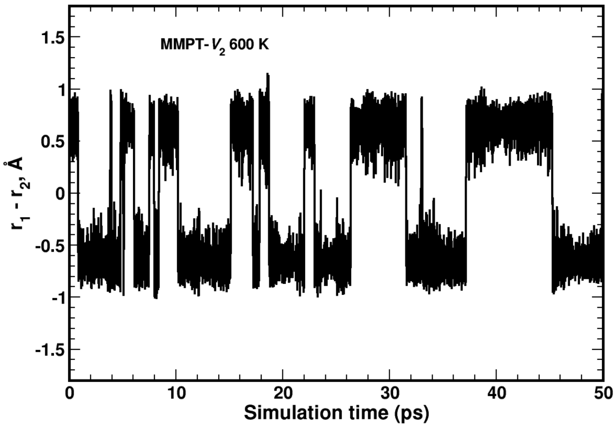

Figure 6. Time series for the proton motion between atoms OA and OB (see Figure 1) for MMPT potential V_2 at 600 K for a 50 ps period. Distances r_1 and r_2 are defined in Figure 1 and the time series establishes that the transferring proton localizes near the oxygen atoms for several vibrational periods which leads to asymmetric instantaneous structures.

4. CONCLUSIONS

In conclusion, through comparison of the IR spectrum for *p*−and *d*−Oxa calculated from MMPT potentials with experimental data, the effective barrier height for proton transfer is found to be 4.2 kcal/mol which is consistent with CCSD(T)/aug-cc-pVTZ calculations. However, the physical meaning of these to barrier heights differs. Without further adjustment, the same PES also gives an IR spectrum for *d*−Oxa in very good agreement with experiment. The barrier for proton transfer from semiempirical DFTB simulations is very low and the IR spectra in the region of the proton transfer mode are shifted too far to the red. On the other hand, B3LYP AIMD performs quite well for the high-frequency part but is less good for some of the framework modes. RPMD simulations with the different MMPT PESs lead to rather broad spectra but the maximum absorption for the proton transfer mode is generally well captured.

As for other systems exhibiting proton transfer between donor and acceptor atoms connected by a molecular framework (acetylacetone)[13] or not (formic acid dimer)[14] the barrier height for proton transfer is found to sensitively affect the position of the main OH-stretch absorption in the infrared region. Conformational sampling at a temperature which yields a proton distribution function corresponding to the quantum ground state wave function along the OH-coordinate leads to a realistic width of the spectrum determined from classical MD simulations. Together with what was learned about previously investigated systems[13,14] estimation of the proton transfer barrier height from a combined computational/IR spectroscopy approach is likely to be a generic way forward for better characterizing this important quantity for a range of donor−acceptor pairs.

■ ASSOCIATED CONTENT

Supporting Information

The Supporting Information is available free of charge on the ACS Publications website at DOI: 10.1021/acs.jpca.7b02234.

MMPT potential with nonlinear proton transfer discussion, tables of parameters used in MMPT force fields and vibrational frequencies, and figures showing a omparison of the isotropic part $V_0(R,\rho)$ between reference MP2/6 311++G(2d,2p) and the MMPT data, analysis of IR spectra, IR and power spectra, analysis for assignemtns of stretching modes, and test simulations (PDF)

■ AUTHOR INFORMATION

Corresponding Author

*(M.M.) E-mail: m.meuwly@unibas.ch.

ORCID

Zhen-Hao Xu: 0000-0002-6800-3158
Markus Meuwly: 0000-0001-7930-8806

Notes

The authors declare no competing financial interest.

■ ACKNOWLEDGMENTS

This work was supported by the Swiss National Science Foundation, NCCR MUST, and the University of Basel. The authors acknowledge helpful discussions with Dr. M. Rossi concerning RPMD simulations for spectroscopic applications.

■ REFERENCES

(1) Cleland, W.; Kreevoy, M. Low-barrier Hydrogen-bonds and Enzymatic Catalysis. *Science* **1994**, *264*, 1887−1890.

(2) Warshel, A.; Papazyan, A.; Kollman, P. On Low-barrier Hydrogen-bonds and Enzyme Catalysis. *Science* **1995**, *269*, 102−104.

(3) Shan, S.; Loh, S.; Herschlag, D. The Energetics of Hydrogen Bonds in Model Systems: Implications for Enzymatic Catalysis. *Science* **1996**, *272*, 97−101.

(4) Borst, D.; Roscioli, J.; Pratt, D.; Florio, G.; Zwier, T.; Muller, A.; Leutwyler, S. Hydrogen Bonding and Tunneling in the 2-pyridone Center Dot 2-hydroxypyridine Dimer. Effect of Electronic Excitation. *Chem. Phys.* **2002**, *283*, 341−354.

(5) Frey, P.; Whitt, S.; Tobin, J. A Low-barrier Hydrogen-bond in the Catalytic Triad of Serine Proteases. *Science* **1994**, *264*, 1927−1930.

(6) Braun, J.; Schlabach, M.; Wehrle, B.; Kocher, M.; Vogel, E.; Limbach, H. NMR-study of the Tautomerism of Porphyrin Including the Kinetic HH/HD/DD Isotope Effects in the Liquid and the Solid State. *J. Am. Chem. Soc.* **1994**, *116*, 6593−6604.

(7) Bondesson, L.; Mikkelsen, K. V.; Luo, Y.; Garberg, P.; Ågren, H. Hydrogen Bonding Effects on Infrared and Raman Spectra of Drug Molecules. *Spectrochim. Acta, Part A* **2007**, *66*, 213−224.

(8) Wolke, C. T.; DeBlase, A. F.; Leavitt, C. M.; McCoy, A. B.; Johnson, M. A. Diffuse Vibrational Signature of a Single Proton Embedded in the Oxalate Scaffold, $HO_2CCO_2^-$. *J. Phys. Chem. A* **2015**, *119*, 13018−13024.

(9) Leavitt, C. M.; DeBlase, A. F.; Johnson, C. J.; van Stipdonk, M.; McCoy, A. B.; Johnson, M. A. *J. Phys. Chem. Lett.* **2013**, *4*, 3450−3457.

(10) Johnson, C. J.; Dzugan, L. C.; Wolk, A. B.; Leavitt, C. M.; Fournier, J. A.; McCoy, A. B.; Johnson, M. A. Microhydration of Contact Ion Pairs in $M^{2+}OH^-(H_2O)_{n=1-5}$(M = Mg, Ca) Clusters: Spectral Manifestations of a Mobile Proton Defect in the First Hydration Shell. *J. Phys. Chem. A* **2014**, *118*, 7590−7597.

(11) Bakker, H. J.; Skinner, J. L. Vibrational Spectroscopy as a Probe of Structure and Dynamics in Liquid Water. *Chem. Rev.* **2010**, *110*, 1498−1517.

(12) Brubach, J.-B.; Mermet, A.; Filabozzi, A.; Gerschel, A.; Roy, P. Signatures of the Hydrogen Bonding in the Infrared Bands of Water. *J. Chem. Phys.* **2005**, *122*, 184509.

(13) Howard, D. L.; Kjaergaard, H. G.; Huang, J.; Meuwly, M. Infrared and Near-Infrared Spectroscopy of Acetylacetone and Hexafluoroacetylacetone. *J. Phys. Chem. A* **2015**, *119*, 7980−7990.

(14) Mackeprang, K.; Xu, Z.-H.; Maroun, Z.; Meuwly, M.; Kjaergaard, H. G. Spectroscopy and Dynamics of Double Proton Transfer in Formic Acid Dimer. *Phys. Chem. Chem. Phys.* **2016**, *18*, 24654−24662.

(15) Meuwly, M.; Karplus, M. Simulation of Proton Transfer Along Ammonia Wires: An ab Initio and Semiempirical Density Functional Comparison of Potentials and Classical Molecular Dynamics. *J. Chem. Phys.* **2002**, *116*, 2572−2585.

(16) Truong, T.; McCammon, J. Direct Dynamics Study of Intramolecular Proton-transfer in Hydrogenoxalate Anion. *J. Am. Chem. Soc.* **1991**, *113*, 7504−7508.

(17) Kroutil, O.; Minofar, B.; Kabelac, M. Structure and Dynamics of Solvated Hydrogenoxalate and Oxalate Anions: Theoretical Study. *J. Mol. Model.* **2016**, *22*, 210.

(18) Lammers, S.; Lutz, S.; Meuwly, M. Reactive Force Fields for Proton Transfer Dynamics. *J. Comput. Chem.* **2008**, *29*, 1048−1063.

(19) Lutz, S.; Tubert-Brohman, I.; Yang, Y.; Meuwly, M. Water-assisted Proton Transfer in Ferredoxin I. *J. Biol. Chem.* **2011**, *286*, 23679−23687.

(20) Yang, Y.; Meuwly, M. A Generalized Reactive Force Field for Nonlinear Hydrogen Bonds: Hydrogen Dynamics and Transfer in Malonaldehyde. *J. Chem. Phys.* **2010**, *133*, 064503.

(21) Meuwly, M.; Hutson, J. Morphing ab Initio Potentials: A Systematic Study of NeHF. *J. Chem. Phys.* **1999**, *110*, 8338−8347.

(22) Behler, J.; Parrinello, M. Generalized Neural-network Representation of High-dimensional Potential-energy Surfaces. *Phys. Rev. Lett.* **2007**, *98*, 146401.

(23) Behler, J. Neural Network Potential-energy Surfaces in Chemistry: A Tool for Large-scale Simulations. *Phys. Chem. Chem. Phys.* **2011**, *13*, 17930−17955.

(24) Pukrittayakamee, A.; Malshe, M.; Hagan, M.; Raff, L. M.; Narulkar, R.; Bukkapatnum, S.; Komanduri, R. Simultaneous Fitting of a Potential-energy Surface and its Corresponding Force Fields Using Feedforward Neural Networks. *J. Chem. Phys.* **2009**, *130*, 134101.

(25) Hollebeek, T.; Ho, T.-S.; Rabitz, H. Constructing Multidimensional Molecular Potential Energy Surfaces from ab Initio Data. *Annu. Rev. Phys. Chem.* **1999**, *50*, 537−570.

(26) Meuwly, M.; Hutson, J. The Potential Energy Surface and Near-dissociation States of He-H_2^+. *J. Chem. Phys.* **1999**, *110*, 3418−3427.

(27) Castro-Palacio, J. C.; Nagy, T.; Bemish, R. J.; Meuwly, M. Computational Study of Collisions between O (3P) and NO (2Π) at Temperatures Relevant to the Hypersonic Flight Regime. *J. Chem. Phys.* **2014**, *141*, 164319.

(28) Soloviov, M.; Meuwly, M. Reproducing Kernel Potential Energy Surfaces in Biomolecular Simulations: Nitric Oxide Binding to Myoglobin. *J. Chem. Phys.* **2015**, *143*, 105103.

(29) Soloviov, M.; Das, A. K.; Meuwly, M. Structural Interpretation of Metastable States in Myoglobin-NO. *Angew. Chem., Int. Ed.* **2016**, *55*, 10126−10130.

(30) Wang, Y.; Braams, B. J.; Bowman, J. M.; Carter, S.; Tew, D. P. Full-dimensional quantum calculations of ground-state tunneling splitting of malonaldehyde using an accurate ab initio potential energy surface. *J. Chem. Phys.* **2008**, *128*, 224314.

(31) Qu, C.; Bowman, J. M. An ab initio potential energy surface for the formic acid dimer: zero-point energy, selected anharmonic fundamental energies, and ground-state tunneling splitting calculated in relaxed 1−4-mode subspaces. *Phys. Chem. Chem. Phys.* **2016**, *18*, 24835−24840.

(32) Vanommeslaeghe, K.; Hatcher, E.; Acharya, C.; Kundu, S.; Zhong, S.; Shim, J.; Darian, E.; Guvench, O.; Lopes, P.; Vorobyov, I.; et al. CHARMM General Force Field: A Force Field for Drug-like Molecules Compatible with the CHARMM All-Atom Additive Biological Force Fields. *J. Comput. Chem.* **2010**, *31*, 671−690.

(33) Head-Gordon, M.; Pople, J. A.; Frisch, M. J. MP2 Energy Evaluation by Direct Methods. *Chem. Phys. Lett.* **1988**, *153*, 503−506.

(34) Frisch, M. J.; Head-Gordon, M.; Pople, J. A. Semi-direct Algorithms for the MP2 Energy and Gradient. *Chem. Phys. Lett.* **1990**, *166*, 281−289.

(35) Head-Gordon, M.; Head-Gordon, T. Analytic MP2 Frequencies without Fifth-Order Storage. Theory and Application to Bifurcated Hydrogen Bonds in the Water Hexamer. *Chem. Phys. Lett.* **1994**, *220*, 122−128.

(36) Frisch, M. J.; Head-Gordon, M.; Pople, J. A. A Direct MP2 Gradient Method. *Chem. Phys. Lett.* **1990**, *166*, 275−280.

(37) Bochkanov, S. *ALGLIB*; http://www.alglib.net.

(38) Bevington, P.; Robinson, D. *Data Reduction and Error Analysis for the Physical Sciences*; McGraw-Hill Higher Education: McGraw-Hill: 2003.

(39) Pauling, L. *The Nature of the Chemical Bond and the Structure if Molecules and Crystals: An Introduction to Modern Structural Chemistry*; 1960.

(40) Brooks, B.; Bruccoleri, R.; Olafson, D.; States, D.; Swaminathan, S.; Karplus, M. CHARMM: A Program for Macromolecular Energy Minimization, and Dynamics Calculations. *J. Comput. Chem.* **1983**, *4*, 187−217.

(41) Elstner, M.; Porezag, D.; Jungnickel, G.; Elsner, J.; Haugk, M.; Frauenheim, T.; Suhai, S.; Seifert, G. Self-consistent-charge Density-functional Tight-binding Method for Simulations of Complex Materials Properties. *Phys. Rev. B: Condens. Matter Mater. Phys.* **1998**, *58*, 7260−7268.

(42) Elstner, M.; Frauenheim, T.; Kaxiras, E.; Seifert, G.; Suhai, S. A Self-consistent Charge Density-functional Based Tight-binding Scheme for Large Biomolecules. *Phys. Status Solidi B* **2000**, *217*, 357−376.

(43) Frauenheim, T.; Seifert, G.; Elstner, M.; Niehaus, T.; Köhler, C.; Amkreutz, M.; Sternberg, M.; Hajnal, Z.; Carlo, A. D.; Suhai, S. Atomistic Simulations of Complex Materials: Ground-State and Excited-State Properties. *J. Phys.: Condens. Matter* **2002**, *14*, 3015−3047.

(44) Cui, Q.; Elstner, M.; Kaxiras, E.; Frauenheim, T.; Karplus, M. A QM/MM Implementation of the Self-Consistent Charge Density Functional Tight Binding (SCC-DFTB) Method. *J. Phys. Chem. B* **2001**, *105*, 569−585.

(45) Riccardi, D.; Schaefer, P.; Yang, Y.; Yu, H.; Ghosh, N.; Prat-Resina, X.; Konig, P.; Li, G.; Xu, D.; Guo, H.; et al. Development of Effective Quantum Mechanical/Molecular Mechanical (QM/MM) Methods for Complex Biological Processes. *J. Phys. Chem. B* **2006**, *110*, 6458−6469.

(46) Brooks, B. R.; Brooks, C. L., III; Mackerell, A. D., Jr.; Nilsson, L.; Petrella, R. J.; Roux, B.; Won, Y.; Archontis, G.; Bartels, C.; Boresch, S.; et al. CHARMM: The Biomolecular Simulation Program. *J. Comput. Chem.* **2009**, *30*, 1545−1614.

(47) Foster, J. P.; Weinhold, F. Natural Hybrid Orbitals. *J. Am. Chem. Soc.* **1980**, *102*, 7211−18.

(48) Reed, A. E.; Weinhold, F. Natural Bond Orbital Analysis of Near hartree-fock Water Dimer. *J. Chem. Phys.* **1983**, *78*, 4066−4073.

(49) Reed, A. E.; Weinhold, F. Natural Localized Molecular Orbitals. *J. Chem. Phys.* **1985**, *83*, 1736−1740.

(50) Reed, A. E.; Curtiss, L. A.; Weinhold, F. Intermolecular Interactions from a Natural Bond Orbital, Donor-Acceptor Viewpoint. *Chem. Rev.* **1988**, *88*, 899−926.

(51) Wang, H.; Agmon, N. Complete Assignment of the Infrared Spectrum of the Gas-phase Protonated Ammonia Dimer. *J. Phys. Chem. A* **2016**, *120*, 3117−3135.

(52) Iyengar, S. S.; Schlegel, H. B.; Millam, J. M.; Voth, G. A.; Scuseria, G. E.; Frisch, M. J. Ab Initio Molecular Dynamics: Propagating the Density Matrix with Gaussian Orbitals. II. Generalizations Based on Mass-weighting, Idempotency, Energy Conservation and Choice of Initial Conditions. *J. Chem. Phys.* **2001**, *115*, 10291−10302.

(53) Iyengar, S. S.; Schlegel, H. B.; Voth, G. A.; Millam, J. M.; Scuseria, G. E.; Frisch, M. J. Ab Initio Molecular Dynamics: Propagating the Density Matrix with Gaussian Orbitals. IV. Formal Analysis of the Deviations from Born-Oppenheimer Dynamics. *Isr. J. Chem.* **2002**, *42*, 191−202.

(54) Schlegel, H. B.; Iyengar, S. S.; Li, X.; Millam, J. M.; Voth, G. A.; Scuseria, G. E.; Frisch, M. J. Ab Initio Molecular Dynamics: Propagating the Density Matrix with Gaussian Orbitals. III. Comparison with Born-Oppenheimer Dynamics. *J. Chem. Phys.* **2002**, *117*, 8694−8704.

DOI: 10.1021/acs.jpca.7b02234
J. Phys. Chem. A 2017, 121, 5389−5398

(55) Breneman, C. M.; Wiberg, K. B. Determining Atom-centered Monopoles From Molecular Electrostatic Potentials. The Need for High Sampling Density in Formamide Conformational Analysis. *J. Comput. Chem.* **1990**, *11*, 361−373.

(56) Habershon, S.; Manolopoulos, D. E.; Markland, T. E.; Miller, T. F., III Ring-polymer Molecular Dynamics: Quantum Effects in Chemical Dynamics from Classical Trajectories in an Extended Phase Space. *Annu. Rev. Phys. Chem.* **2013**, *64*, 387−413.

(57) Shiga, M.; Nakayama, A. Ab Initio Path Integral Ring Polymer Molecular Dynamics: Vibrational Spectra of Molecules. *Chem. Phys. Lett.* **2008**, *451*, 175−181.

(58) Habershon, S.; Fanourgakis, G. S.; Manolopoulos, D. E. Comparison of Path Integral Molecular Dynamics Methods for the Infrared Absorption Spectrum of Liquid Water. *J. Chem. Phys.* **2008**, *129*, 074501.

(59) Rossi, M.; Ceriotti, M.; Manolopoulos, D. E. How to Remove the Spurious Resonances From Ring Polymer Molecular Dynamics. *J. Chem. Phys.* **2014**, *140*, 234116.

(60) Ceriotti, M.; More, J.; Manolopoulos, D. E. I-Pi: A Python Interface for ab Initio Path Integral Molecular Dynamics Simulations. *Comput. Phys. Commun.* **2014**, *185*, 1019−1026.

(61) Lammers, S.; Meuwly, M. On the Relationship between Infrared Spectra of Shared Protons in Different Chemical Environments: A Comparison of Protonated Diglyme and Protonated Water Dimer. *J. Phys. Chem. A* **2007**, *111*, 1638.

(62) Liu, H.; Wang, Y.; Bowman, J. M. Quantum Calculations of the IR Spectrum of Liquid Water Using ab Initio and Model Potential and Dipole Moment Surfaces and Comparison with Experiment. *J. Chem. Phys.* **2015**, *142*, 194502.

(63) MacKerell, A. D.; Bashford, D.; Bellott, M.; Dunbrack, R. L.; Evanseck, J. D.; Field, M. J.; Fischer, S.; Gao, J.; Guo, H.; Ha, S.; et al. All-atom Empirical Potential for Molecular Modeling and Dynamics Studies of Proteins. *J. Phys. Chem. B* **1998**, *102*, 3586−3616.

(64) Meuwly, M.; Bemish, R. The N_2H^+−He Intermolecular Potential Energy Surface: A Vibrational Adiabatic Correction. *J. Chem. Phys.* **1997**, *106*, 8672−8680.

DOI: 10.1021/acs.jpca.7b02234
J. Phys. Chem. A 2017, 121, 5389−5398

Supporting Information

Vibrational Spectroscopy and Proton Transfer Dynamics in Protonated Oxalate

Zhen-Hao Xu* and Markus Meuwly*

Department of Chemistry, University of Basel, Klingelbergstrasse 80 , CH-4056 Basel, Switzerland.

E-mail: z.xu@unibas.ch; m.meuwly@unibas.ch

Table 1: Parameters used in MMPT force fields for PESs V_1 to V_3 with reaction barriers of 3.5 kcal/mol (V_1), 4.2 kcal/mol (V_2) and 4.5 kcal/mol (V_3), respectively. Among p_1 to p_{14}, only p_1, p_4, p_{10} and p_{11} need to be modified for morphing the barrier height to the desired value.

In $V(R, \rho, d)$	V_1	V_2	V_3
p_1, kcal/mol	357.821	432.288	463.166
p_2, Å^{-1}	1.937	1.937	1.937
p_3, Å	1.622	1.622	1.622
p_4, kcal/mol	-76.859	-92.854	-99.487
p_5, Å^{-1}	-0.855	-0.855	-0.855
p_6, Å^{-2}	1.016	1.016	1.016
p_7, Å	325952	325952	325952
p_8, Å^{-1}	7.040	7.040	7.040
p_9, Å	-0.0638	-0.0638	-0.0638
p_{10}, Å^{-2}	64.0	53.0	49.4
p_{11}, kcal/mol	49.7	60.1	64.3
p_{12}, kcal/mol·Å^{-2}	74.0	74.0	74.0
p_{13}, Å	1.235	1.235	1.235
p_{14}, Å	0.357	0.357	0.357
Force Field for Coupled Representations upon CO Bonds			
$k_{\mathrm{C-OA,I}}$, kcal/mol· Å^2	770	$l_{\mathrm{C-OA,eq,I}}$, Å	1.21
$k_{\mathrm{C-OA,II}}$, kcal/mol· Å^2	310	$l_{\mathrm{C-OA,eq,II}}$, Å	1.36
$k_{\mathrm{C-OC,I}}$, kcal/mol· Å^2	640	$l_{\mathrm{C-OC,eq,I}}$, Å	1.24
$k_{\mathrm{C-OC,II}}$, kcal/mol· Å^2	580	$l_{\mathrm{C-OC,eq,II}}$, Å	1.28
Charges			
q_{C}	0.653 $\boldsymbol{e}$	$q_{\mathrm{H^*}}$	0.356 $\boldsymbol{e}$
q_{OA} and q_{OB}	-0.633 $\boldsymbol{e}$	q_{OC} and q_{OD}	-0.698 $\boldsymbol{e}$

Table 2: Vibrational frequencies (cm^{-1}) of minimum energy (MIN) and transition state (TS) geometries of p-Oxa from the calculations by using MMPT force field with PES V_3 (MMPT-V_3) and the MP2/6-311++G(2d,2p) level (MP2), compared with MMPT-MD (using PES V_3 at 300 K) simulated and experimental spectra (ν_8 to ν_{15} were not further analyzed).[2]

a) MIN

Vibration	MMPT-V_3	MP2	MMPT-MD	Experiment[2]	Description
ν_1	2835	3206	2860	2600∼3400	OH stretch
ν_2	1706	1792	1765	1770∼1820	C=O stretch
ν_3	1650	1709	1715	1675∼1700	CO_2 asymmetric stretch
ν_4	1385	1454	1410	1380∼1430	OH bend
ν_5	1282	1316	1335	1250∼1330	CO_2 symmetric stretch
ν_6	1057	1125	1095	1090	C-O stretch
ν_7	929	968	920	940	H, out of plain
ν_8	850	852	-	-	C, out of plain, symmetric
ν_9	697	828	-	-	OCO bend, symmetric
ν_{10}	590	702	-	-	OCO bend, asymmetric
ν_{11}	389	567	-	-	OCC bend, asymmetric
ν_{12}	521	492	-	-	C, out of plain, asymmetric
ν_{13}	542	434	-	-	C-C stretch
ν_{14}	285	301	-	-	OCC bend, symmetric
ν_{15}	97	103	-	-	C-C bond rotation

b) TS

vibration	MMPT-V_3	MP2	Description
ν_1	2088	2105	OH bend
ν_2	1759	1768	C=O stretch, asymmetric
ν_3	1658	1722	C=O stretch, symmetric
ν_4	1288	1305	C-O stretch, symmetric
ν_5	884	1289	H, out of plain
ν_6	1171	1282	C-O stretch, asymmetric
ν_7	602	862	OCO bend, asymmetric
ν_8	854	857	C, out of plain, symmetric
ν_9	828	753	OCO bend, symmetric
ν_{10}	709	707	C-C stretch
ν_{11}	420	605	OCC bend, asymmetric
ν_{12}	545	498	C, out of plain, asymmetric
ν_{13}	294	334	OCC bend, symmetric
ν_{14}	184	143	C-C bond rotation
ν_{15}	-1305	-1116	Imaginary frequency

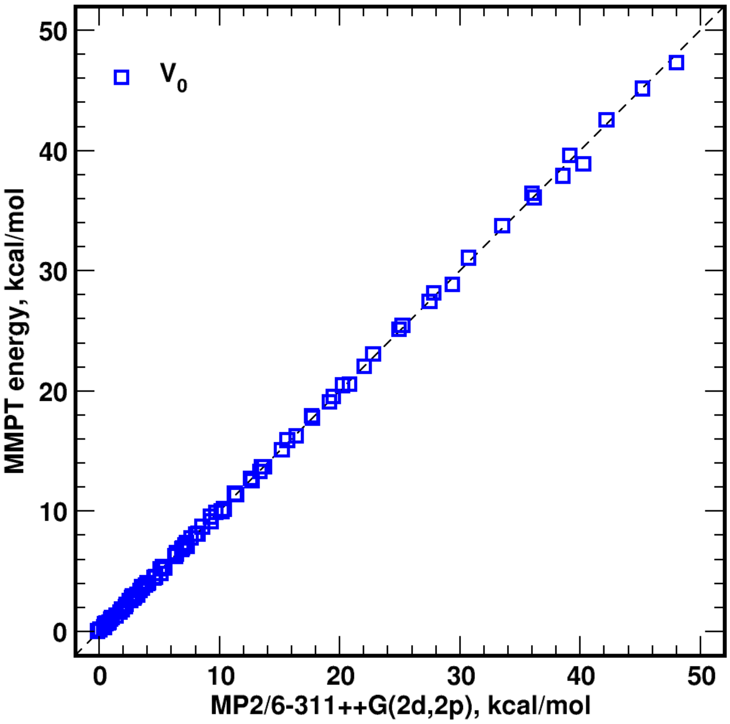

Figure 1: Comparison of the isotropic part $V_0(R, \rho)$ between reference MP2/6-311++G(2d,2p) and the MMPT data. The weighted RMSE is 0.2 kcal/mol.

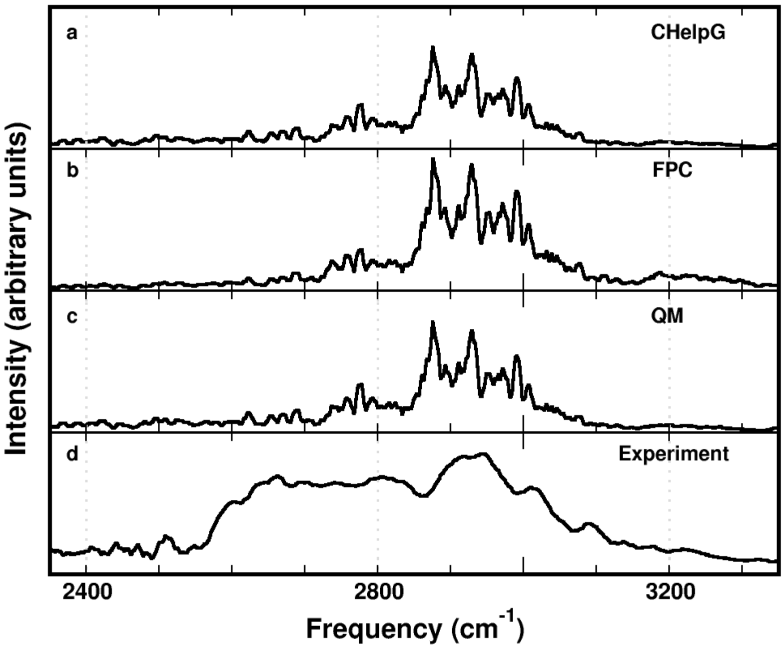

Figure 2: Analysis of IR spectra for $p-$Oxa from MD-B3LYP simulations by using different charge models: a) CHelpG charges; b) fixed point charges (in classical MD simulation) and c) from self-consistent calculation. They are also compared with d) experimental data.

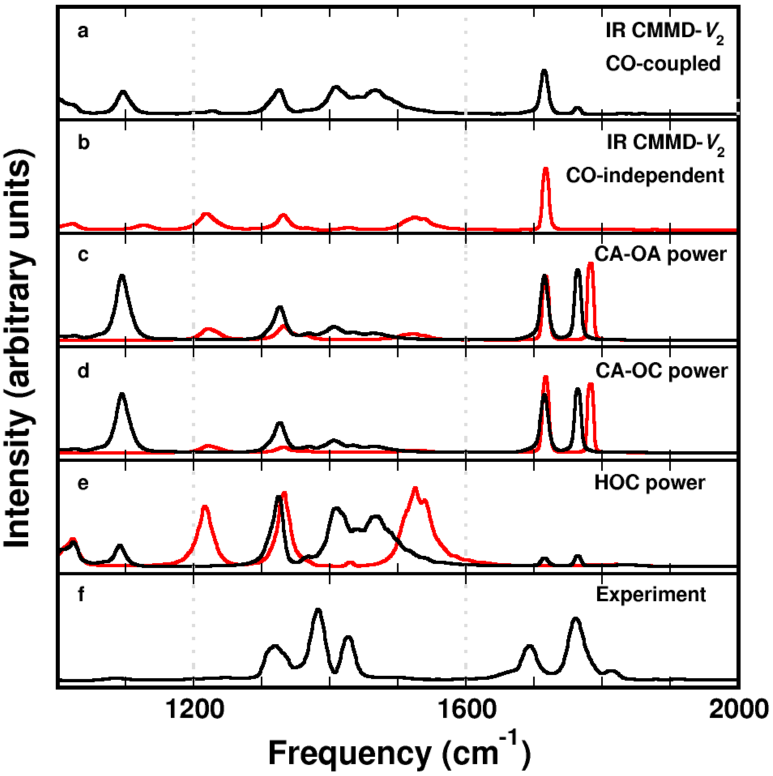

Figure 3: IR and power spectra of $p-$Oxa between 1000 and 2000 cm^{-1} from the simulations by MMPT force field with PES V_2 at 600 K with a) coupled (black) and b) independent (red) representation for CO-bonds. Power spectra of c) CA-OA and d) CA-OB bonds and e) HOC bend with the black and red traces corresponding to infrared traces a and b respectively; f) Experimental data.

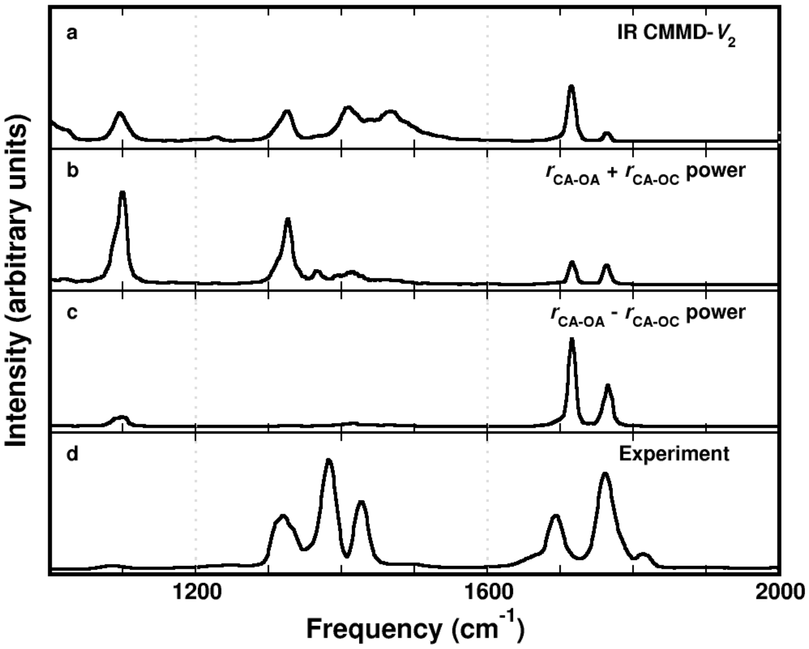

Figure 4: Analysis for assignments of CO_2 asymmetric and CO_2 symmetric stretching modes: a) IR spectra of $p-$Oxa from the simulations with PES V_2 at 600 K; Power spectra of b) the sum and c) the difference of the bond lengths of CA−OA and CA−OC; d) Experimental data.

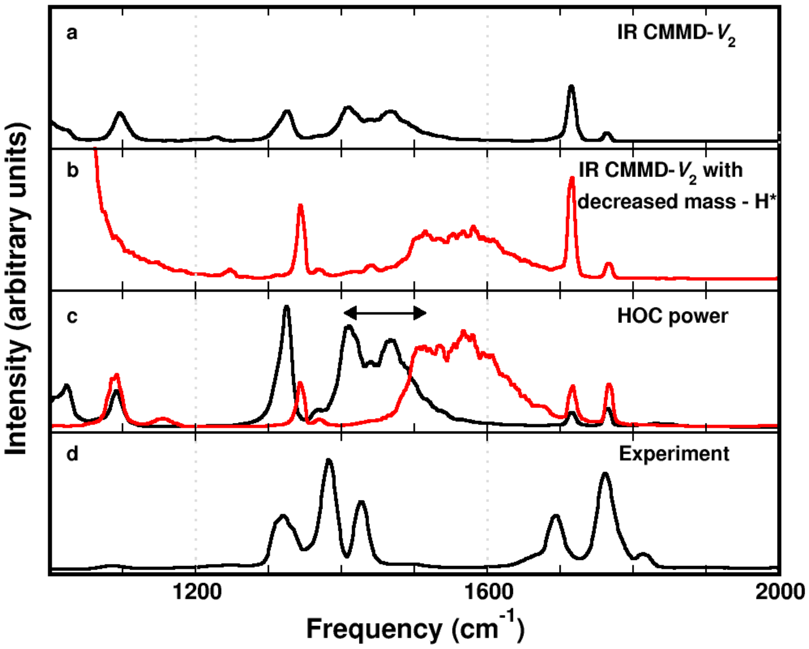

Figure 5: Test simulations with decreased mass for H* (0.8 m_H): IR spectra of p−Oxa from the simulations with PES V_2 at 600 K with a) standard H* and b) lighter H*; c) Power spectra of HOC bends with the black and red traces corresponding to infrared traces a and b respectively; d) Experimental data.

References

(1) Yang, Y.; Meuwly, M. A Generalized Reactive Force Field for Nonlinear Hydrogen Bonds: Hydrogen Dynamics and Transfer in Malonaldehyde. *J. Chem. Phys.* **2010**, *133*, 064503.

(2) Wolke, C. T.; DeBlase, A. F.; Leavitt, C. M.; McCoy, A. B.; Johnson, M. A. Diffuse Vibrational Signature of a Single Proton Embedded in the Oxalate Scaffold, $HO_2CCO_2^-$. *J. Phys. Chem. A* **2015**, *119*, 13018–13024.

Additional graphs

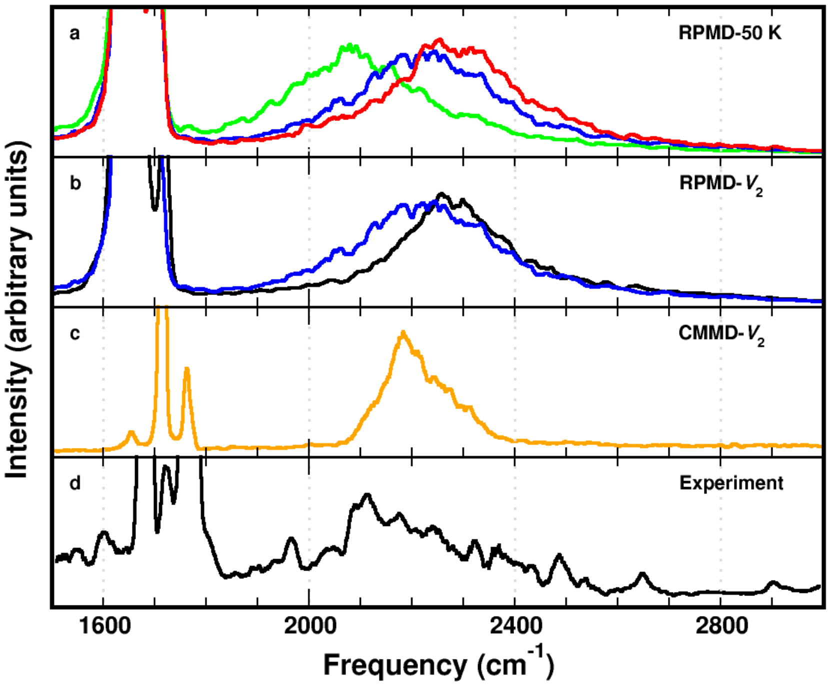

Figure 5.1.: From top to bottom: a) The simulated IR spectra of deuterated oxalate (d–Oxa) from RPMD simulations with 128 beads per particle at 50 K with PES V_1 (green, $E_b = 3.5$ kcal/mol), V_2 (blue, $E_b = 4.2$ kcal/mol) and V_3 (red, $E_b = 4.5$ kcal/mol); b) The RPMD spectra at 50 K (blue, the same to panel a) and 300 K (black) with PES V_2; c) The spectrum from classical MD (CMMD) simulations at 600 K with PES V_2; d) The experimental data.[11] The MMPT force field is the same to what had been used for MD simulations of protonated oxalate (p–Oxa), namely no further parametrization was specifically carried on for simulating both classical and quantum spectra for d–Oxa.

6. Application II: Kinetic Isotope Effects of Malondialdehyde and Acetylacetone

In this chapter, MD simulations of non-linear proton transfer reactions for malondialdehyde (MAL) and acetylacetone (AcAc) were revised with the MMPT force field. Both simulations using MMPT force field (with the non-linear transfer model) had been carried out for computing reaction kinetics and spectroscopy.[12,18,26] In these previous studies, the force field parameters were determined and spectroscopies were compared to the experimental data, especially in OH-stretching frameworks. In the current work, the reaction kinetics for MAL and AcAc was continued and simulations in the gas phase were studied, in addition with primary isotope effects. In order to include quantum effects to the systems, MMPT force field has been integrated into a path-integral approach in the CHARMM program.[168–170]

6.1. Classical MD simulation

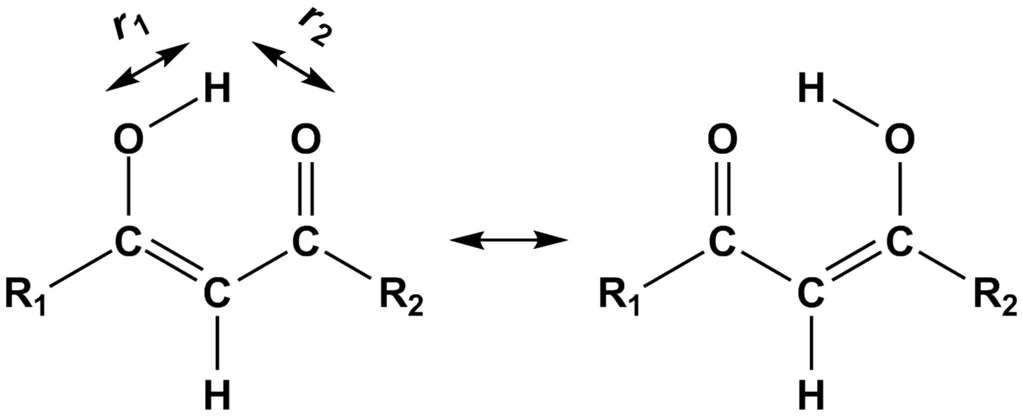

Figure 6.1.: Intra-molecular PT reactions of malondialdehyde ($R_1 = R_2 = H$) and acetylacetone ($R_1 = R_2 = CH_3$) in enol forms.

As previously mentioned in Sec. 3.1.1, the model systems for PT reactions with non-linear paths were parametrized to reproduce the results from *ab initio* calculations and to be spectroscopically accurate.[12,26] To revise the formulation of MMPT, a PES for describing a non-linear proton transfer model (NLM) can be given as a sum of double Morse functions and a harmonic approximation to the angular degree of freedom (DOF) with respect to the H^* atom (See Eq. 3.17). The isotropic part $V_0(R, \rho)$ is obtained by morphing a barrier-contained SDM potential (Eq. 3.4, $H_3NH^+ \cdots NH_3$) which provides two symmetric energy minimums. $V_d(R, \rho, d)$ is a harmonic approximation to the bending degree of freedom. A detailed explanation for Eq. 3.17 was provided in Ref. 26.

Up to here the MMPT force field makes it possible to understand the reaction kinetics (in particular the chemical contribution) of a non-linear PT reaction by doing classical but reactive MD simulations. A thorough investigation of such barrier-contained reactions requires the inclusion of quantum effects which include but are not limited in zero point energies and tunneling effects. Currently, there have been several methods which are able to simulate tunneling effects[171–173] but all of them are time demanding quantum simulation methods. Zero point vibrational effects (ZPVE) are one of the most important quantum which had been extensively studied.[174–176] The zero point energy (or ground state energy) is the lowest possible energy of a quantum mechanical system. Unlike the interpretation from classical mechanics, quantum systems constantly fluctuate in their lowest energy states (which never vanish) due to the Heisenberg uncertainty principle.[177–179] Within classical MD simulations, Fernandez-Serra *et al.*[180] introduced a selective mode thermostatting scheme, which combines generalized Langevin equation (with suppressed noise) and Nose-Hoover thermostats and can easily include quantum zero-point vibrational effects. For MMPT force field, there gives an alternative and straightforward way to include ZPVE, which is to morph the electronic potential surface until a desired barrier is reached. This approximate approach can be justified by the followings: Regarding the degree of freedom for the reaction coordinate, around the energy minimum region the transition mode vibrates with a high energy (or frequency) which is, however, missing in the transition state. Therefore, the ZPVE usually influence the effective potential of motion with respect to the reactive process[181] and the effective barrier is usually decreased from the barrier from the electronic structures. And such reduction captures the difference of reaction kinetics between a molecule and its isotopologue whereas only mapping the electronic potential surface can not achieve it.

In practice, to introduce zero-point effects into classical MD simulations with MMPT force field, $V(R, \rho, d)$ (Eq. 3.17) was further modified as:

$$V_{\mathrm{ZPVE}}(R, \rho, d) = V(R, \rho, d) + E_{\mathrm{ZPVE}}(\mathbf{q}) = V_0(R, \rho) + \sum_{i=0}^{n} \frac{\hbar \cdot \omega_i(\mathbf{q})}{2} \tag{6.1}$$

where $\mathbf{q}$ stands for configurations of the molecule and $\omega_i(\mathbf{q})$ is the non-imaginary frequency of a non-transrotational vibration mode. To obtain the ZPVE correction to the given PT PES, configurations were generated in dimensions of R, ρ and d ($R \in [2.2, 3.0]$ Å with an increment of 0.1 Å, $r \in [0.8, (R - 0.8)]$ Å with an increment of 0.05 Å and $d \in [0.1, 0.5]$ Å with an increment of 0.1 Å). Using MMPT force field, these configurations were energy minimized and based on optimized structures normal mode frequencies were calculated which finally resulted in $E_{\mathrm{ZPVE}}(\mathbf{q})$.

For the malondialdehyde (CHOCHCHOH) and its isotopologue of deuteration (CHOCHCHOD), the classical MD simulations were carried out in the gas phase at 250 K ∼ 1500 K using MMPT force field with ZPVE correction.[26,31] Starting from energy minimized structures, the heating and equilibration were run for 60 ps in total with a time-step of $\Delta t = 0.1$ fs. Then, 50 ns *NVE* productions were followed and configurations were collected every 1 fs in analysis. For calculating the reaction rates of hydrogen/deuterium transfer (HT/DT), the cumulative hazard plots (or survival analysis[182,183]) were employed. In details, each trajectory was divided in n_k residence times ($k = 1, 2, \cdots, n_k$). The length of a residence time was determined by a period in which H* is either bonded to H*−donor (D) or acceptor (A). In the other word, the residence stops as the either of the O-H* bonds is broken, given by a criterion of $r_{\mathrm{D-H^*}} - r_{\mathrm{H^*-A}} = 0$. The residence times were further sorted in ascending order as $\{t_1 < t_2 < \cdots < t_{n_k}\}$. For the j-th residence the cumulative Hazard function can be defined as $H_j = \sum_{i=0}^{j-1} h_i$, where $h_i = 1/(n_k - i)$. Finally, the reaction rate is given by the slope of hazard plots which also suggests the probability expectation of a next occurrence of HT/DT reactions is independent of the residence time[184,185]. All recorded reaction rates were resulted from 10 independent MD simulations (10×50 ns). Simulations and analysis were repeated for acetylacetone and the isotopologues for both molecules.

6.2. Path Integral Simulations

The path integral (PI) simulation method is a description of quantum theory that generalizes the principle of classical mechanics into a regime of quantum mechanics. In this method, the classical concept of a unique and deterministic classical trajectory for a system is replaced with a functional integral of quantum mechanically possible trajectories to compute physical quantities.[186] In the discrete Feynman's path integral method, a quantized particle can be represented by a number of N quasi-particles (beads), connected as a string with harmonic forces acted on each pair of neighboring beads. The coordinates denote as $\mathbf{r} = \{r_1, r_2, \cdots, r_N; r_{N+1} = r_1\}$[187], where r_i ($i = 1, \cdots, N$) is the coordinates of the i-th bead and the centroid is defined as

$$\bar{\mathbf{r}} = \frac{1}{N} \sum_{i=1}^{N} r_i \tag{6.2}$$

For a centroid path integral simulation, the quantum mechanically corrected partition function of a system in the example case with one quantized atom can be expressed as follows[169,170,187],

$$Q_N = \int d\mathbf{S} \int d\mathbf{s} (\frac{N}{2\pi\lambda^2})^{3N/2} \int d\mathbf{R} e^{-\beta V(\mathbf{r},\mathbf{S})}, \tag{6.3}$$

where $\mathbf{S}$ and $\mathbf{s}$ represent for the coordinates of classical (e.g. solvents) and quantized particles, and $\int d\mathbf{R}$ denotes as $\int d\mathbf{R} = \int dr_1 \cdots \int dr_n \delta(\bar{r} = \mathbf{s})$ which indicates the averaged coordinates of all quasi-particles exactly correspond to the classical position of the quantized atom. The effective potential, $V(\mathbf{r})$, is given by

$$V(\mathbf{r}) = \frac{N}{2\beta\lambda^2}\sum_{i=1}^{N}(r_i - r_{i+1})^2 + \frac{1}{N}\sum_{i=1}^{N}U(r_i) \tag{6.4}$$

where the first component is the sum of harmonic potentials between the beads, with $\lambda^2 = \beta\hbar^2/\mu$ denotes as the square of the de Broglie thermal wavelength of a particle with a mass of μ and $\hbar$ is Plank's constant. $U(r_i)$ refers to the external potential, acted on the i-th bead, given by the MMPT force field.

In CHARMM program, Gao *et al.* provided a path integral scheme which calculates the contributions of quantum effects in a free energy surface from classical reactive trajectories. This method is called path integral with bisection quantized classical path sampling (PI-BQCP)[168] and employed to study proton transfer reactions with the correction of quantum effects. In that work, calculations of kinetic isotope effects (KIE) was especially of interests. The value of KIE can be obtained by calculating quantum corrections to the free energies of activation:

$$\text{KIE} = k_{\text{HT}}/k_{\text{DT}} = e^{-\beta(\Delta F_{\text{H}}^{\ddagger} - \Delta F_{\text{D}}^{\ddagger})} \tag{6.5}$$

where k_{HT} and k_{DT} are the reaction rates of HT and DT reactions and $\Delta F_{\text{H}}^{\ddagger}$ and $\Delta F_{\text{D}}^{\ddagger}$ are the energy corrections to free energies of activation.

Later on, the integrated path integral-free energy perturbation/umbrella sampling (PI-FEP/UM) method was developed for reducing statistical errors.[169] Here, it needs to be stressed that error reduction can be fundamentally important if the difference in reaction kinetics between unsubstituted and isotopically substituted systems is too small to be observed (KIE $\simeq$ 1). This can happen in calculating reaction rates of a reaction which involves with ^{12}C-^{13}C or ^{14}N-^{15}N isotope substitution. For example of primary ^{12}C/^{13}C kinetic isotope effects for the decarboxylation of N-methyl picolinate in water,[169] PI-BQCP gives KIE $= 1.0346 \pm 0.8773$ ($\pm$85%) and the error was considerably decreased to $\pm$0.3% using PI-FEP/UM method (KIE $= 1.0345 \pm 0.0028$). In the PI-FEP/UM method, the value of KIE can be factorized as

$$\text{KIE} = \frac{Q_{\text{H}}(\bar{z}_{\text{H}}^{\neq})}{Q_{\text{D}}(\bar{z}_{\text{D}}^{\neq})} / \frac{Q_{\text{H}}(\bar{z}_{\text{H}}^{\text{R}})}{Q_{\text{D}}(\bar{z}_{\text{D}}^{\text{R}})} \cdot e^{-\beta(F^{\text{R}}(\bar{z}_{\text{H}}^{\text{R}}) - F^{\text{R}}(\bar{z}_{\text{D}}^{\text{R}}))} \tag{6.6}$$

where $\bar{z}^{\mathrm{R}}$ and $\bar{z}^{\neq}$ stand for the centroid reaction coordinates at reactant and transition states, respectively. Q_{H} and Q_{D} are the quantum mechanical partition functions with the transferring H* treated as hydrogen (H) and deuterium (D), and $F^{\mathrm{R}}(\bar{z}^{\mathrm{R}}_{\mathrm{H/D}})$ is the vibrational free energy of the mode at the reactant state that correlates with the progress coordinate.[170] All technical details for PI-BQCP and PI-FEP/UM method can be found in Ref. 168–170.

For HT/DT reactions in MAL, path-integral simulations was first carried out with conventional umbrella sampling simulations using the MMPT force field (to note that here ZPVE is not needed for correction). For each selected temperature between 250 K and 1500 K, heating and equilibration simulation were run for 20 ps. Then, harmonic constraints ($k = 50\ \mathrm{kcal \cdot mol^{-1} \cdot Å^{-2}}$) were applied to the reaction coordinate $z = r_1 - r_2$ (see Figure 6.1) between $z = -0.9$ and $z = 0.9$ Å. The equilibrations were further extended by 50 ps with the constraint applied for each UM window and production simulations were then run for 1 ns at the NVT ensemble. For every recorded configuration (every 10 ps), the quantum mechanical partition function was calculated with $N = 256$ beads for both HT and DT reactions.

6.3. Results and Discussion

6.3.1. Classical MMPT Simulations and Kinetic Isotope Effects

For HT/DT reactions of Mal, using MMPT force field simulations were carried out for selected temperatures from 250 K $\sim$ 1500 K at the gas phase. Figure 6.2 shows examples of hazard analysis for 50-ns simulations at 300 K for both HT and DT, in which the $x-$axis refers to the residence period between two neighboring transfer events while the $y-$axis stands for the cumulative hazard function (discussed in Section 6.1). For HT reaction, approximately 33000 residence times were found from MMPT simulations and ~80% of all data were found at $t < 0.5$ ps. For data points with low residence time, these corresponds to fast hops which across the transition state regions forth and back.[188] And that is attributed to recrossing effects[189,190] for a barrier-contained reaction, which is not considered of real contributions into reaction rates. Therefore, only long residence times t_k were taken into account. As a result, the cumulative hazard function leads to that the data agree with a linear relationship with the residence time and the slope of the plot should correspond to reaction rates. For HT reaction at 300 K, the reaction rate is 0.047 ps^{-1} while for DT reaction the rate decreased to 0.012 ps^{-1}. Moreover in

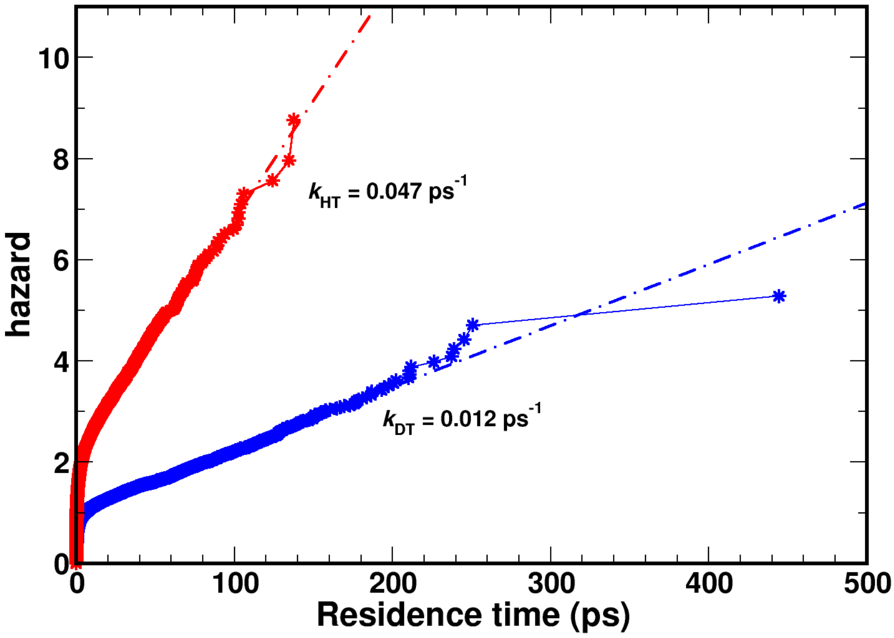

Figure 6.2.: Hazard plots of classical MMPT simulations using ZPVE corrected force field. Simulations were run at 300 K for HT and DT. The fitting lines record fits of data above $t = 5$ ps and data with extraordinarily lone residence time were removed from fitting as well.

Figure 6.2, for those data with the longest residence periods it was found that they are not accurately located on the fitted lines which eventually give the reaction rate. For the example of the rightmost point in the hazard plot for DT reaction, it refers to a extremely long residence time (445 ps) in which there was no reaction occurred. The expect hazard value for this residence time is 6.4 but the data yield with a lower 5.2. That is due to the limitation with the given length of MD simulations so such rare events have yet to be statistically meaningful unless long enough MD simulations are run.

The computed reaction rates of HT and DT reactions from MMPT-MD simulations are given in Table 6.3.1 for both malondialdehyde and acetylacetone. Starting with the case of Mal, for the ZPVE-corrected PESs the barriers for H- and D-transfer were reduced to 2.1 and 2.8 kcal/mol (from 4.3 kcal/mol with the original MMPT parameters without ZPVE correction[26]), respectively. The simulations yield with reaction rates ranging from 0.020 ps^{-1} to 2.6 ps^{-1} for temperatures from 250 K and 1500 K. As expected, DT reaction rates are lower than those for HT reactions due to

Table 6.1.: The kinetic isotope effects from classical MD simulations using MMPT force field with zero-point energy correction for malondialdehyde and acetylacetone. Results from MD simulations with ZPVE uncorrected MMPT force field are shown only at 300 K for Mal. The statistical errors are given in brackets and correspond to the last digits for each calculated value.

	Mal		
T (K)	k_{H}, ps^{-1}	k_{D}, ps^{-1}	KIE
1500	2.6(1)	1.6(1)	1.6(1)
750	0.96(3)	0.47(2)	2.0(2)
500	0.30(1)	1.2(1)	2.5(2)
375	0.12(1)	0.035(3)	3.3(4)
300	0.047(1)	0.012(1)	4.1(4)
250	0.020(1)	0.0033(4)	5.9(10)
300 (w/o ZPVE)	0.009(2)	0.010(3)	0.9(5)

	AcAc		
T (K)	k_{H}, ps^{-1}	k_{D}, ps^{-1}	KIE
1500	8.1(3)	5.4(2)	1.5(1)
750	4.5(3)	2.5(2)	1.8(2)
500	2.3(2)	1.2(1)	1.9(2)
375	1.5(1)	0.66(2)	2.2(2)
300	0.98(6)	0.39(2)	2.5(3)
250	0.69(2)	0.23(1)	2.9(2)

the increased mass. Results range from 0.0033 ps^{-1} to 1.6 ps^{-1} at the same range of temperatures. It was also obviously found that with the increase of temperature the reaction rates of DT evolved faster and approached closer to that of HT reaction. This can be analyzed by calculating kinetic isotope effects. At the low temperature (e.g. 250 K) the KIE value gives 5.9 ± 1.0 while at the high temperature (1500 K) KIE was found equal to 1.6 ± 0.1. That suggests the mass effect becomes less significant at high temperatures and the rate differences between HT and DT tend to be zero at an infinite high temperature. Test simulations were also carried out at 300 K, using the original MMPT parameters (with ZPVE not considered) for Mal. The averaged reaction rates were 0.009 ± 0.002 ps^{-1} and 0.010 ± 0.003 ps^{-1} for HT and DT respectively. From the simulation standpoint, the isotope effects are due to the change of mass and PES in which the reactive simulations were performed. The current results may imply that the change of mass may not be the main reason that attributes into the difference of reaction rates between HT and DT. The previous study calculated rates for HT/DT in malondialdehyde by using conventional transition state theory (CTST).[191] For a comparison, the CTST method gives rates of 0.540 ps^{-1} and 0.080 ps^{-1} for HT and DT reactions at 300 K, respectively, which are around 11- and 7-fold larger than those from the rates obtained by MD simulations.

For acetylacetone, similar analysis was carried out. Within MMPT modeling the reaction barrier of the transfer reactions is 2.1 kcal/mol using original MMPT parameters (without ZPVE correction). With zero-point energy correction, the force field gives reduced barriers of 1.0 and 1.8 kcal/mol for HT and DT respectively. Compared to the results for Mal, for AcAc the reaction rates were found all higher than those from simulations for Mal with equivalent input conditions (i.e. temperatures, HT/DT etc.). For MD simulations of AcAc, the KIE values range from 2.9±0.2 (250 K) to 1.5±0.1 (1500 K), which implies the deuteration effects are also less significant if the barrier of a reactive potential surface is reduced.

6.3.2. Umbrella Sampling Based Path Integral Simulations

From classical MMPT simulations, only the chemical contribution of KIEs were considered and computed. In order to introduce quantum effects into the systems, the path integral simulations were carried out for malondialdehyde and all results were reported in Table 6.2. As mentioned in Sec 6.2, there are two schemes for obtaining KIEs. One is the PI-FEP/UM scheme which refers to Eq. 6.6 and the other is the BQCP scheme which directly calculates the difference of free energies of activation.

Table 6.2.: The kinetic isotope effects from PI-BQCP and PI-FEP/UM simulations[169] using MMPT potential for malondialdehyde. All contributing components are given for computing the overall KIE values, according to Eq. 6.5 and Eq. 6.6. The statistical errors are given in brackets and stand for the last digits for each calculated value. $\mathrm{KIE}_{F^{\mathrm{R}}} = e^{-\beta(F^{\mathrm{R}}(\bar{z}_{\mathrm{H}}^{\mathrm{R}}) - F^{\mathrm{R}}(\bar{z}_{\mathrm{D}}^{\mathrm{R}}))}$

T (K)	$\frac{Q_{\mathrm{H}}^{\mathrm{QM}}(\bar{z}_{\mathrm{H}}^{\neq})}{Q_{\mathrm{D}}^{\mathrm{QM}}(\bar{z}_{\mathrm{D}}^{\neq})}$	$\frac{Q_{\mathrm{H}}^{\mathrm{QM}}(\bar{z}_{\mathrm{H}}^{\mathrm{R}})}{Q_{\mathrm{D}}^{\mathrm{QM}}(\bar{z}_{\mathrm{D}}^{\mathrm{R}})}$	KIE_{Q}	$\mathrm{KIE}_{F^{\mathrm{R}}}$	$\mathrm{KIE}_{\mathrm{FEP/UM}}$
1500	0.9907(9)	0.7711(11)	1.285(3)	0.9611	1.235(3)
750	0.9395(30)	0.4488(19)	2.093(16)	0.9235	1.933(15)
500	0.8493(47)	0.2219(19)	3.827(54)	0.8915	3.412(48)
375	0.7123(75)	0.1082(8)	6.583(118)	0.8595	5.658(101)
300	0.5513(54)	0.04318(51)	12.77(28)	0.8238	10.52(23)
250	0.3969(62)	0.01603(19)	24.76(67)	0.7235	17.91(48)
T (K)	$\Delta F_{\mathrm{H}}^{\ddagger}$		$\Delta F_{\mathrm{D}}^{\ddagger}$		$\mathrm{KIE}_{\mathrm{BQCP}}$
1500	4.581(11)		5.281(6)		1.26(1)
750	2.851(12)		3.828(5)		1.93(4)
500	1.987(17)		3.144(9)		3.20(15)
375	1.439(17)		2.680(9)		5.29(38)
300	1.018(15)		2.293(10)		8.48(69)
250	0.624(13)		1.976(8)		15.2(14)

Table 6.2 reports all necessary components for calculating KIE values. Using the FEP/UM scheme, with the evolution of temperatures KIE values decreased from 17.91 ± 0.48 to 1.235 ± 0.003. Figure 6.3 shows the ratios of quantum corrections to the partition functions of given UM trajectories with the free energy profile along with the reaction coordinates. From UM simulations, the classical free energies of activation evolve from 4.8 to 6.3 kcal/mol from 250 K to 1500 K. Using the BQCP scheme, the quantum corrected free energies of activation were also given in Table 6.2. The barriers for HT reactions were from 0.624 ± 0.013 kcal/mol at 250 K to 4.581 ± 0.011 kcal/mol at 1500 K, while for DT reactions they are slightly higher which are from 1.976 ± 0.008 kcal/mol at 250 K to 5.281 ± 0.006 kcal/mol at 1500 K. Compared to the classical free energies of activation, introducing the quantum effects in fact reduced the effective barriers in all range of selected temperatures. The kinetic isotope effects yield with a range of 1.26 ± 0.01 $\sim$ 15.2 ± 1.4 from 1500 K to 250 K. Compared to the result from the FEP/UM scheme, using the BQCP scheme led to larger statistical errors into KIE values, of which the maximum error is up to ± $\sim$10% (< 3% in the FEP/UM scheme at 250 K). That is due to

error propagation during the calculating Eq. 6.5, whereas the FEP/UM scheme shows an advantage in avoiding of such error amplifications by calculating direct ratios of partition function. KIE values from malondialdehyde simulations using both classical MMPT MDs and path integral methods were summarized in Figure 6.4. For the current work, all results suffice the linear relationship between $1/T$ and KIE values in a logarithmic form, which also agrees with the previous studies[18].

It needs to note that the current path integral approach could be only suitable for reactive systems with relatively high barrier heights. Literatures[168,169] reported studies using the current path integral approach for reactive systems which give the barrier heights in a range of 6 to 25 kcal/mol. And no systems with lower barriers were studied. In this approach, all quantum simulations were based on the given classical trajectories from UM samplings. Based on the given potential of mean force, quantum corrections were applied in forms of free energy correction. If the barrier is too low, such correction may change the fundamental topology of the potential surface and consequently the equilibrium geometries will be shifted along the reaction coordinate. Thereby, F_R can not be easily determined. Hence, path integral simulations for AcAc were not reported because of the low barrier. And it would be more meaningful that direct MD simulations can be performed by other techniques like centroid molecular dynamics[192,193] and ring polymer molecular dynamics (RPMD) is another useful approach (i.e. RPMDrate[194,195]) to calculate reaction rates.[196–202]

6.4. Summary

To sum up, the kinetics isotope effects were computed from MD simulations using classical MMPT force field and the path integral approaches. For the classical MMPT simulations of Mal and AcAc, ZPVEs were introduced into the effective PESs. For these unimoleuclar reactions, the barrier heights were reduced to 2.1 and 2.8 kcal/mol for HT and DT reactions in Mal and to 1.0 and 1.8 kcal/mol for HT and DT reactions in AcAc, respectively. That leads to differentiations of reaction rates between the non-substituted molecule and its deuterated isotopologue. The KIE values ranges from 1.6 to 5.9 for Mal and 1.5 to 2.9 for AcAc at selected temperatures from 1500 K to 250 K. Different KIEs between Mal and AcAc in the simulations at the same temperature are due to the different barriers. In addition to the classical MD simulations, using path integral technique introduced the nuclear quantum effects into the systems. For the reaction in Mal, KIEs were found between 1.235 (1500 K) and 17.91 (250

K) using the PI-FEP/UM scheme and between 1.26 (1500 K) and 15.2 (250 K) using the PI-BQCP scheme which led to relatively larger statistical errors. For both classical and quantum simulations, results were compared to those from previous studies and similarly sufficed linear correlation to 1/T.

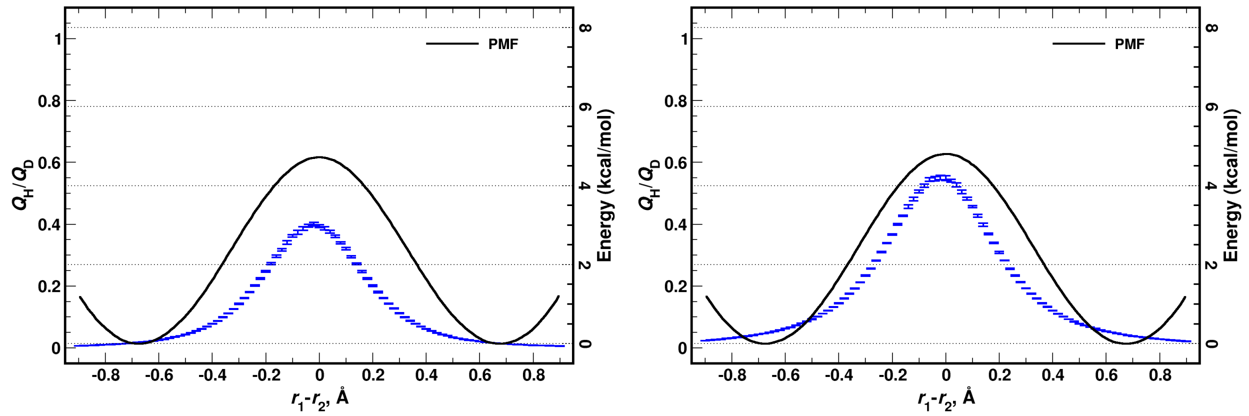

(a) T=250K (b) T=300K

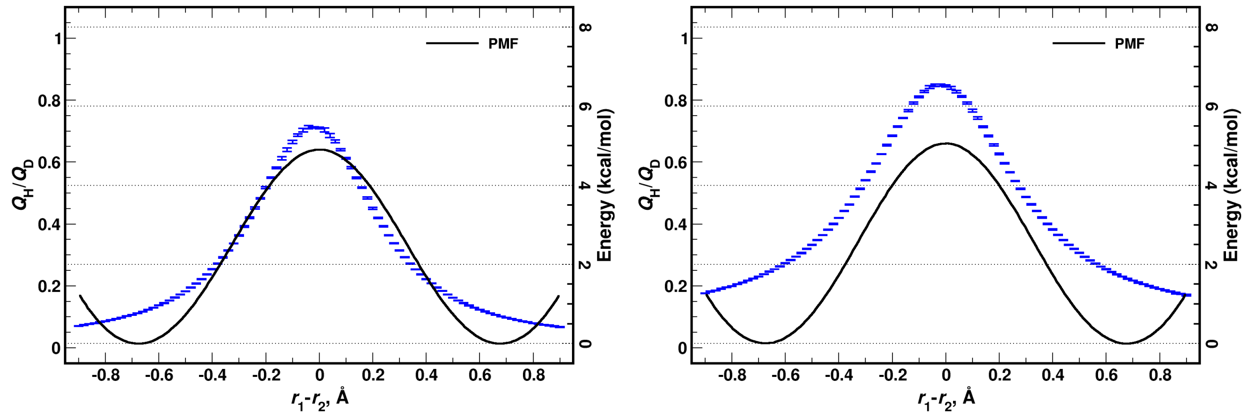

(c) T=375K (d) T=500K

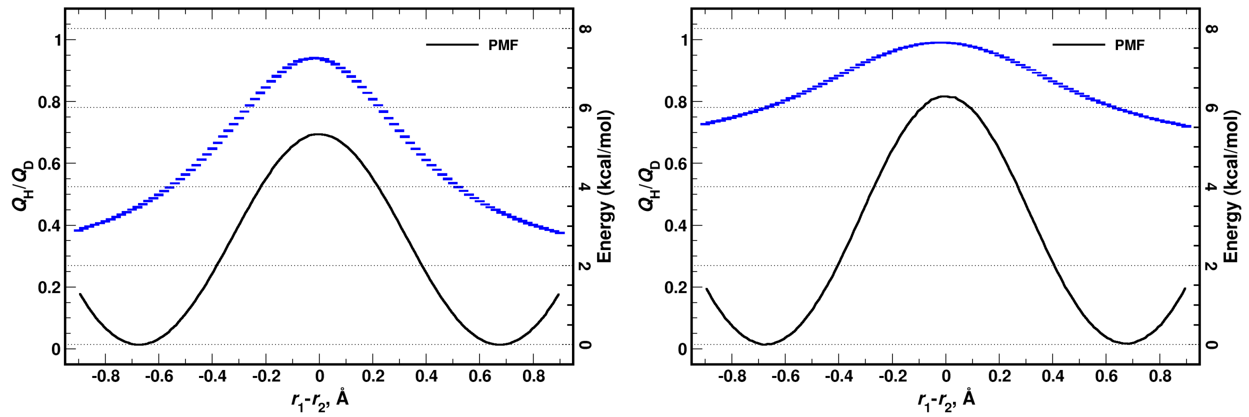

(e) T=750K (f) T=1500K

Figure 6.3.: 1) Blue data points: the ratio of quantum corrections to partition functions for [O_1-$H^* \cdots O_2$] hydrogen transfer reaction of Mal and its deuterated isotopologue; 2) Black curves: classical potentials of mean force of this reaction (HT). The reaction coordinate is defined as $r_{O_1H^*} - r_{O_2H^*}$

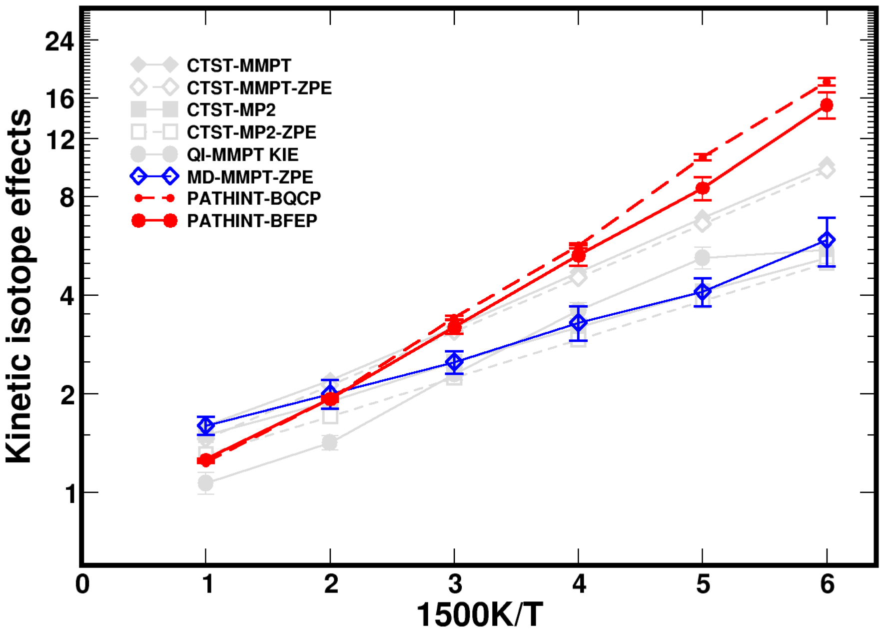

Figure 6.4.: Temperature dependence of KIEs for malondialdehyde by using different methods: 1) MD simulations using MMPT force field with ZPVE corrected PT potential (blue solid) and 2) path integral simulations with PI-BQCP (red solid) and PI-BFEP (red dashed) schemes. The data of other plots (gray) are Ref. 18 which correspond to 3) conventional transition state theory using MMPT force field (solid and dashed with diamonds) and MP2 method (solid and dashed with squares)[191] and 4) quantum instanton path integral Monte Carlo simulations (solid lines with round dots).

7. Application III: Grotthuss Proton Transport in Aqueous Systems

7.1. Simulation Details

All MD simulations were performed using the MS-MMPT force field for water clusters ($[H_2O]_nH^+$, n = 6, 10, 21, 31, 50 and 100) in the gas phase and water bulks with one excess proton, using the CHARMM-c39b1 package.[31] In order to avoid water molecules from diffusing to the vacuum, for water clusters all atoms are constrained to the center of mass with a weak force constant of $k = 0.001$ kcal·mol^{-1}·Å^{-2}. Starting from the energy optimized structure, heating and equilibration (NVT, 300 K) simulations were respectively run for 10^5 MD steps with a time-step of $\Delta t = 0.1$ fs because bonds involving H-atoms are flexible. For water clusters, 1 ns production simulations were carried out in micro-canonical ensembles (NVE) and the entire procedures (from heating to production) were repeated to collect 10 independent trajectories. For bulk systems, 16 MD trajectories were collected in the same way (500-ps for each production). The solvent water molecules were modeled by SPC/fw water model[145,146] but with MP2 equilibrium in bonded energy terms. Snapshots for analysis were collected every 5 fs.

7.2. Results I: MD Simulations of $[H_2O]_nH^+$ Water Clusters

7.2.1. Minimum energy structures of $[H_2O]_nH^+$ water clusters

Minimum energy structures were calculated for $[H_2O]_nH^+$ ($n = 2, 3, 4, 6$). Results were compared with optimized structures from MP2/6-311++G(d,p) calculations. In general, the results from MS-MMPT are in good agreement with those from MP2 references. Table 7.1 records important internal coordinates of water clusters and the deviation from MS-MMPT data to the reference MP2 calculations is lower

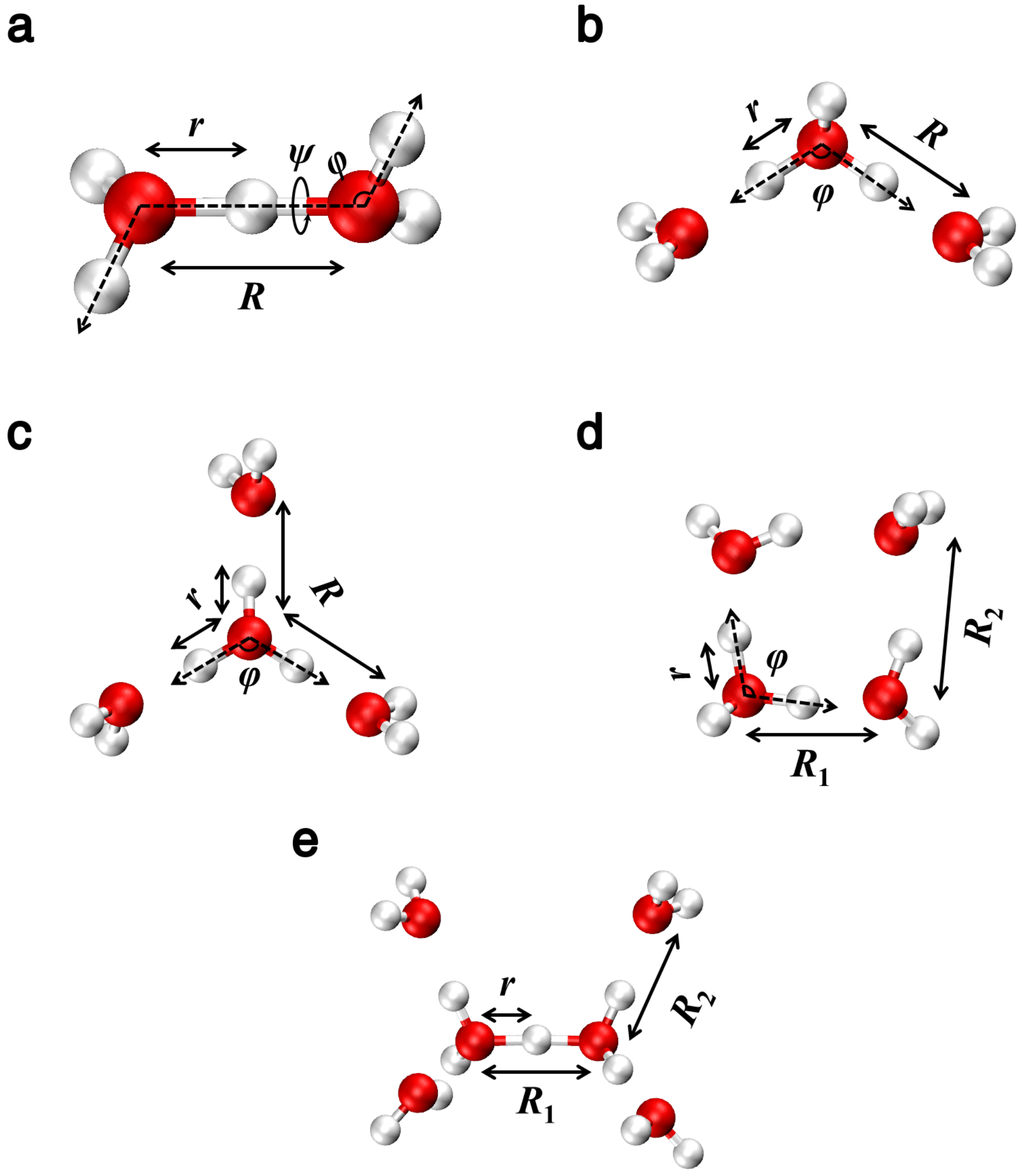

Figure 7.1.: The minimum energy conformations of $[H_2O]_nH^+$ ($n = 2, 3, 4, 6$) using the MS-MMPT force field and the MP2/6-311++G(2d,2p) level of theory.

Table 7.1.: Geometric values for optimized $[H_2O]_nH^+$ conformations in Figure 7.1.

$[H_2O]_nH^+$		MMPT	MP2
$n = 2$	r	1.179 Å	1.196 Å
	R	2.395 Å	2.389 Å
	ϕ	117.0°	114.4°
	ψ	-137.7°	-113.3°
$n = 3$	r	1.019 Å	1.029 Å
	R	2.514 Å	2.499 Å
	ϕ	110.4°	114.1°
$n = 4$	r	1.008 Å	1.005 Å
	R	2.536 Å	2.566 Å
	ϕ	108.4°	112.0°
$n = 4$, ring	r	1.025 Å	1.038 Å
	R_1	2.485 Å	2.488 Å
	R_2	2.830 Å	2.851 Å
	ϕ	108.4°	106.2°
$n = 6$	r_1	1.233 Å	1.195 Å
	R_1	2.464 Å	2.389 Å
	r_2	0.986 Å	0.983 Å
	R_2	2.611 Å	2.678 Å

than 4 % in average. It is also worth to mention that in MP2 calculations those energy-minimum structures show different symmetries with the number of water molecule (n). To detail more, at $n = 3$ and 4 the central part – H_3O^+ of the respective cluster molecules has a typical Eigen structure that the bond lengths of hydrogen-bonded OH bonds are identical to each other. To explain it in an MS-MMPT language, the symmetric Eigen structures can be formed at $n = 3$ and 4 due to the equi-distribution of two and three local states, respectively. In the other word, these two (or three) states are both the energy minimum states and equally contribute to the total potential energies of the systems. As the other local minimum in energy, the loop conformations of $[H_2O]_4H^+$ were both captured using MS-MMPT and MP2 methods. However, compared to the Eigen conformation the loop conformer gives with an energy higher by 11.2 kcal/mol for MS-MMPT but the energy difference is 3.8 kcal/mol for MP2 calculations. This gap of energy estimation is attributed to the deficiency of the force field model for describing water-water interactions which are not specifically parametrized in the current MS-MMPT development. For $n = 6$, however, a Zundel ion is formed by energy minimization. That means among all candidate states only one of them is the energy minimum state which is considerably more stable than other candidate states and weighs most in describing the energetics of a system.

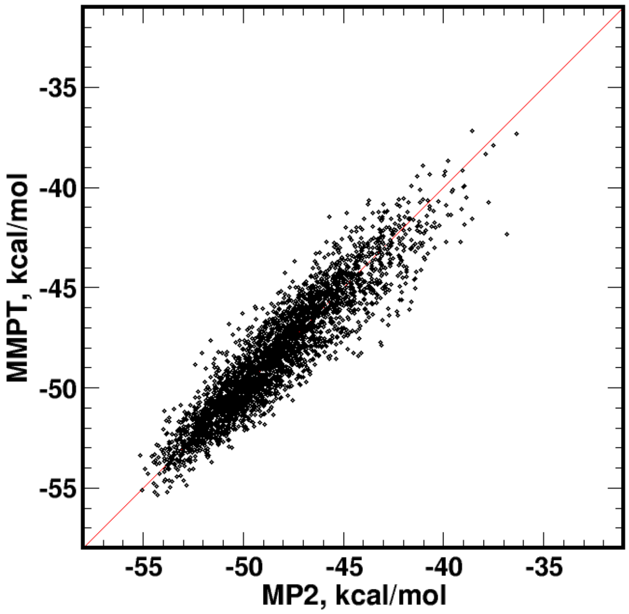

Figure 7.2.: The binding energies of arbitrary MD frames from MMPT simulations for $[H_2O]_3H^+$, compared to *ab initio* calculations at the level of MP2/6-311++G(2d,2p). MD frames were collected from simulations at 300 K.

In prior to massive simulations for obtaining and analyzing the proton diffusivity, test simulations were first carried out for validating parametrization of non-bonded parameters, similar to Figure 4.4 . Figure 7.2 shows the arbitrary MD frames from MS-MMPT simulations for $n = 3$ and the RMSE is 1.2 kcal/mol.

7.2.2. Energy conservation of MS-MMPT simulations

For validating the current MS-MMPT development, the investigations were first carried out for finding whether MD simulations are energy conserved or not. Thereby, the total energies of the simulations (potential + kinetic energy) were recorded from MS-MMPT simulations using both first-shell and second-shell modes. The results are shown in Figure 7.3 for $[H_2O]_{10}H^+$. Using the first-shell mode, the energy has been found well conserved at $\Delta E = 5$ kcal/mol but drifts were seen with $\Delta E = 10$ and 15 kcal/mol with rates of +1.2 and +180 kcal/mol·ns^{-1} , respectively. Using the second-shell mode for MDs for $n = 10$, the energy conservation has been significantly improved for all selected ΔE. Similar to the results for $n = 10$, in other water clusters and water bulks no obvious energy drifts were found

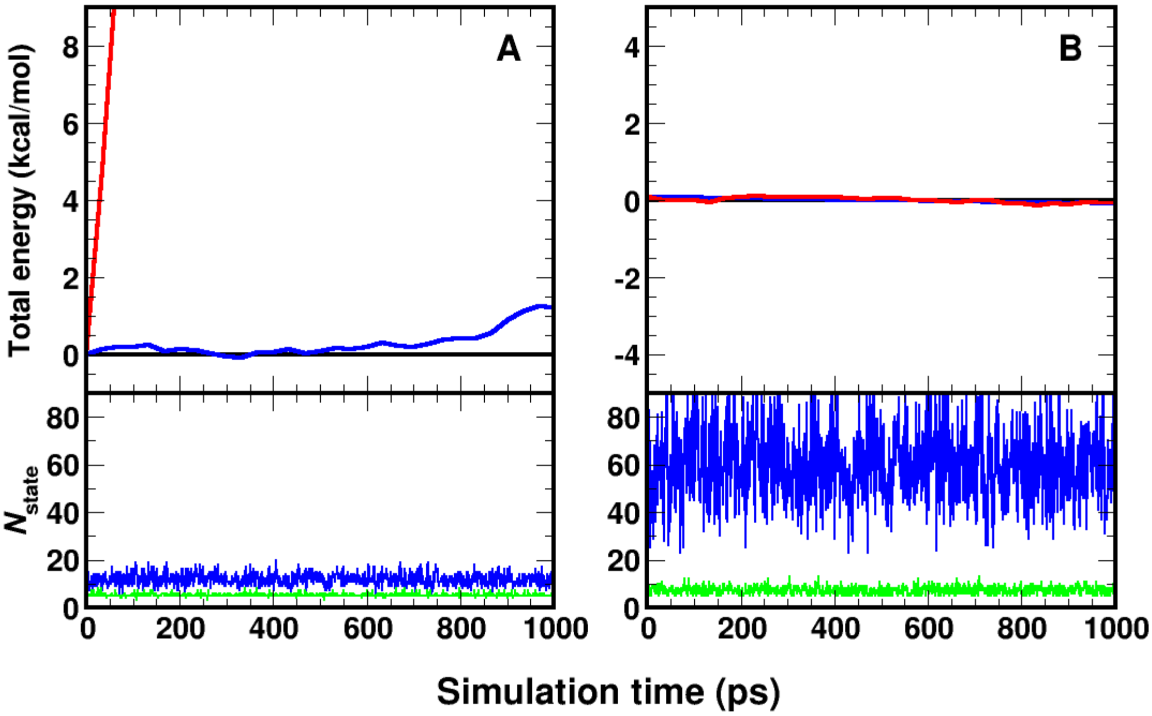

Figure 7.3.: Energy fluctuations from MS-MMPT simulations with $n = 10$, using first- (A) and second-shell (B) modes. For each panel, traces stand for simulations with $\Delta E = 5$ (black), 10 (blue) and 15 kcal/mol (red). For $\Delta E = 10$ kcal/mol, the numbers of included states (blue) and effective states (green, with $w > w_{\mathrm{cutoff}}$) were shown in the bottom panels.

in MD simulations using the second-shell mode.

The improvement of energy conservation from simulations using first-shell mode to using second-shell mode is mainly attributed to the fact that in a larger solvation shell more PT states can be included. Given with the example simulations from Figure 7.3, for simulations with $n = 10$, the average number of PT states is 11.8 (with $\Delta E = 10$ kcal/mol) if the first-shell motifs are considered. When the second-shell mode is considered, the average number of states increases to 60.2. Within the MS-MMPT framework, Eq. 4.13 specifies all necessary terms to constitute a state energy. Practically, $V^{\mathrm{intra}}_{\mathrm{H_5O_2^+}}$ (Eq 4.10) for all selected states (which suffice the geometric criteria) were first computed (fast) and the weights $\{w_i\}$ were calculated (Eq. 4.15-4.16). Next, $V^{\mathrm{inter}}_{\mathrm{H_5O_2^+-solv}}$ (slow) were only computed for states with $w_i > 10^{-11}$ (called as effective states). After all, the total MS-MMPT energy was in fact calculated by re-writing Eq. 4.14 into

$$V_{\text{tot}}(\mathbf{x}) = \sum_{j=1}^{m_{\text{eff}}} w_j(\mathbf{x}) \cdot V_j^{\text{eff}}(\mathbf{x}) \tag{7.1}$$

If only these effective states are counted, the average numbers of states are 5.3 and 7.2 for first- and second-shell modes (see green traces in Figure 7.3), respectively. That substantiates the meaningfulness of introducing the second shell mode because the first-shell mode fails to include sufficient states which are necessary for converging the total potential energies of the system. Failure to do so leads to energy jumps during the simulation, especially when the identity of minimum energy state (with the 'seed' PT motif) is changed. This, in fact, leads to non-conservation of the total energy.

7.2.3. Proton Hops in Water Clusters with One Excess Proton

In order to measure the reactivity of a proton transport process, the analysis was carried out to calculate a time-course accumulation function which probes hopping events with the evolution of time. Hereby, $h(t)$ is given as[76]

$$h(t) = h(t - \delta t) + \delta h(t) \tag{7.2}$$

where t is the simulation time and δt is the step size between collected frames ($\delta t = 5$ fs). Initially, $h(t = 0) = 0$, and for each new MD frame $\delta h(t)$ assumes one of three values: 0, 1 and -1. $\delta h(t) = 0$ if the proton does not hop; $\delta h(t) = +1$ if the proton hops to a new donor atom and $\delta h(t) = -1$ if the proton hops backward to the donor from the previous frame.

Figure 7.4 shows such a plot using the time-course accumulation function. In this figure, MD simulations for $n = 6$ and $n = 10$ with $\delta E = 10$ kcal/mol were reported and the identities of H*-carrying oxygen (determined by a geometric criterion[203] (to be discussed in Sec. 7.2.4) and indexing from 1 to n) were recored as a function of simulation time (see the inset of Figure 7.4). The index plot for $n = 10$ appears with a denser pattern which suggests 'busy' proton hopping activities. For $n = 6$, PT events occurred much less frequently. From literatures[57,58], $h(t)$ was found sufficing a linear relationship to the simulation time - t. Hence, to quantify the hopping activities $h(t)$ was computed with the slope standing for the average hopping rate at the long time-scale. For these MD simulations, the hopping rates are 10 ± 2 ns^{-1} and 42 ± 2 ns^{-1} for $n = 6$ and $n = 10$, respectively. In previous studies[2], the

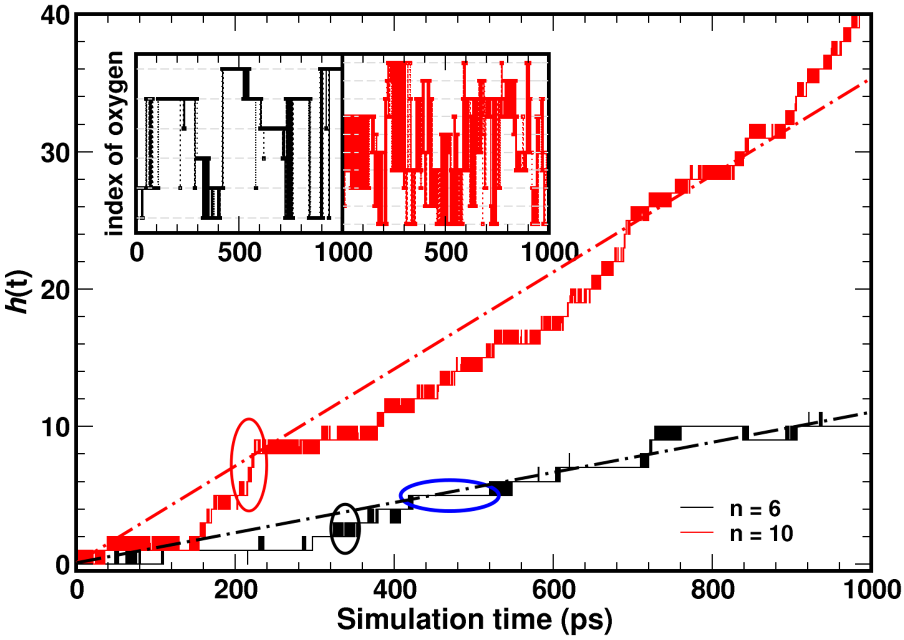

Figure 7.4.: Time accumulation functions of proton hopping from MS-MMPT MD simulations for $n = 6$ (black) and 10 (red) at $\Delta E = 10$ kcal/mol. For each of n, one representative trajectory (of which the hopping rate is the closest to trajectory averages) was chosen. The insets show the index profiles of H*-carrying oxygens.

PT behaviors were identified with burst and rest behaviors. A 'burst' behavior (or hopping mode – $\mathrm{O_A} \rightarrow \mathrm{O_B} \rightarrow \mathrm{O_C}$) refers to the proton hops through several donor atoms within a short simulation time (< 10 ps), which leads to rapid increases of $h(t)$ rates (see red circle in Figure 7.4). A 'rest' behavior, on the other hand, corresponds to localization of the excess proton in a relatively long period. Furthermore, the 'rest' behavior can be recognized as a proton retains captured by the same hydronium oxygen (for which $h(t)$ stays unchanged – $\mathrm{O_A} \rightarrow \mathrm{O_A} \rightarrow \mathrm{O_A}$, see the blue circle) and a proton oscillates between two oxygens ($h(t)$ jumps up and down – $\mathrm{O_A} \rightarrow \mathrm{O_B} \rightarrow \mathrm{O_A}$, see the black circle). Among the three modes, only the $\mathrm{O_A} \rightarrow \mathrm{O_B} \rightarrow \mathrm{O_C}$ mode contributes to the increase of hopping rates.

Hop rates from all MD simulations of water clusters (from $n = 6$ to $n = 100$) were recorded in Table 7.2. Besides the results for $\Delta E = 10$ kcal/mol, for $n = 6$ the averaged hopping rates reduced to 2 ns^{-1} for $\Delta E = 5$ kcal/mol and to complete no hops with $\Delta E = 15$ kcal/mol. Similar in MD simulations for

Table 7.2.: Hopping rates from MS-MMPT simulations with ΔE = 5, 10, 12 and 15 kcal/mol. Results were averaged from 10 1-ns MD simulations for each data.

	ΔE, kcal/mol	r_{hop}, ns^{-1}
$n = 6$	5	2 ± 2
	10	10 ± 2
	15	0
$n = 10$	5	3 ± 1
	10	38 ± 8
	12	42 ± 6
	15	4 ± 2
$n = 21$	5	2 ± 1
	10	38 ± 8
	12	104 ± 14
	15	26 ± 8
$n = 31$	5	2 ± 1
	10	43 ± 8
	12	101 ± 6
	15	18 ± 5
$n = 50$	5	3 ± 2
	10	44 ± 6
	12	97 ± 10
	15	21 ± 5
$n = 100$	5	3 ± 1
	10	47 ± 11
	12	109 ± 12
	15	18 ± 4

$n = 10$, MDs with $\Delta E = 10$ kcal/mol leads to a faster hopping activity than those from MD simulations with $\Delta E = 5$ and 15 kcal/mol for which the rates were 3 to 4 hopping events per ns. The highest hopping rate for $n = 10$ was found at $\Delta E = 12$ kcal/mol, which gives 42 ns^{-1} in rate. In addition to $n = 6$ and 10, MD simulations were also carried out for water clusters at the sizes of $n = 21$, 31, 50 and 100. For $n = 21$ and 31, hopping rates are obviously increased compared to results from MDs with $n = 10$ with most of values of ΔE. That is attributed to the presence of more partner water molecules near to the H_3O^+ ion, which provide more potential proton receptor and lead to higher probabilities of proton hopping events. For $n = 21$ and 31, the maximum hopping rates was found with $\Delta E = 12$ kcal/mol, which gives 104 ns^{-1} and 101 ns^{-1}, respectively. With $\Delta E = 5$ kcal/mol the lowest rate (2 ns^{-1} for both MD simulations) is given. For MD simulations with $n = 50$ and 100, the hopping rates were found not noticeably different to those from MDs with $n = 31$ at all selected values of ΔE. As results of trajectory averaging, the statistical errors were also recorded in Table 7.2. For simulations which give slow proton hops, the relative errors are up to ± 100%, which implied that for some MD trajectories no hopping event was found. For simulations which maximize the hopping rates for their respective water clusters ($n = 21 \sim 100$), the relative statistical errors were given from 6% to 15%.

7.2.4. Free Energy Calculations and Proton Transport Mechanism

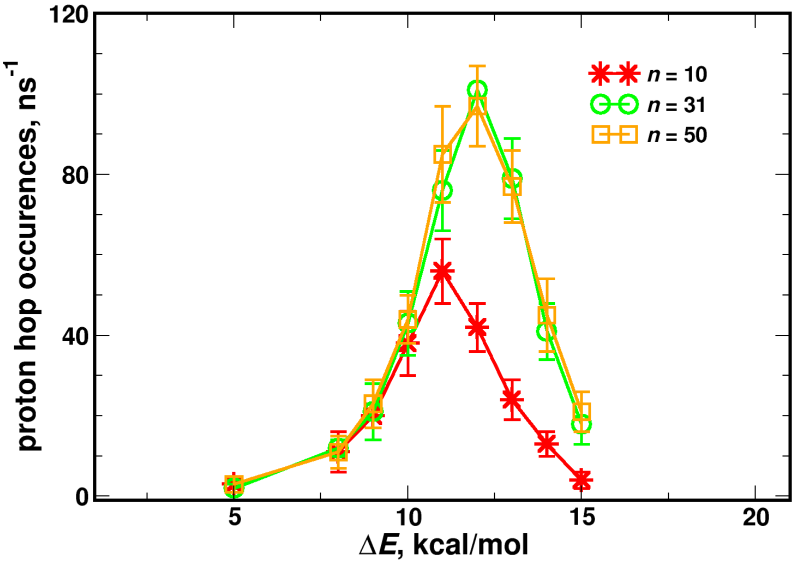

Figure 7.5.: The number of hopping occurrences in 10 ns MS-MMPT simulations of water clusters at the sizes of $n = 10$ (red), 31 (green) and 50 (orange).

Learning from the data in Table 7.2, the hopping rates of proton transport were found depending on the values of ΔE. Then, it became necessary to work out the relation between ΔE and reaction rates. Figure 7.5 shows such results for clusters with $n = 10$, 31 and 50. For $n = 10$, the highest PT hopping rate is 53 ns^{-1} at $\Delta E = 11$ kcal/mol, which is approximately twenty-fold and tenfold increased from the results at $\Delta E = 5$ and 15 kcal/mol. Results were also compared between $n = 31$ and $n = 50$ and similar rates were found with all selected values of ΔE. The maximum rates of 101 ns^{-1} and 97 ns^{-1} were respectively given for $n = 31$ and $n = 50$ at $\Delta E = 12$ kcal/mol.

For analyzing the dynamics of proton hop simulations, the free energy calculations were carried out by

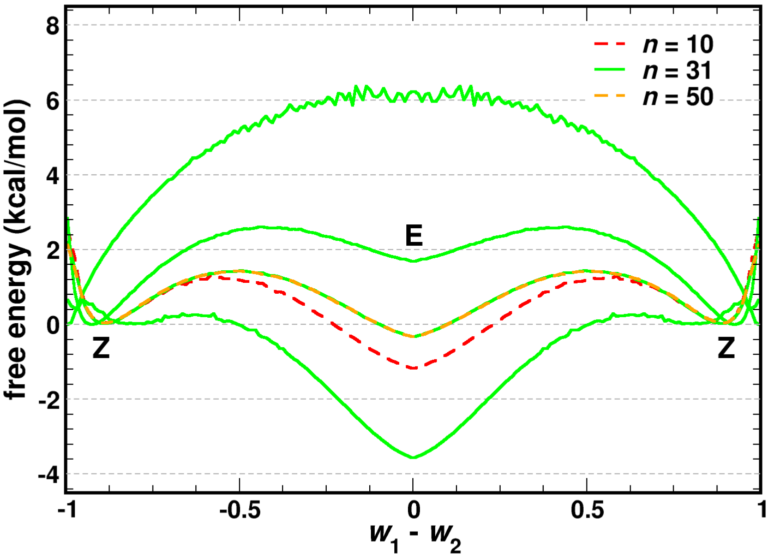

Figure 7.6.: Free energy profile of proton transfer moves for $n = 10$ (red) and $n = 50$ (orange) at $\Delta E = 12$ kcal/mol and for $n = 31$ (green) with i) $\Delta E = 5, 10$, 12 and 15 kcal/mol (from top to bottom). The $x-$axis refers to the difference between the two largest MS-MMPT weights. Region Z corresponds to Zundel structures whereas region E stands for Eigen structures. For each trace, 2×10^6 MD frames were sampled.

calculating the population probabilities with given coordinates,. The free energy surfaces (FES) are given in Figure 7.6 for cluster simulations at $n = 10$, 31 and 50. Here, the reaction coordinate was defined as the difference between the two maximum weights (w_1 and w_2) in the multi-state framework.[76] For $|w_1 - w_2| = 1$, the energy-minimum state is a predominant state in the multi-state framework and H^+ is usually contained in a Zundel structure. For $w_1 - w_2 = 0$, there are at least two states sharing the same contributions into the overall potential and the H^* carrying ion has more Eigen character. For MD simulations of $n = 31$ at $\Delta E = 10$ kcal/mol, the free energy profile suggested that a Zundel structure is the most stabilized form of a H^*-carrying ion. Then the Eigen structure region can be reached by overcoming a first barrier of 2.6 kcal/mol. As a comparison, the Eigen region is less stabilized for $n = 31$, for which a local minimum (+1.6 kcal/mol to the zero reference) was found at $w_1 - w_2 = 0$. For the process from Eigen to Zundel, the second barrier is found 1.0 kcal/mol for $n = 31$. Hence, at $\Delta E = 10$ kcal/mol an effective proton transport process should follow an $O_A \rightarrow O_B \rightarrow O_C$ mode with a Zundel to Zundel process via an intermediate Eigen conformational state. At $\Delta E = 5$ kcal/mol, most of the MD frames were populated in the Zundel region, which results in a Zundel to Zundel process without an intermediate state and a barrier height of +6.2 kcal/mol was given. It needs to note that the wiggling pattern for this FES at the Eigen region is due to the lacks of configuration samplings (because of the high energy). At $\Delta E = 15$ kcal/mol, the Eigen region becomes more energy favorable. The PT process, in the contrary, follows an Eigen to Eigen path (via a barely noticeable Zundel intermediate) with a rate determinant reaction barrier of 3.8 kcal/mol. Figure 7.6 also compares among MD simulations of water clusters with n = 10, 31 and 50 at the $\Delta E = 12$ kcal/mol which maximizes the hopping rates for larger water clusters. For $n = 31$, the Eigen and Zundel regions are almost equally distributed, for which the free energy difference is 0.3 kcal/mol. For $n = 50$, the FES is almost the same to that of $n = 31$, which substantiates the finding that the hopping activities get converged as the cluster grows. For $n = 10$, the determinant barrier height is determined by the Eigen region ($E_b = 2.5$ kcal/mol). That agrees with the fact that to obtain a fastest proton hop in $n = 10$, ΔE should be reduced (to 11 kcal/mol). And once the Eigen and Zundel region are roughly the same stable to each other, the overall reaction barrier reaches its minimum.

Nevertheless, w_1 and w_2 are variables which provide energetic information of how states are mixed but do not give a direct indication on whether the conformations are Eigen or Zundel. And it was found difficult to illustrate an Eigen to Eigen process from Figure 7.6 for the study case with $\Delta E = 15$ kcal/mol. Hence, it becomes necessary to further provide geometric coordinate to supplement one-dimensional FES. Then, a second reaction coordinate, δ, was introduced. Proposed by Marx *et al.*,[203] $|\delta|$ is defined as the minimum value among $|\delta_1|$, $|\delta_2|$ and $|\delta_3|$, each of which is the bond length difference between the $O_{hyd} - H_{hyd}$ bond of a hydronium ion and its closest hydrogen bond which connects as $H_{hyd} \cdots O_{wat}$. Geometrically, an Eigen structure is identified if $|\delta| > 0.3$ while with $\delta = 0$ a Zundel structure is formed. Combined with $w_1 - w_2$, two-dimensioned free energy surfaces (FES) were thereby built for proton transports of the water cluster with.

Enhanced from Figure 7.7 shows such FESs from MD simulations with $n = 31$ using both MS-MMPT force fields with different ΔE. In panel a, MD simulations were run with $\Delta E = 5$ kcal/mol and two global minima were found at the edges of this 2D plot. That means most of the conformational population was around $\{|w_1, w_2|, \delta\}$=(1.0,0). Unlike the one-dimensional FES, at the transition state (around $w_1 - w_2 = 0$) MD samplings were further diluted with the addition of the new dimension. Therefore, it is not easy to determine the barrier height from the two-dimensional surface but the effective proton transport process should follow with a Zundel to Zundel process. For panel b and c, the 2D FES appears with a total of four local minima for each panel, for which two Zundel regions (left-right) and two Eigen regions (top-bottom) were identified. Whether the proton transports proceed with an Eigen-to-Eigen or Zundel-to-Zundel process depends on whether the global minimum is found in their respective regions. For panel b from MD simulations with $\Delta E = 10$ kcal/mol, the global minima were found in the Zundel regions, whereas for panel c ($\Delta E = 12$ kcal/mol) the minimum energies for Zundel and Eigen are relatively equal to each other. That leads to a lowest barrier which maximizes the hopping rate. With $\Delta E = 15$ kcal/mol, panel d shows that the proton transport process follows a Eigen to Eigen mechanism. With a further increase of ΔE, the disappearance of the Zundel minima should be expected.

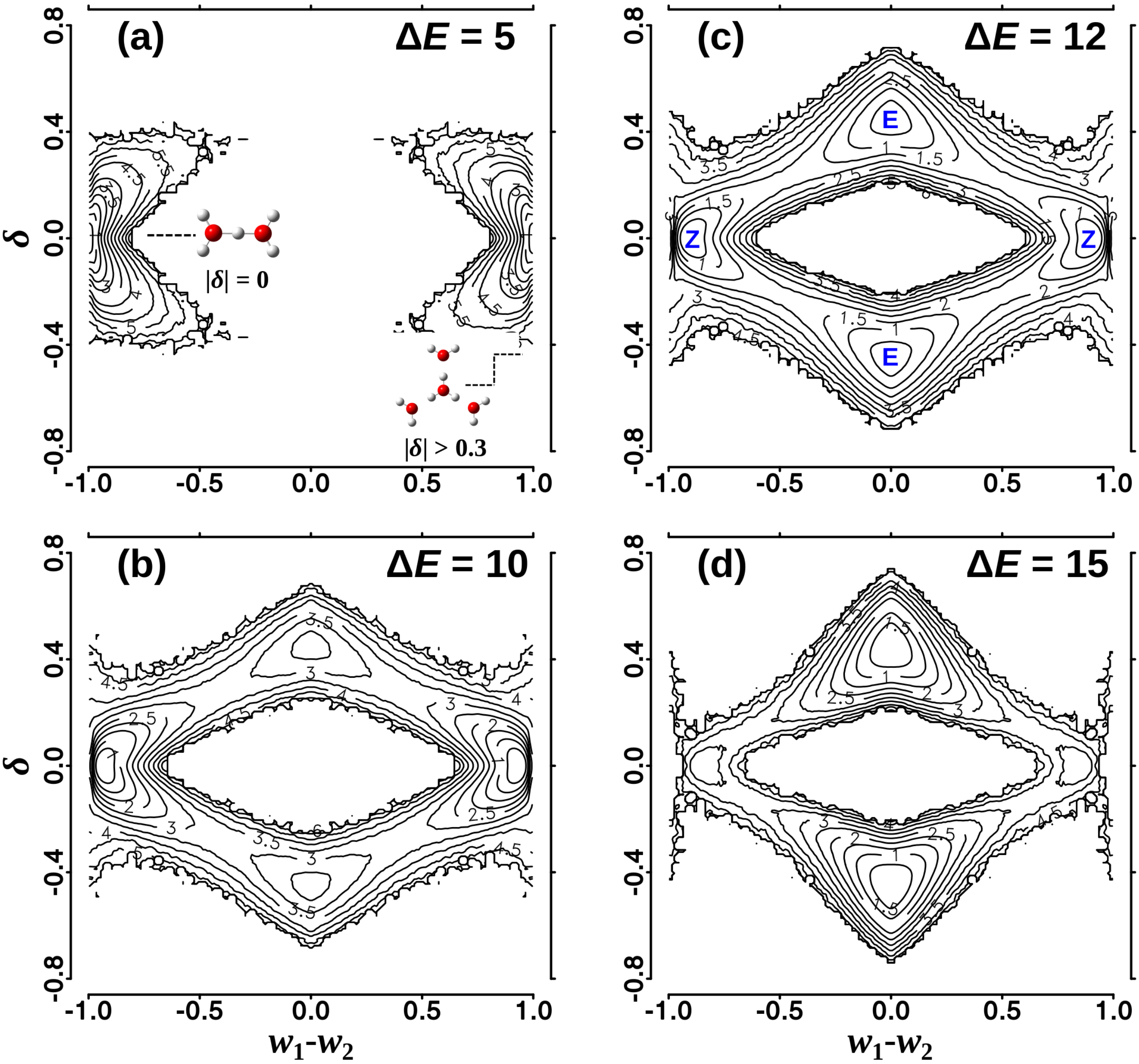

Figure 7.7.: Two-dimensioned free energy surface for PT reaction at $n = 31$. The coordinates are δ and $w_1 - w_2$, which were collected from 10 ns MS-MMPT simulations for $n = 31$ with a) $\Delta E = 5$, b) 10 c) 12 and d) 15 kcal/mol. For the example of panel c, the top-bottom minima stand for a region where most of the conformations are Eigen while the left-right minima correspond to the Zundel region.

7.3. Results II: MD Simulations of Water Bulks with One Excess Proton

In the previous section, the reaction dynamics of water clusters (or droplets) were investigated using MS-MMPT method. The water cluster is simple to model but nevertheless an interesting system, which helps understand proton activities especially for liquid-vapor[79,81] and liquid-hydrophobic interfaces.[80,82] In this section, the condensed phase simulations were carried out for water bulk systems which are equally important (compared to water clusters) but more challenging in the standpoint of method development. Using the MS-MMPT force field, MD simulations were run for a bulk system with the size of $25.0 \times 25.0 \times 25.0$ Å^3 (which contains 523 water molecule and one H$^+$ ion and is labeled as bulk-25 Å) at $\Delta E = 5$, 10, 12 and 15 kcal/mol. The MD time-steps were chosen for 0.25 fs and 0.5 fs. MDs were also run for a bulk system with the size of $31.0 \times 31.0 \times 31.0$ Å^3 (bulk-31 Å, 997 water molecules and one H$^+$) at $\Delta E = 12$ kcal/mol with an MD time-step of 0.5 fs. For simulations of bulk-25 Å, the cutoff for non-bonded interactions was set 10 Å while for bulk-31 Å different cutoffs were chosen, which are 10, 12 and 14 Å. All simulations were performed with periodic boundary conditions (PBC) and the NVE ensemble.

7.3.1. Energy conservation

Similar to what were found for cluster simulations, the energy conservations were seen in both simulations for bulk-25 Å and bulk-31 Å, as shown in Figure 7.8. Unlike the cluster simulations in the gas phase, for bulk simulations it requires additional modifications to the CHARMM code (incl. "./source/energy/eintern.src", "./source/energy/enbonda.src" and "./source/ltm/number_ltm.src") to adapt with PBC applied, especially for modeling charge transfers. For running a CHARMM simulation with PBC,[30,204] using a standard keyword "IMAGE BYREsidue" is usually specified for non-reactive bulk simulations, which means if a molecule reaches and is about to cross the boundary the entire residue will move to the image space as a whole. For MS-MMPT simulations, however, it is mandatory to specify the key "IMAGE BYATom", which means, the boundary crosses apply to individual atoms because all OH bonds have possibilities to dissociate and hydrogen atoms can diffuse from their host oxygens.

For MS-MMPT simulations with bulk-25 Å, moreover, averagely 17 candidate states was identified as first-shell motifs and finally a total of 110 states were obtained by considering water molecules

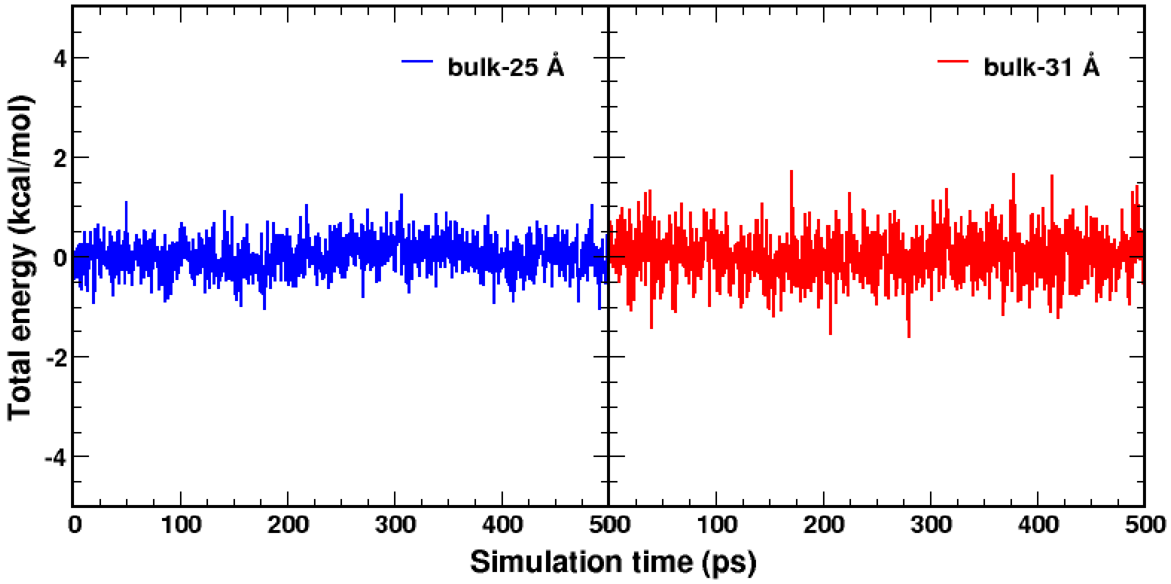

Figure 7.8.: Energy fluctuations from example MD trajectories of MS-MMPT bulk simulations for bulk-25 Å (left) and bulk-31 Å (right) with $\Delta E = 12$.

in the second shell. As the same to cluster simulations, the criterion $w \leq 10^{-11}$ was set, which leads to 8 and 13 effective states from first- and second-shell mode motif searches (Figure 7.9), respectively.

7.3.2. Self-diffusion Coefficient of Proton Transport from MS-MMPT Simulations

A typical measurement of the mobility (or diffusivity) of a molecule or a particle in the liquid or the gas phase is the diffusion coefficient. The diffusion coefficient is a physical constant dependent on many factors, i.e. the size of molecules, temperature, pressure etc.[1] Without external forces (e.g. electric field), molecules diffuse spontaneously and isotropically in a bulk system and such diffusivity is called as self-diffusion coefficient, which is in unit of Å^2/ps and stands for a spatial propagation per unit time.[205] Experimentally, the self-diffusion coefficient for a water molecule was determined, which gives 0.23 Å^2/ps[113] in pure water while the lighter H$^+$ diffuses four-fold as fast as that of water molecules and the self-diffusion coefficient was 0.94 Å^2/ps.[111,112,118]

For calculating the self-diffusion coefficient for the excess proton, the concept of the center of excess

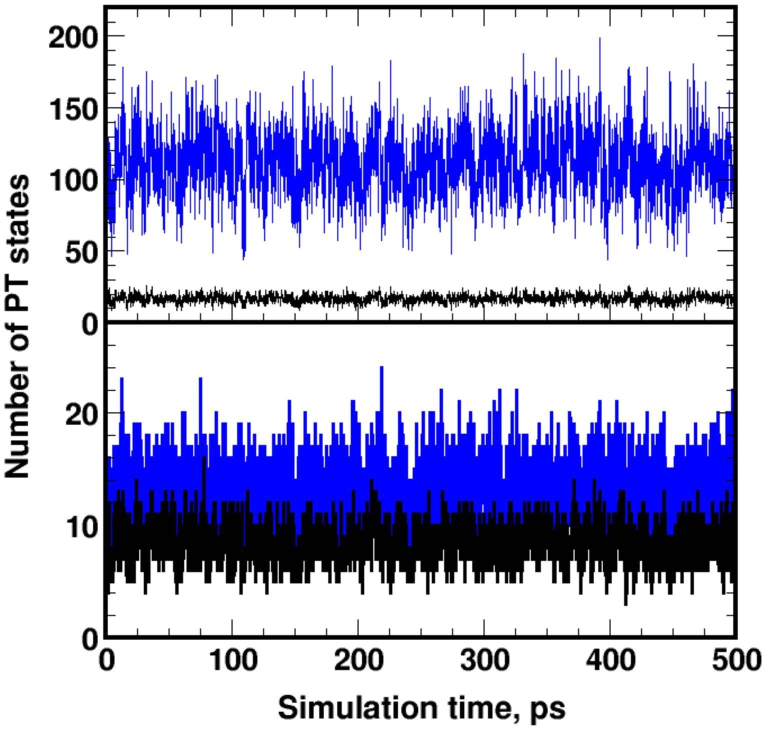

Figure 7.9.: The number of states that were selected in the MS-MMPT-ARMD framework (top) and the number of effective states for 4000 MD frames. Data were analyzed using first- (black) and second-shell (blue) modes. The average numbers of selected states are 16.7 and 110.0 for first- and second-shell modes, respectively. The average numbers of effective states are 8.3 and 13.0, correspondingly.

charge (CEC) was first introduced.[75,76] Here, the position of the CEC is

$$\boldsymbol{r}_{\mathrm{CEC}} = \sum_{j=1}^{N} w_j \cdot \boldsymbol{r}_j \tag{7.3}$$

where w_j is the weight of the j-th state and $\boldsymbol{r}_j$ is the coordinate of weighted center of excess charge (water charges were removed from calculating $\boldsymbol{r}_j$).

Figure 7.10 shows one trajectory following the CEC from a 100 ps simulation. Quantitatively, the self-diffusion coefficient is obtained by calculating the mean square displacement (MSD) of the CEC,

Table 7.3.: Self-diffusion coefficients ($Å^2 \cdot ps^{-1}$) from MS-MMPT bulk simulations with different input values.

size of bulk	ΔE kcal/mol	Δt fs	R_{cutoff} Å	r_{hop} ns^{-1}	D_{CEC}	D_{H_2O}
25.0 Å	5	0.5	10	2 ± 1	0.11 ± 0.02	0.333 ± 0.008
	8	0.5	10	4 ± 2	0.12 ± 0.02	
	10	0.5	10	15 ± 5	0.13 ± 0.02	
	10	0.25	10	20 ± 6	0.13 ± 0.03	
	12	0.5	10	61 ± 9	0.17 ± 0.03	
	12	0.25	10	53 ± 9	0.17 ± 0.03	
	15	0.5	10	35 ± 9	0.16 ± 0.02	
	15	0.25	10	31 ± 10	0.14 ± 0.03	
31.0 Å	12	0.5	10	58 ± 13	0.19 ± 0.05	0.337 ± 0.010
	12	0.5	12	74 ± 11	0.24 ± 0.06	0.400 ± 0.007
	12	0.5	14	99 ± 13	0.28 ± 0.05	0.444 ± 0.011

Method	r_{hop} ns^{-1}	$D_{H_3O^+}$	D_{H_2O}
MS-EVB 3[76]	108 ± 9	0.29 ± 0.03	0.232 ± 0.005[146]
MS-EVB 3 (CMD)[76]	(n.a.)	0.50 ± 0.05	0.24 ± 0.01[206]
MS-EVB 3.2[78]	(n.a.)	0.37 ± 0.01	0.232 ± 0.005[146]
MS-EVB 3.2 (CMD)[78]	(n.a.)	0.55 ± 0.06	(n.a.)
*a*MS-EVB 3.2[78]	(n.a.)	0.36 ± 0.01	0.233 ± 0.001[77]
*a*MS-EVB 3.2 (CMD)[78]	(n.a.)	0.51 ± 0.06	(n.a.)
DFTB3[56]	(n.a.)	0.66 ± 0.02	0.38 ± 0.03
CPMD (HCTH)[58]	(4 ± 2)×10^2	0.33	0.1
experiment		0.94 ± 0.01[111]	0.23[113] (298.15 K)

i.e.

$$D(t) =< |\boldsymbol{r}_{\text{CEC}}(t) - \boldsymbol{r}_{\text{CEC}}(0)|^2 > / \ 6t \tag{7.4}$$

Figure 7.11 shows the MSD from MS-MMPT simulations with $\Delta E = 12$ kcal/mol. From 16 500-ps independent MD trajectories, the PT activities differed by more than a factor of 2 from the slowest (0.10 $Å^2$/ps) to the fastest (0.23 $Å^2$/ps) proton diffusions. Averagely, the diffusion coefficient of CEC from these simulations was 0.17 ± 0.03 $Å^2$/ps for bulk-25 Å. More simulation results were reported in Table 7.3. For bulk-25 Å, the diffusion constants were found at lower values of 0.13∼0.14 $Å^2$/ps with $\Delta E = 10$ and 15 kcal/mol. With $\Delta E = 5$ kcal/mol, only few hop events were found (2 ns^{-1}) and the diffusion constant came to the lowest: 0.11 ± 0.02 Å^2/ps. At ΔE = 10, 12 and 15 kcal/mol, results were compared between MDs using different sizes of MD time-step and no significant differences were found, considering the statistical error up to ±20%. That suggests the MD time-step can be further increased to 0.5 fs which was used for MD simulations (especially for a larger bulk size) in the following discussion. For bulk-31 Å, MS-MMPT simulations were compared using different cutoff ranges for non-bonded interactions. With $R_{\text{cutoff}} = 10$ Å, the similar result (0.19 ± 0.02 Å^2/ps) was given compared to simulations using the same cutoff in bulk-25 Å. With $R_{\text{cutoff}} = 12$ and 14 Å, the diffusion constants were further increased to 0.24 and 0.28 Å^2/ps, respectively. That is attributed to faster water diffusion rates with the increase of R_{cutoff}. Similar to the discussion for cluster simulations, Figure 7.12 reports the two-dimensioned free energy surfaces for bulk simulations using the MS-MMPT force fields. In general, for all investigated ΔE except $\Delta E = 5$ kcal/mol FESs show with similar topologies with but with four local energy minima. What differs, however, are the barriers between Eigen and Zundel regions. With $\Delta E = 5$ kcal/mol, the H*-carrying ion structures have localized conformations which are mostly Zundel (panel a). Similar to what were found in cluster simulations, lacks of MD samplings lead to the difficulties in determining the reaction barrier. For FES with the reduced dimension (using $w_1 - w_2$ as the only progression coordinate), the barrier height is 7.7 kcal/mol. With $\Delta E = 10$ kcal/mol, the barriers are 3.8 kcal/mol for Zundel to Eigen process and 0.7 kcal/mol for a cross from Eigen to Zundel. And thus, the 3.8 kcal/mol barrier determines the reaction process which is Zundel to Zundel via Eigen intermediate states. The barriers decreased with $\Delta E = 12$ kcal/mol for Zundel to Eigen pathway ($E_b = 2.4$ kcal/mol) but increased to $E_b = 1.4$ kcal/mol for Eigen to Zundel, which leads the fastest proton diffusion but still in a form of Zundel to Zundel process. At $\Delta E = 15$ kcal/mol, the Eigen regions become more stable and the PT process undergoes with an Eigen to Eigen path via a metastable Zundel intermediate state in Zundel region. The determinant barrier height this process is 3.3 kcal/mol. For the current MS-MMPT simulations, the solvation structures of water-water and hydronium-water were reported in the radial distribution functions (RDFs). Figure 7.13 shows the RDFs of $\text{O}_\text{w} - \text{O}_\text{w}$ (water oxygen – water oxygen), $\text{O}_\text{w} - \text{H}_\text{w}$ (water oxygen – water hydrogen) and $\text{H}_\text{w} - \text{H}_\text{w}$ (water hydrogen – water hydrogen) from test simulations of pure water bulks in which the excess proton was removed. The MS-MMPT force fields were employed but only the water force field was applied. Results were compared with the experimental data[207]. For RDF of $\text{O}_\text{w} - \text{O}_\text{w}$, the first density peak appears at $r = 2.80$ Å compared with $r = 2.75$ Å from the experiment. The experimental data shows a second peak at ~4.5 Å, which was not found from the bulk simulations. For technical reasons, simulations also recorded $O - H$ bond lengths in the RDF of $O_w - H_w$ while it was not shown in the experiment. Nevertheless, the inter-molecular distance yields with a first peak at $r = 1.85$ Å from MD simulations, compared with 1.75 Å from the experiments. However, the simulations predicts well for the second solvation structures to the experiment (which peaks at 3.30 Å). The similar agreement was also found in the RDF of $H_w - H_w$ (the internal distance of $H_w - H_w$ was not reported in the experiment).

Calculations of RDFs were further carried out for the solvation structure over the hydronium ion, see Figure 7.14. Simulations were run with $\Delta E = 12$ and 15 kcal/mol. The experimental data was from Ref. 208. For this, RDFs of $O^* - O_w$ (hydronium oxygen – water oxygen), $O^* - H_w$ (hydronium oxygen – water hydrogen), $H^* - H_w$ (hydronium hydrogen – water hydrogen) and $H^* - O_w$ (hydronium hydrogen – water oxygen) were reported for both simulations. For RDFs of $O^* - O_w$ and $O^* - H_w$, focusing MDs with $\Delta E = 15$ kcal/mol (blue) the first solvation shell was well predicted from MDs using MS-MMPT force field, compared to the experiment. Though, at the long range the simulated RDFs were not well described. For RDFs of $H^* - H_w$ and $H^* - O_w$, similarly, the simulated $g(r)$ predicts well in the first peaks which give $r_{H^*-H_w} = 2.20$ Å and $r_{H^*-O_w} = 1.55$ Å were found in good agreement with the experimental data. As the same to results for $g(r)_{O^*-O_w}$ and $g(r)_{O^*-H_w}$, in RDFs of $H^* - H_w$ and $H^* - O_w$ simulations failed to give good agreement on the second solvation shell with the experiment. Moreover, the intensities of the first distribution peaks in all panels were found higher than those from the experiments. That implies the non-bonded interactions between H_3O^+ ion and water solvents are too strong. Compared to MS-MMPT simulations with $\Delta E = 15$ kcal/mol, with $\Delta E = 12$ kcal/mol the RDF comparisons with the experiments were no better as a result. Even for the first solvation shell, the simulations led to double peaks which can be obviously seen in panel b-d. That is because for MS-MMPT simulations with $\Delta E = 12$ kcal/mol Zundel and Eigen structures are more or less equally distributed, according to the free energy analysis. If a Zundel structure is modeled for an H_3O^+ ion, one of the $O^* - H^* \cdots O_w$ motifs is treated by MMPT potential and the rest are treated by the classical force field. That leads to the differentiation of equilibrium values of certain coordinates due to the different treatments. For the simulations of RDFs, it is worth a note that our MMPT force field was not in particular parametrized for such agreement with both experimental RDFs (water-water and hydronium-water). Nevertheless, these computed RDFs were qualitatively comparable with the experiments. That should justify with a reasonable solvation structure over either a H^*-carrying ion or a neutral water molecule.

7.3.3. Discussion

The previous section discussed the self-diffusion coefficient of the center of excess charge which represent for the diffusion of a proton. For bulk-25 Å, the maximal self-diffusion coefficient is 0.17 $Å^2$/ps based on the background diffusion of water solvents which gives 0.333 ± 0.008 $Å^2$/ps (see Figure 7.16a). The ratio of $D_{\mathrm{CEC}}/D_{\mathrm{H_2O}}$ is equal to 0.51. For bulk-31 Å, the maximal diffusion constant rises up to 0.28 $Å^2$/ps but the $D_{\mathrm{CEC}}/D_{\mathrm{H_2O}}$ ratios range from 0.56 to 0.63, which was not considered as a significant improvement to that given in bulk-25 Å. That is because experimentally the diffusions of water and active protons differ, approximately, by a factor of 4. From the experiment, the fast proton hopping mobility is based on water diffusion of 0.23 $Å^2$/ps, compared to which the water diffusion constants were overestimated from MS-MMPT simulation (e.g. by ~50% for bulk-25 Å). For a Grotthuss picture for proton transports, the proton diffusion can be decomposed with the mass diffusion (vehicular contribution) and Grotthuss hops.[76,112,116] In the other word, the self-diffusion coefficient is the sum of both contributions. The mass diffusion refers to the diffusion of an ion carrier, such as a hydronium ion. And experimentally, it was postulated that the diffusivity of a hydronium ion is that of a potassium ion (0.20 $Å^2$/ps) since they have similar ionic radius.[76,112] The Grotthuss contribution, in fact, can be calculated by subtracting the mass contribution from the experimentally measured proton diffusion. From the simulation standpoint, alternatively, this component can be estimated from the hopping rate (r_{hop})[57,76] but such calculations were not carried out in the current work because the overall proton diffusion was explicitly calculated from the charge diffusion.

It needs to note that for the current MS-MMPT method it is however impossible to simulate a free diffusion of a hydronium ion. That is because the for each PT state a Zundel structure is in fact modulated with MMPT potential. That leads to the simulations of the hydronium ion always with its partnering water associated. Thus, (if one-state MMPT simulation is performed) to calculate the mass contribution the H^+ carrier is at the smallest a Zundel ion instead of a hydronium molecule. As a consequence, the mass diffusion in MS-MMPT simulation is slower by a factor of 2 compared to the experimental approximation. Figure 7.16b shows such test runs of one-state MMPT simulations, which led to an average of 0.11 $Å^2$/ps as the diffusion constant for a Zundel ion.

Table 7.3 also lists MD simulations using other methods. For MS-EVB[76–78], the classical MD simulations resulted in the self-diffusion coefficients of 0.29 for MS-EVB 3 and further improved to 0.37 Å^2/ps in later MS-EVB 3.2 with the water diffusion constants all close to that of the experiment. Focusing on the mass contribution (a hydronium is modeled), for MS-EVB simulations the data were not shown and discussed but could have been done by doing MD simulations with only one valence bond state considered. Luckily, in the early development of MS-EVB 2[75] such test simulations were performed and the resulting self-diffusion coefficient is 0.21 Å^2/ps for a hydronium ion. Using this value, the ratio of proton diffusion to its vehicular contribution was up to 1.7 for classical MS-EVB simulations, similar to what was obtained for MS-MMPT (1.6). For the MS-EVB method, simulations were also carried out including the nuclear quantum effects (NQE) by running centroid molecular dynamics (CMD), for which the proton diffusions were boosted by 50 $\sim$ 70%. From these literature works, it remained however unclear how this PT acceleration is contributed from. Using the same force field (i.e. the water model), introducing the quantum effects may lead to a faster diffusion of water by a factor of 1.5$\sim$2.[206] In the earlier literature work,[206] a factor of 1.4 was obtained. That remains a suspect that for MS-EVB 3.2, the accelerated proton diffusion could be partially contributed by faster water diffusion or even because the hydronium ion was accelerated. For MS-EVB 3, the qSPC/fw water model[206] was introduced to stabilize the water solvent from accelerated diffusion. However, it remains questionable of whether the classical and quantum simulations were comparable since different force fields were used, respectively.

Nevertheless, for the current MS-MMPT method it is a bit unrealistic that the proton diffusion (lighter) is slower than that of a water molecule (heavier). Therefore, in the next section attempts of some improvement to the self-diffusion coefficient of the proton are committed and discussed.

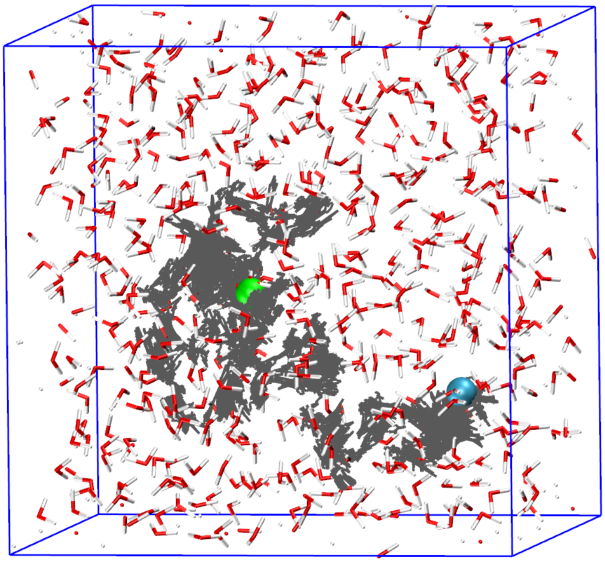

(a) full bulk

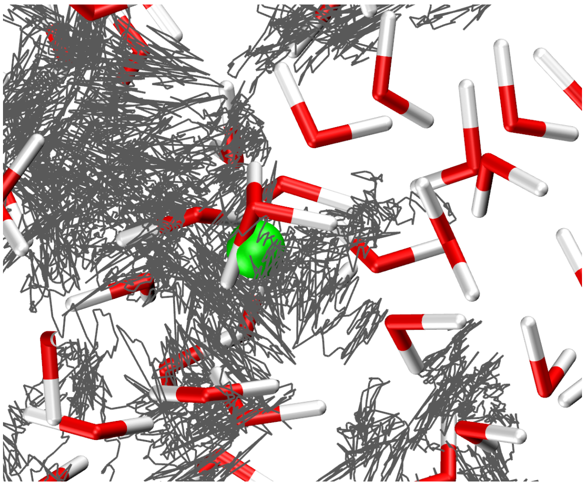

(b) zoomed in

Figure 7.10.: Diffusion of the center of excess charge in bulk-25 Å simulation. Data were collected from a 250-ps MD trajectory. The diffusion trace is colored in gray and the green and blue dots are the starting and end points, respectively.

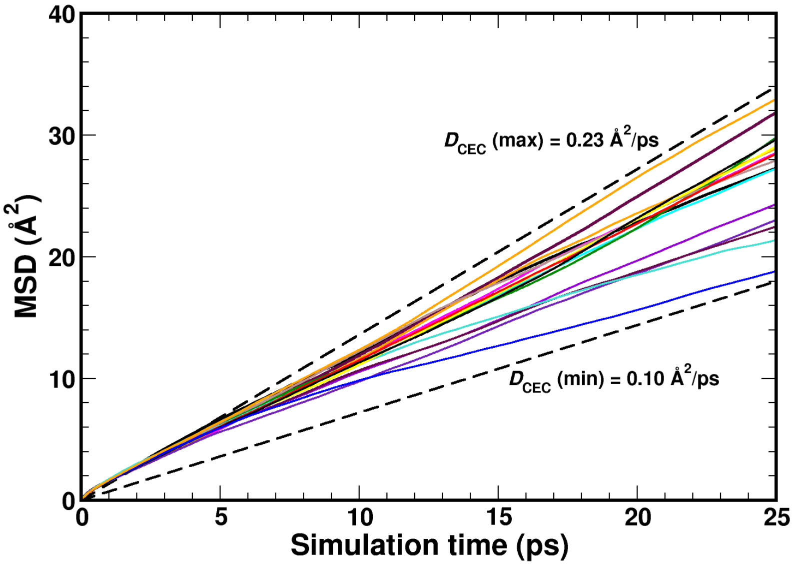

Figure 7.11.: Mean square displacement of CEC for 16 500-ps MD trajectories from MS-MMPT simulations for bulk-25 Å with $\Delta E = 12$ kcal/mol. The maximum diffusion constant is 0.23 Å^2/ps while the minimum value is 0.10 Å^2/ps.

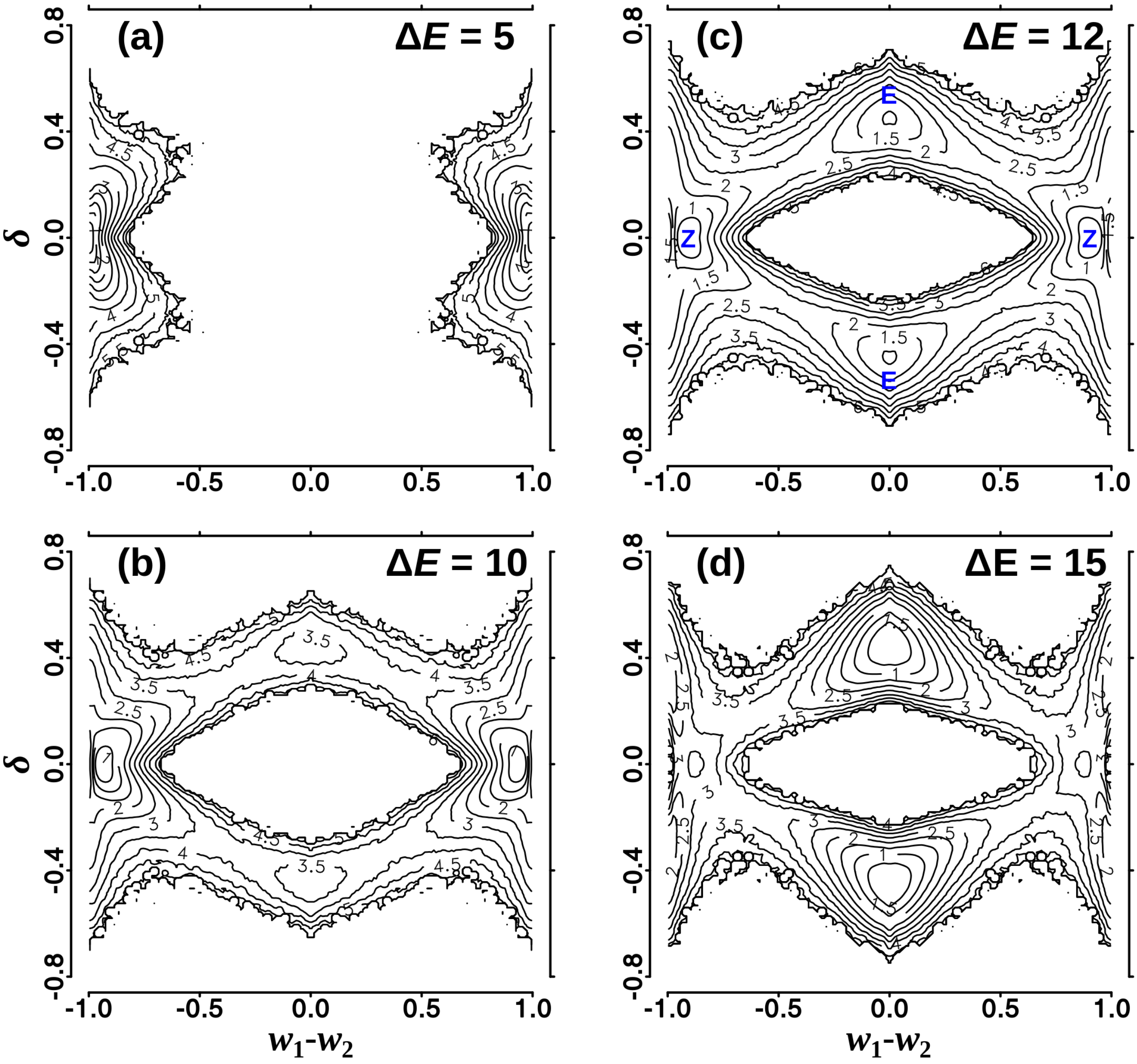

Figure 7.12.: Tow-dimensional free energy surface of proton transport moves from MS-MMPT bulk simulations with a) $\Delta E = 10$, b) 10, c) 12 and d) 15 kcal/mol. For each panel, MDs were run for 8 ns.

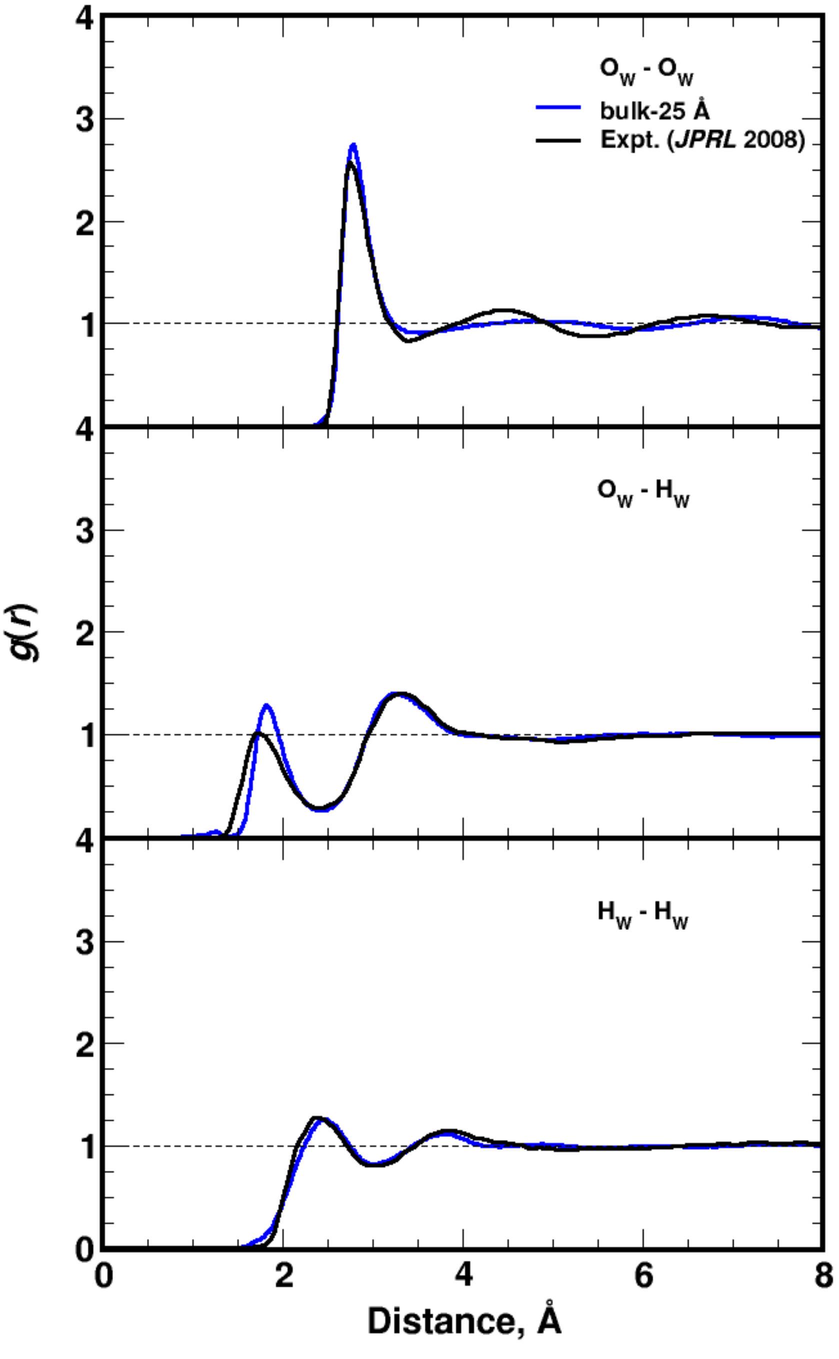

Figure 7.13.: Radial distribution functions of bulk water (bulk-25 Å) for (from top to bottom) oxygen-oxygen, oxygen-hydrogen and hydrogen-hydrogen. Each plot contains experimental data (black, Ref. 207) and data from MS-MMPT simulations (blue).

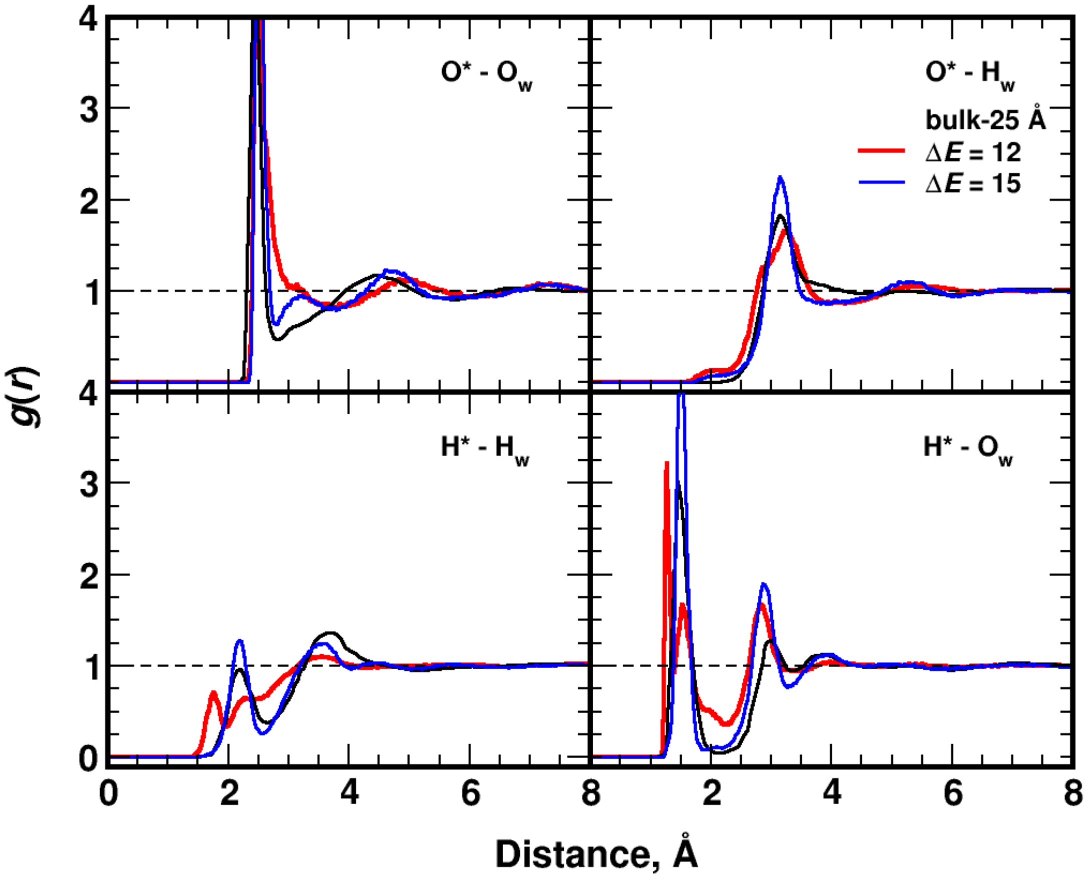

Figure 7.14.: Radial distribution functions of H_3O^+ ion, including (from top-left to bottom-right) $O^* - O_{\mathrm{wat}}$, $O^* - H_{\mathrm{wat}}$, $H^* - H_{\mathrm{wat}}$ and $H^* - O_{\mathrm{wat}}$. Each plot contains experimental data (Ref. 208) and data from MS-MMPT simulations with $\Delta E = 12$ (red) and 15 kcal/mol (blue).

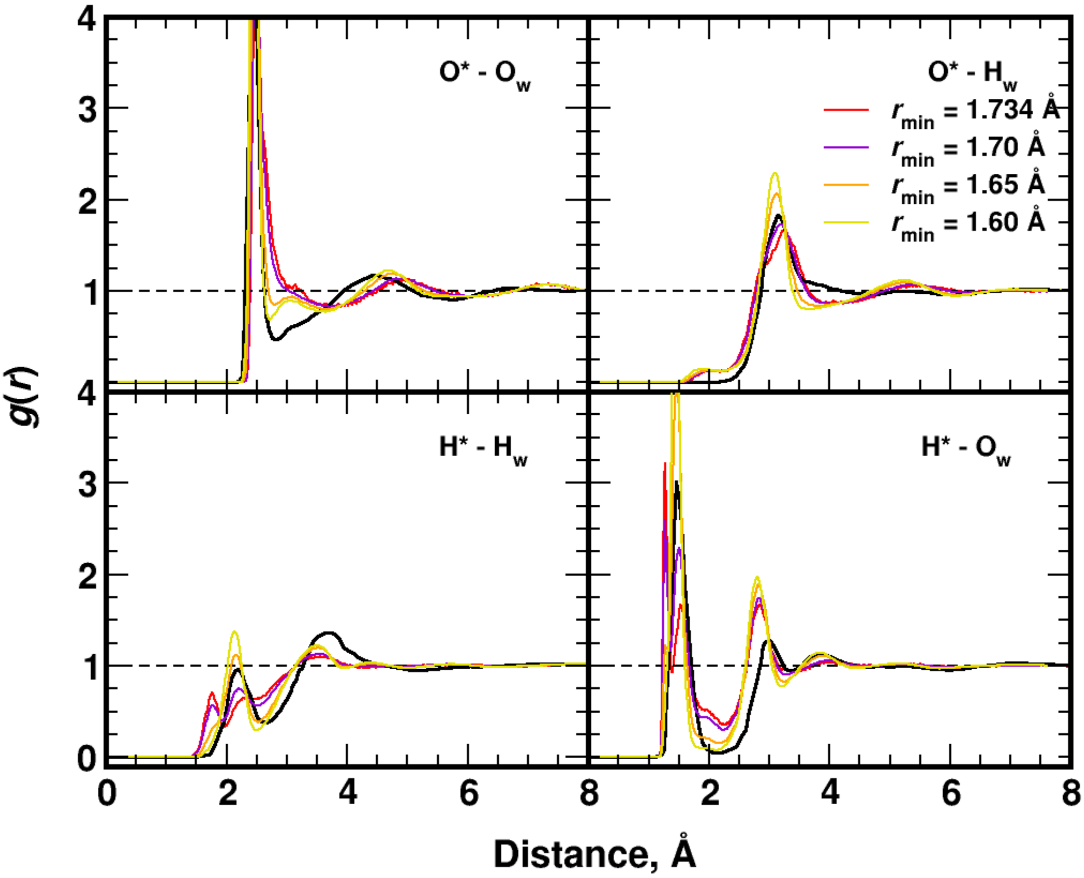

Figure 7.15.: Radial distribution functions of H_3O^+ ion, including (from top-left to bottom-right) $O^* - O_{wat}$, $O^* - H_{wat}$, $H^* - H_{wat}$ and $H^* - O_{wat}$. Each plot contains experimental data (Ref. 208) and data from MS-MMPT simulations with $\Delta E = 12$ (red) and 15 kcal/mol (blue).

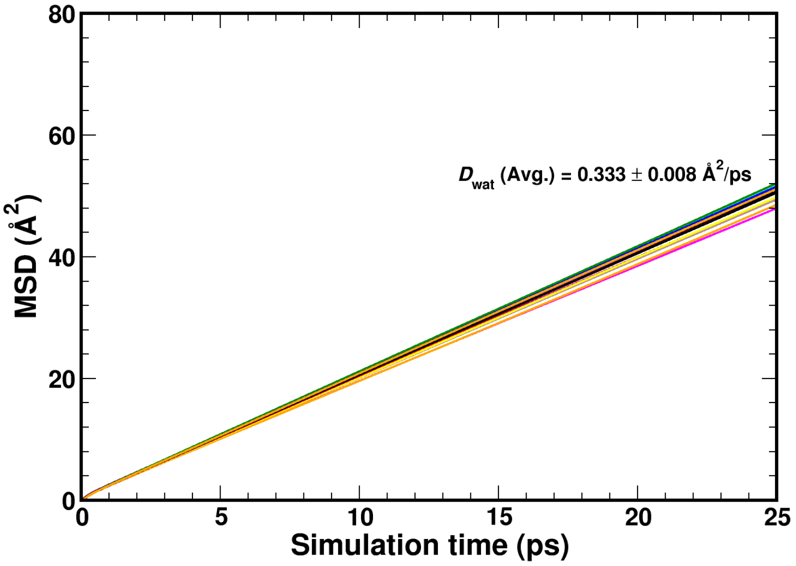

a) water

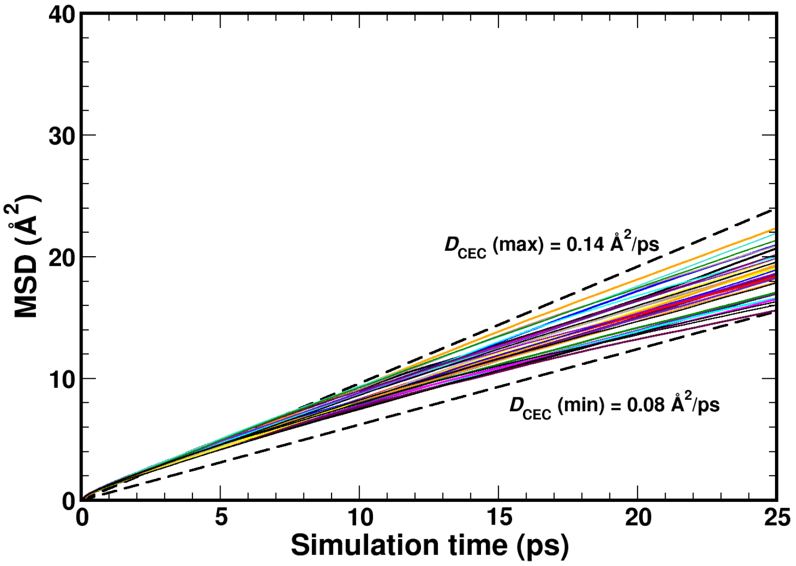

b) Zundel

Figure 7.16.: Mean square displacement of a) water diffusions from 16 500-ps MD trajectories from pure-water bulk simulations (25 × 25 × 25 Å^3) and b) diffusions of $H_5O_2^+$ ions from 16 500-ps one-state MMPT simulations (namely the multi-state framework was deactivated). The non-bonded cutoff for CHARMM simulations is 10 Å. For one-state MMPT simulation, the mass diffusion of a Zundel structure is 0.11 ± 0.02 Å^2/ps in average.

7.4. Improvement of Proton Diffusivity

7.4.1. Attempt I: Infrared Spectroscopy Based MS-MMPT Parametrization

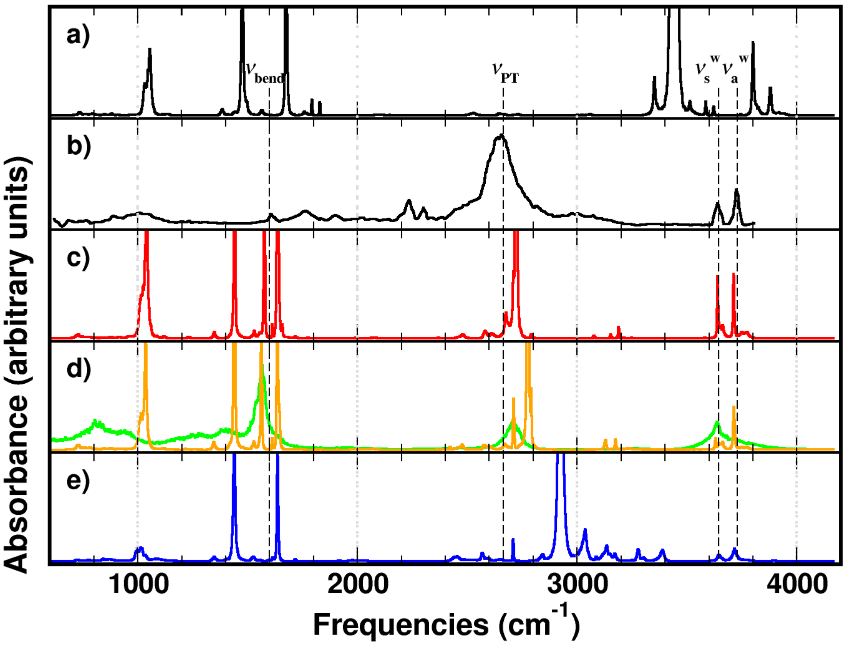

Figure 7.17.: From top to bottom: IR spectra from a) MS-MMPT simulations at 50 K using MP2-parametrized MMPT force field (MS-MMPT-MP2) with ΔE = 10 kcal/mol, b) the experiment from Ref. 209 and MS-MMPT simulations using IR-parametrized MMPT force field (MS-MMPT-IR) with ΔE = c) 5 (red), d) 10 (orange) and e) 15 kcal/mol (blue). For panel d, simulations were also run at 600 K (with ΔE = 10 kcal/mol, green).

In general, there are two directions for force field parametrization: to be experimentally accurate[210,211] or (/and) fitted to *ab initio* data.[67,68,212] The current MS-MMPT force field is parametrized to the *ab initio* calculations at the level of MP2/6-311++G(2d,2p). The quality of fits and parametrization is discussed in Sec. 4.1 and shown in Figure 4.4 and Figure 7.2. Besides the proton transport, it is also of interests in validating the force field to the spectroscopies,[14,209] especially of the proton transferring spectral signatures. Simulations of the infrared spectra were carried out using MS-EVB[78] and many-body PES methods.[108]

Figure 7.17 shows the infrared spectra from MS-MMPT simulations, compared to the experimental data (black dashed lines with labels). For panel a, simulations at 50 K (with $\Delta E = 10$ kcal/mol) were run using MP2-parametrized MS-MMPT force field (labeled as MS-MMPT-MP2), of which the proton diffusion is extensively discussed in this chapter for water clusters and bulks. This yields stable Eigen structures during the entire simulation time. In the high frequency region, the doublet pattern with 3800 cm^{-1} and 3880 cm^{-1} peaks are the symmetric and asymmetric water-OH stretch modes, compared with 3620 cm^{-1} and 3700 cm^{-1} from experiment (panel b). The water $O - H - O$ bending mode is between 1800 cm^{-1} and 1830 cm^{-1} while experimentally it is near 1600 cm^{-1}. For the H_3O^+ ion, the asymmetric OH stretching band is at 3440 cm^{-1} whereas the H_3O^+ bending modes appear as a doublet at 1480 cm^{-1} and 1680 cm^{-1}. For both experimental spectra[14,209] (Ar-tagged, also shown in Figure 7.17), the asymmetric hydronium OH stretches are broad and centered at 2660 cm^{-1}, some $\sim$ 800 cm^{-1} red shifted compared to the band from the simulations. For the H_3O^+ bending mode, the assignment were not given and specifically discussed from the experiments. Hence, the IR spectrum for $n = 4$ from the MS-MMPT-MP2 force field does not compare well with the experimental data.

Table 7.4.: A modification to force field parameters of bonded interactions in H_3O^+ and H_2O representations in IR refined MS-MMPT force field (MS-MMPT-IR). Unchanged parameters are the same to and listed in Table 4.2.

	H_3O^+	H_2O
k_b, kcal/mol·Å^{-2}	250	550
l_{eq}, Å	0.973	0.966
k_a, kcal/mol·rad^{-2}	31.1	45
ϕ_{eq}	112.7°	106.6°

Vibrational spectroscopy is in fact sensitive to the motion around minimum energy equilibriums. Based on this comparison, the empirical energy function was refined (labeled as MS-MMPT-IR). In particular, the OH stretching force constants were changed to $k_b = 250$ kcal/mol $\cdot$ Å^{-2} and 550 kcal/mol $\cdot$ Å^{-2} for H_3O^+ and H_2O, respectively, and the water HOH bending force constant was decreased to $k_a = 45$ kcal/mol$\cdot$Å^{-2} (Table 7.4). A comparison of the computed spectra before and after optimization and compared with experiment is provided in Figure 7.17. It is found that specifically the modes involving the H_3O^+ moiety are improved upon fitting to the IR spectra. Overall, the readjusted parameters yield a softer H_3O^+ ion and water molecules compared to the MS-MMPT-MP2 force field. Using the MS-MMPT-IR force field (with $\Delta E = 10$ kcal/mol, panel c) the water-OH doublet agrees well with the experimental data ($3640 \sim 3720$ cm^{-1} compared with $3644 \sim 3730$ cm^{-1}).[14] The largest differences between simulations with the MS-MMPT-MP2 and MS-MMPT-IR parametrization, however, concern the position for the asymmetric OH band of H_3O^+ ion which is red shifted by 660 cm^{-1} using MS-MMPT-IR. The water bending mode is located at 1580 cm^{-1} whereas the H_3O^+ bending vibrations are not affected. Similar simulations using the MS-MMPT-IR force field were also run with $\Delta E = 5$ and 15 kcal/mol (see Figure 7.17 b and d) for which the H_3O^+ asymmetric stretch OH band shifts to the blue with increasing ΔE.

MD simulations for water clusters (n=10, 31 and 50)

Table 7.5.: Hopping rates from MS-MMPT-IR simulations with $\Delta E = 5$, 7, 10 and 15 kcal/mol, compared to the corresponding results for simulations using the MS-MMPT-MP2 force field. Results were averaged from 10 1-ns MD simulations for each data.

	MS-MMPT-IR		MS-MMPT-MP2	
	ΔE, kcal/mol	r_{hop}, ns^{-1}	ΔE, kcal/mol	r_{hop}, ns^{-1}
$n = 10$	5	43 ± 7	5	3 ± 1
	7	69 ± 7	10	38 ± 8
	10	22 ± 4	12	42 ± 6
	15	1 ± 1	15	4 ± 2
$n = 31$	5	52 ± 10	5	2 ± 1
	7	130 ± 12	10	43 ± 8
	10	52 ± 7	12	101 ± 6
	15	3 ± 5	15	18 ± 5
$n = 50$	5	55 ± 9	5	3 ± 2
	7	132 ± 12	10	44 ± 6
	10	49 ± 9	12	97 ± 10
	15	3 ± 2	15	21 ± 5

With IR refined MS-MMPT force field, simulations were first carried for the water cluster with $n = 10$, 31 and 50 and the proton hopping rates were reported in Table 7.5. For $n = 10$, the hopping rate peaks at 69 ns^{-1} for $\Delta E = 7$ kcal/mol and slowed down to 43 and 22 hops/ns with $\Delta E = 5$ and 10 kcal/mol, respectively. With $\Delta E = 15$ kcal/mol, Eigen structures are too stable to transmit a proton out of such moieties and the hopping rate is not statistically countable (though the number given). In addition to $n = 10$, MD simulations were also carried out for water clusters with $n = 31$ and 50

For $n = 31$, hopping rates increase compared to those for $n = 10$ with the same values of ΔE and similarly the maximal hopping rate was found at 130 ± 12 ns^{-1} with $\Delta E = 7$ kcal/mol. For $n = 50$, the hopping rates do not further increase compared to those for $n = 31$ for all values of ΔE. Finally, Figure 7.18 reported more hopping counts with the dependence of ΔE.

Like the cluster simulations using the MS-MMPT-MP2 force field, the energetics of proton transport in simulation using the MS-MMPT-IR force field were presented by two-dimensional free energy surfaces. Figure 7.19 shows such FESs from MD simulations for $n = 31$with different values of ΔE. For $\Delta E = 5$ kcal/mol, the free energy profile suggests that a Zundel structure is the most stabilized form for a H*-carrying ion. The barrier height for Zundel to Zundel reaction path is 2.7 kcal/mol. For $\Delta E = 7$ kcal/mol, the FES features two Zundel and two Eigen minima regions, see Figure 7.19b. Overcoming barriers of 0.5 and 0.6 kcal/mol leads to Zundel to Eigen and Eigen to Zundel PT processes, respectively. Compared to Figure 7.7c (which maximizes the hopping rate using the MS-MMPT-MP2 force field), such low barriers explain why the hopping rate is maximal for $\Delta E = 7$ kcal/mol and greater than the maximum from MD simulations using MS-MMPT-MP2. For both $\Delta E = 10$ and 15 kcal/mol, the PT process follows an Eigen to Eigen path (Figure 7.19c and d). When ΔE increases to 10 kcal/mol,

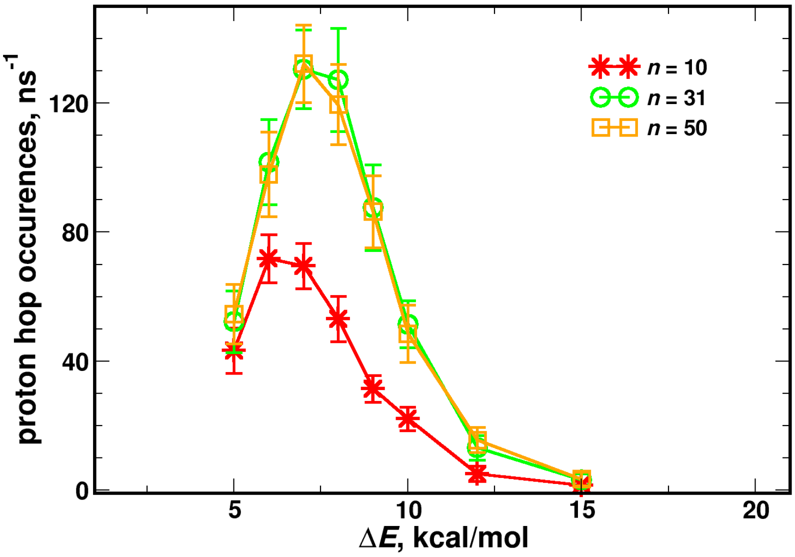

Figure 7.18.: The number of hopping occurrences in 10 ns MS-MMPT simulations of water clusters at the sizes of $n = 10$ (red), 31 (green) and 50 (orange). MDs simulations were run with the MS-MMPT-IR force field.

the Zundel minima region starts being diminished which yields to a determinant barrier height of 3.1 kcal/mol. For simulations with $\Delta E = 15$ kcal/mol, the Eigen regions are even more stable in energy and no enough MD samplings covered on the transition states.

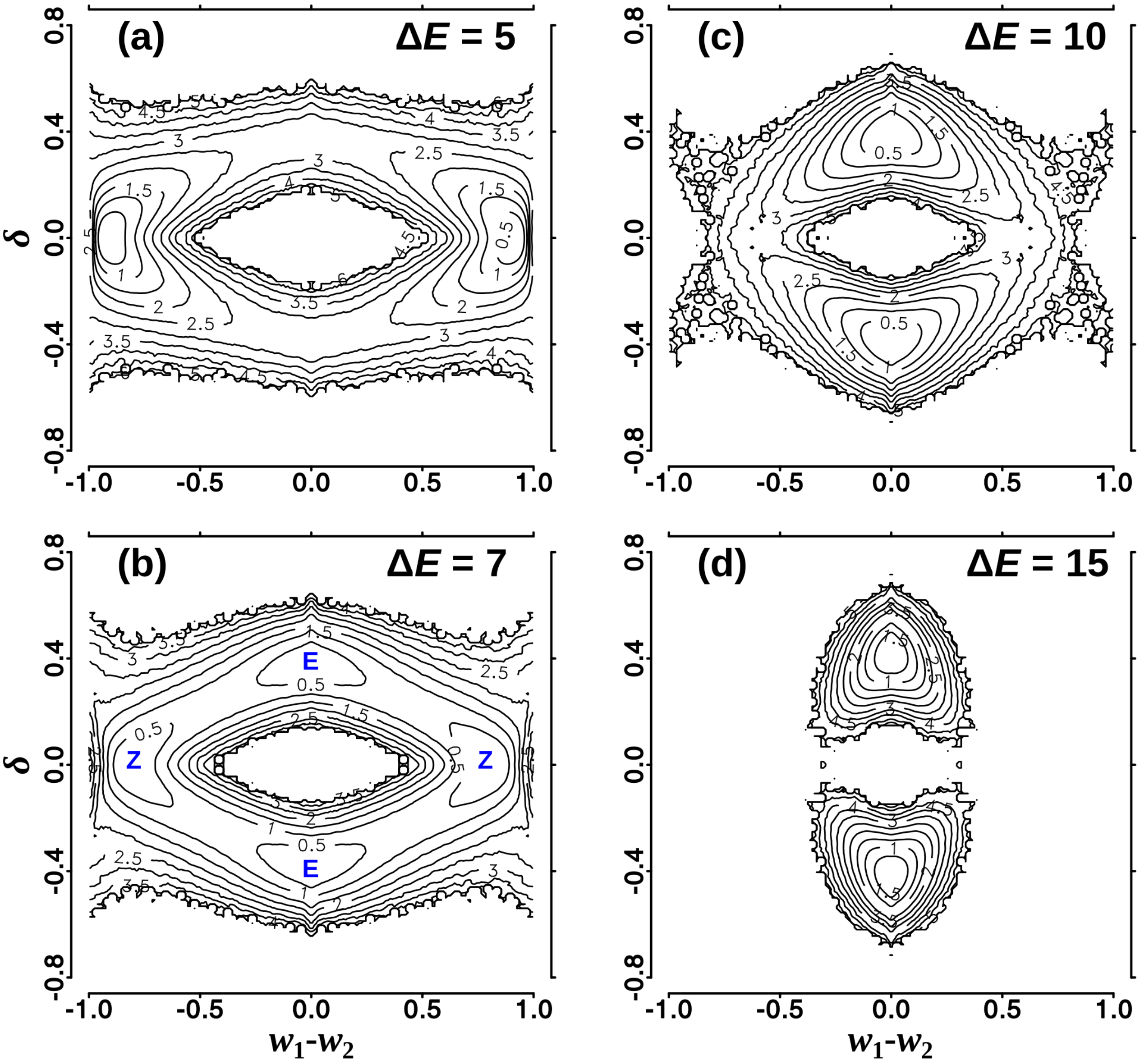

Figure 7.19.: Two-dimensioned free energy surface for PT reaction at $n = 31$. Simulations were run by using MS-MMPT-IR force field. The coordinates are δ and $w_1 - w_2$, which were collected from 10 ns MS-MMPT simulations for $n = 31$ with a) $\Delta E = 5$, b) 10, c) 12 and d) 15 kcal/mol. For the example of panel b, the top-bottom minima stand for a region where most of the conformations are Eigen while the left-right minima correspond to the Zundel region.

Table 7.6.: Self-diffusion coefficients (Å^2·ps^{-1}) from bulk simulations using MS-MMPT-IR force field. Selected data from Table 7.3 are listed for comparisons (hence the corresponding references are not specifically given in this table).

Method	ΔE kcal/mol	ensemble	r_{hop} ns^{-1}	D_{CEC}	$D_{\text{H}_2\text{O}}$
MS-MMPT-IR	5	NVE	21 ± 7	0.17 ± 0.03	0.316 ± 0.009
	7	NVE	64 ± 9	0.21 ± 0.03	
	8	NVE	80 ± 13	0.22 ± 0.03	
	10	NVE	52 ± 10	0.20 ± 0.03	
	7	NVT	66 ± 14	0.22 ± 0.04	
	8	NVT	84 ± 18	0.22 ± 0.05	
MS-MMPT-MP2	12	NVE	61 ± 9	0.17 ± 0.03	0.333 ± 0.008
MS-EVB 3		NVE	108 ± 9	0.29 ± 0.03	0.233 ± 0.005
MS-EVB 3 (CMD)		NVE	(n.a.)	0.50 ± 0.05	0.24 ± 0.01
experiment				0.94 ± 0.01	0.23

MD simulations in bulk-25 Å

For MD simulations using the MS-MMPT-IR force field for bulk-25 Å, the fastest diffusion was 0.22 ± 0.3 Å^2/ps with $\Delta E = 8$ kcal/mol whereas $\Delta E = 7$ kcal/mol maximized the proton hopping rate for water clusters. For solving the energy drift issue (discussed further below), NVT simulations were carried out using the same input values. As a result, 0.22 ± 0.05 Å^2/ps was obtained for this simulation. The hopping rates for all MS-MMPT-IR simulations were also recorded in Table 7.6. From MS-MMPT-IR simulations, the two-dimensional FESs has a similar topology to that from MS-MMPT-MP2 simulations. What differs, however, are the barriers between the E and Z states. For bulk simulations using MS-MMPT IR force field, The determinant process is Eigen to Eigen and the barrier is 0.9 kcal/mol, compared to 3.3 kcal/mol for MS-MMPT-MP2 simulations with $\Delta E = 12$ kcal/mol.

Discussion: Issues of energy non-conservation

Compared to MS-MMPT-MP2 simulations, the maximal self-diffusion coefficient from MS-MMPT-IR simulations increased by ~30%. The main difference between the two force fields is the softened OH bond for an H_3O^+ representation with a reduced force constant by a factor of 2.2. However that leads to the energy non-conservation problems using the MS-MMPT-IR force field. Figure 7.21

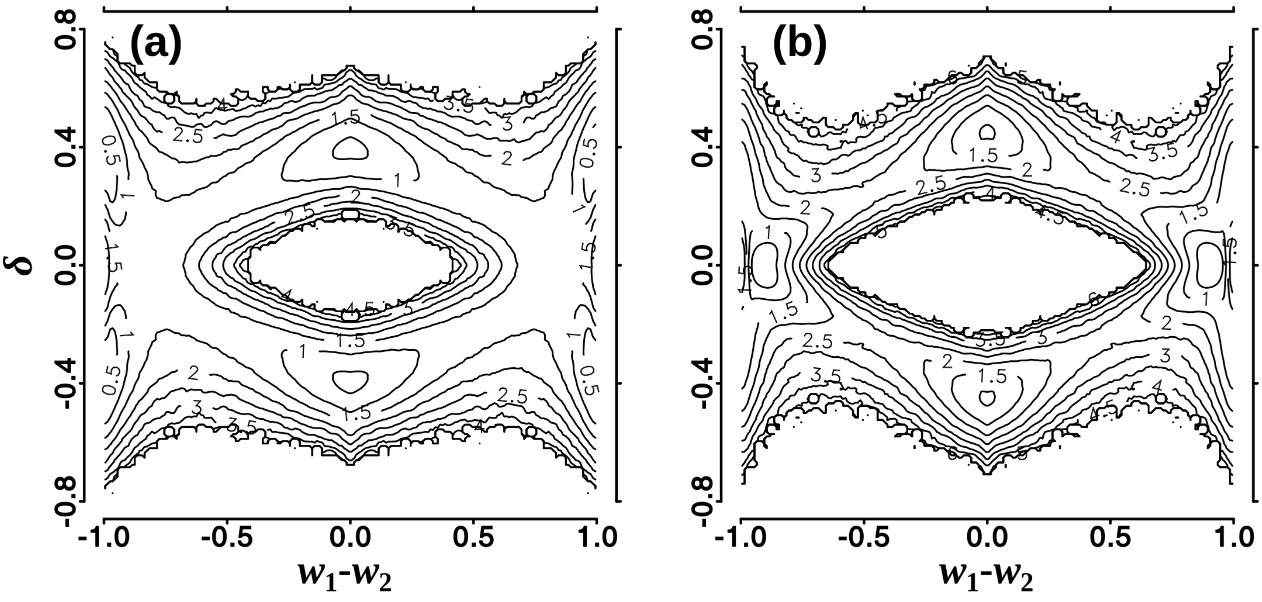

Figure 7.20.: Tow-dimensional free energy surface from a) MS-MMPT-IR simulations for bulk-25 Å with ΔE = 8 kcal/mol, compared to b) that from MS-MMPT simulations using MS-MMPT-MP2 force field (also see Figure 7.12c). For each panel, MDs were run for 8 ns.

shows such result and it was found that for simulations with $n = 31$ the energy drifts at a rate of -1.4 kcal/mol·ns^{-1}. If the force constant of this OH bond is further weakened to $k_b^{\mathrm{H_3O^+}} = 100$ kcal/mol·Å^{-2}, the drift increased to -3 kcal/mol·ns^{-1}. If the force constant is restored to 550 kcal/mol·Å^{-2}, the energy conservation was seen as the same to simulations using the MS-MMPT-MP2 force field. For bulk simulations, using the MS-MMPT-IR force field leads to the energy drift at -3 kcal/mol·ns^{-1}.

Then, a question could be raised why a softer OH bond lead to the energy non-conservation. In fact, it is not easy to answer. However, during the development of MS-MMPT, various implementations to the weighting function (Eq. 4.15) had been tried and tested. For more details, the PT potential and the square of O–O distance of a Zundel molecule were used as the scoring function $S(\mathbf{x})$, which gives $S(\mathbf{x}) = V(R, \rho, d)$ (Eq. 4.1) and $S(\mathbf{x}) = (R_{\mathrm{O-O}} - R_e)^2$ respectively. Rather than Eq. 4.16 which describes a full degrees of freedom of the Zundel molecule, using the PT potential only 3 DOFs participate in the determination of the weights (namely how states are mixed). For $S(\mathbf{x}) = (R_{\mathrm{O-O}} - R_e)^2$ (where R_e is the O–O distance at the energy-minimum structure), it was further reduced to a one-dimensional problem to decide whether a PT moiety more likely performs a PT reaction. With these two scoring

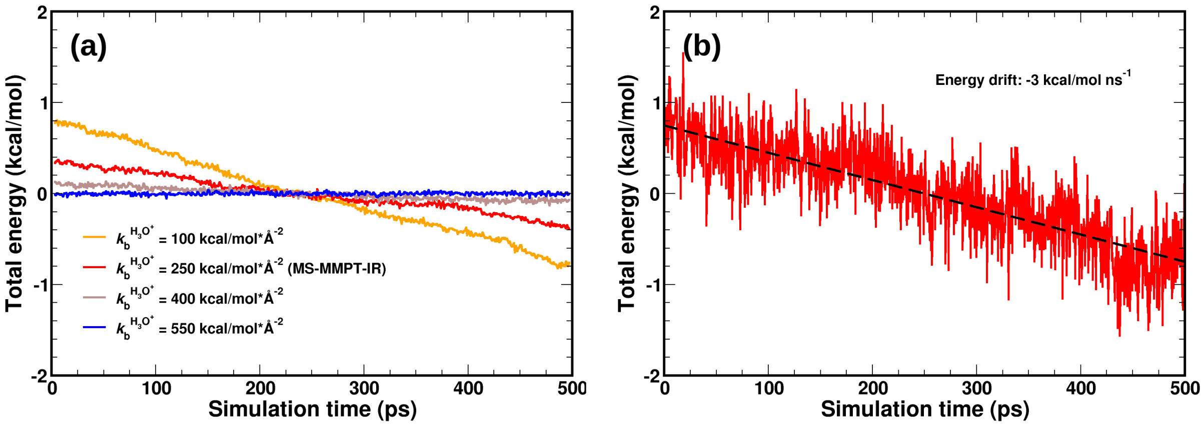

Figure 7.21.: Energy fluctuations from MS-MMPT-IR simulations for a) water clusters with $n = 31$ (with $\Delta E = 7$ kcal/mol) and b) bulk-25 Å (with $\Delta E = 8$ kcal/mol). In panel a, besides using MS-MMPT-IR (red) test simulations were also run with different force constant for $\mathrm{H_3O^+}$ OH bonds. For cluster simulations, the energy drifts are -3, -1.4 and -0.4 kcal/mol·ns^{-1} (orange, red and brown) and no energy drift were found for using $k_b^{\mathrm{H_3O^+}} = 550$ kcal/mol·Å^{-2}. For bulk simulations, the energy drift was -3 kcal/mol·ns^{-1}.

functions, test simulations were run but quickly failed due to the exceed of the energy jumping tolerance a next MD step (here, the default value was used given by CHARMM). Therefore, using the test scoring functions was considered with the lacks of essential DOFs (i.e. OH bonds) which leads to energy drift during the simulations. For MS-MMPT-IR, such lacks of DOFs took into effects due to the softened OH bonds. That also leads to the energy non-conservation.

7.4.2. Attempt II: MS-MMPT-BETA – A New Format of Weighting Function

The IR-parametrized MS-MMPT force field leads to a shortcoming of the energy non-conservation, which is one of the key issues and technical aim that the current work has been pursuing. Weakened force constants on OH bond of the H_3O^+ ion is one of the key reason for the energy drifts which has been discussed in the previous section. Aiming to obtaining a higher PT performance in the bulk simulations with one excess proton, the second solution is hereby introduced. The origin of the MS-MMPT method is multi-state adiabatic reactive MD (MS-ARMD), which is to couple multiple reaction pathway and describe an adiabatic potential energy surface for performing a classical but reactive dynamics.[147,213,214] Focusing on the weighting function (Eq. 4.15) of the MS-MMPT framework, the difference of the contribute to the MS-MMPT global potential energies depends on both the energy difference between two states and ΔE. In the MS-ARMD works, such determination of state contribution was found accurately reproducing the reactive potentials to the *ab initio* calculations. However, it does not necessarily mean that such mathematical formulation is unchangeable. In this attempt, a simple modification was introduced into the weighting function. To Eq. 4.15, an index is added to the energy component, which gives the unnormalized weight with

$$w_j^0(\mathbf{x}) = \exp\Big(- (\frac{V_{[\mathrm{H_5O_2^+}]_j}(\mathbf{x}) - V_0}{\Delta E})^{\beta}\Big) \tag{7.5}$$

where β is given with a constant which is not necessarily an integer. If $\beta = 1$, it is no different to the standard MS-MMPT scheme. And V_0 can be an arbitrary value and is in practice assigned to the minimum energy of the states because the normalized weights are independent of this term (see Eq. 4.15). If $\beta \neq 1$, however, the choice of V_0 does influence on the surface cross and it may bring out with a discontinuity to the force field it is still state-dependent, especially when the minimum energy state changes. Therefore, to this point V_0 is given with a constant value in this scheme. If the potential energy of an $H_5O_2^+$ structure is used as the scoring function, in the current work V_0 is assigned with the minimum energy of an MMPT Zundel ion in the gas phase. That assures $(V_{[\mathrm{H_5O_2^+}]_j}(\mathbf{x}) - V_0)/\Delta E$ never turns negative during the simulations.

In the current work, this trial approach (named as MS-MMPT-BETA) has been applied to bulk simulations. From test simulations (data not shown), it gives $\beta = 0.7$ (which is why $(V_{[\mathrm{H_5O_2^+}]_j}(\mathbf{x}) - V_0)/\Delta E$ should not be negative) for maximizing the diffusivity of the excess proton. Table 2 reports

Table 7.7.: Self-diffusion coefficients from bulk simulations using the MS-MMPT-BETA scheme. Simulations were run in the NVE ensemble with a time-step of $\Delta t = 0.5$ fs. Selected data from Table 7.3 and Table 7.6 are listed for comparisons (references are not specifically given in this table).

Method	ΔE kcal/mol	r_{hop} ns^{-1}	D_{CEC} $\mathrm{Å}^2/\mathrm{ps}$	$D_{\mathrm{H_2O}}$ $\mathrm{Å}^2/\mathrm{ps}$	$\frac{D_{\mathrm{CEC}}}{D_{\mathrm{H_2O}}}$	$\frac{D_{\mathrm{CEC}}}{D_{\mathrm{v}}}$
MS-MMPT-BETA ($q_{\mathrm{O}^*} = -0.98$ $\boldsymbol{e}$, $q_{\mathrm{H}^*} = 0.66$ $\boldsymbol{e}$)	4.5	76 ± 20	0.20 ± 0.05	0.333 ± 0.008	0.60 ± 0.16	1.8 ± 0.8
	5.0	103 ± 21	0.20 ± 0.05		0.60 ± 0.16	1.8 ± 0.8
	5.5	110 ± 17	0.21 ± 0.05		0.63 ± 0.17	1.9 ± 0.8
	6.0	79 ± 20	0.19 ± 0.08		0.60 ± 0.27	1.7 ± 1.0
	6.5	52 ± 13	0.17 ± 0.05		0.51 ± 0.16	1.5 ± 0.7
MS-MMPT-BETA ($q_{\mathrm{O}^*} = -0.5$ $\boldsymbol{e}$, $q_{\mathrm{H}^*} = 0.5$ $\boldsymbol{e}$)	4.0	126 ± 23	0.24 ± 0.05	0.333 ± 0.008	0.72 ± 0.17	1.8 ± 0.7
	4.5	135 ± 26	0.29 ± 0.10		0.87 ± 0.32	2.2 ± 1.1
	5.0	108 ± 17	0.23 ± 0.04		0.59 ± 0.14	1.8 ± 0.6
	5.5	74 ± 17	0.03 ± 0.04		0.09 ± 0.12	0.2 ± 0.3
MS-MMPT-IR	8	82 ± 9	0.22 ± 0.03	0.316 ± 0.009	0.70 ± 0.11	2.0 ± 0.8
MS-MMPT-MP2	12	61 ± 9	0.17 ± 0.03	0.333 ± 0.008	0.51 ± 0.10	1.5 ± 0.6
MS-EVB 3		108 ± 9	0.29 ± 0.03	0.232 ± 0.005	1.3 ± 0.2	1.4 ± 0.1
MS-EVB 3 (CMD)		(n.a.)	0.50 ± 0.05	0.24 ± 0.01	2.1 ± 0.3	2.4 ± 0.2
experiment			0.94 ± 0.01	0.23	4.1	4.7

the MD simulations using the MS-MMPT-BETA scheme. It needs to note that with one-state MMPT simulation, MS-MMPT-BETA is the same to MS-MMPT-MP2 since they use the same parameters of force fields. For the simulations, the maximum self-diffusion coefficient was obtained with $\Delta E = 5.5$ kcal/mol, which gives 0.21 ± 0.05 $\mathrm{Å}^2$/ps in rate. Compared to the standard MS-MMPT-MP2 simulations, the self-diffusion coefficient increased by $\sim 20\%$ and is roughly equal to that from energy non-conserved MS-MMPT-IR simulations. Given with the fact that MS-MMPT is not capable of simulating a free diffusion of an hydronium ion, which is always confined within a Zundel moiety. The diffusion constant for the H^*-carry ion from one-state MMPT simulation is 0.11 ± 0.02 $\mathrm{Å}^2$/ps. And MS-MMPT simulations give maximal ratios of $D_{\mathrm{CEC}}/D_{\mathrm{mass}}$ which are equal to 2.0 and 1.5 for using MS-MMPT-MP2 and MS-MMPT-IR force fields, respectively. Seeking for the possibility of further accelerated proton diffusion, in the current simulations a modified partial point charges was given to the $\mathrm{H_3O^+}$ ion ($q_{\mathrm{O}^*} = -0.5\boldsymbol{e}$ and $q_{\mathrm{H}^*} = 0.5\boldsymbol{e}$). Figure 7.22 shows the MSD traces from one-state MMPT simulations and the diffusion constant for the ion was increased by 20% and to 0.13 ± 0.02 $\mathrm{Å}^2$/ps which is relatively closer to the postulated mass contribution (0.20 $\mathrm{Å}^2$/ps) of proton diffusion (in the water system). Using this partial point charge model, MS-MMPT simulations were run using the MS-MMPT-BETA scheme. Results found that the maximal diffusion for CEC increased to 0.29 ± 0.10 Å^2/ps with $\Delta E = 4.5$ kcal/mol. That is a 70% improvement compared to the first MS-MMPT simulation using the MS-MMPT-MP2 force field (with $\Delta E = 12$ kcal/mol) and the hopping rates increased by more than 100%. Last but not least, within the current MS-MMPT frame the maximal self-diffusion coefficient of the excess proton has been reached with the energy conservation satisfied during the simulation. However, the potential of such improvement remains plausible and requires careful parametrization of the force field but such works can be expected in the future and would be helpful for simulating a more realistic proton transport with experimentally accurate mass diffusion of water and ion molecules.

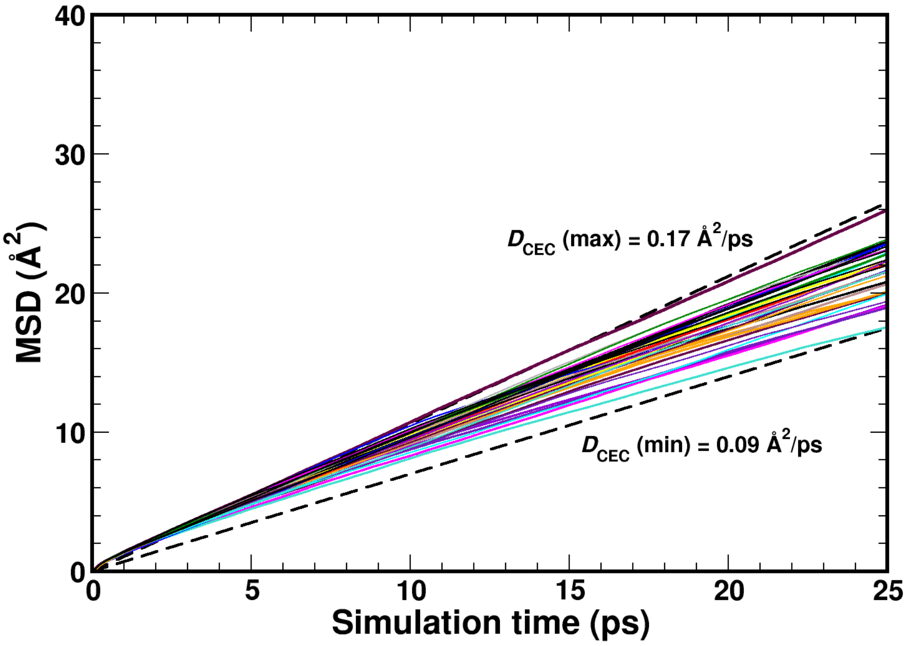

Figure 7.22.: Mean square displacement of the Zundel ion for 32 500-ps MD trajectories from one-state MMPT simulations for bulk-25 Å. The charges for the H_3O^+ ion were given as $q_{O^*} = -0.5\boldsymbol{e}$ and $q_{H^*} = 0.5\boldsymbol{e}$. The average self-diffusion coefficient for the Zundel ion is 0.13 ± 0.02 Å^2/ps.

7.5. Summary

To sum up, Grotthuss proton transport reactions were investigated from MD simulations using the new developmental MS-MMPT approach. The reactivity of proton transport was determined by calculating proton hopping rates ($h(t)$) and self-diffusion coefficients for both water clusters and bulk systems. For MS-MMPT-MP2 simulations in water clusters, the hopping rates were found dependent of the value of ΔE. That leads to a finding that the maximal hopping rate can be reached from simulation with $\Delta E = 12$ kcal/mol for $n > 10$ which gives ~100 hopping event per nanosecond. Such dependence of ΔE was explained by building two-dimensional free energy surfaces, which suggest mainly two PT pathways: one is the Zundel to Zundel process and the other is the Eigen to Eigen process. Choosing which PT process depends on the energy stability of the local minima regions of Zundel and Eigen. With $\Delta E = 12$ kcal/mol for $n = 31$, MS-MMPT simulations should overcome a barrier height of 2.6 kcal/mol which maximized the hopping rates. For bulk simulations, with $\Delta E = 12$ kcal/mol the maximal self-diffusion coefficient of 0.17 ± 0.03 Å^2/ps was given which was not comparable to the experimental value of 0.94 Å^2/ps. For the current MS-MMPT scheme, only a Zundel structure can be modeled which effectively leads to a low mass diffusion of a hydronium particle and the charge diffusion was thereby limited. The realistic proton diffusion also relies on whether the nuclear quantum effects are introduced or not. That would be expected in the future work.

Seeking for the solution to accelerate proton diffusion, two alternative schemes for MS-MMPT parametrization were proposed and simulations were carried out. The first scheme is to refine the MS-MMPT-MP2 force field by referencing to the infrared spectroscopy experiments. For the IR refined force field, the main change is the softened OH bond for a hydronium molecule in the resonance picture. For both simulations of clusters and bulks, the ~30% acceleration was seen using both hopping rates and self-diffusion coefficients. However, due to the softer bonds, the energy conservations can not be retained compared to the simulations using the MS-MMPT-MP2 force field in which energies were well conservation under the NVE ensemble. The second scheme introduced an index $-\beta$ into the weighting function (Eq. 7.5). Then, the fastest ever (in the current thesis) proton diffusion was given among all MS-MMPT simulations for bulk-25 Å and the energy conservation was reached in those simulations.

Part IV.

Conclusion and Outlook

8. Conclusion and Outlook

The methodology, new implementation and applications of the MMPT force field are presented and discussed in the current thesis. MMPT provides a reactive potential energy landscape to a triatomic motif which includes a transferring proton (or hydrogen) and the donor and acceptor atoms of this proton. Such reactive potentials are described in a three-dimensional potential energy surface and parametrized to *ab initio* calculations at high level of theory such as MP2/6-311++G(2d,2p). The new implementation to the MMPT force field includes a new potential energy surface for performing double proton transfer reactions in a concerted pathway, for which a multi-dimensional switch factor is introduced to provide coupling effects and association between two formerly independent proton transfer motifs. Furthermore, the modeling of resonance structures has been introduced to control the variance of bonding characters (e.g. a single bond to a double bond), depending on whether a proton transfer move is complete. And it is now possible to include charge transfer along with the proton transfer reaction path.

In addition to these refinements of force field description to a PT-contained molecule or complex, a completely new development is accomplished in the current thesis and greatly improve the usability and capability of the current MMPT force field. The new MS-MMPT method enables a simulation of continuous proton transport processes such Grotthuss mechanism.[3] Utilizing the MS-ARMD approach,[147] for each state in a MS-MMPT framework a unique PT motif is specifically defined with the corresponding bond topology. The total potential energy of the system is given as a weighted sum of potential energies for each state and the minimum energy state usually includes a active proton. With the thermodynamic fluctuation, such minimum energy state will finally change to the other and by that a proton transport move is simulated. This method bring new possibilities in studying proton transport reactions in complex chemical and biological systems with reasonable computing costs.

In this thesis, three application of MMPT and MS-MMPT have been presented. The first one is to predict infrared spectra of formic acid dimer and protonated oxalate from MD simulations in the gas phase using the MMPT force field. MMPT parameters are generated for both systems. For formic acid dimer, the special double proton transfer is modeled by MMPT with the coupling factor applied; For $p-$Oxa, the resonance structures are introduced to transform CO bonds among single-, double- and partial double-bond characters. For both studies, it was found that changing the curvature of the PES around minimum energy regions leads to shifts of proton transfer band. And such a change can be approached by morphing the potential surface. With the given experimental data which indicates a realistic position of PT spectral bands, the aim of MMPT simulation is to find out how much a PES should be morphed in order to predict a PT band in good agreement with the experiments. Morphing such a PES leads to an effective potential surface. That greatly helps predict the effective reaction barrier for systems in which the barrier height is difficult to be determined experimentally.

The second application focuses on the kinetic isotope effects of intramolecular PT reactions of malondialdehyde and acetylacetone. Classical MD simulations are carried out with the MMPT force field with specific parametrization including zero point vibrational effects. Effectively, the barrier heights are decreased compared to the original MMPT parametrization with reference to *ab initio* calculations. The reduction of reaction barriers is different for hydrogen and deuterium transfers, which leads to the chemical contribution to the KIEs for both molecules. In order to explicitly include nuclear quantum effects, path-integral simulations are carried out (only for Mal) based on the UM trajectories. Thereby, quantum corrections to the free energies of activation are computed for both HT and DT. And KIE values can be also computed by directly calculating the ratio of quantum corrections to the partition functions and that leads to much lower statistical errors. Both classical and quantum simulations agree with that the KIE values (in a logarithmic form) follow a linear relationship to $1/T$ and results were compared to previous studies.[18]

In the last application, Grotthuss proton diffusion is investigated by preforming MD simulations using the MS-MMPT method. The great improvement of the MS-MMPT development compared to other multi state approaches, such as MS-EVB[22,75,76,78] and TS-EVB[24,215], is that the energy is conserved during the simulations with a reasonable number of states took into account. Simulations are run for water clusters and water bulks with one excess proton. Using different values of ΔE leads to different reactivity of proton diffusion. The analysis of free energy surface suggests two different pathways for proton hops. One is the Zundel to Zundel process when ΔE is low, and the other is the Eigen to Eigen process when ΔE is high. If the Zundel and Eigen regions are equally stable in the two-dimensional free energy landscape, it leads the lowest determinant barrier height for proton transport and the diffusivity of proton is maximized. The force field parameters for MS-MMPT are first parametrized to *ab initio* calculations at the MP2/6-311++G(2d,2p) level of theory. In the bulk phase (bulk-25 Å), the maximal self-diffusion coefficient is 0.17 ± 0.03 Å^2/ps. Then the MS-MMPT force field is refined and parametrized to IR spectra with $n = 4$. As a result, the self-diffusion coefficient of the excess proton is increased by ~25% albeit the simulations lead to energy non-conservation. For the other attempt to accelerate the diffusivity of proton, the weighting function is modified. And the maximal self-diffusion coefficient of 0.29 ± 0.10 Å^2/ps is reached with the water solvent with the same background diffusion rate.

To outlook, the following improvement and research works can be expected in the future. For the standard MMPT method, anharmonicity can be introduced into the classical part of a molecule or ion which contains the PT motif. That should improve the spectroscopy compared to the experiments. In addition, more accurate fluctuating charge model or the multipole model[216,217] can be implemented especially to provide more accurate dipole moment surface which should provide a more comparable spectral patterns (e.g. intensity) to the experiments.

For the MS-MMPT method, the development in this thesis is considered a milestone that the simulation of complicated proton diffusion processes is now accomplished with energy conservation. Nevertheless, there are many things which have yet to be worked out or improved. The first one is to adapt MS-MMPT into a situation with multiple excess protons, which is important for a more complicated application in real biomolecular systems or concentrated solutions. Technically it is implemented in code but it has yet to be tested and validated. One of the most important challenges is to avoid conflicts of PT states that shared by different excess proton. The current charge transfer model is only correctly coded for a two-atom pair which includes one atom with fluctuating charge and the other with fixed point charge. With multiple protons, interactions between two fluctuating charges are inevitable and that requires careful works on such correction. In the current thesis work, the diffusion of the current water model (SPC with MP2 bond equilibriums) is too fast, increased by a factor of 1.5 compared to water diffusion measured in the experiment. That is because the CHARMM non-bonded cutoff is applied all through the current simulations (that is the only model compatible with MS-MMPT). For water models such as SPC[145] or SPC/fw,[146] usually simulations were carried out with particle mesh Ewald (PME) summation applied.[76–78] For this, a possible solution could be a differential treatment to water- water and $H_5O_2^+$-water interactions so that the water-water interactions are modeled with PME while the $H_5O_2^+$-water interactions are modeled using the standard non-bonded cutoff. Once the water diffusion rate is reset to an experimental value, it can be expected that it may likely result in slower proton diffusion even MS-MMPT-BETA is used. In fact, the slow proton diffusion is one of the major deficiencies of the current development of MS-MMPT. More recent AIMD simulations[218] suggested that the proton may hop in a concerted fashion (so called correlated proton transfer). With the current MS-MMPT simulations, only stepwise proton transfer (or a single jump) was found. In fact, from these AIMD simulations double- to quadruple- jumps have occurrence frequencies combinedly higher than that of single jump by a factor of 7. That challenges the validity of the current MS-MMPT method but points out the direction for future development. A possible solution is to extend PT motif search to outer (third-, fourth- etc.) solvation shells but may require specific parametrization to reduce the barriers of correlated proton transfer.

Part V.

Bibliography

Bibliography

[1] J. Finney, *Water: A Very Short Introduction*, Oxford University Press, 2015.

[2] A. Hassanali, F. Giberti, J. Cuny, T. D. Kühne and M. Parrinello, *Proc. Natl. Acad. Sci.*, 2013, **110**, 13723–13728.

[3] D. Marx, *Comput. Phys. Commun.*, 2007, **8**, 209–210.

[4] D. Marx, A. Chandra and M. E. Tuckerman, *Chem. Rev.*, 2010, **110**, 2174–2216.

[5] L. Masgrau, A. Roujeinikova, L. O. Johannissen, P. Hothi, J. Basran, K. E. Ranaghan, A. J. Mulholland, M. J. Sutcliffe, N. S. Scrutton and D. Leys, *Science*, 2006, **312**, 237–241.

[6] J. F. Nagle and H. J. Morowitz, *Proc. Natl. Acad. Sci.*, 1978, **75**, 298–302.

[7] P. Morsomme and M. Boutry, *Biochim. Biophys. Acta*, 2000, **1465**, 1–16.

[8] C. T. Wolke, J. A. Fournier, L. C. Dzugan, M. R. Fagiani, T. T. Odbadrakh, H. Knorke, K. D. Jordan, A. B. McCoy, K. R. Asmis and M. A. Johnson, *Science*, 2016, **354**, 1131–1135.

[9] J. A. Fournier, C. J. Johnson, C. T. Wolke, G. H. Weddle, A. B. Wolk and M. A. Johnson, *Science*, 2014, **344**, 1009–1012.

[10] K. Mackeprang, Z.-H. Xu, Z. Maroun, M. Meuwly and H. G. Kjaergaard, *Phys. Chem. Chem. Phys.*, 2016, **18**, 24654–24662.

[11] C. T. Wolke, A. F. DeBlase, C. M. Leavitt, A. B. McCoy and M. A. Johnson, *J. Phys. Chem. A*, 2015, **119**, 13018–13024.

[12] D. L. Howard, H. G. Kjaergaard, J. Huang and M. Meuwly, *J. Phys. Chem. A*, 2015, **119**, 7980–7990.

[13] J. Kim, U. W. Schmitt, J. A. Gruetzmacher, G. A. Voth and N. E. Scherer, *J. Chem. Phys.*, 2002, **116**, 737–746.

[14] J. M. Headrick, E. G. Diken, R. S. Walters, N. I. Hammer, R. A. Christie, J. Cui, E. M. Myshakin, M. A. Duncan, M. A. Johnson and K. D. Jordan, *Science*, 2005, **308**, 1765–1769.

[15] G. C. Barker and D. C. SAMMON, *Nature*, 1967, **213**, 65.

[16] M. C. Rose and J. Stuehr, *J. Am. Chem. Soc.*, 1968, **90**, 7205–7209.

[17] G. Bouchoux, J. Salpin and D. Leblanc, *Int. J. Mass Spectrom.*, 1996, **153**, 37–48.

[18] J. Huang, M. Buchowiecki, T. Nagy, J. Vanicek and M. Meuwly, *Phys. Chem. Chem. Phys.*, 2014, **16**, 204–211.

[19] G. A. Ludueña, T. D. Kühne and D. Sebastiani, *Chem. Mater.*, 2011, **23**, 1424–1429.

[20] P. Choi, N. H. Jalani and R. Datta, *J. Electrochem. Soc.*, 2005, **152**, 123–130.

[21] M. E. Selvan, D. J. Keffer, S. Cui and S. J. Paddison, 2010, **114**, 11965–11976.

[22] U. Schmitt and G. Voth, *J. Phys. Chem. B*, 1998, **102**, 5547–5551.

[23] O. Rahaman, A. C. T. van Duin, W. A. Goddard, III and D. J. Doren, *J. Phys. Chem. B*, 2011, **115**, 249–261.

[24] S. Walbran and A. A. Kornyshev, *J. Chem. Phys.*, 2001, **114**, 10039–10048.

[25] S. Lammers, S. Lutz and M. Meuwly, *J. Comput. Chem*, 2008, **29**, 1048–1063.

[26] Y. Yang and M. Meuwly, *J. Chem. Phys.*, 2010, **133**, 064503.

[27] R. Car and M. Parrinello, *Phys. Rev. Lett.*, 1985, **55**, 2471–2474.

[28] D. Marx and J. Hutter, *Ab Initio Molecular Dynamics*, Cambridge University Press, 2009.

[29] S. Alavi, *Angew. Chem. Int. Ed.*, 2009, **48**, 9404–9405.

[30] B. Brooks, R. Bruccoleri, D. Olafson, D. States, S. Swaminathan and M. Karplus, *J. Comp. Chem.*, 1983, **4**, 187–217.

[31] B. R. Brooks, C. L. Brooks, III, A. D. Mackerell, Jr., L. Nilsson, R. J. Petrella, B. Roux, Y. Won, G. Archontis, C. Bartels, S. Boresch, A. Caflisch, L. Caves, Q. Cui, A. R. Dinner, M. Feig, S. Fischer, J. Gao, M. Hodoscek, W. Im, K. Kuczera, T. Lazaridis, J. Ma, V. Ovchinnikov, E. Paci, R. W. Pastor, C. B. Post, J. Z. Pu, M. Schaefer, B. Tidor, R. M. Venable, H. L. Woodcock, X. Wu, W. Yang, D. M. York and M. Karplus, *J. Comp. Chem.*, 2009, **30**, 1545–1614.

[32] I. N. Levine, *Quantum Chemistry (5th Edition)*, Prentice Hall, 1999.

[33] M. Born and R. Oppenheimer, *Annalen der Physik*, **389**, 457–484.

[34] J. M. Millam, V. Bakken, W. Chen, W. L. Hase and H. B. Schlegel, *J. Chem. Phys.*, 1999, **111**, 3800–3805.

[35] D. L. Farnham, R. S. Van Dyck and P. B. Schwinberg, *Phys. Rev. Lett.*, 1995, **75**, 3598–3601.

[36] T. Helgaker, E. Uggerud and H. J. A. Jensen, *Chem. Phys. Lett.*, 1990, **173**, 145 – 150.

[37] E. Uggerud and T. Helgaker, *J. Am. Chem. Soc.*, 1992, **114**, 4265–4268.

[38] R. N. Barnett and U. Landman, *Phys. Rev. B*, 1993, **48**, 2081–2097.

[39] D. A. Vaccari, P. F. Strom and J. E. Alleman, *Environmental Biology for Engineers and Scientists*, Wiley-Interscience, 2005.

[40] D. J. E. Callaway and A. Rahman, *Phys. Rev. Lett.*, 1982, **49**, 613–616.

[41] D. A. Gibson, I. V. Ionova and E. A. Carter, *Chem. Phys. Lett.*, 1995, **240**, 261 – 267.

[42] A. Szabo and N. S. Ostlund, *Modern Quantum Chemistry: Introduction to Advanced Electronic Structure Theory (Dover Books on Chemistry)*, Dover Publications, 1996.

[43] *Semiempirical Methods*, Springer Berlin Heidelberg, Berlin, Heidelberg, 2008, pp. 139–154.

[44] M. J. S. Dewar, E. G. Zoebisch, E. F. Healy and J. J. P. Stewart, *J. Am. Chem. Soc.*, 1985, **107**, 3902–3909.

[45] J. Stewart, *J. Comp. Chem.*, 1989, **10**, 209–220.

[46] J. J. P. Stewart, *J. Mol. Model.*, 2007, **13**, 1173–1213.

[47] M. J. S. Dewar and W. Thiel, *J. Am. Chem. Soc.*, 1977, **99**, 4899–4907.

[48] S. Liang and A. E. Roitberg, *J. Chem. Theo. Comp.*, 2013, **9**, 4470–4480.

[49] K. Nam, Q. Cui, J. Gao and D. M. York, *J. Chem. Theo. Comp.*, 2007, **3**, 486–504.

[50] S. Wang, L. MacKay and G. Lamoureux, *J. Chem. Theo. Comp.*, 2014, **10**, 2881–2890.

[51] M. Elstner, D. Porezag, G. Jungnickel, J. Elsner, M. Haugk, T. Frauenheim, S. Suhai and G. Seifert, *Phys. Rev. B*, 1998, **58**, 7260–7268.

[52] M. Elstner, T. Frauenheim, E. Kaxiras, G. Seifert and S. Suhai, *Phys. Stat. Sol. B*, 2000, **217**, 357–376.

[53] D. Riccardi, P. Schaefer, Y. Yang, H. Yu, N. Ghosh, X. Prat-Resina, P. Konig, G. Li, D. Xu, H. Guo, M. Elstner and Q. Cui, *J. Phys. Chem. B*, 2006, **110**, 6458–6469.

[54] L. Walewski, D. Krachtus, S. Fischer, J. C. Smith, P. Bala and B. Lesyng, *Int. J. Quantum Chem.*, 2006, **106**, 636–640.

[55] C. M. Maupin, B. Aradi and G. A. Voth, *J. Phys. Chem. B*, 2010, **114**, 6922–6931.

[56] P. Goyal, M. Elstner and Q. Cui, *J. Phys. Chem. B*, 2011, **115**, 6790–6805.

[57] H. Nakai, A. W. Sakti and Y. Nishimura, *J. Phys. Chem. B*, 2016, **120**, 217–221.

[58] C. M. Maupin, B. Aradi and G. A. Voth, *J. Phys. Chem. B*, 2010, **114**, 6922–6931.

[59] A. Warshel and M. Levitt, *J. Mol. Biol.*, 1976, **103**, 227 – 249.

[60] U. N. Morzan, D. J. Armiño, N. O. Foglia, F. Ramírez, M. C. G. Lebrero, D. A. Scherlis and D. A. Estrin, *Chem. Rev.*, 2018, **118**, 4071–4113.

[61] E. Brunk and U. Rothlisberger, *Chem. Rev.*, 2015, **115**, 6217–6263.

[62] R. E. Bulo, B. Ensing, J. Sikkema and L. Visscher, *J. Chem. Theo. Comp.*, 2009, **5**, 2212–2221.

[63] J.-L. Rivail, M. Ruiz-Lopez and X. Assfeld, *Quantum Modeling of Complex Molecular Systems*, Springer, 2015, vol. 21.

[64] M. Korth, *J. Chem. Theo. Comp.*, 2010, **6**, 3808–3816.

[65] A. W. Duster, C. Wang, C. M. Garza, D. E. Miller and H. Lin, *Wiley Interdiscip. Rev. Comput. Mol. Sci.*, 2017, **7**, e1310.

[66] A. Leach, *Molecular Modelling: Principles and Applications*, Prentice Hall, 2001.

[67] K. Vanommeslaeghe, E. Hatcher, C. Acharya, S. Kundu, S. Zhong, J. Shim, E. Darian, O. Guvench, P. Lopes, I. Vorobyov and A. D. Mackerell, *J. Comp. Chem.*, 2009, **31**, 671–690.

[68] K. Vanommeslaeghe, E. Hatcher, C. Acharya, S. Kundu, S. Zhong, J. Shim, E. Darian, O. Guvench, P. Lopes, I. Vorobyov and A. D. MacKerell, Jr., *J. Chem. Phys.*, 2010, **31**, 671–690.

[69] Z.-H. Xu and M. Meuwly, *J. Phys. Chem. A*, 2017, **121**, 5389–5398.

[70] P.-A. Cazade, S. Lutz, M. W. Lee and M. Meuwly, *CHIMIA*, 2011, **65**, 326–329.

[71] A. MacKerell Jr., C. Brooks III, L. Nilsson, B. Roux, Y. Won and M. Karplus, *CHARMM: The Energy Function and Its Parameterization with an Overview of the Program*, John Wiley & Sons: Chichester, 1998, vol. 1, pp. 271–277.

[72] A. Warshel and R. Weiss, *J. Am. Chem. Soc.*, 1980, **102**, 6218–6226.

[73] A. Warshel and R. M. Weiss, *Ann. N. Y. Acad. Sci.*, 1981, **367**, 370–382.

[74] A. E. Lefohn, M. Ovchinnikov and G. A. Voth, *J. Phys. Chem. B*, **105**, 6628–6637.

[75] T. Day, A. Soudackov, M. Cuma, U. Schmitt and G. Voth, *J. Chem. Phys.*, 2002, **117**, 5839–5849.

[76] Y. Wu, H. Chen, F. Wang, F. Paesani and G. A. Voth, *J. Phys. Chem. B*, 2008, **112**, 467–482.

[77] K. Park, W. Lin and F. Paesani, *J. Phys. Chem. B*, 2012, **116**, 343–352.

[78] R. Biswas, Y.-L. S. Tse, A. Tokmakoff and G. A. Voth, *J. Phys. Chem. B*, 2016, **120**, 1793–1804.

[79] J. Köfinger and C. Dellago, *J. Phys. Chem. B*, 2008, **112**, 2349–2356.

[80] S. Iuchi, H. Chen, F. Paesani and G. A. Voth, *J. Phys. Chem. B*, 2009, **113**, 4017–4030.

[81] M. K. Petersen, S. S. Iyengar, T. J. F. Day and G. A. Voth, *J. Phys. Chem. B*, 2004, **108**, 14804–14806.

[82] C. Dellago and G. Hummer, *Phys. Rev. Lett.*, 2006, **97**, 245901.

[83] A. M. Smondyrev and G. A. Voth, *Biophys. J.*, 2002, **83**, 1987 – 1996.

[84] Y. Wu and G. A. Voth, *Biophys. J.*, 2005, **89**, 2402—2411.

[85] A. A. Kornyshev, A. M. Kuznetsov, E. Spohr and J. Ulstrup, *J. Phys. Chem. B*, 2003, **107**, 3351–3366.

[86] M. Eikerling, A. A. Kornyshev and A. A. Kulikovsky, in *Physical Modeling of Fuel Cells and their Components*, American Cancer Society, 2007.

[87] A. A. Kornyshev and E. Spohr, in *Proton Transport in Polymer Electrolyte Membranes Using Theory and Classical Molecular Dynamics*, ed. S. J. Paddison and K. S. Promislow, Springer New York, New York, NY, 2009, pp. 349–363.

[88] J. W. Halley, J. R. Rustad and A. Rahman, *J. Chem. Phys.*, 1993, **98**, 4110–4119.

[89] F. H. Stillinger and C. W. David, *J. Chem. Phys.*, 1978, **69**, 1473–1484.

[90] C. W. David, *J. Chem. Phys.*, 1996, **104**, 7255–7260.

[91] S. S. Iyengar, H. B. Schlegel, J. M. Millam, G. A. Voth, G. E. Scuseria and M. J. Frisch, *J. Chem. Phys.*, 2001, **115**, 10291–10302.

[92] S. S. Iyengar, H. B. Schlegel, G. A. Voth, J. M. Millam, G. E. Scuseria and M. J. Frisch, *Isr. J. Chem.*, 2002, **42**, 191–202.

[93] H. B. Schlegel, S. S. Iyengar, X. Li, J. M. Millam, G. A. Voth, G. E. Scuseria and M. J. Frisch, *J. Chem. Phys.*, 2002, **117**, 8694–8704.

[94] A. C. T. van Duin, S. Dasgupta, F. Lorant and W. A. Goddard, *The Journal of Physical Chemistry A*, 2001, **105**, 9396–9409.

[95] K. Chenoweth, A. C. T. van Duin and W. A. Goddard, *J. Phys. Chem. A*, 2008, **112**, 1040–1053.

[96] A. C. T. van Duin, C. Zou, K. Joshi, V. Bryantsev and W. A. Goddard, in *Computational Catalysis*, The Royal Society of Chemistry, 2014, pp. 223–243.

[97] A. Asthagiriand, M. J. Janikand, J. J. Spiveyand, L. Grabowand, W. Schneiderand, T. Manzand, A. van Duinand, S. Sinnottand and D. Scholl, *Computational Catalysis*, Royal Society of Chemistry, 2013.

[98] M. A. Lill and V. Helms, *J. Chem. Phys.*, 2001, **115**, 7993–8005.

[99] M. A. Lill and V. Helms, *J. Chem. Phys.*, 2001, **115**, 7985–7992.

[100] E. Herzog, T. Frigato, V. Helms and C. R. D. Lancaster, *J. Comp. Chem.*, 2006, **27**, 1534–1547.

[101] M. Mucha, T. Frigato, L. M. Levering, H. C. Allen, D. J. Tobias, L. X. Dang and P. Jungwirth, *J. Phys. Chem. B*, 2005, **109**, 7617–7623.

[102] M. A. Lill and V. Helms, *Proc. Natl. Acad. Sci.*, 2002, **99**, 2778–2781.

[103] W. Gu, B. Zhou, T. Geyer, M. Hutter, H. Fang and V. Helms, *Angew. Chem. Int. Ed.*, 2011, **50**, 768–771.

[104] W. Gu and V. Helms, *J. Am. Chem. Soc.*, 2009, **131**, 2080–2081.

[105] R. Devanathan, A. Venkatnathan, R. Rousseau, M. Dupuis, T. Frigato, W. Gu and V. Helms, *J. Phys. Chem. B*, 2010, **114**, 13681–13690.

[106] M. G. Wolf and G. Groenhof, *J. Comp. Chem.*, 2014, **35**, 657–671.

[107] Q. Yu and J. M. Bowman, *J. Chem. Theo. Comp.*, 2016, **12**, 5284–5292.

[108] Q. Yu and J. M. Bowman, *J. Chem. Phys.*, 2017, **146**, 121102.

[109] Zundel G. and Metzger H., *Phys. Chem.*, 1968, **58**, 225.

[110] W. E., E. M. and A. T., *Phys. Chem.*, 1954, **1**, 340.

[111] N. K. Roberts and H. L. Northey, *J. Chem. Soc., Faraday Trans. 1*, 1974, **70**, 253–262.

[112] B. D. Cornish and R. J. Speedy, *J. Phys. Chem.*, 1984, **88**, 1888–1892.

[113] M. Holz, S. R. Heil and A. Sacco, *Phys. Chem. Chem. Phys.*, 2000, **2**, 4740–4742.

[114] P. Choi, N. H. Jalani and R. Datta, *J. Electrochem. Soc.*, 2005, **152**, 123–130.

[115] T. von Grotthuss and S. Nomine, *Mémoire sur la décomposition de l'eau et des corps qu'elle tient en dissolution à l'aide de l'électricité Galvanique par C.J.T. de Grotthuss*, 1805.

[116] N. Agmon, *Chem. Phys. Lett.*, 1995, **244**, 456–462.

[117] L. E. Strong, *J. Chem. Eng. Data*, 1980, **25**, 104–106.

[118] N. K. Roberts and H. L. Northey, *J. Chem. Soc., Faraday Trans. 1*, 1972, **68**, 1528–1532.

[119] T. S. Light, S. Licht, A. C. Bevilacqua and K. R. Morash, *Electrochem. Solid State Lett.*, 2005, **8**, 16–19.

[120] J. Huang, *Ph.D. thesis*, University of Basel, 2011.

[121] M. J. Frisch, G. W. Trucks, H. B. Schlegel, G. E. Scuseria, M. A. Robb, J. R. Cheeseman, G. Scalmani, V. Barone, B. Mennucci, G. A. Petersson, H. Nakatsuji, M. Caricato, X. Li, H. P. Hratchian, A. F. Izmaylov, J. Bloino, G. Zheng, J. L. Sonnenberg, M. Hada, M. Ehara, K. Toyota, R. Fukuda, J. Hasegawa, M. Ishida, T. Nakajima, Y. Honda, O. Kitao, H. Nakai, T. Vreven, J. A. Montgomery, Jr., J. E. Peralta, F. Ogliaro, M. Bearpark, J. J. Heyd, E. Brothers, K. N. Kudin, V. N. Staroverov, R. Kobayashi, J. Normand, K. Raghavachari, A. Rendell, J. C. Burant, S. S. Iyengar, J. Tomasi, M. Cossi, N. Rega, J. M. Millam, M. Klene, J. E. Knox, J. B. Cross, V. Bakken, C. Adamo, J. Jaramillo, R. Gomperts, R. E. Stratmann, O. Yazyev, A. J. Austin, R. Cammi, C. Pomelli, J. W. Ochterski, R. L. Martin, K. Morokuma, V. G. Zakrzewski, G. A. Voth, P. Salvador, J. J. Dannenberg, S. Dapprich, A. D. Daniels, O. Farkas, J. B. Foresman, J. V. Ortiz, J. Cioslowski, and D. J. Fox, *Gaussian 09, Revision A.02*, Gaussian, Inc., Wallingford, CT, 2009.

[122] M. Law and J. Hutson, *Comput. Phys. Commun.*, 1997, **102**, 252–268.

[123] S. Bochkanov, *ALGLIB. http://www.alglib.net.*

[124] S. Lammers and M. Meuwly, *Aust. J. Chem.*, 2004, **57**, 1223–1228.

[125] M. Head-Gordon, J. A. Pople and M. J. Frisch, *Chem. Phys. Lett.*, 1988, **153**, 503–506.

[126] M. J. Frisch, M. Head-Gordon and J. A. Pople, *Chem. Phys. Lett.*, 1990, **166**, 281–289.

[127] M. J. Frisch, M. Head-Gordon and J. A. Pople, *Chem. Phys. Lett.*, 1990, **166**, 275–280.

[128] M. Head-Gordon and T. Head-Gordon, *Chem. Phys. Lett.*, 1994, **220**, 122–128.

[129] A. D. Becke, *Phys. Rev. A*, 1988, **38**, 3098–3100.

[130] A. D. Becke, *J. Chem. Phys.*, 1993, **98**, 5648–5652.

[131] C. Lee, W. Yang and R. G. Parr, *Phys. Rev. B*, 1988, **37**, 785–789.

[132] S. H. Vosko, L. Wilk and M. Nusair, *Can. J. Phys.*, 1980, **58**, 1200–1211.

[133] G. Zheng, H. A. Witek, P. Bobadova-Parvanova, S. Irle, D. G. Musaev, R. Prabhakar, K. Morokuma, M. Lundberg, M. Elstner, C. Koehler and T. Frauenheim, *J. Chem. Theo. Comp.*, 2007, **3**, 1349–1367.

[134] J. A. Montgomery, M. J. Frisch, J. W. Ochterski and G. A. Petersson, *J. Chem. Phys.*, 1999, **110**, 2822–2827.

[135] J. A. Montgomery, M. J. Frisch, J. W. Ochterski and G. A. Petersson, *J. Chem. Phys.*, 2000, **112**, 6532–6542.

[136] L. A. Curtiss, P. C. Redfern and K. Raghavachari, *J. Chem. Phys.*, 2007, **126**, 084108.

[137] L. A. Curtiss, P. C. Redfern and K. Raghavachari, *J. Chem. Phys.*, 2007, **127**, 124105.

[138] G. D. Purvis and R. J. Bartlett, *J. Chem. Phys.*, 1982, **76**, 1910–1918.

[139] G. E. Scuseria, C. L. Janssen and H. F. Schaefer, *J. Chem. Phys.*, 1988, **89**, 7382–7387.

[140] G. E. Scuseria and H. F. Schaefer, *J. Chem. Phys.*, 1989, **90**, 3700–3703.

[141] R. A. Kendall, T. H. Dunning and R. J. Harrison, *J. Chem. Phys.*, 1992, **96**, 6796–6806.

[142] J. M. Hutson, *J. Chem. Phys.*, 1992, **96**, 6752–6767.

[143] M. Meuwly and J. M. Hutson, *J. Chem. Phys.*, 1999, **110**, 8338–8347.

[144] S. Lammers and M. Meuwly, *J. Phys. Chem. A*, 2007, **111**, 1638–1647.

[145] H. J. C. Berendsen, J. P. M. Postma, W. F. van Gunsteren and J. Hermans, in *Interaction Models for Water in Relation to Protein Hydration*, ed. B. Pullman, Springer Netherlands, Dordrecht, 1981, pp. 331–342.

[146] Y. Wu, H. L. Tepper and G. A. Voth, *J. Chem. Phys.*, 2006, **124**, 024503.

[147] T. Nagy, J. Yosa Reyes and M. Meuwly, *J. Chem. Theo. Comp.*, 2014, **10**, 1366–1375.

[148] W. Reutemann and H. Kieczka, in *Formic Acid*, American Cancer Society, 2000.

[149] R. M. Balabin, *J. Phys. Chem. A*, 2009, **113**, 4910–4918.

[150] Özgür Birer and M. Havenith, *Annu. Rev. Phys. Chem.*, 2009, **60**, 263–275.

[151] V. V. Matylitsky, C. Riehn, M. F. Gelin and B. Brutschy, *J. Chem. Phys.*, 2003, **119**, 10553–10562.

[152] K. G. Goroya, Y. Zhu, P. Sun and C. Duan, *J. Chem. Phys.*, 2014, **140**, 164311.

[153] Y. T. Chang, Y. Yamaguchi, W. H. Miller and H. F. Schaefer, *J. Am. Chem. Soc.*, 1987, **109**, 7245–7253.

[154] C. Qu and J. M. Bowman, *J. Chem. Phys.*, 2018, **148**, 241713.

[155] M. V. Vener, O. Kühn and J. M. Bowman, *Chem. Phys. Lett.*, 2001, **349**, 562–570.

[156] I. Matanović and N. Došlić, *Chem. Phys.*, 2007, **338**, 121–126.

[157] K. Ito and H. J. Bernstein, *Can. J. Chem.*, 1956, **34**, 170–178.

[158] K. I. Peterson and D. P. Pullman, *J. Chem. Educ.*, 2016, **93**, 1130–1133.

[159] R. L. Frost, J. Yang and Z. Ding, *Sci. Bull.*, 2003, **48**, 1844–1852.

[160] D. Applin, M. Izawa, E. Cloutis, D. Goltz and J. Johnson, *Earth Planet. Sci. Lett.*, 2015, **420**, 127–139.

[161] A. Frey-Wyssling, *Am. J. Bot.*, 1981, **68**, 130–141.

[162] I. R. Craig and D. E. Manolopoulos, *J. Chem. Phys.*, 2004, **121**, 3368–3373.

[163] M. Rossi, M. Ceriotti and D. E. Manolopoulos, *J. Chem. Phys.*, 2014, **140**, 234116.

[164] S. Habershon, D. E. Manolopoulos, T. E. Markland and T. F. Miller-III, *Annu. Rev. Phys. Chem.*, 2013, **64**, 387–413.

[165] M. Shiga and A. Nakayama, *Comput. Phys. Commun.*, 2008, **451**, 175–181.

[166] S. Habershon, G. S. Fanourgakis and D. E. Manolopoulos, *J. Chem. Phys.*, 2008, **129**, 074501.

[167] M. Ceriotti, J. More and D. E. Manolopoulos, *Comput. Phys. Commun.*, 2014, **185**, 1019–1026.

[168] D. T. Major, M. Garcia-Viloca and J. Gao, *J. Chem. Theo. Comp.*, 2006, **2**, 236–245.

[169] D. T. Major and J. Gao, *J. Chem. Theo. Comp.*, 2007, **3**, 949–960.

[170] J. Gao, K.-Y. Wong and D. T. Major, *J. Comp. Chem.*, 2008, **29**, 514–522.

[171] J. Meisner, J. B. Rommel and J. Kästner, *J. Comp. Chem.*, 2011, **32**, 3456–3463.

[172] F. Trixler, *Curr. Org. Chem.*, 2013, **17**, 1758–1770.

[173] J. P. Bothma, J. B. Gilmore and R. H. McKenzie, *New J. Phys.*, 2010, **12**, 055002.

[174] J. N. Woodford and G. S. Harbison, *J. Chem. Theo. Comp.*, 2006, **2**, 1464–1475.

[175] A. Gross and M. Scheffler, *J. Vac. Sci. Technol.*, 1997, **15**, 1624–1629.

[176] K. Ruud, P.-O. Åstrand and P. R. Taylor, *J. Am. Chem. Soc.*, 2001, **123**, 4826–4833.

[177] W. Heisenberg, *Z. Phys.*, 1927, **43**, 172–198.

[178] E. H. Kennard, *Z. Phys.*, 1927, **44**, 326–352.

[179] P. Busch, T. Heinonen and P. Lahti, *Phys. Rep.*, 2007, **452**, 155–176.

[180] S. Ganeshan, R. Ramirez and M. V. Fernandez-Serra, *Phys. Rev. B*, 2013, **87**, 134207.

[181] N. J. Green, in *Unimolecular Kinetics*, ed. N. Green, Elsevier, 2003, vol. 39, pp. 1–53.

[182] R. G. Miller, *Survival Analysis*, John Wiley & Sons Inc, 1997.

[183] C. Kartsonaki, *Diagn. Histopathol.*, 2016, **22**, 263–270.

[184] E. Helfand, *J. Chem. Phys.*, 1978, **69**, 1010–1018.

[185] M. Meuwly and M. Karplus, *J. Chem. Phys.*, 2002, **116**, 2572–2585.

[186] S. Albeverio, R. Høegh-Krohn and S. Mazzucchi, *Mathematical Theory of Feynman Path Integrals: An Introduction (Lecture Notes in Mathematics)*, Springer, 2008.

[187] D. T. Major and J. Gao, *J. Mol. Graph. Model.*, 2005, **24**, 121 – 127.

[188] S. Lammers, *Ph.D. thesis*, University of Basel, 2006.

[189] J. A. Sansón, M.-L. Sánchez and J. C. Corchado, *J. Phys. Chem. A*, 2006, **110**, 589–599.

[190] Z. Wang, J. S. Hirschi and D. A. Singleton, *Angew. Chem. Int. Ed.*, **48**, 9156–9159.

[191] J. Huang, M. Buchowiecki, T. Nagy, J. Vanicek and M. Meuwly, *Phys. Chem. Chem. Phys.*, 2014, **16**, 204–211.

[192] I. Navrotskaya, Q. Shi and E. Geva, *Isr. J. Chem.*, **42**, 225–236.

[193] E. Geva, Q. Shi and G. A. Voth, *J. Chem. Phys.*, 2001, **115**, 9209–9222.

[194] Y. Suleimanov, J. Allen and W. Green, *Comput. Phys. Commun*, 2013, **184**, 833 – 840.

[195] Y. V. Suleimanov, F. J. Aoiz and H. Guo, *J. Phys. Chem. A*, 2016, **120**, 8488–8502.

[196] Y. V. Suleimanov, R. P. de Tudela, P. G. Jambrina, J. F. Castillo, V. Saez-Rabanos, D. E. Manolopoulos and F. J. Aoiz, *Phys. Chem. Chem. Phys.*, 2013, **15**, 3655–3665.

[197] R. Collepardo-Guevara, I. R. Craig and D. E. Manolopoulos, *J. Chem. Phys.*, 2008, **128**, 144502.

[198] R. Collepardo-Guevara, Y. V. Suleimanov and D. E. Manolopoulos, *J. Chem. Phys.*, 2009, **130**, 044131.

[199] I. R. Craig and D. E. Manolopoulos, *J. Chem. Phys.*, 2005, **122**, 084106.

[200] I. R. Craig and D. E. Manolopoulos, *J. Chem. Phys.*, 2005, **123**, 034102.

[201] R. P. de Tudela, F. J. Aoiz, Y. V. Suleimanov and D. E. Manolopoulos, *J. Phys. Chem. Lett.*, 2012, **3**, 493–497.

[202] T. E. Markland and D. E. Manolopoulos, *Chem. Phys. Lett.*, 2008, **464**, 256–261.

[203] D. Marx, M. E. Tuckerman, J. Hutter and M. Parrinello, *Nature*, 1999, **397**, 601–604.

[204] E. A. Dolan, R. M. Venable, R. W. Pastor and B. R. Brooks, *Biophys. J.*, 2002, **82**, 2317–2325.

[205] D. H. Everett, in *International Union of Pure and Applied Chemistry Division of Physical Chemistry*, Pure Appl. Chem., 1972, pp. 577–638.

[206] F. Paesani, W. Zhang, D. A. Case, I. Thomas E. Cheatham and G. A. Voth, *J. Chem. Phys.*, 2006, **125**, 184507.

[207] A. K. Soper and C. J. Benmore, *Phys. Rev. Lett.*, 2008, **101**, 065502.

[208] A. Botti, F. Bruni, S. Imberti, M. A. Ricci and A. K. Soper, *J. Chem. Phys.*, 2004, **121**, 7840–7848.

[209] J. A. Fournier, C. T. Wolke, C. J. Johnson, M. A. Johnson, N. Heine, S. Gewinner, W. Schöllkopf, T. K. Esser, M. R. Fagiani, H. Knorke and K. R. Asmis, *Proc. Natl. Acad. Sci.*, 2014, **111**, 18132–18137.

[210] J. H. Lii and N. L. Allinger, *J. Am. Chem. Soc.*, 1989, **111**, 8566–8575.

[211] H. Sellers, P. Pulay and J. E. Boggs, *J. Am. Chem. Soc.*, 1985, **107**, 6487–6494.

[212] T. A. Halgren, *J. Comp. Chem.*, 1996, **17**, 490–519.

[213] J. Yosa Reyes, S. Brickel, O. T. Unke, T. Nagy and M. Meuwly, *Phys. Chem. Chem. Phys.*, 2016, **18**, 6780–6788.

[214] S. Brickel and M. Meuwly, *J. Phys. Chem. A*, 2017, **121**, 5079–5087.

[215] T. Mabuchi, A. Fukushima and T. Tokumasu, *J. Chem. Phys.*, 2015, **143**, 014501.

[216] T. Bereau, C. Kramer, F. W. Monnard, E. S. Nogueira, T. R. Ward and M. Meuwly, *J. Phys. Chem. B*, 2013, **117**, 5460–5471.

[217] T. Bereau, C. Kramer and M. Meuwly, *J. Chem. Theo. Comp.*, 2013, **9**, 5450–5459.

[218] M. Chen, L. Zheng, B. Santra, H.-Y. Ko, R. A. DiStasio Jr, M. L. Klein, R. Car and X. Wu, *Nat. Chem.*, 2018, **10**, 413–419.

Part VI.

Appendix

Abbreviation and Units

B3LYP	Becke-3-parameter-Lee-Yang-Parr
CCSD(T)	Coupled-Cluster with single, double and perturbative triple excitations
CHARMM	Chemistry at HARvard Molecular Mechanics
CM	Classical Mechanics
CMMD	Classical Mechanics Molecular Dynamics
DFT	Density Functional Theory
DFTB	Density-Functional Tight-Binding
DPT	Double proton transfer
FF	Force Field
FPC	Fixed Point Charge
HMFW	Half Maximum Full Width
IR	infrared
KIE	Kinetic Isotope Effect
LJ	Lennard-Jones
MD	Molecular Dynamics
MEP	Minimum Energy Path
MM	Molecular Mechanics
MMPT	Molecular Mechanics with Proton Transfer
MP2	Møller-Plesset second order
MS-EVB	Multi-state empirical valence bond
MS-MMPT	Multi-state Molecular Mechanics with Proton Transfer
n.a.	not available
NVE	microcanonical ensemble
NVT	canonical ensemble
PI	Path Integral
PT	Proton Transfer
QM	Quantum Mechanics
TS-EVB	Two-state empirical valence bond
vdW	van der Waals
ZPVE	Zero Energy Vibrational Effect

Å	Ångström
cm^{-1}	Wavenumber
$\boldsymbol{e}$	Elementary charge
rad	Radian
K	Kelvin
kcal	Kilo-calorie
mol	Mole
nm	Nanometer
fs	Femtosecond
ps	Picosecond
ns	Nanosecond
L	Liter

Deduction to the gradient of MS-MMPT total potential energy (Eq. 4.17)

a) $$\mathrm{V}_{\text{total}}(\mathbf{x}) = \sum_{i=1}^{m} w_i(\mathbf{x}) \cdot V_i(\mathbf{x})$$

b) $$\begin{aligned}
\nabla w_j^0(\mathbf{x}) &= \nabla\Big[e^{-\Big(\frac{V_j^{\mathrm{H_5O_2^+}}(\mathbf{x}) - V_{\min}^{\mathrm{H_5O_2^+}}(\mathbf{x})}{\Delta E}\Big)}\Big] \\
&= -\Big(\frac{\nabla V_j^{\mathrm{H_5O_2^+}}(\mathbf{x}) - \nabla V_{\min}^{\mathrm{H_5O_2^+}}(\mathbf{x})}{\Delta E}\Big) \cdot w_j^0(\mathbf{x})
\end{aligned}$$

c)

$$\begin{aligned}
\nabla V_{\text{total}}(\mathbf{x}) &= \nabla\Big[\sum_{j=1}^{m} w_j(\mathbf{x}) \cdot V_j(\mathbf{x})\Big] \\
&= \sum_{j=1}^{m} w_j(\mathbf{x}) \cdot \nabla V_j(\mathbf{x}) + \sum_{j=1}^{m} \nabla w_j(\mathbf{x}) \cdot V_j(\mathbf{x}) \\
&= \sum_{j=1}^{m} w_j(\mathbf{x}) \cdot \nabla V_j(\mathbf{x}) + \sum_{j=1}^{m} \nabla\Big[w_j^0(\mathbf{x}) \cdot \frac{1}{\sum\limits_{i=1}^{m} w_i^0(\mathbf{x})}\Big] \cdot V_j(\mathbf{x}) \\
&= \sum_{j=1}^{m} w_j(\mathbf{x}) \cdot \nabla V_j(\mathbf{x}) + \sum_{j=1}^{m} \frac{\nabla w_j^0(\mathbf{x})}{\sum\limits_{i=1}^{m} w_i^0(\mathbf{x})} \cdot V_j(\mathbf{x}) - \sum_{j=1}^{m} \nabla\Big[\sum_{i=1}^{m} w_i^0(\mathbf{x})\Big] \cdot \frac{w_j^0(\mathbf{x})}{\big[\sum\limits_{i=1}^{m} w_i^0(\mathbf{x})\big]^2} \cdot V_j(\mathbf{x}) \\
&= \sum_{i=1}^{m} w_j(\mathbf{x}) \nabla V_j(\mathbf{x}) - \frac{1}{\Delta E} \sum_{j=1}^{m} \big[\nabla V_j^{\mathrm{H_5O_2^+}}(\mathbf{x}) - \nabla V_{\min}^{\mathrm{H_5O_2^+}}(\mathbf{x})\big] \cdot w_j(\mathbf{x}) \cdot V_j(\mathbf{x}) \\
&\quad + \frac{\sum\limits_{i=1}^{m} w_i(\mathbf{x}) \cdot V_i(\mathbf{x})}{\sum\limits_{i=1}^{m} w_i^0(\mathbf{x})} \cdot \frac{1}{\Delta E} \sum_{j=1}^{m} w_j^0(\mathbf{x}) \cdot \big[\nabla V_j^{\mathrm{H_5O_2^+}}(\mathbf{x}) - \nabla V_{\min}^{\mathrm{H_5O_2^+}}(\mathbf{x})\big] \\
&= \frac{1}{\Delta E} \cdot \sum_{j=1}^{m} \Big\{ w_j(\mathbf{x}) \nabla V_j(\mathbf{x}) \cdot \Delta E - \big[\nabla V_j^{\mathrm{H_5O_2^+}}(\mathbf{x}) - \nabla V_{\min}^{\mathrm{H_5O_2^+}}(\mathbf{x})\big] \cdot w_j(\mathbf{x}) \cdot V_j(\mathbf{x}) \\
&\quad + \big[\nabla V_j^{\mathrm{H_5O_2^+}}(\mathbf{x}) - \nabla V_{\min}^{\mathrm{H_5O_2^+}}(\mathbf{x})\big] \cdot w_j(\mathbf{x}) \cdot \sum_{i=1}^{m} \big[w_i(\mathbf{x}) \cdot V_i(\mathbf{x})\big] \Big\} \\
&= \frac{1}{\Delta E} \cdot \sum_{j=1}^{m} \Big\{ w_j(\mathbf{x}) \nabla V_j(\mathbf{x}) \cdot \Delta E + \big[\nabla V_j^{\mathrm{H_5O_2^+}}(\mathbf{x}) - \nabla V_{\min}^{\mathrm{H_5O_2^+}}(\mathbf{x})\big] \cdot w_j(\mathbf{x}) \cdot (V_{\text{total}}(\mathbf{x}) - V_j(\mathbf{x})) \Big\} \\
&= \frac{1}{\Delta E} \cdot \sum_{j=1}^{m} \Big\{ w_j(\mathbf{x}) \nabla V_j(\mathbf{x}) \cdot \Delta E + w_j(\mathbf{x}) \cdot \big[V_{\text{total}}(\mathbf{x}) - V_j(\mathbf{x})\big] \\
&\quad \cdot \nabla V_j^{\mathrm{H_5O_2^+}}(\mathbf{x}) - w_j(\mathbf{x}) \cdot \big[V_{\text{total}}(\mathbf{x}) - V_j(\mathbf{x})\big] \cdot \nabla V_{\min}^{\mathrm{H_5O_2^+}}(\mathbf{x}) \Big\} \\
&= \sum_{j=1}^{m} w_j(\mathbf{x}) \cdot \Big(\nabla V_j(\mathbf{x}) + \frac{V^{\mathbf{TOT}}(\mathbf{x}) - V_j(\mathbf{x})}{\Delta E} \cdot \nabla V_j^{\mathrm{H_5O_2^+}}(\mathbf{x})\Big)
\end{aligned}$$